UNIVERSITY OF SOUTHAMPTON

Hydrothermal mineral deposits and the behaviour of Au within the Earth

by

Alexander Patrick Webber

A thesis submitted in partial fulfillment for the degree of Doctor of Philosophy

in the

Faculty of Natural and Environmental Sciences

Ocean and Earth Science

May 2013

Declaration of Authorship

I, Alexander Webber, declare that this thesis titled, 'Hydrothermal mineral deposits and the behaviour of Au within the Earth' and the work presented in it are my own. I confirm that:

- This work was done wholly or mainly while in candidature for a research degree at this University.
- Where any part of this thesis has previously been submitted for a degree or any other qualification at this University or any other institution, this has been clearly stated.
- Where I have consulted the published work of others, this is always clearly attributed.
- Where I have quoted from the work of others, the source is always given. With the exception of such quotations, this thesis is entirely my own work.
- I have acknowledged all main sources of help.
- Where the thesis is based on work done by myself jointly with others, I have made clear exactly what was done by others and what I have contributed myself.

Signed: _____

Date: _____

"I think the problem, to be quite honest with you, is that you've never actually known what the question is."

Deep Thought (Douglas Adams)

UNIVERSITY OF SOUTHAMPTON

Abstract

Faculty of Natural and Environmental Sciences
Ocean and Earth Science

Doctor of Philosophy

by Alexander Patrick Webber

High metal concentrations in source rocks has been implicated as an important control on the metal budget of a mineralising hydrothermal system. Consequently, the behaviour of Au in rocks and magmas before it enters a hydrothermal system is important in constraining the occurrence and size of any mineral deposit that might result. This thesis focuses on the behaviour of Au in magmatic and metamorphic systems such as the formation of oceanic crust, the subduction of oceanic crust and the high-level arc magmatic system. The creation and subduction of oceanic crust and chemical fluxes from the slab is critical to the formation of an arc, arc volcanism and the occurrence of a hydrothermal system. Chapter 3 shows that mantle plumes are able to create vast quantities of Au-rich oceanic crust during ridge-plume interaction, and therefore provide a viable mechanism for supplying Au-rich source rocks to the subduction system and, additionally, hydrothermal mineral deposits on the sea-floor. Chapter 4 investigates the subduction of oceanic crust and the flux of Au from the downgoing slab. It shows that a proportion of Au might be lost during metamorphism to eclogite, and the fluids released are capable of producing Au-rich melts in the mantle wedge. Crucially, it shows that the subduction of particularly Au-rich crust provides a viable mechanism for the creation of Au-rich magmas in the arc system. Finally, Chapter 5 shows that magnetite crystallisation in the high-level magmatic system is capable of sequestering the majority of Au from a melt, and as such strongly controls the Au budget of the melt-hydrothermal system. However, this does not preclude the possibility of Au mineralisation and may actually make Au mineralisation more likely by the creation of Au-rich cumulates which could provide a source of Au for any scavenging hydrothermal fluid. Chapter 6 examines fluid mixing and thermal regimes within the PACMANUS hydrothermal system, Papua New Guinea. It shows that anhydrite precipitation happened rapidly, preventing the equilibration of oxygen isotopes during precipitation. The helium isotopes indicate significant contamination of atmospheric helium.

Acknowledgements

I'd like to thank my project supervisor Prof. Steve Roberts for help, guidance and beer throughout, Dr. Bob Foster and Stratex International for help and support with the Turkey field trip, funding and scientific guidance and Dr. Iain Pitcairn for teaching me the gold analysis technique used in this thesis and scientific advice. I thank Dr. Matt Cooper, Dr. Andy Milton and Prof. Ian Croudace for help with lab practices and analysing samples. I thank Dr. Rex Taylor for donating Reykjanes Ridge samples and scientific guidance and Prof. Damon Teagle for advice concerning the PACMANUS chapter and gold analysis, and Dr. Adrian Boyce and Dr. Ray Burgess for help with the PACMANUS chapter. I'd like to thank Prof. Robert Kerrich, Prof. Reid Keays and one anonymous reviewer for reviewing the Reykjanes paper, and Prof. David Vanko, Dr. Eoghan P. Reeves and one anonymous reviewer for reviewing the PACMANUS paper. I thank Bob and John for thin section preparation. I thank all of my friends especially Steve Hollis for support, advice and plenty of beer.

Finally, I thank Catriona Menzies for an enormous amount of moral support and help with many different things over the past 4 years.

Contents

List of Figures

List of Tables

Chapter 1

Introduction

1.1 Gold and the need for further understanding

Gold deposits occur where some process has concentrated the background level of gold in the crust. Although these deposits are sometimes re-worked by weathering and erosion to create placer deposits, hydrothermal systems are almost always the primary method of concentrating Au. Hydrothermal systems move Au from one large volume of rock (the leached or source rocks) to another, smaller volume of rock; the mineral deposit. The behaviour of Au in hydrothermal systems is relatively well understood - Au is transported by the presence of ligands in hot, usually low pH fluids driven by some heat source, such as an emplaced magmatic body or a raised geothermal gradient (e.g. Seward 1973; Stefansson and Seward 2004; Henley and Ellis 1983). The source of fluid is either metamorphic, magmatic, meteoric or a combination of those. However, finding these gold deposits has become increasingly difficult (Fig. 1.1) and so further research is welcomed in order to better understand and find deposits.

1.1.1 Au in the early Earth

During the accretion of the Earth, heat generated by large impacts and the decay of short-lived radionuclides such as ^{26}Al is thought to have resulted in one or more magma oceans (e.g. Rubie and Frost 2007; Walter and Tronnes 2004) in which the Earth was allowed to differentiate into the layers we can observe today - the crust, mantle and core. Smaller bodies, from which the chondritic meteorites are derived, did not differentiate and are thought to represent the bulk composition of the Earth and other terrestrial planets. Due to the highly siderophile nature of Au (Borisov and Palme, 1997), it is expected to

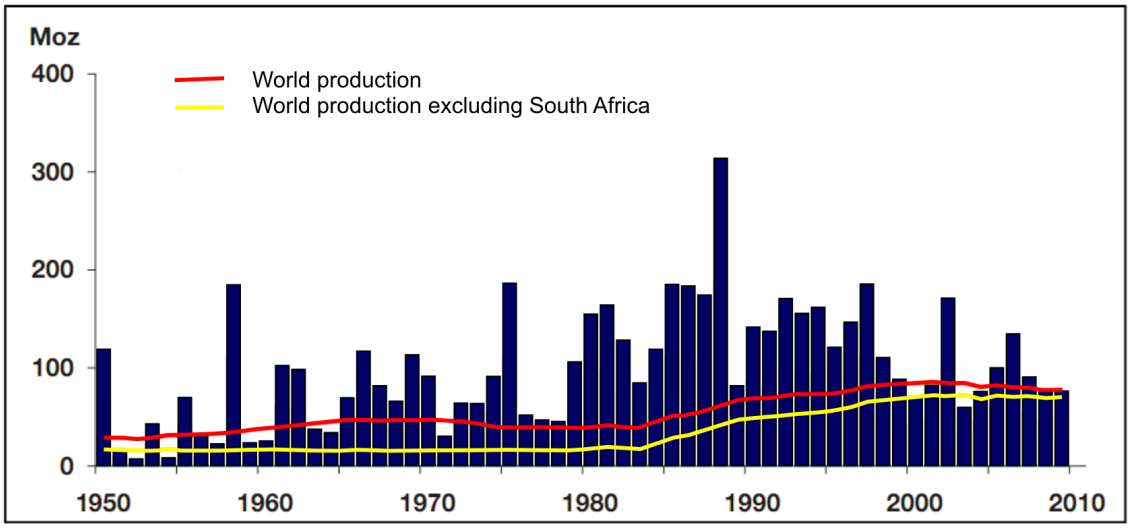

FIGURE 1.1: Gold discoveries (million ounces) since 1950. The amount of gold discovered peaked in the 1980s-1990s, and has since stagnated. Meanwhile production has appeared to plateaued. Adapted from the Society of Economic Geologist's newsletter, April 2010

have been strongly concentrated into the Fe-Ni core rather than the silicate mantle. In comparison to chondrite, the mantle should contain less than 10^{-4} the amount of Au (Holzheid et al., 2000). However, the mantle has been shown instead to contain only ~150 times less Au than chondrite (Morgan et al., 1981; Jagoutz et al., 1979). This discrepancy can be resolved by considering the addition of siderophile elements to the silicate earth by meteorites after differentiation occurred, known as the Late Veneer hypothesis (e.g. Kimura et al. 1974, Fig. 1.2).

1.1.2 Au in mantle plumes

Mantle plumes are an important aspect of the distribution of elements within the Earth because they link two very different parts of the Earth: the core/mantle boundary and the upper mantle and crust (e.g. Brandon and Walker 2005), leading to the possibility that mantle plumes could be enriched in the siderophile elements (Boyle, 1979; Brimhall, 1987; Rock and Groves, 1988; Brandon and Walker, 2005; Burke et al., 2008; Hawkesworth and Schersten, 2007; Bierlein and Pisarevsky, 2008; Fryer and Greenough, 1992). This could occur by entraining material that has incorporated outer core, either physically or by chemical equilibration (Fig. 1.4), or by entraining material that failed to make it to the core during core-mantle differentiation (Fryer and Greenough, 1992). Geochemical data from basalts derived from mantle plumes indicate plumes contain rock from several different reservoirs, including material which is possibly derived from the lower mantle (Hofmann, 1997). Plumes originating in the deep mantle could be enriched in siderophile

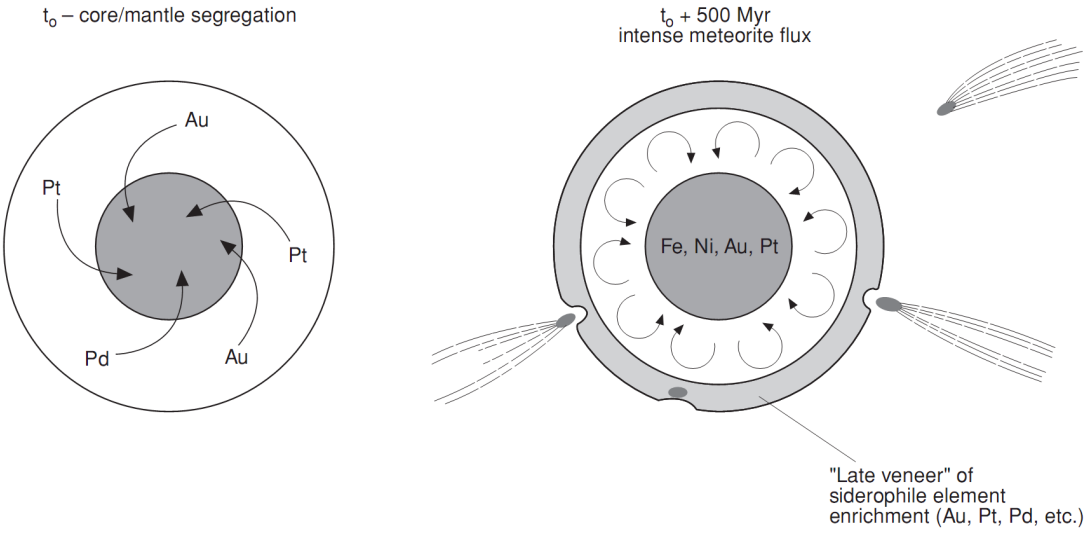

FIGURE 1.2: The differentiation of the Earth. The early Earth differentiated from a magma ocean to separate core (Fe-Ni) and mantle (silicate) layers. Because of the siderophile nature of Au, it strongly accumulated in the core. However, observed concentrations of Au and other siderophile elements in the mantle is higher than expected, which can be explained by a later addition of these elements by meteorite impacts. (Robb, 2005)

elements, including Au. This hypothesis is supported by the radiogenic osmium isotopic signature of some ocean-island basalts (OIBs). During the crystallisation of the solid inner core, the Re/Os system is fractionated, with Os being strongly partitioned into the inner core. This left the outer core with high Re/Os and consequently a highly radiogenic $^{186}Os/^{187}Os$ today (Walker et al., 1995). Therefore addition of outer core material to the lower mantle should greatly increase the radiogenic $^{186}Os/^{187}Os$ ratio, explaining the radiogenic signature of OIB.

Enrichment of metals at the source has been implicated in the genesis of metal-rich provinces (Keays, 1983, 1987; McInnes et al., 1999; Bierlein and Pisarevsky, 2008). If mantle plumes are enriched in siderophile elements, they might present an excellent source of metal for a mineralising system. The available data (Table 1.1) suggest Au in plume-derived lavas can be high relative to MORB and other reservoirs such as primitive and depleted mantle. However, such figures are not necessarily indicative of the concentration of Au in the source mantle because Au is strongly affected by the presence of sulphides and the saturation state of sulphur in the partial melt (e.g. Peach et al. 1990). The partition coefficient of Au between sulphide and basaltic silicate melt ($D_{Au}^{sulphide-melt/silicate-melt}$) is 10,000-13,000 (Peach et al., 1990). Since melts have a limited sulphur capacity - the amount of sulphur that can be dissolved in a melt - and assuming Au is strongly sequestered by those sulphides in the mantle, melts will not contain significant Au until higher degrees of partial melting are reached. Likewise, if the mantle source has already seen one phase

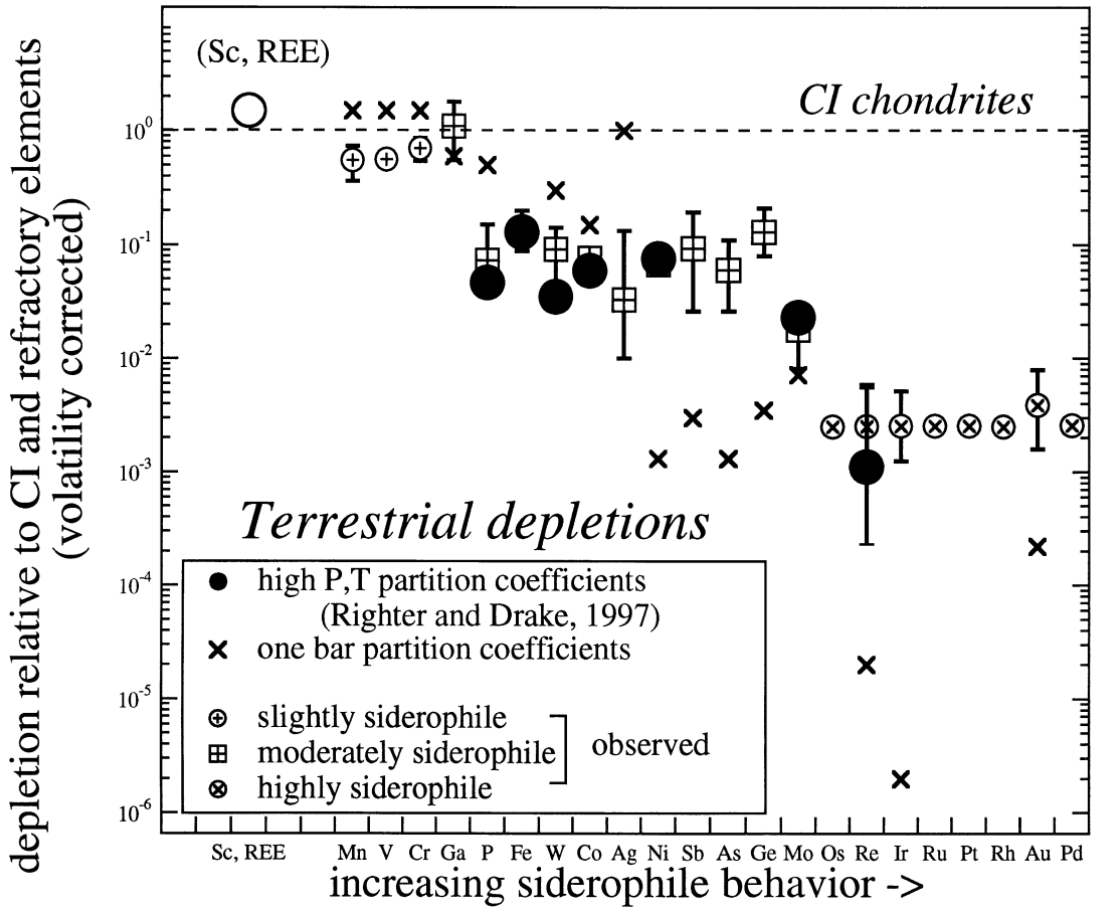

FIGURE 1.3: The behaviour of siderophile elements in the Earth. Au is amongst the most depleted elements in the silicate Earth compared to chondrite. However, its observed concentration is greater than would be expected from its partition coefficient between silicate and metal phases (Drake, 2000).

of partial melting, further melting can lead to complete dissolution of the mantle sulphide and therefore elevated Au and chalcophile concentrations in the melts. Having said that, a mantle source with a higher initial Au concentration will produce higher Au concentrations in the melt over the entire range of partial melting (Peach et al., 1990). Thus, elevated Au concentrations in the mantle source appear to be the most convenient way to explain the reliably high Au concentrations in plume derived lavas. It should also be noted that there is some suggestion that plume-derived melts, unlike primary MORB melts, might not be sulphur saturated initially, and so sulphides may play less of a role in the generation of chalcophile-rich magmas. Hawaiian magmas may be sulphur undersaturated due to the lack of evidence for Pt/Pd fractionation in the presence of sulphide melt (Lassiter, 2006; Jamais et al., 2008). This lack of S might be due to the presence of old lithosphere in the mantle plume which has undergone volatile depletion during subduction (Lassiter, 2006). Whilst this does not necessarily fit with the idea that plumes may be enriched in

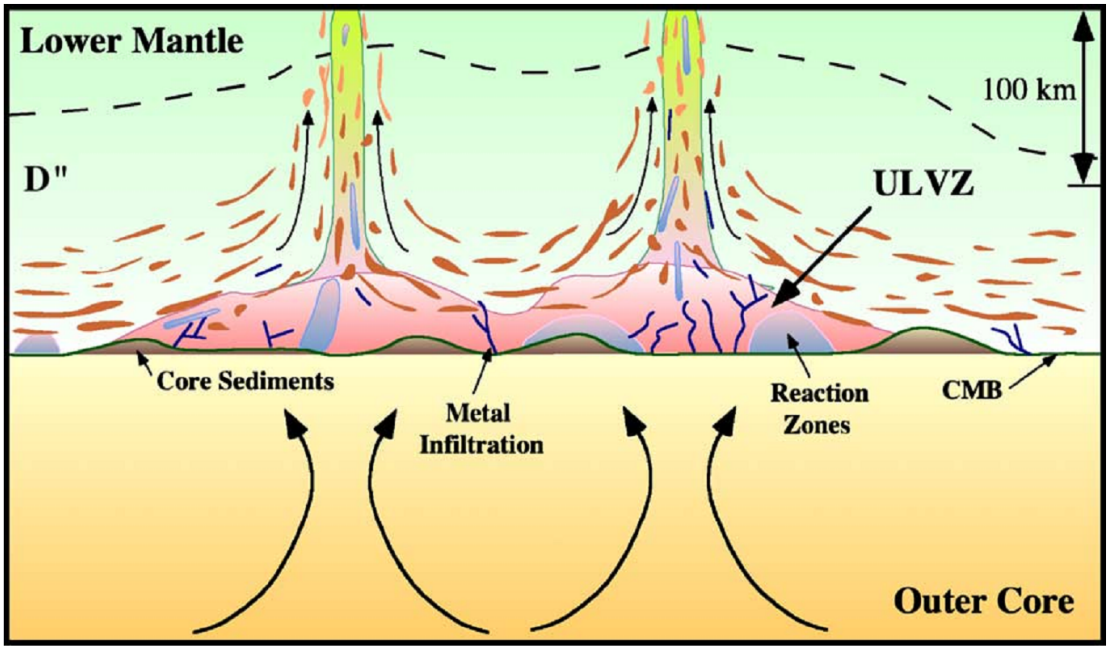

FIGURE 1.4: This cartoon depicts some ways in which chemical signatures from the outer core may be incorporated into the lower mantle and, in turn, transported by mantle plumes into the upper mantle and crust. CMB = core-mantle boundary, ULVZ = Ultra-low velocity zone (Brandon and Walker, 2005).

siderophile elements due to mantle-core interaction, it does provide a viable alternative mechanism for generating metal-enriched magmas from a plume source.

Province	Mean Au (ppb)	Log-normal Mean (ppb)	Min	Max	s.d.	n	Reference(s)
Iceland	3.38	3.17	1.09	7.44	1.26	30	Momme et al. 2003
East Greenland Rifted Margin	8.41	6.99	1.5	24.7	4.76	35	Momme et al. 2002
Hawaii	1.42	1.16	0.16	3.2	0.75	38	Tatsumi et al. 1999, Crocket et al. 2000, Crocket 2002
Deccan	1.42	1.16	0.16	3.2	0.75	38	Crocket et al. 2004, Keays and Lightfoot 2010
Siberian Traps	1.48	1.11	0.01	4.49	1.01	132	Brugmann et al. 1993, Hawkesworth et al. 1993, Lightfoot and Keays 2005
Reunion hotspot track	2.44	1.35	0.02	14.08	2.57	51	Greenough and Fryer, 1990
Average:	3.09	1.81	0.01	24.7	3.28	324	
Primitive Mantle	0.88						Kallemeyn et al. 1989
Depleted Mantle	1						Salters and Stracke 2004
MORB	1	0.47	0.06	4.27	1.23	22	Hertogen et al. 1980, Keays 1976, Tatsumi 1999, Lapukhov 1999
MORB	1.45	1.09	0.17	5.79	1.14	112	Jenner et al. 2012
N-MORB	1.99	1.52	0.31	5.79	1.4	38	Jenner et al. 2012
E-MORB	1.17	0.92	0.17	5.02	0.87	74	Jenner et al. 2012
MORB (Total)	1.38	0.95	0.06	5.79	1.2	134	above MORB refs.
Oceanic Gabbros	0.26	0.22	bdl	0.8	0.18	36	Miller et al. 2002

TABLE 1.1: Au concentration in some plume-sourced lavas and other reservoirs for comparison.

1.1.3 Au in oceanic crust and subduction

Chalcophile elements all have $D^{sulphidemelt/silicatemelt}$ values on the order of 10^4 (Peach et al., 1990) and so the concentration of chalcophile elements in oceanic crust is strongly controlled by the presence of sulphides in the mantle. When the mantle is partially melted, the melt has a limited capacity for sulphur, or S content at sulphide saturation (SCSS), which is controlled by various parameters such as the temperature and fO_2. Li and Ripley (2005) describe an empirical equation for the SCSS:

$$\begin{aligned} lnX_S = 1.229 - 0.74(10^4/T) - 0.021(P) - 0.311lnX_{FeO} \\ - 6.166X_{SiO2} - 9.153X_{Na2O+K2O} \\ - 1.914X_{MgO} + 6.594X_{FeO} \end{aligned} \quad (1.1)$$

where T is degrees Kelvin, P is pressure in kbar and X is a mole fraction. As the partial melt fraction increases, the sulphide melt is gradually incorporated into the silicate melt until it is consumed. During this process, the chalcophile elements are largely retained in the sulphide melt due to their high D values until virtually all of the sulphide melt is consumed. For most MORB this is expected to be at approximately 20 to 25% melt fraction (Peach et al., 1990). Since the thickness of most oceanic crusts can be achieved with a melt fraction of around 10% (e.g. Plank et al. 1995), it follows that most MORBs are depleted in chalcophile elements relative to their mantle source. Comparing basalts to mantle nodules, Hertogen et al. (1980) found this to be the case.

Before 2012, few data existed to properly assess the Au concentration of (plume-free) MORB (see Table 1.1). Pre-2012 data suggests a log-normal average of 0.47 ppb Au. However, Jenner and O'Neill (2012) released a dataset including 112 Au analyses measured by laser-ablation ICP-MS (LA-ICP-MS) from ocean-floor basalts around the world. The technique has a detection limit of ~0.25 ppb and as such the reliability of any averages obtained from the data is uncertain. This dataset, excluding results from lavas which may be plume-influenced such as the Red Sea and Galapagos spreading centres, suggests higher log-normal averages of 1.52 ppb (N-MORB), 0.92 ppb (E-MORB) and 0.95 ppb (combined MORB), where N-MORB and E-MORB are defined by La/Sm < 1 and La/Sm ≥ 1, respectively (Arevalo et al., 2009). This leads to a MORB concentration of 0.95 ppb Au when including all available data. The discrepancy between the older and newer datasets is probably a result of a bias that results from using the older datasets as they tend to focus on particular segments of spreading centres, such as 30°N on the Atlantic

Ridge (Keays and Scott, 1976) or 14-18°S on the East pacific Rise and 23°N on the Atlantic Ridge (Tatsumi et al., 1999). The true average may be better represented by combining the older and newer datasets.

The concentration of Au in MORB is not well constrained, yet MORB is the most accessible of the lithologies that make up an oceanic crustal section. The number of analyses on oceanic dyke and gabbroic rocks are even fewer. A tectonically exposed section of gabbroic crust on the Southwest Indian Ridge was drilled on ODP legs 118 and 176 and rocks from the latter cruise (hole 735B) were analysed for Au and platinum group elements. These medium to coarse grained olivine grabbros had Au values ranging from below detection to 0.796 ppb, mean average 0.264 ppb (Miller and C., 2002). One value of 0.013 ppb Au exists for the dolerite dyke section (Hoernes et al., 1979), although these should be chemically similar to MORB.

1.1.3.1 Subduction of slab-hosted Au

The presence of Au-rich VMS deposits on oceanic crust attests to the mobility of Au in ocean crust during hydrothermal circulation. However, it is unclear how much of the total Au is mobilised, from what volume of rock and from how deep in the crust it is mobilised, nor how much Au is lost to the water column. So, whilst we might be able to put a value on the Au concentration of average fresh MORB, it is not known how much of this Au enters the subduction system.

Metasomatised mantle xenoliths show Au enrichments over non-altered xenoliths from beneath both the Kamchatka arc and Tabar-Lihir-Tanga-Feni Island arc (McInnes et al., 1999; Kepezhinskas et al., 2002). However, conflicting evidence suggests this Au is either sourced from the mantle (McInnes et al., 1999) or slab fluids (Kepezhinskas et al., 2002). The $^{187}Os/^{188}Os$ composition of gold ore at the Ladolam gold deposit, Lihir Island, and the nominal (<10%) crustal Os contribution suggest a primarily mantle source for the Au rather than the subducting slab (McInnes et al., 1999). The slab's role is to supply oxidising fluids which redistribute existing metals within the mantle wedge, rather than supplying significant metal itself. The authors extend this conclusion to all arc systems, but it should be noted that the deposit on Lihir island is not typical as it is an unusually large deposit of >1,300 metric tons of gold with a 1.5g/t cutoff, with locally occurring bonanza grades of 120 g/t (Muller et al., 2002). The tectonic situation is also abnormal, with collision of the Ontong-Java plateau with the trench preventing further subduction, possibly leading to increased dehydration of the slab and the generation of a particularly effective supercritical oxidising fluid (Mungall, 2002). It is unclear whether the Au budget of this example could be extended to more normal subduction situations. A suite of mantle

xenoliths from beneath the Kamchatka Arc, Russia, exhibit higher Au concentrations in samples metasomatised by a slab-derived fluid (Kepezhinskas et al., 2002). The authors attribute this to fertilisation by the slab fluid rather than re-distribution, although the observation of increased Au in metasomatised mantle is not inconsistent with the evidence from mantle xenoliths from beneath the Ladolam gold deposit.

1.1.4 Au in arc magmas

Available Au data for fresh arc lavas of all types have a log-normal mean of 1.6 ppb Au ($1\sigma = 4.22$, data from 23 different sources extracted from the GeoRoc database of fresh volcanic rocks in an arc setting and a 25 ppb Au limit). This suggests arc rocks in general exhibit a slightly higher Au concentration than upper-mantle derived oceanic basalts, consistent with metasomatic concentration in the mantle wedge. The behaviour of Au within arc systems is discussed in Chapter 5. To date, the main control on the behaviour of Au in high level magmatic systems such as Konya is thought to be accessory minerals such as magnetite and sulphide (Keays and Scott, 1976; Bird et al., 1991; Peach et al., 1990; Togashi and Terashima, 1997). However, the process is not well constrained, with significant inconsistencies found between natural and experimental work. In addition, it is not known what effect the sequestering of Au by accessory minerals has on the probability of developing a mineral deposit.

1.2 Questions

The above discussion reveals several questions that need to be answered:

1.2.1 In relation to plumes

Addressed in Chapter 3.

- If mantle plumes carry Au from the lower mantle to the crust, how much do they bring? Does this represent a significant amount over normal upper mantle levels?
- Do melts generated under such conditions supply more Au than normal upper mantle melts? Do they create crust richer in Au than crust derived from normal upper mantle?

1.2.2 Au in oceanic crust and subduction

Addressed in Chapter 4.

- How much Au is removed from the downgoing slab during subduction and dehydration of the slab? How much is recycled back into the mantle?
- Would subducting slabs of different Au concentrations create a significant difference in the amount of Au that is found in the arc system?

1.2.3 Au in arc magmas

Addressed in Chapter 5.

- Is magnetite crystallisation the main control on Au concentrations in arc magmas?
- How much does the Au concentration of an arc magma change during melt evolution?
- Does magnetite crystallisation and fractionation affect the likelihood of generating a mineral deposit?

1.3 PACMANUS

Chapter 6 in this thesis examines the behaviour of helium and oxygen isotopes within the PACMANUS hydrothermal system. PACMANUS is a hydrothermal system in the Manus basin, off the coast of Papua New Guinea (Barriga et al., 2007). It is sited within a back-arc basin and has created a hydrothermal mound with economic concentrations of Cu, Pb, Zn, Ag and Au (Moss and Scott, 2001; Parr et al., 1996; Scott and Binns, 1995). As such, PACMANUS is a good analogue for ancient volcanogenic massive sulphide (VMS) deposits since it displays characteristic metal enrichments and sits in a tectonic position, a back-arc, where preservation by uplift onto a land mass at some stage in the future is a possibility. In contrast, mid-ocean ridge VMS deposits have a low preservation potential because they are likely to be subducted along with the oceanic crust on which they have formed.

The helium isotopes analysed in the study were present in fluid inclusions formed in hydrothermally precipitated anhydrite and pyrite, and so should represent the original helium isotope composition of the hydrothermal fluid. Using this premise, the helium

isotopes could be used to constrain fluid mixing within the hydrothermal system, since seawater and rock have very different helium isotope compositions.

The oxygen isotopic composition of anhydrite was examined to constrain the thermal regime within the system. Since the fractionation of oxygen between the hydrothermal fluid and seawater is temperature-dependant, the oxygen isotope composition of the anhydrite can be used to predict what the temperature of the system was at the time.

As can be seen in Chapter 6, both these experiments encountered significant problems. It was found that the helium isotopic composition of the samples had become contaminated by atmospheric helium in a way that could not be easily corrected. It was also found that the anhydrite analysed for oxygen isotopes had precipitated so quickly that equilibrium between the anhydrite and hydrothermal solution was almost certainly not achieved.

Chapter 2

Methods

2.1 The Au technique

In the following chapters Au is analysed in geological materials using the technique outlined by Pitcairn et al. (2006b). During this process, it became apparent the technique could be improved in several ways, in order to produce more accurate and reproducible results.

2.1.1 Digestion

Due to the low concentration and uneven distribution of Au in most geological materials, known as the nugget effect, a large quantity of material needs to be digested in order to raise the signal above the detection limit and ensure a representative result is produced. The technique generally calls for around 4g of material to be digested at a time. Digestion is achieved with a joint HNO_3 + HF attack followed by HCl and aqua regia (HCl:HNO_3 3:1) attacks to ensure total dissolution of Au particles. This technique has worked well for the dissolution of siliceous sediments or metamorphic rock, such as the Otago Schists of New Zealand (Pitcairn et al., 2006a). However, if a sample contains a high proportion of Mg, Al, Na or Fe, digestion of large quantities of powder results in the formation of insoluble fluorides such as ralstonite ($Na_{0.88}Mg_{0.88}Al_{1.12}(F,OH)_6 \cdot H2O$, Langmyhr and Kringstad 1966; Croudace 1980; Boer et al. 1993; Yokoyama et al. 1999). These fluorides have been shown to sequester large quantities of trace elements (Yokoyama et al. 1999, Fig 2.1) resulting in recoveries as low as 20% for Y and La. No data exists for Au, however even if the fluorides do not sequester Au directly, the gel-like substance contains a significant quantity of sample solution and therefore must contain at least some Au (Fig. 2.2).

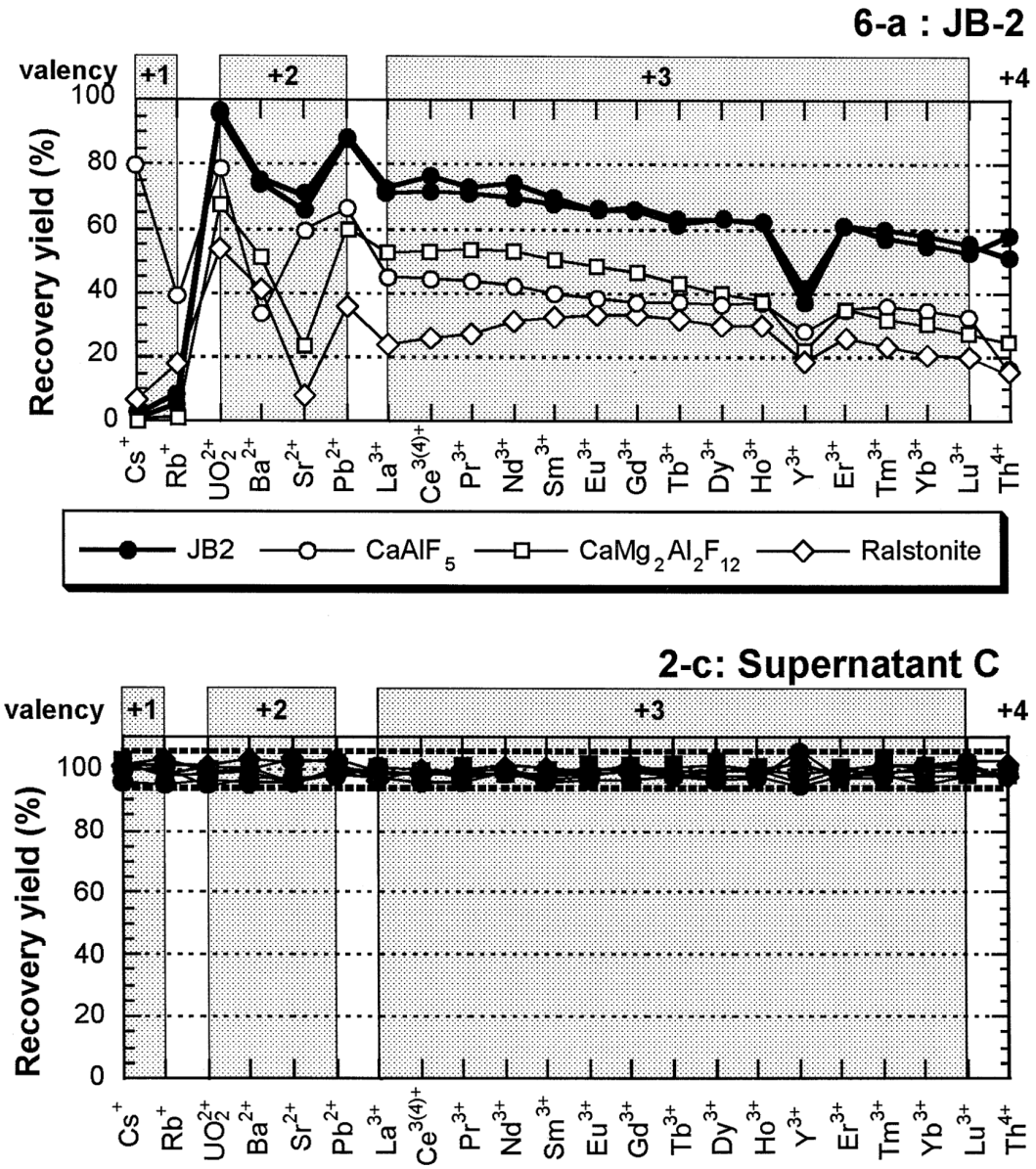

FIGURE 2.1: Top pane shows the recovery of various trace elements in the presence of certain insoluble fluorides. JB2 shows the recovery of a rock sample dissolved in a $HF+HNO_3$ attack. Lower pane shows the recoveries of rock samples using a combined HNO_3 + HF + $HClO_4$ attack, detailed in the text. Figures from Yokoyama et al. (1999)

FIGURE 2.2: During HF+HNO_3 attack of large quantities of rock, insoluble fluorides can be formed. Directly after the attack they form large, polygonal grains (top pane). After further attack with HCl and Aqua Regia, the fluorides are broken down into a gel. The yellow colour of the gel indicates a significant quantity of digested rock is present within the structure of the gel. Teflon pots are approximately 3cm in diameter.

A digestion method has been developed which avoids the precipitation of these fluorides, utilising a combined HNO_3 + HF + $HClO_4$ attack (Yokoyama et al., 1999). However, whilst trace element recoveries from this method are good (Fig. 2.1), it has several disadvantages. The method requires working with large quantities of $HClO_4$, and apart from being dangerous, it has a very high boiling point of 203℃, requiring a high temperature dry-down. The method outlined by Yokoyama et al. (1999) suggests drying down at 190℃ in order to drive off the HF whilst also evaporating $HClO_4$. This temperature is uncomfortably close to the melting temperature of the teflon vessels which poses the risk of destruction of the vessel, the sample, and a dangerous acid spill. Apart from these concerns, the high boiling point and the quantity of $HClO_4$ required necessitates a very long dry-down period, doubling the time it takes to digest a set of samples. This technique was used successfully to avoid insoluble fluorides in Chapter 4, where the small number of samples made the process logistically acceptable. It is also important to note that whilst this technique avoids insoluble fluorides, it does produce a small quantity (∼0.1g) of $TiO_2 \pm KClO_4$. This material was shown not to sequester the trace elements analysed in Yokoyama et al. (1999), but it is not known whether it sequesters Au. However, the amount produced is so small that it is vastly preferable to fluoride formation. In chapters 3 and 5, insoluble fluoride formation was a problem but it was dealt with using repeated aqua regia attacks, which was noted to both reduce the volume of the fluoride and produce good recoveries for Au in the reference materials.

2.1.1.1 Alternative digestion methods

Fusion of the sample using an alkali flux such as lithium tetraborate to produce a glass disk is commonly used in the preparation of samples for XRF major element analysis. However, this method would need to be modified for the analysis of Au. Fusion is usually performed in a platinum crucible which raises the possibility of Au contamination from the walls of the crucible. A lithium and boron based flux would create contamination problems for people measuring Li and B isotopes in the same labs and on the same analysis equipment. More recently, flux-free techniques have been developed (e.g. Shimizu et al. 2010; Nehring et al. 2008; Stoll et al. 2008), which involve heating the rock to a temperature at which a glass is produced upon quenching, around 1300-1600℃. MgO can be added to the rock to lower its melting temperature (Nehring et al., 2008). However there are concerns surrounding the homogeneity of the glass produced (Shimizu et al., 2010) and the fact that a platinum crucible is used to hold the sample.

If a fused sample is produced, it still needs to be analysed. Any technique necessitating wet-chemistry, such as Au separation by solid-phase extraction columns used in this work,

would still require digestion of the fused sample by HF acid and thus insoluble fluorides would still be produced. However, the concentration of Au in basaltic glasses has been successfully measured by LA-ICP-MS (Jenner and O'Neill, 2012). For Au, Pt and Re, a wide 187μm beam was used with increased counting times of 30s background and 50s ablation, together with corrections for oxide formation. They note detection limits of $\sim$0.25 ppb. This seems promising and, if the detection limit could be improved, could offer an effective and rapid measurement technique for Au and other trace elements. Basaltic glasses can be analysed as they are, but coupled with an effective fusion method potentially any geological sample could be analysed in this way.

2.1.2 Column chemistry

The Au analysis method used here utilises solid-phase extraction columns, whereby the organic compound diisobutyl ketone (DIBK), which has a high partition coefficient for Au, is bound to a chromatographic resin. An appropriate amount of sample is then fed through the column followed by 6 molar HCl which removes the majority of the Fe and other major elements, reducing the matrix concentration of the sample and allowing lower detection limits for Au. Gold is removed from the resin using ammonia, dried down and redissolved in 5% HCl for analysis.

During the loading of the sample on the resin, it is possible to effectively see the resin "filling up" (Fig. 2.3) as it becomes green or orange coloured (presumably from Cu, Fe and other metals). Usually this colouration does not reach the bottom of the resin, however occasionally it does and in these cases it might be that the resin is then unable to sequester any more Au. In these cases, anecdotally, low recoveries have been observed. This could be easily solved using either a smaller quantity of sample - not always possible due to detection limit requirements - or by increasing the amount of resin in the column. In the latter case the technique would need to be re-evaluated to ensure the correct quantities of elutant are used when flushing out unwanted elements and when collecting the Au.

2.1.3 Analysis of solution

After the column chemistry is complete, the sample is dissolved in 5% HCl and stored in scintillation vials until analysis. It is known that low concentration solutions have a finite shelf life, with some elements forming oxides and dropping out of solution or bonding to the plastic of the container (Reimann et al., 1999). Dramatic loss of Au from the 5% HCl solution was observed over a period of days (Fig. 2.4). After this process was identified as a problem, samples were kept dry in the collection vessel until the morning of analysis.

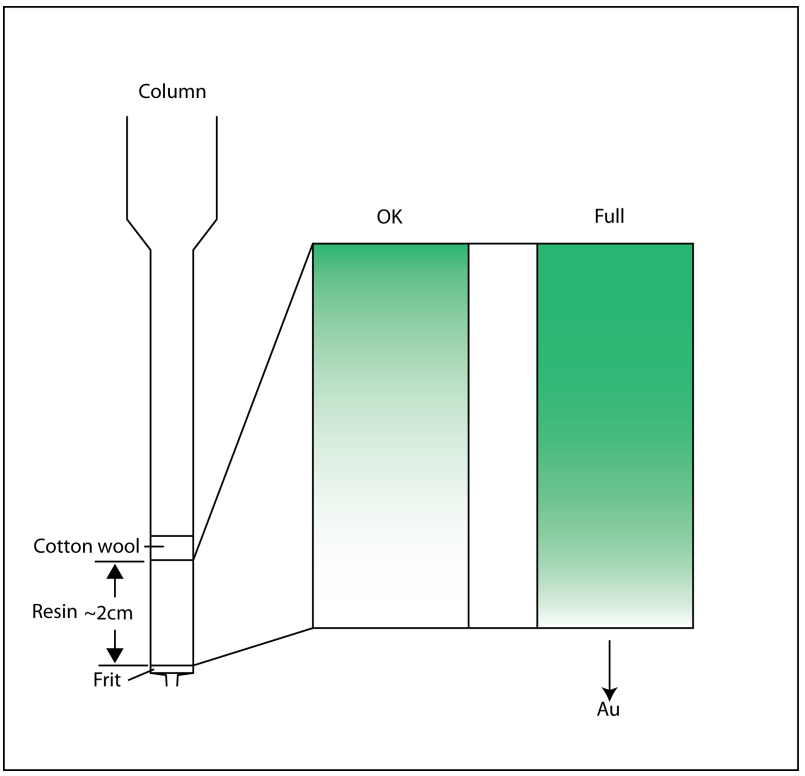

FIGURE 2.3: The column set-up is pictured above. As the sample is added to the column, the resin can change colour to a greenish or orange hue. This progresses from the top to the bottom of the resin. If the colour reaches the bottom, as above, then the resin could be full and Au could be lost, resulting in a low recovery.

2.1.4 Recovery and Internal Standards

Problems with digestion, column chemistry and solution analysis outlined here all lead to potential low recoveries and precision. Introducing an internal standard to the sample would be an ideal way to mitigate these problems. A radiotracer Au^{195} ($t_{1/2}$ = 183d) has been used successfully to measure the concentration of Au in seawater (Falkner, 1989). Adding a radiotracer to the sample solution at each step could be used initially to gauge the Au loss at each stage and finally to calibrate the yield of each individual sample, improving precision and reproducibility of results.

2.1.5 Technique Procedure

Below is outlined the full procedure used in Au analysis.

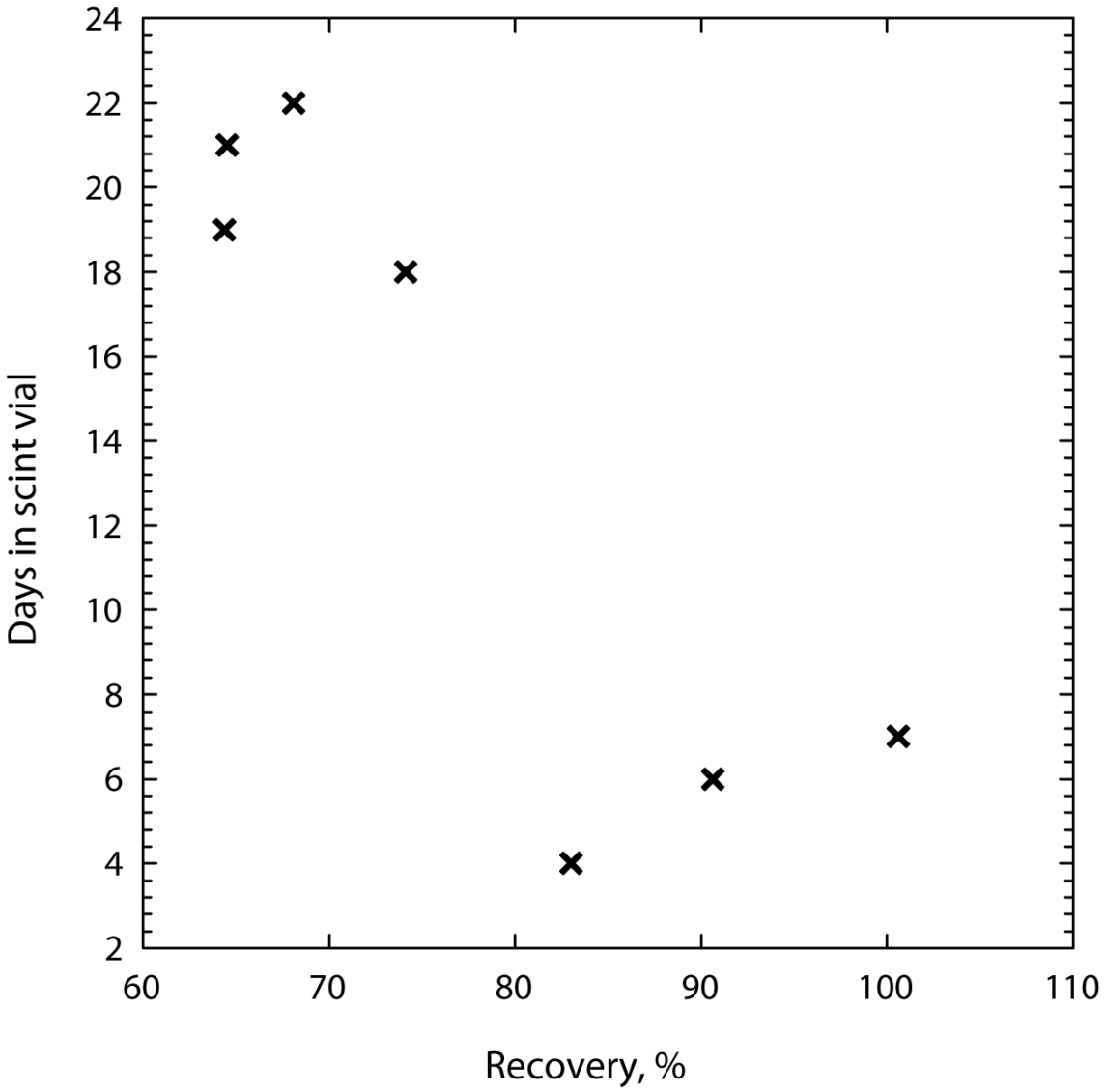

FIGURE 2.4: A graph of Au recovery vs the number of days a sample was kept in a plastic scintillation vial. Dramatic loss of Au is observed after a number of days. Recovery is measured against the reference material EMC-1, an amphibolite with a low Au concentration (Pitcairn et al., 2006b)

.

2.1.5.1 Digestion method 1

Modified after Pitcairn et al. (2006b).

1. Measure 10ml of conc. HNO_3 into 60ml teflon pots.
2. Weigh an appropriate quantity of sample into the 60ml teflon pots. For normal geological materials this is usually 4g. For anything which might have a greater quantity of Au, such as ores or altered rocks, estimate quantity based on 0.1 ppb Au final daughter solution, where the mother solution is 60ml and the daughter solution is 20ml. If measuring materials with a wide range of Au concentrations, aim for as narrow a range of concentrations in the daughter solution as possible.
3. Fit lids and place on hotplate at 150℃ for 2 hours. Take off to cool.
4. Add 20ml of hydrofluoric acid, taking all precautions associated with this substance.
5. Place on hotplate at 150℃ overnight.
6. Take off to cool. Remove lids and dry down. If fluorides are a problem, consider adding HNO_3 regularly throughout the dry-down in order to minimise fluoride formation.
7. When dry, add 20ml 6 molar (M) HCl. Place on hotplate at 150℃ overnight.
8. Take off to cool. Remove lids and dry down. Add 13ml aqua regia (concentrated HCl:HNO_3 3:1). Place on hotplate at 150℃ overnight.
9. Take off to cool. Remove lids and add 45ml H_2O. Place on hot plate for 2 hours.
10. Decant into labelled 60ml bottles. If fluorides are a problem, repeat the above step to reduce the quantity of fluoride and break it down into a gel. If no dissolution of fluoride is seen, they can be repeatedly leached with aqua regia and finally centrifuge to separate fluoride from solution. If needed, dry down the sample and treat as previous step.

2.1.5.2 Digestion method 2

As Yokoyama et al. (1999), used in Chapter 4.

1. Measure 10ml of conc. HNO_3 into 60ml teflon pots and add appropriate sample quantity, as above.

2. Add 12ml conc. $HClO_4$ and 20ml conc. HF. Place on hotplate at 100℃ overnight.
3. Dry down: 120℃ for 12 hours; 165℃ for 12 hours; 195℃ until dry.
4. add 12ml conc. $HClO_4$. Place on hotplate at 100℃ overnight.
5. Dry down: 120℃ for 12 hours; 165℃ for 12 hours; 195℃ until dry.
6. Add 20ml HCl. Place on hotplate at 150℃ overnight.
7. Remove lids and dry down.
8. Remove lids and dry down. Add 13ml aqua regia (HCl:HNO_3 3:1). Place on hotplate at 150℃ overnight.
9. Take off to cool. Remove lids and add 45ml H_2O. Place on hot plate for 2 hours.
10. Decant into clean centrifuge tubes and centrifuge to separate small quantity of TiO_2 and/or $KClO_4$.
11. Decant into labelled 60ml bottles.

After digestion, proceed with column chemistry as soon as possible so that Au does not drop out of solution beforehand.

2.1.5.3 Columns

1. Prepare resin. Add DIBK to the resin at the ratio of 1:1.6 DIBK:resin. For 14 columns, start with 6-7g of resin. Add a small quantity of DIBK and stir rapidly until DIBK is absorbed. Repeat until all DIBK is absorbed, being careful not to add too much.
2. Add a sufficient amount of 6M HCl to the resin to form a fluid slurry which can be added to the columns.
3. Place a rubber stopper over the column tip and pour an amount of slurry into the column. Once enough is added, wash resin from the sides of the column with 6M HCl. Remove stopper to allow HCl to drain. Check that at least 2cm of resin has settled after HCl has drained. If not, replace stopper and add more slurry.
4. Add a small quantity of cotton wool to the column and push down with a glass rod. Take care not to compress the resin as this will result in columns that do not flow. The cotton wool should just sit on top of the resin so that the resin does not suspend when the sample is added.

5. Place waste collection bottle beneath columns.
6. Add 5ml 6M HCl to wash the columns and ensure they all flow well.
7. Load an appropriate quantity of sample, usually between 5 and 30ml. Do not overload the column or low recoveries might result.
8. Add 10ml 6M HCl.
9. Replace waste vessel with collection teflon.
10. Add 10ml of ammonia solution, which is 5% of the concentrated form.
11. Add 10ml H_2O.
12. Add 5ml of ammonia solution.
13. Add 5ml H_2O.
14. Place collection teflon onto hotplate at 150°C to dry.
15. Keep samples dry until the morning of analysis.

2.1.5.4 Sample preparation for ICP-MS Analysis

1. Redissolve sample by adding 1ml conc. HCl (preferably warm) and a small (5ml) amount of H_2O. Roll the vessel so that the HCl solution touches all surfaces the sample has.
2. Add the solution to a 20ml scintillation vial for analysis. Top up the sample to 20ml, using the water to wash out the collection vessel to ensure all sample is retained.
3. If teflon with lids are used for collection, sample can be dissolved by adding 10ml 5% HCl on the sample and placing on a hotplate for 2 hours or until fully dissolved. Cool and add to scint vials. Use 10ml of 5% HCl to rinse teflon and add to vials.
4. Prepare external standards in 5% HCl. Avoid standards with too high a Au concentration as washout will take too long.
5. Use 5% HCl washout solution. Use monitored washout if available to ensure counts return to background before the next sample is loaded.

2.1.6 Accuracy, Precision and Limit of Detection

Repeated analysis was performed on Reykjanes Ridge glasses to measure precision and the reference materials ORE-A5 and EMC-1 to give accuracy (Table 2.1). ORE-A5, which has a certified Au concentration, shows good accuracy but less than ideal precision. Since it has a higher Au concentration than the samples, less material was digested each time, which could explain the low precision. EMC-1, which is not certified, shows good precision but poor accuracy. The accuracy is based on a value of 0.29 ppb which was generated when the technique was developed.

The limit of detection is based on the blank value + 10 $\times\sigma$ of the background count. Typically this would be 15-50 counts, equal to roughly 1 to 5 ppt Au in the analyte. Since dilution factors for samples was tyically 20 this equates to 20-100 ppt Au in the sample, or 0.02 to 0.1 ppb Au.

TABLE 2.1: Precision and accuracy of repeated Au analysis.

Sample	n	Average (ppb)	$\pm1\sigma$ (ppb)	$\pm1\sigma$ (%)	Reference (ppb)	Accuracy (%)
12aD1	3	0.9	0.23	25.2		
13D2	3	0.5	0.06	10.7		
02D6	2	0.9	0.23	26.8		
17D1	3	1.4	0.27	19.7		
33aD1	3	0.4	0.05	12.4		
75D10	4	0.7	0.08	11.0		
78D2	1	1.7	-			
100D1	3	0.2	0.03	17.2		
121D3	3	1.7	0.23	13.8		
136D2	2	0.8	0.12	14.2		
144D2	2	0.6	0.07	11.0		
150D3	3	1.0	0.20	19.6		
157D3	2	3.0	0.09	2.9		
160D4	2	1.2	0.02	1.5		
169D6	3	1.0	0.12	11.9		
173D1	3	1.3	0.33	25.2		
177D3	2	4.3	0.16	3.7		
179D3	2	3.2	0.31	9.6		
182D3	2	1.6	0.03	2.0		
185D4	2	2.5	0.09	3.7		
ORE-A5	5	61.5	8.9	16.4	56	3.2
EMC-1	6	0.21	0.044	21.4	0.29	28.5

2.2 XRF analysis

The Konya samples (Chapter 5) were analysed by XRF for major and trace elements. The procedure is outlined below.

1. Large samples were collected (2kg) to mitigate the nugget effect of Au within geological materials.

2. Samples were sawn to remove weathered edges and sawn faces were ground to remove contamination of the saw blade.

3. Samples were crushed using a fly press and plastic sheets to prevent contamination with the metal of the fly press

4. Half the sample was then powdered in agate.

5. 12g of powdered sample was mixed with a binding compound and pressed into a pellet.

Samples were analysed for the trace major and trace elements in table 2.2.

TABLE 2.2: Precision and accuracy of XRF pressed-powder analysis

	Precision						Accuracy
	K034 n=2	K058 n=2	K066 n=6	K084 n=2	K092 n=2	Mean average	BCR-1
SiO2	0.11%	0.75%	0.80%	0.36%	0.08%	0.42%	5.30%
TiO2	0.51%	0.70%	0.32%	0.24%	0.21%	0.40%	-2.40%
Al2O3	0.36%	0.29%	0.66%	0.28%	0.18%	0.35%	4.40%
Fe2O3	0.34%	0.45%	0.35%	0.58%	0.33%	0.41%	-2.90%
MnO	0.00%	0.00%	0.45%	0.84%	0.00%	0.26%	-5.00%
MgO	0.39%	0.08%	0.67%	0.36%	0.31%	0.36%	-7.30%
CaO	0.20%	0.09%	0.20%	0.79%	0.16%	0.29%	-7.30%
K2O	0.02%	0.95%	0.22%	0.20%	0.19%	0.32%	2.40%
Na2O	0.16%	0.89%	0.74%	0.11%	0.42%	0.46%	6.60%
P2O5	0.00%	0.00%	1.25%	0.33%	0.00%	0.32%	2.10%
Zn	0.69%	0.26%	0.73%	0.80%	0.57%	0.61%	-2.32%
Pb	3.03%	0.40%	6.10%	1.43%	0.00%	2.19%	3.70%
Ba	1.39%	0.16%	1.30%	0.70%	0.49%	0.81%	-3.28%
Rb	0.50%	0.51%	0.37%	1.20%	0.23%	0.56%	-5.37%
Zr	1.99%	2.85%	1.16%	0.08%	0.48%	1.31%	0.48%
Th	2.01%	5.70%	3.64%	1.10%	1.95%	2.88%	-0.83%
U	0.91%	1.10%	8.37%	4.96%	8.00%	4.67%	5.00%
Ga	1.23%	0.77%	1.51%	2.29%	0.00%	1.16%	-0.89%

2.3 ICP-MS Analysis

The Konya samples (chapter 5) were analysed by ICP-MS for trace and rare earth elements. The procedure followed is outlined below.

1. Samples prepared as in section 2.2.

2. 50mg of powder was added to 10 drops of HNO_3 to form a slurry in 30ml teflon.

3. 50 drops of HF were added and placed on a hotplate, lids on, overnight.

4. Samples were dried down and redissolved in 15ml 6M HCl.

5. Samples were dried down and re-dissolved in approximately 20ml 6M HCl.

6. Samples were made to 30ml with H_2O and stored in 30ml HDPE bottles.

7. Samples were diluted to 6000x dilution by drying down the appropriate quantity and re-dissolving in 3% HNO_3 with an In-Re spike for internal drift calibration.

Samples were run on a Thermo X-series ICP-MS in solution mode. The instrument was tuned with a multi-element solution (Co, Y, In, La, Re, Bi and U) to achieve optimum sensitivity and stability. Samples were calibrated against the external reference materials JB1A, JB-3, BIR-1, JGB-1, BHVO2, and BCR-1 at dilutions ranging from 4000 to 30000. Results were corrected for REE oxide formation. Precision and accuracy is reported in table 2.3.

TABLE 2.3: Precision and accuracy of ICP-MS analysis

	Precision									Accuracy
	K002 n=2	K015 n=2	K024 n=2	K043 n=2	K066 n=6	K084 n=2	K087 n=2	K091 n=2	Average	JA-2
Li	0.22%	0.06%	2.74%	1.14%	1.66%	1.10%	3.61%	1.62%	1.52%	3.00%
Sc	0.57%	1.99%	4.27%	0.63%	1.90%	1.83%	3.88%	3.56%	2.33%	-0.69%
V	0.61%	1.48%	1.63%	0.24%	2.45%	0.90%	2.37%	4.91%	1.82%	-7.79%
Cr	1.66%	9.60%	0.34%	3.14%	1.15%	3.03%	2.14%	0.08%	2.64%	-12.95%
Co	0.27%	0.63%	0.70%	0.64%	2.53%	1.66%	0.01%	0.61%	0.88%	3.30%
Ni	2.86%	4.59%	0.14%	0.74%	3.89%	2.53%	0.24%	0.58%	1.95%	-3.46%
Cu	0.48%	12.18%	4.95%	0.36%	1.90%	2.47%	5.84%	10.47%	4.83%	6.96%
Sr	0.52%	0.67%	1.95%	0.35%	2.59%	1.40%	2.55%	3.32%	1.67%	-0.84%
Y	1.50%	6.11%	5.85%	0.44%	2.97%	1.19%	6.27%	6.89%	3.90%	6.38%
Nb	0.89%	0.45%	0.19%	0.95%	2.39%	1.90%	0.82%	0.57%	1.02%	0.24%
Mo	7.75%	0.48%	3.53%	0.35%	4.03%	0.04%	5.42%	6.07%	3.46%	9.22%
Sn	3.62%	7.60%	3.68%	0.77%	1.56%	1.79%	5.37%	7.68%	4.01%	6.94%
Cs	0.30%	4.56%	4.70%	0.08%	2.57%	1.64%	4.51%	5.46%	2.98%	-0.93%
La	1.83%	0.95%	1.44%	0.11%	2.54%	0.18%	0.81%	1.57%	1.18%	-0.65%
Ce	2.13%	1.92%	2.73%	0.15%	2.40%	0.03%	2.15%	2.70%	1.78%	-1.07%
Pr	1.56%	0.56%	0.35%	0.66%	2.27%	0.16%	0.28%	0.11%	0.74%	4.50%
Nd	1.57%	0.70%	0.20%	0.19%	2.04%	0.29%	0.03%	0.58%	0.70%	2.38%
Sm	2.53%	1.40%	0.91%	0.70%	3.44%	1.87%	0.85%	1.01%	1.59%	0.25%
Eu	0.30%	0.42%	3.15%	0.65%	2.11%	0.04%	2.15%	1.95%	1.35%	-2.05%
Gd	1.09%	2.17%	2.62%	0.61%	2.12%	1.34%	2.77%	3.38%	2.01%	0.58%
Tb	0.30%	4.00%	1.86%	0.08%	1.38%	0.04%	3.06%	3.60%	1.79%	4.14%
Dy	0.98%	3.25%	1.32%	0.28%	1.99%	0.32%	2.92%	2.92%	1.75%	2.80%
Ho	1.32%	2.17%	0.62%	1.94%	2.15%	1.38%	1.44%	0.27%	1.41%	-1.27%
Er	0.26%	3.99%	3.60%	1.00%	3.18%	1.54%	2.97%	4.08%	2.58%	3.09%
Tm	0.30%	2.42%	0.68%	0.08%	2.47%	3.49%	3.68%	5.39%	2.32%	-0.40%
Yb	0.30%	5.57%	4.86%	1.26%	1.33%	0.46%	5.40%	7.12%	3.29%	3.96%
Lu	0.30%	1.64%	5.07%	0.08%	2.47%	0.04%	5.98%	5.45%	2.63%	1.18%
Ta	1.29%	4.47%	2.41%	0.57%	2.48%	1.71%	1.28%	0.82%	1.88%	10.13%

2.3.1 Zircon Dissolution and REEs

Zircon was not dissolved during the ICP-MS dissolution technique. Zircon is known to sequester rare earth elements (REEs), and as such the presence of zircon may have altered the REE profiles given by the ICP-MS analysis (e.g. Sano et al. 2002). XRF analysis is not affected by this. Zr_{XRF}/Zr_{ICPMS} gives an indication of how much zircon was present in the sample, where a number >1 indicates zircon was present. This value can then be plotted against REE ratios to give an indication of how strongly the REE profiles were altered by the presence of zircon. Since the HREEs are more strongly partitioned into zircon in order of increasing atomic number, the HREE slope can be steepened, and consequently positive correlation could be seen on a plot of Zr_{XRF}/Zr_{ICPMS} vs a HREE ratio such as Sm/Lu. No such correlation is seen and so it is assumed that, for most samples, the REE element profiles are not strongly affected by the incomplete dissolution of zircon (Fig. 2.5).

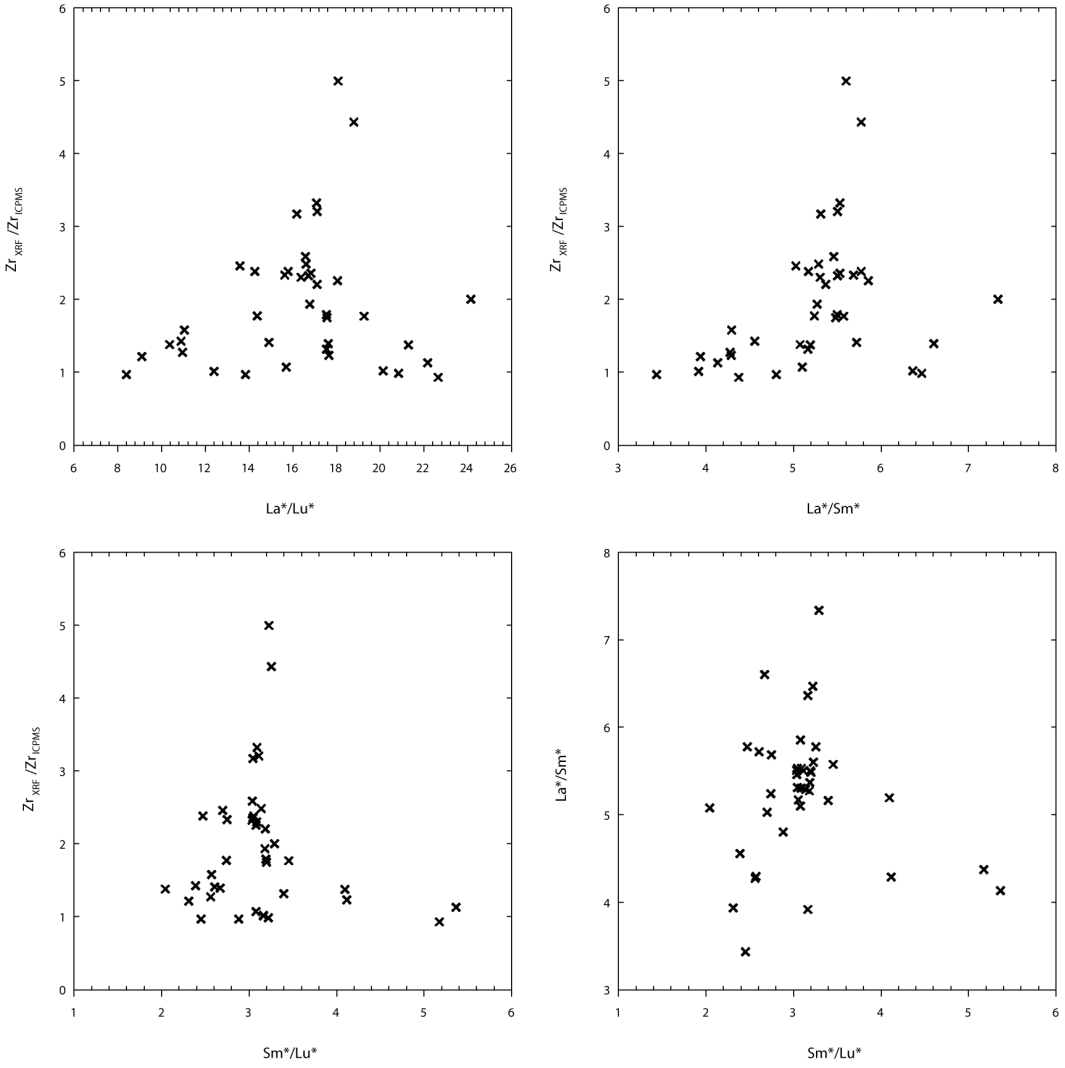

FIGURE 2.5: Plots of Zr_{XRF}/Zr_{ICPMS} vs REE ratios such as Sm/Lu indicate the REE element profiles are not strongly affected by the incomplete dissolution of zircon. Values are normalised to chondrite (Boynton, 1984)

Chapter 3

Au enrichment of oceanic crust during ridge-plume interaction

3.1 Prologue

This chapter is based upon a manuscript accepted for publication in Geology (Webber et al., In Press).

3.2 Introduction

A crucial control on the formation of a hydrothermal mineral deposit is the concentration of the metal of interest within the hydrothermal fluid, which in turn is variably controlled by the fluid chemistry, temperature, salinity, fO_2 and the chemistry of the source and host rocks (Keays, 1983, 1987). Consequently, higher Au concentrations in the source rock may provide an important control on the size of any resulting Au deposit. Enrichment at the source has been recognised as an important factor in the production of several world-class Au deposits and districts (Keays, 1983, 1987; McInnes et al., 1999; Bierlein and Pisarevsky, 2008). This enrichment of Au could be supplied by a mantle plume carrying Au into the upper mantle and, ultimately, into the mineralizing system (Oppliger et al., 1997; Kerrich et al., 2000; Bierlein et al., 2006). Plumes, having originated closer to the core than the upper mantle, may carry siderophile elements like Au into the upper mantle where it can be incorporated into oceanic crust (e.g. Brandon and Walker 2005). In a subduction setting, Au enrichment may involve the subduction of plume-enriched oceanic crust, or by entraining plume material into the mantle wedge, either through a slab window or tear, or by entering the wedge from behind the arc (Kerrich et al., 2000). All of these models are

predicated on a substantive enrichment of Au within the plume environment. However, few data exist to support this assertion, in particular a lack of very low detection limit and high precision geochemical analyses for Au.

Iceland presents an interesting test case. There are no gold mines on Iceland, yet volcanic and geothermal systems are extensive, with geothermal fluid on the Reykjanes Peninsula actively precipitating metal-rich crusts containing up to 589 ppm Au (Hardardottir et al., 2010). Such high amounts of Au could well be due to elevated Au concentrations in the host rocks. Here, we find that the Iceland Plume is creating Au-enriched crust along the Reykjanes Ridge, with Au levels up to 13 times that of normal mid-ocean ridge basalt.

3.3 Reykjanes Ridge

The Reykjanes Ridge is a section of the Mid-Atlantic Ridge south of Iceland where the spreading Iceland plume head is mixing with Atlantic depleted upper mantle (Fig. 3.1). The chemistry of basaltic samples from along the ridge show a continuously variable chemistry indicating progressive mixing between several end-members. These end-members have been given various names in publication; here we refer to notation set out by (Thirlwall et al., 2004, 2006). North of 60°N binary mixing occurs between an enriched Iceland member (RRE) and a more depleted Iceland member (RRD1) (Taylor et al., 1997; Murton et al., 2002; Thirlwall et al., 2004, 2006). The enriched member, which moves southwards beneath the Reykjanes Ridge, is interpreted as an intermediate mixture of enriched and depleted components from beneath Iceland. South of 60°N, a third end-member (RRD2) exists with depleted trace element ratios and isotope characteristics similar to North Atlantic MORB. End members are most easily distinguished using Pb isotope ratios such as $^{206}Pb/^{204}Pb$ and $\Delta^{208}Pb$.

3.4 Gold in MORB

To establish the Au concentration of normal mid-ocean ridge basalt, i.e. a composition free of plume influence and representing an asthenospheric baseline, we have compiled suitable available Au concentrations from mid-ocean ridges (Keays and Scott, 1976; Hertogen et al., 1980; Lapukhov et al., 1999; Tatsumi et al., 2000). The mean concentration of these samples, 1.0 ppb (1s = 1.2, n = 22) is heavily biased towards 6 anomalous results with 2.3 to 4.5 ppb (Fig. 3.2). As 14 values are in the range 0 to 0.5 ppb and the distribution of the data appears to be log-normal, a more realistic baseline Au value is the log-normal mean which is 0.47 ppb Au.

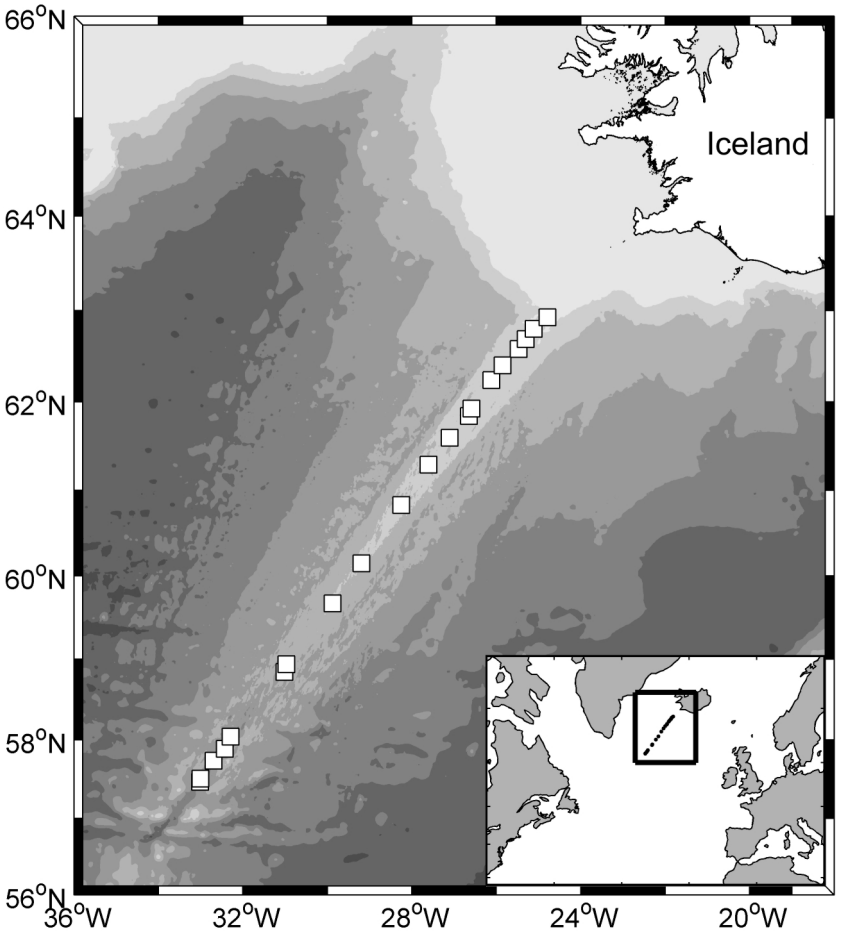

FIGURE 3.1: Map of the Reykjanes Ridge with Iceland (top right). Grey shades show bathymetry, with darker shades corresponding to greater depth at 500m intervals. Sample locations shown in open squares. Inset map shows wider area and sample locations (dots).

3.5 Method

We analysed 20 volcanic glasses from the length of the Reykjanes Ridge (Fig. 3.1) using a recently developed ultra low-level Au technique to precisely measure Au concentrations (Pitcairn et al., 2006b). The technique uses solid-phase extraction columns utilizing the organic compound Diisobutyl Ketone (DIBK), which has a high partition coefficient for Au. Repeated analysis of reference materials GXR-1, GXR-4, CH-3 and SARM-7 give 1σ error better than 5%. Blank values were below detection, which was 10 ppt using background count + 10σ. Only samples of unaltered basalt glass were analysed, as previous studies showed that Au may be depleted within the crystalline interior of pillows (Keays and Scott, 1976). Sample 12AD1 was slightly more crystalline material from just below a glassy rim, however the sample lies well within the range of the data analysed and so is included. The basalt glasses have previously been analysed for major and trace elements, $^{87}Sr/^{86}Sr$,

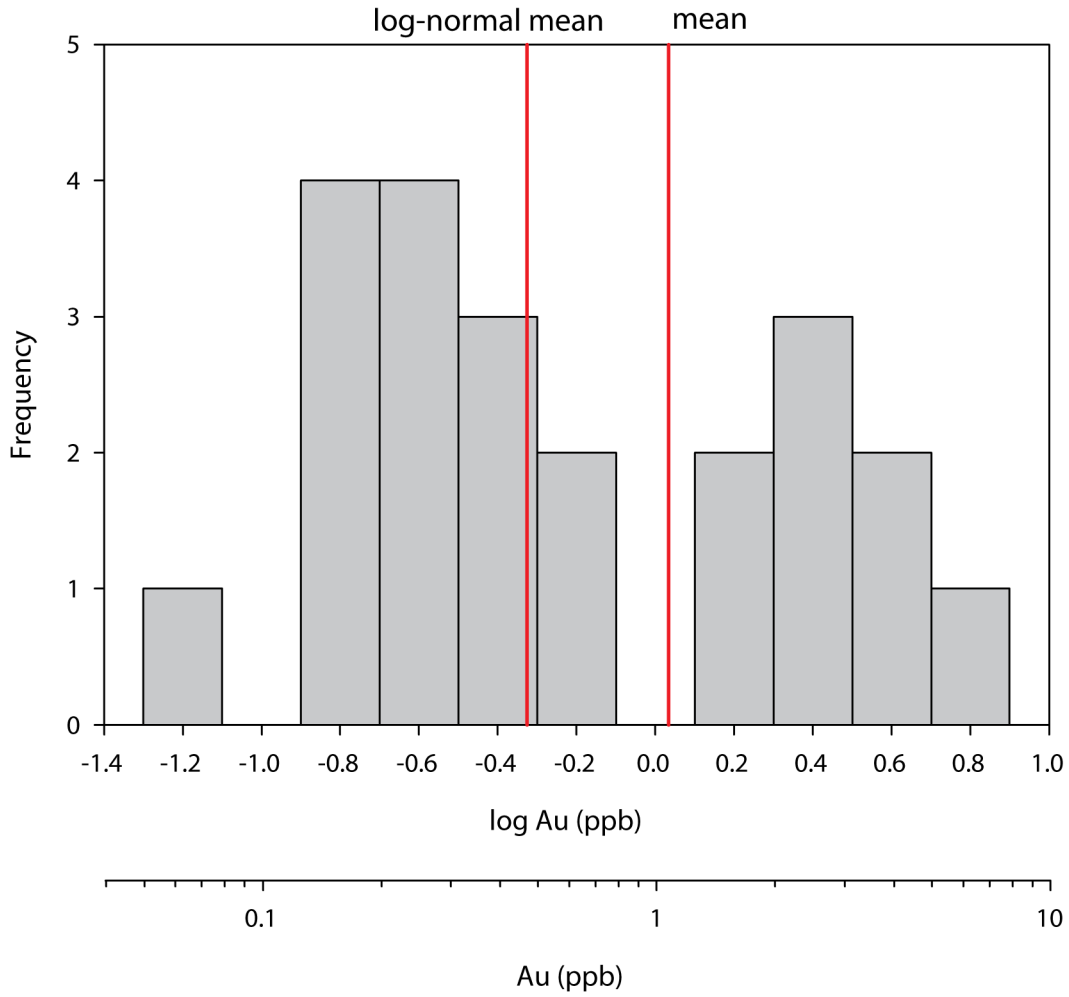

FIGURE 3.2: Histogram of mid-ocean ridge basalt Au data. This histogram of logged data demonstrates that taking the mean of the dataset is skewed towards a few higher values, whereas the bulk of the data are lower than the mean value. The log-normal mean is a better representation of the dataset. MORB data: Keays and Scott (1976); Hertogen et al. (1980); Lapukhov et al. (1999); Tatsumi et al. (2000), n = 22.

$^{143}Nd/^{144}Nd$, Pb isotopes and $^{3}He/^{4}He$ (Taylor et al., 1997; Hilton et al., 2000; Murton et al., 2002; Thirlwall et al., 2004).

3.6 Results

Gold concentrations ranged from 0.21 to 4.22 ppb (Table 3.1). Samples analysed from south of 61°N show a range of Au values between 0.2 and 1.7 ppb, whilst samples from north of 61°N show a range of 1 to 4.3 ppb, comparable to values recorded on Iceland (Fig. 3.3). No correlations are observed between Au and indices of basalt magma evolution or mantle melting such as Mg#, Fe[8] and Na[8]. Correlation of Au with $^{87}Sr/^{86}Sr$ and

$^{143}Nd/^{144}Nd$, which are not affected by magma evolution, suggests that variation in the Au concentration is due to mantle source mixing (Fig. 3.4A). Comparison of Au with Pb isotope data shows that the RRE, RRD2 and RRD1 end-members described by Thirlwall et al. (2004) can be identified (Fig. 3.4B). Plotting Au against an incompatible trace element ratio, such as La/Sm, suggests at least three end-member mixing involving an enriched mantle component and two components with depleted trace element ratios, one with slightly higher Au concentrations than the other (Fig. 3.4C). The companion plot (Fig. 3.4D) shows the data divides into two arrays with distinct gradients, converging on a point with low 1/Au (or high Au) and low La/Au. This is a position taken by two very different compositions, one with a very depleted La/Sm ratio, such as the reference material BIR-1, and another with a very enriched La/Sm ratio. This suggests two separate end-members with low La/Au; one with high La and high Au, and one with low La and low Au. Taken together, the Pb isotopes and Au versus trace element plots suggest four component mixing occurs. The fourth end-member does not fit easily into established mixing models, and may represent a suggested MORB (Taylor et al., 1997) or RR3 component (Thirlwall et al., 2004). We will refer to this as RR3 for ease of use. The standard BIR-1, an extremely depleted sample from Iceland, lies close to RR3 on the mixing line between RRD2 and RR3 with a Au concentration of 1.6 ppb (Constantin, 2009). The most significant positive correlations are observed with Sr and Cu (Fig. 3.6).

3.7 Discussion

In the upper mantle, the distribution of Au and other chalcophile elements is strongly controlled by the behavior of sulphur (e.g. Peach et al. 1990; Keays 1995). Sulphur-saturated silicate melt will be depleted in chalcophile elements that are sequestered by the sulphide-bearing mantle residual, whereas sulphur-undersaturated silicate melts will have the full complement of chalcophile elements. MORB, for example, is generally considered to be sulphur-saturated at the time of extraction and thus depleted in chalcophile elements (Peach et al., 1990). As the mantle undergoes increased partial melting, a greater fraction of the residual sulfide is consumed and chalcophile elements are increasingly released to the melt. We observe elevated Au concentrations compared to MORB in both enriched and highly depleted lavas, and so proportion of partial melting cannot alone explain the high Au concentrations in the Reykjanes Ridge lavas (Fig. 3.4C). The most convenient way, and the method we favour, of explaining the Au concentrations of the Reykjanes samples is by assuming the mantle source regions had different primary compositions. The enriched plume component may have had a lower sulphur content leading to a higher

Sample	Total weight of sample analysed (g)	Latitude (∘ N)	Au (ppb)	La/Sm
12aD1	8.12	57.47	0.90	0.64
13D2	9.12	57.51	0.54	0.61
02D6	4.01	57.74	0.85	0.72
17D1	9.01	57.89	1.35	0.63
33aD1	8.27	58.04	0.39	0.76
75D10	14.87	58.84	0.75	0.75
78D2*	4.00	58.94	1.73	1.12
100D1	9.67	59.67	0.20	0.67
121D3	14.30	60.15	1.70	0.58
136D2	5.05	60.83	0.82	0.70
144D2	8.06	61.29	0.62	0.81
150D3	12.16	61.60	1.01	1.32
157D3*	7.96	61.84	2.97	1.29
160D4*	1.41	61.93	1.25	1.19
169D6	8.46	62.24	1.04	1.30
173D1	8.18	62.40	1.29	1.57
177D3	5.20	62.58	4.26	1.93
179D3	0.79	62.69	3.21	1.92
182D3	0.72	62.80	1.62	1.73
185D4	0.80	62.93	2.50	1.83

TABLE 3.1: Results of Au analyses for the Reykjanes Ridge lavas. La/Sm data from (Murton et al., 2002)

.

proportion of chalcophile elements released at lower partial melt fractions. Such an explanation has been suggested previously to explain PGE distributions in volcanic rocks from Iceland (Momme et al., 2003). The plume may also have had an elevated primary Au concentration, consistent with the idea that plumes may be enriched in siderophile elements (Boyle, 1979; Brimhall, 1987; Rock and Groves, 1988; Brandon and Walker, 2005; Burke et al., 2008; Hawkesworth and Schersten, 2007; Bierlein and Pisarevsky, 2008). This is easily demonstrated using the partition coefficients and model of Peach et al. (1990), which shows increasing the Au concentration of the source rock greatly increases the Au concentration in the resulting melt over the entire range of melt fractions (Fig. 3.9A).

These new data show that basalts derived from all Reykjanes mantle components except RRD2 contain as much as 13 times more Au than MORB. There are several approaches to obtain a true understanding of the amount of Au-enrichment the Iceland plume is supplying. One appoach is to examine the overall trend of the data with latitude and take the termination of a best-fit line as being the highest average enrichment (Fig. 3.7). Such an approach should probably include data from Iceland itself because the centre of the plume is beneath it. This approach yields values of approximately 2.5 ppb for just the reykjanes ridge and 3.8 ppb Au for all data, corresponding to enrichment factors of

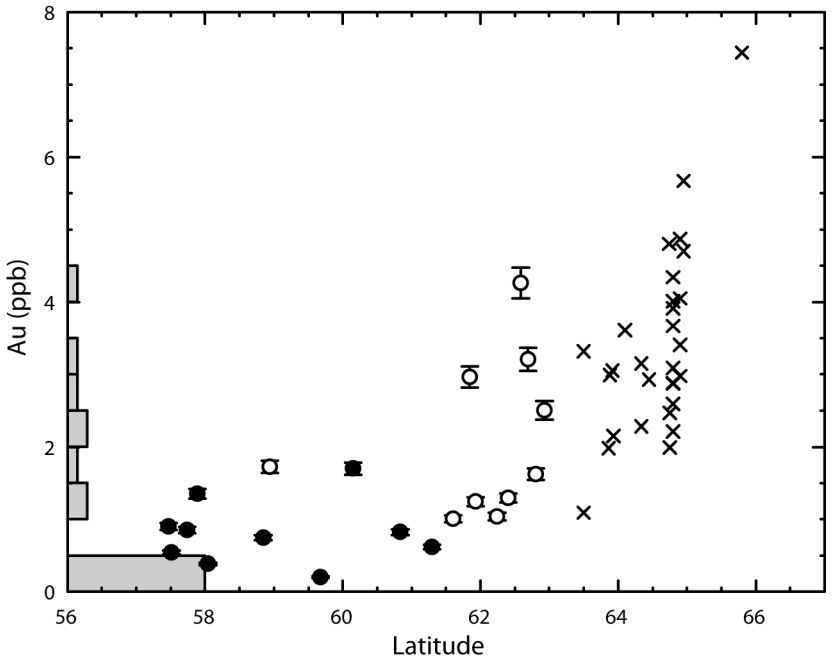

FIGURE 3.3: Au in volcanic glasses vs latitude. We observe a trend from Atlantic MORB, shaded histogram on y-axis (n = 22), to Icelandic lavas (crosses). Closed circles have La/Sm <1, open circles have La/Sm >1. Error bars represent a conservative 5% error. MORB data: Keays and Scott (1976); Hertogen et al. (1980); Lapukhov et al. (1999); Tatsumi et al. (2000). Iceland data: Momme et al. (2003)

5 and 8, respectively. The weakness of this method is assuming that the melt evolution beneath Iceland is similar to that beneath the Reykjanes Ridge, which it clearly is not due to the much greater thickness of crust and far more varied lava compositions of Iceland. A second approach would be to examine the variation of Au with isotopes ratios which are not affected by melt evolution (Fig. 3.8). Using published end-member values (Thirlwall et al., 2004), these plots suggest a basalt composed of 100% the end-member RRE should have a Au concentration of 4-4.3 ppb, an enrichment factor of 8.5 to 9 over normal MORB. RRE itself is thought to be a mixture of components found beneath Iceland, such as IE1, IE2 and ID1. IE1 in particular has strontium and lead isotope ratios that suggest even higher Au concentrations could be found on that end-member, though the relationship between these end-members is not constrained enough to make an estimate. This could explain some of the anomalously high values of 5-8 ppb found on Iceland.

Basalts derived from mixtures containing a high proportion of RRE contain the most Au, followed by RR3 then RRD1. RRD2-rich basalts are close to MORB in their Au value, thus lending weight to this member being background upper mantle of some sort. If we consider the traditional model that plumes originating deep in the mantle transport siderophile elements from the core/mantle boundary layer (Boyle, 1979; Brimhall, 1987; Rock and Groves, 1988; Brandon and Walker, 2005; Burke et al., 2008; Hawkesworth and

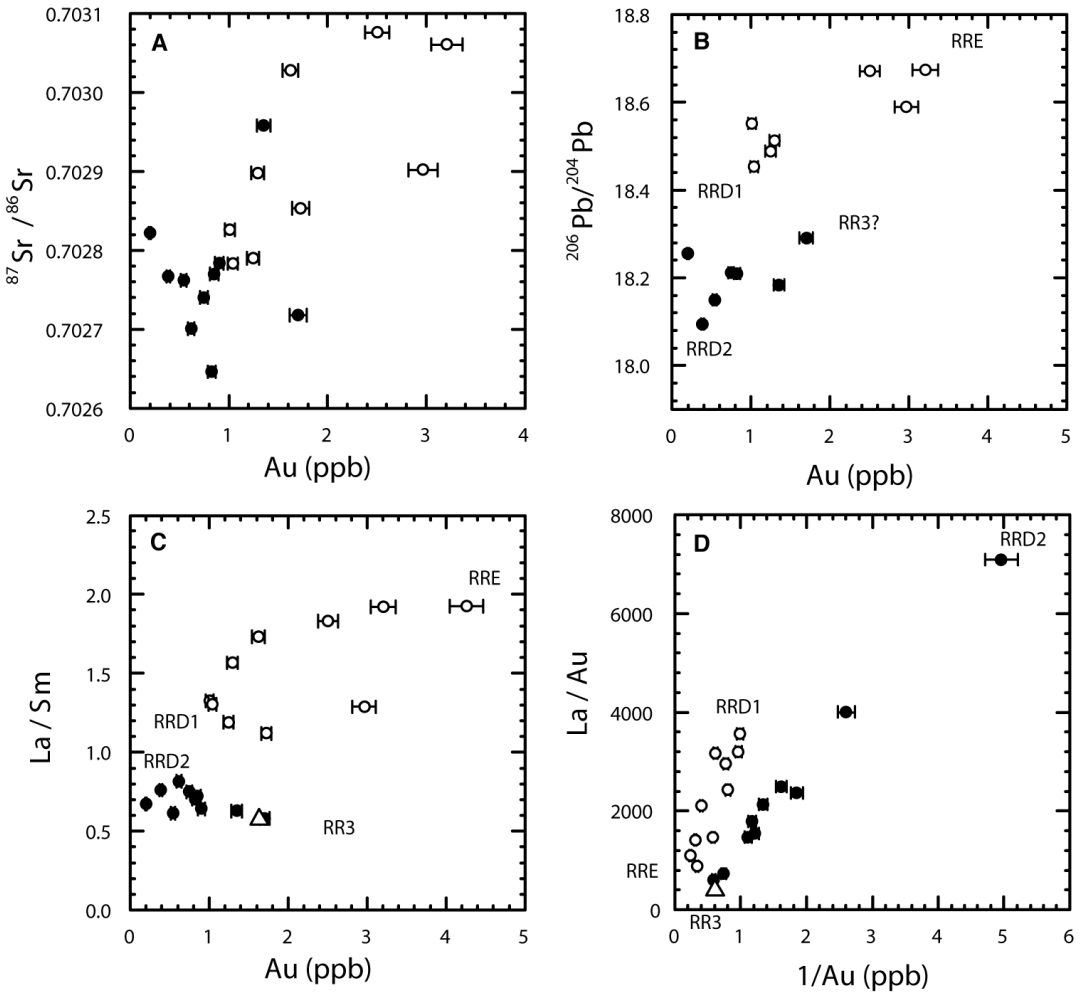

FIGURE 3.4: A: Au vs $^{87}Sr/^{86}Sr$. Higher Au values correspond to more radiogenic $^{87}Sr/^{86}Sr$, and correlation suggests variation in Au is produced by mantle source mixing. B: Au vs $^{206}Pb/^{204}Pb$. The end-members involved are well recognised with Pb isotopes (e.g. Thirlwall et al. 2004), allowing the trends in Au plots to be defined. C: Au vs La/Sm indicates mixing occurs primarily between RRE-RRD1 and RRD2-RR3. Error bars are 5% for Au and are smaller than the symbol size for La/Sm. D: The companion plot confirms 4 end-member mixing. In both plots end-member labels do not necessarily represent their actual positions on the plots, but show which end-members the data are mixing between. Symbols as Fig. 3.3 and the open triangle is standard BIR-1.

Schersten, 2007; Bierlein and Pisarevsky, 2008), these results suggest that the Iceland components may have a deep-mantle origin. This is consistent with evidence from $\delta^{18}O$ in olivine and $^{3}He/^{4}He$, which also suggest the enriched Iceland component has a deep source (Thirlwall et al., 2006). We observe a general trend from MORB toward compositions with higher Au values and higher $^{3}He/^{4}He$. Samples with the highest Au concentrations lie between MORB and a theoretical component consisting of the highest $^{3}He/^{4}He$ and Au values recorded on Iceland of 34 R_A (where R_A is the ratio of $^{3}He/^{4}He$ in the atmosphere) (Macpherson et al., 2005) and 7.44 ppb (Momme et al., 2003), (Fig. 3.4B). Other samples

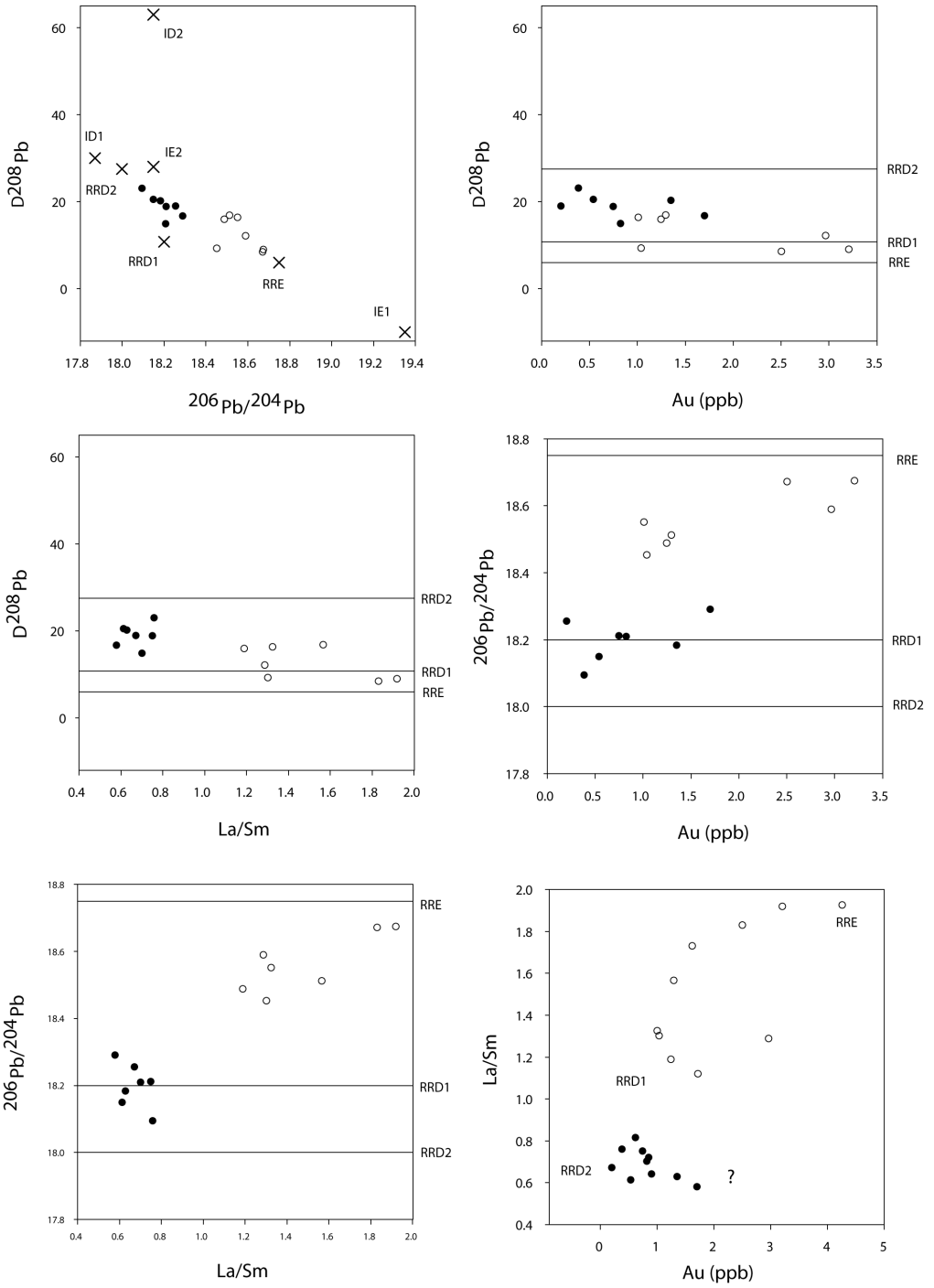

FIGURE 3.5: Pb isotope systematics are used to distinguish the various end-members. (A) shows the components as defined in Thirlwall et al. (2004). Subsequent plots show how Au values and the La/Sm ratio can be attributed to the various end-members. In particular it shows that mixing between RRD1 and RRD2 is not well defined and that the current end-members cannot easily explain the trend to low Au in the enriched samples (La/Sm >1). Fig. 3.4D confirms a 4th end-member is required. Symbols as Fig. 3.3 and crosses indicate composition of end-members.

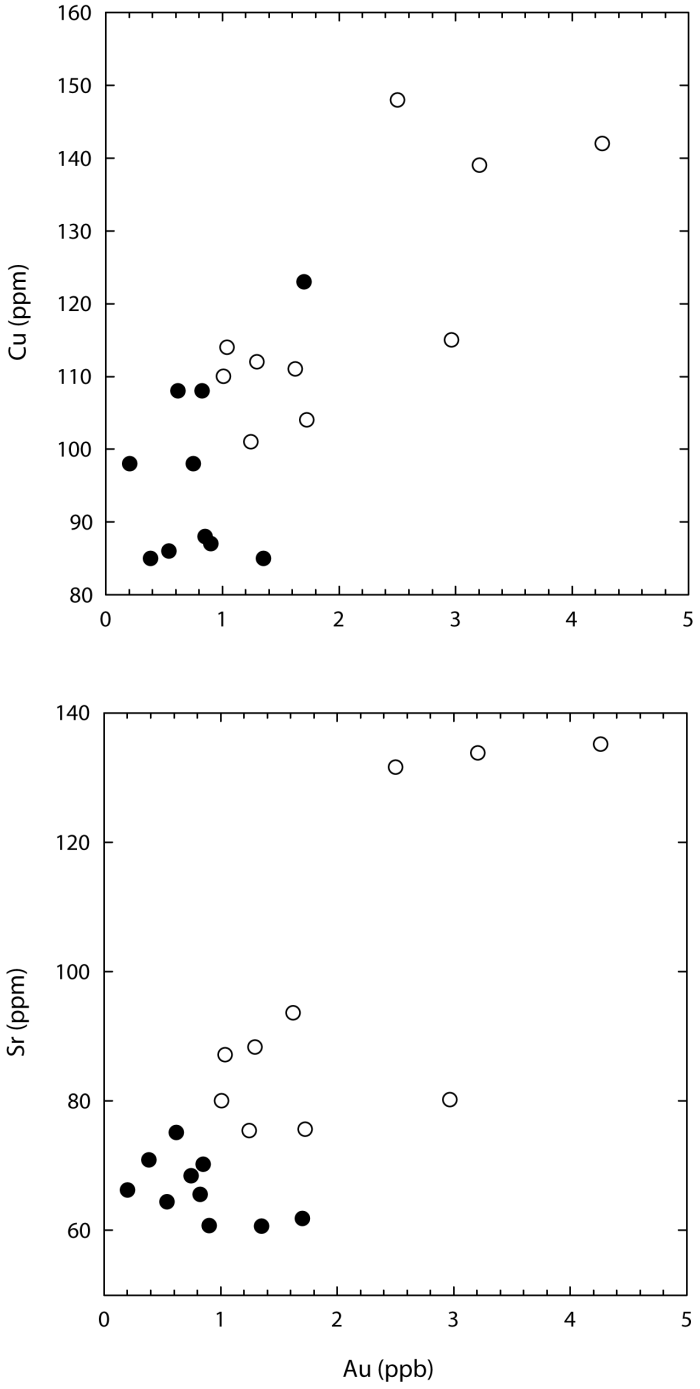

FIGURE 3.6: Au (ppb) vs Cu (ppm) and Sr (ppm). Statistically significant correlations are observed ($r^2 = 0.62$ and 0.63, respectively).

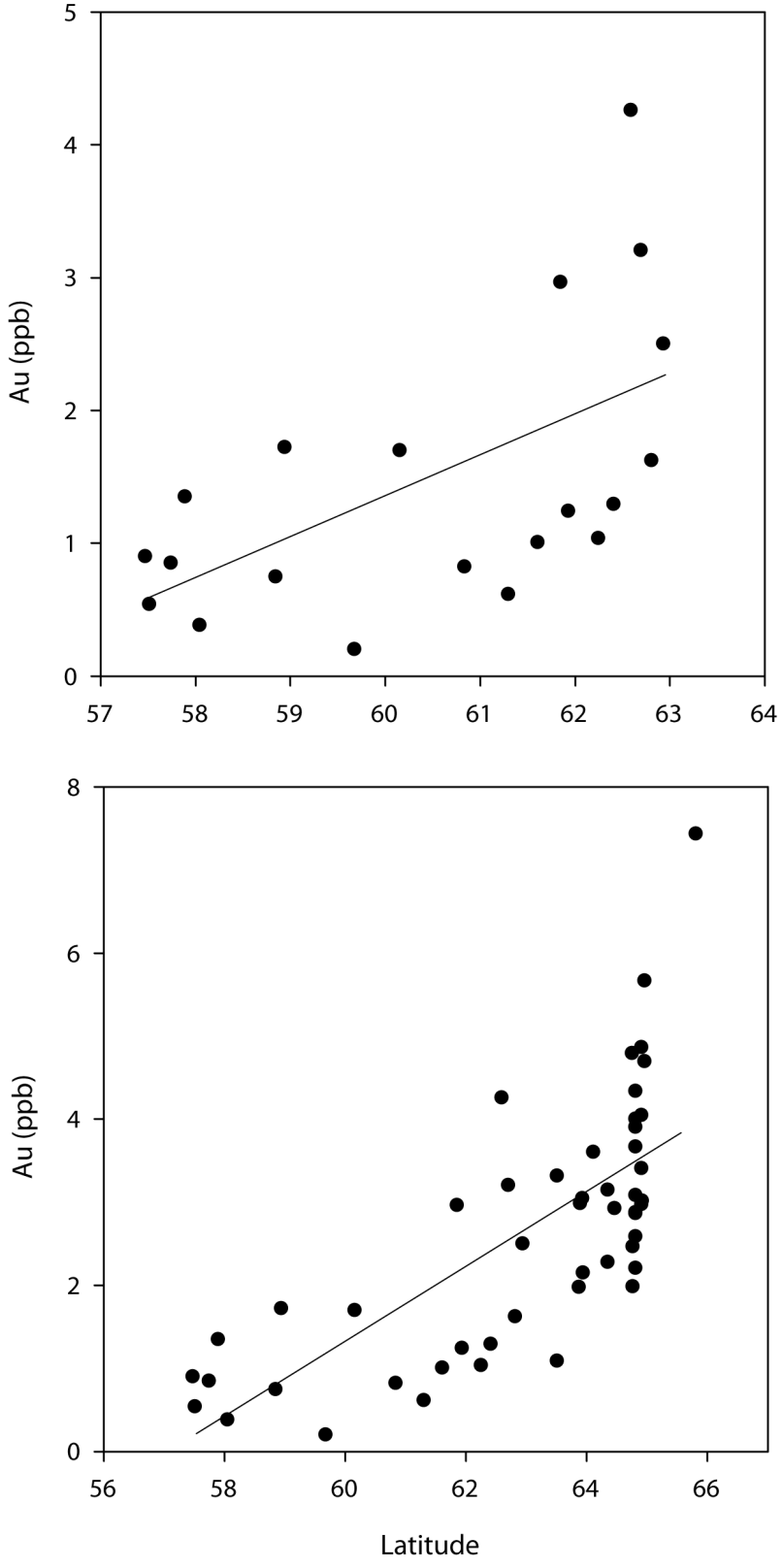

FIGURE 3.7: The overall enrichment of Au over normal MORB can be gauged in several ways. One is to take a best-fit of the Reykjanes data (top pane). However, such an approach should include Iceland, which sits over the plume centre (lower pane).

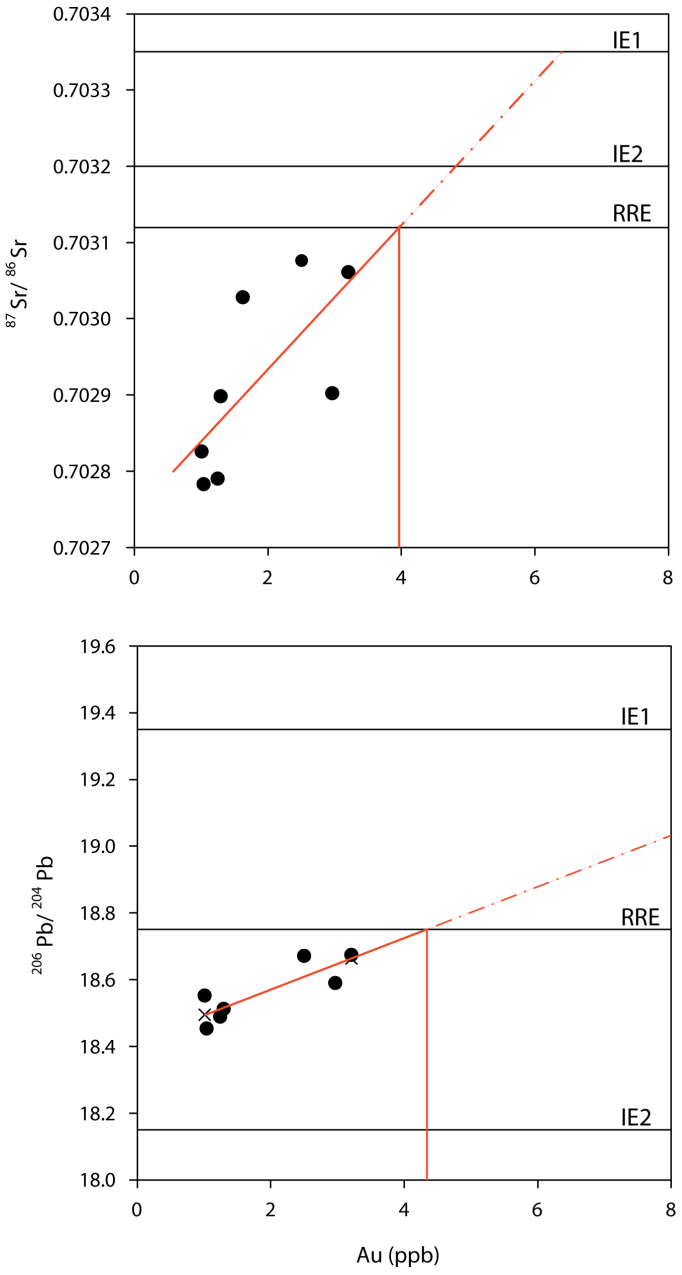

FIGURE 3.8: The Au value of the end-member RRE can be estimated using the trend of the enriched mixing array (RRE-RRD1) versus strontium and lead isotopes. These trends suggest a Au value of 4-4.3 ppb Au. RRE itself is a mix of components found beneath Iceland such as IE1 and IE2. The position of IE1 in particular on these plots suggest that even greater Au concentrations could be found in those components. End-member isotope values are from Thirlwall et al. (2004).

plot to the left of this line, indicating they contain components with lower Au concentrations, He concentrations or $^{3}He/^{4}He$. At least one sample may be strongly affected by ingrowth of radiogenic ^{4}He, as it showed a particularly low He concentration (Hilton et al., 2000).

Mixing beneath the Reykjanes Ridge has long been recognized as being divided between the northern and southern sections of the ridge at 60-61°N (e.g. Sun et al. 1975). Our data show four component mixing, with RRE-RRD1 and RRD2-RR3 forming separate mixing lines, with some scatter suggesting either mixing between the two arrays or variable end-member compositions. Together with the scattered correlation between Au concentration and latitude, this suggests a somewhat disorganized structure. The presence of a fourth component, possibly RR3 is confirmed by these data, however we can only speculate on its nature. Its high Au, spatial relationship with the plume and similarity to BIR-1 would suggest it is a plume component rather than upper mantle. In addition, the trend of data toward a MORB-like Au concentration supports the idea that background Atlantic upper mantle is mixing with the plume head.

We find that Iceland plume mantle would provide an excellent source rock for any Au-scavenging mineralizing system. Ridge-plume interaction along the Reykjanes Ridge have allowed the formation of basaltic melts with as much as 13 times more Au than MORB. Further from the plume center, these levels fall to a more modest 3-5 times MORB. Due to the observed width of plume heads being hundreds to thousands of kilometers, the enrichment identified can potentially produce vast quantities of metal-enriched oceanic crust, representing a significant source of Au for any mineralizing system tapping plume-enriched crust. Potential targets would include: plume enriched oceanic crust; plume-influenced rift settings such as Iceland and East Africa; and arcs under the influence of plume-enriched subducted crust or mantle.

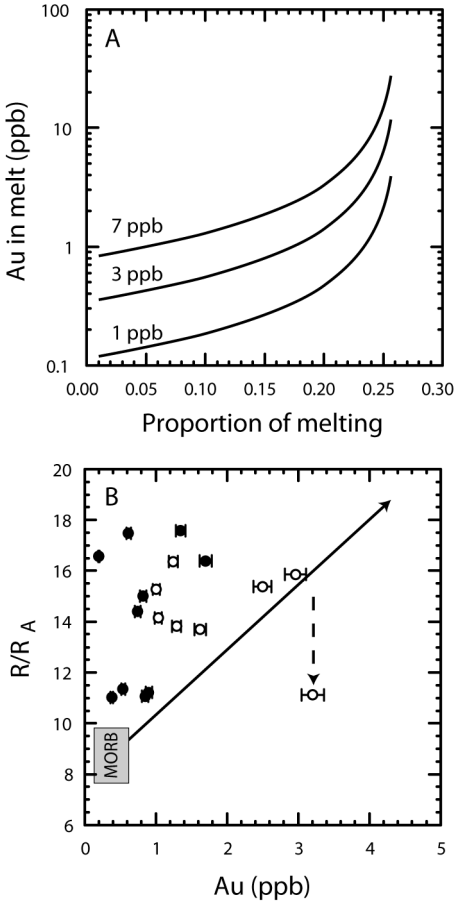

FIGURE 3.9: A: Curves distinguish the Au concentration in the mantle source. A 1 ppb mantle source does not generate high (>1 ppb) Au concentrations until 23-25% partial melting, after which all sulphides have dissolved. Raising the Au concentration of the mantle source increases the Au concentration of the silicate melt across the entire range of partial melt fractions. In both panels lines terminate at complete sulphide dissolution. Model parameters are from Peach et al. (1990). B: Au vs R/R_A, where R/R_A is the $^3He/^4He$ ratio of the sample normalized to that of the atmosphere. Samples lie between some high R/R_A, high Au end-member (Iceland) and MORB. Solid arrow is projected towards a theoretical maximum value of 34 R_A (Macpherson et al., 2005), and 7.5 ppb Au (Momme et al., 2003). The MORB box is given by the average R/R_A of N-MORB (Graham, 2002) and median average Au content presented here. The indicated sample (dashed arrow) had a particularly low He concentration (Hilton et al., 2000), suggesting it could have been significantly affected by radiogenic ingrowth of ^4He. Symbols as Fig. 3.3.

Chapter 4

Au Recycling at Subduction Zones

4.1 Introduction

Copper-gold mineralisation is strongly associated with convergent plate margins, where rising magmas deliver metals and volatiles to high-level hydrothermal systems. However, beyond this well established association, the nature of the genetic link remains an open question. Certain magma types, including shoshinite and alkaline suites (Sillitoe, 1997), high fO_2 subduction conditions (Mungall, 2002) and unusual subduction settings including polarity reversal (Solomon, 1990), flat subduction (Kay and Mpodozis, 2001), thermal or topographic anomalies on the subducting slab (Cooke et al., 2006) and slab detatchment (Wortel and Spakman, 2000; de Boorder et al., 1998) have all been advanced as important factors in the development of substantial Cu-Au mineralisation in the overlying arc. It has also been shown that enriching the mantle wedge with Au may be an important process in the formation of large Au deposits such as Ladolam on Lihir Island (McInnes et al., 1999). The subduction of enriched oceanic crust of mantle-plume origin, such as a plateau or a plume-influenced spreading centre, could potentially supply this enrichment since mantle plumes are thought to carry siderophile elements from the lower mantle to the crust (Bierlein et al., 2006; Bierlein and Pisarevsky, 2008; Kerrich et al., 2000). However, this hypothesis relies on the assumption that Au is mobile during subduction metamorphism and dehydration of the slab, which is not well established. If Au is mobile, then anomalous Au concentrations in the slab could be an important step towards generating Au deposits in the overlying arc.

This work presents low detection limit Au analyses of basaltic eclogites from the Zermatt-Saas ophiolite, Switzerland. This ophiolite was subducted to a depth of 75 km before being rapidly exhumed and emplaced during the Alpine orogeny (e.g. Angiboust et al. 2009). By

comparing the Au concentration and trace-element geochemistry of these basaltic eclogites with published global MORB data, we show that approximately half of Au has been lost from these eclogites during the eclogite facies metamorphism. Over geological timescales this represents a significant amount of Au added to the arc system and suggests that oceanic crustal Au enrichment is an important process in arc Au metalogenesis.

4.2 Geological setting and deformation

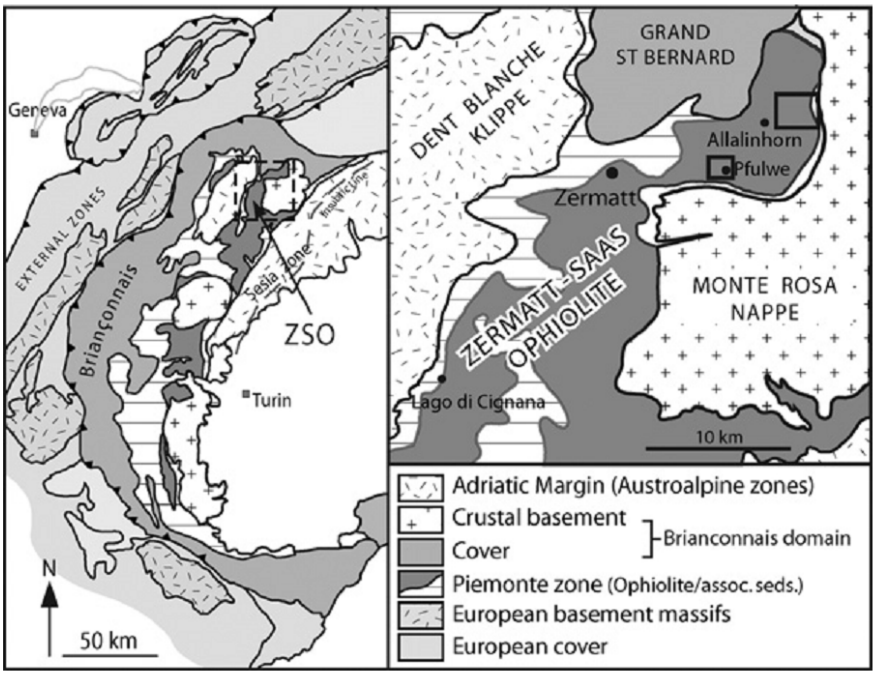

FIGURE 4.1: Regional and local view of sample locations in the Western European Alps. Basaltic eclogite samples were collected from the Pfulwe area.

The Zermatt-Saas ophiolite is a series of well preserved slices of eclogitic oceanic crust emplaced within the European Alps (Fig. 4.1), which formed during spreading of the Mesozoic Tethys. The ophiolite preserves a complete section of oceanic crust from sedimentary cover to pillows, dykes, gabbros and ultramafic serpentinites (Bearth, 1967; Bearth and Schwander, 1981). It is also remarkably complete laterally, with recent data showing it likely comprises a 60km long continuous slice of slab which underwent similar depths of burial and exhumation paths across its width (Angiboust et al., 2009).

Magmatic zircon ages from the Mellichen and Allalin metagabbros of 164.0 ± 2.7 Ma and 163.5 ± 1.8 Ma constrain the oceanic crustal age to the middle Jurassic, consistent with overlying sedimentary zircon ages (Rubatto et al., 1998) and the general tectonic setting.

Trace element geochemistry from across the western Alpine ophiolites indicates the basalts are uniformly N- to E-MORB (Pfeifer et al., 1989).

The basalts and gabbros appear to have been hydrated and altered by seafloor hydrothermal circulation to varying degrees. Mineral assemblages and $\delta^{18}O$ ratios identify areas as being little altered, such as Pfulwe, to high-T alteration and mineralised zones, such as that found at Servette (Barnicoat and Cartwright, 1995). Alteration of the gabbros appears to control eclogitisation, with little altered rocks retaining their magmatic assemblage (Barnicoat and Cartwright, 1997). Since the eclogitic mineral assemblage in the gabbros are often discontinuous and restricted to narrow pathways, hydrothermal alteration of the gabbros is interpreted to have been focussed along these discrete pathways. In turn, fluid flow during eclogite facies metamorphism was likely restricted to such pathways, whilst the preservation of stable isotope ratios suggest these rocks did not encounter fluids from an external source (Barnicoat and Cartwright, 1995).

Maximum P-T condition estimates for the ophiolite are varied, however, a modern study yields remarkably consistent conditions of 540 ± 20℃ and 23 ± 1 kbar for all rocks of the ophiolite (Angiboust et al., 2009). This pressure corresponds to a burial of 75 km. In modern arcs, an important parameter is the depth to the slab beneath the arc front, D. The burial depth of the Zermatt-Saas ophiolite of 75 km is significant since this is recognised as the shallowest value for D found in modern arcs (England and Katz, 2010). This implies that they could have been subducted deep enough to contribute fluid to the mantle wedge and, eventually, to the volcanic system in the over-riding plate.

Ultra-high pressure zircon rim ages indicate that the deepest subduction occurred during the middle Eocene (44.1 ± 0.7 Ma) (Rubatto et al., 1998). A mineral assemblage of omphacite + garnet + glaucophane + epidote + rutile was formed at maximum subduction depth. Estimations of water content of the protoliths and eclogites suggest as much as 0.25-2.5 wt% H_2O has been lost during this process (Barnicoat and Cartwright, 1995). Initial exhumation rate is estimated at 10-26 km/m.y., followed by 0.3 km/m.y. from 34 to 14 Ma (Amato et al., 1999). This rapid exhumation rate together with the presence of fluid-deficient symplectite rims on grain boundaries suggests retrograde fluid was absent (Bucher et al., 2005).

4.3 Metal recycling at subduction zones

Most base and precious metals are soluble in hot, high oxygen fugacity, saline fluids typically produced by dehydration of the subducting slab. In particular, the metals Pb, As and Sb, together with Tl and perhaps Cu have been shown to be strongly mobilised by

these fluids (Noll et al., 1996). The Zermatt-Saas eclogites have been shown to be depleted in Pt, Pd and Re compared to MORB, and are thus interpreted to be mobile in this setting (Dale et al., 2009).

The subduction of plume-influenced oceanic crust occurs where the Galapagos plume trail subducts beneath the South American plate and where the Ontong-Java Plateau has partially subducted in the Southwest Pacific. The subduction of such crust has been shown to influence the chemistry of arc lavas at both locations (e.g. Gazel et al. 2009; McInnes et al. 1999), with isotope ratios confirming plume-derived chemical input from the downgoing slabs. This leads to the possibility that the subduction of metal-rich crust compared to N-MORB could lead to the generation of metal-rich arc magmas and, therefore, to more metals entering mineralising systems. However, this might only be a significant process if the amount of slab-derived metals entering the arc magmatic system is significant compared to the amount of mantle-derived metals.

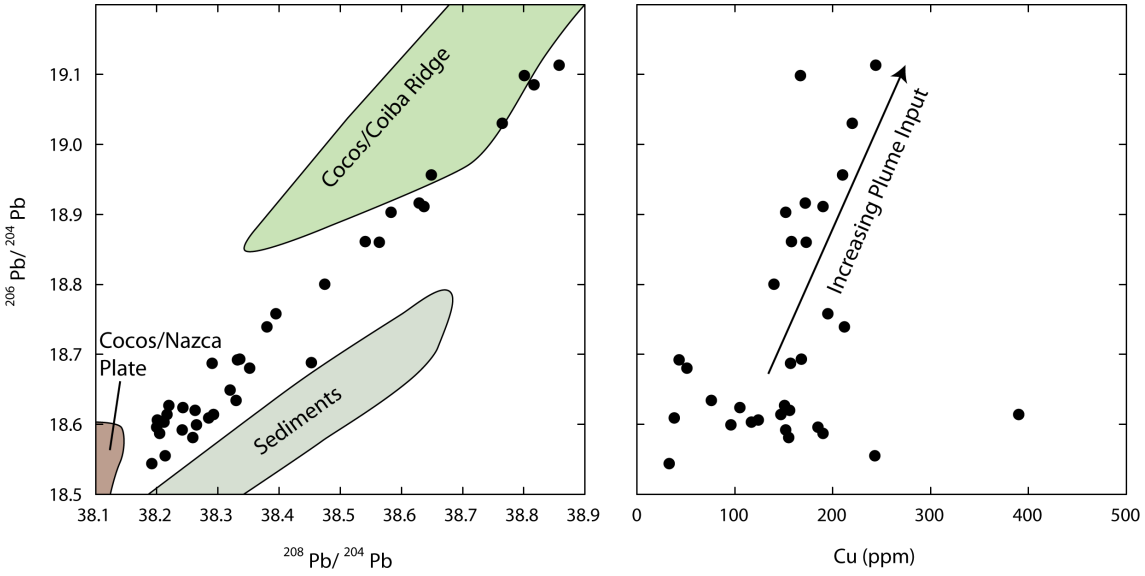

FIGURE 4.2: The Pb isotope systematics of lavas from the Costa Rican arc indicate addition of Galapagos plume-derived Pb (left panel). Lavas showing a strong plume signature also have relatively high copper contents. Figure adapted from Gazel et al. (2009)

In the case of the Galapagos plume track, this association is demonstrated by available data showing that lavas with plume-derived isotope ratios contain high copper contents (Fig. 4.2, Gazel et al. 2009). However, it is not clear whether the high Cu contents are due to high Cu concentrations in the slab, more efficient removal of Cu from the slab or more efficient extraction of Cu from the mantle under such circumstances. In the case of Au and PGE, the picture is further complicated by the presence of sulphides in the mantle wedge which strongly sequester those elements. Residual sulphides could hide the

addition of slab-derived Au and PGEs. In contrast, the dissolution of sulphide by release of highly oxidising fluids during subduction locking or subduction of a hot slab (Mungall, 2002), both possible scenarios in the subduction of a plume track, could produce Au and PGE rich melts without additional Au and PGE sourced from the subducting slab.

4.4 Element mobility in metamorphic rocks

When assessing the mobility of an element in rock, consideration must be paid to passive enrichment due to the mobility of other elements. This is particularly the case for major elements which make up the cast majority of a rock's mass. Although the Zermatt-Saas MORB eclogites are metamorphosed MORB, all trace elements are present at higher concentrations compared to MORB, with a few exceptions in the case of Rb and K (Fig. 4.3). This relative enrichment is because the rock has lost mass overall, primarily in major oxides, and so a trace element may have a higher or equal concentration compared to MORB yet still have been lost from the rock. Comparison can be made with elements thought to be relatively immobile in hydrothermal and metamorphic conditions such as Zr and Yb (Humphris and Thompson, 1978a,b; Finlowbates and Stumpfl, 1981; Pearce and Peate, 1995). The immobile element in the protolith and altered rocks is commonly denoted C_i (e.g. Ague 1994). On a graph of C_i vs an element m, assuming C_i is perfectly immobile, data will move in response to relative mass loss and gain in the bulk rock and mass changes of m (Fig. 4.4). This can be expressed as the ratio of m/C_i: if m/C_i $<(m/C_i)_{protolith}$ then m is immobile and mass has been lost; if m/C_i $>(m/C_i)_{protolith}$ then m is mobile and mass has been gained and if $m/C_i \approx (m/C_i)_{protolith}$ then m is immobile. However, it becomes difficult to judge mobility when the data has moved along a vector close to the ratio of $(m/C_i)_{protolith}$ because this ratio relies on a well-constrained protolith composition (Fig. 4.10), which can vary to a high degree in MORBs due to primary compositional variations (N- and E-MORB, for example, Figs 4.5 and 4.6).

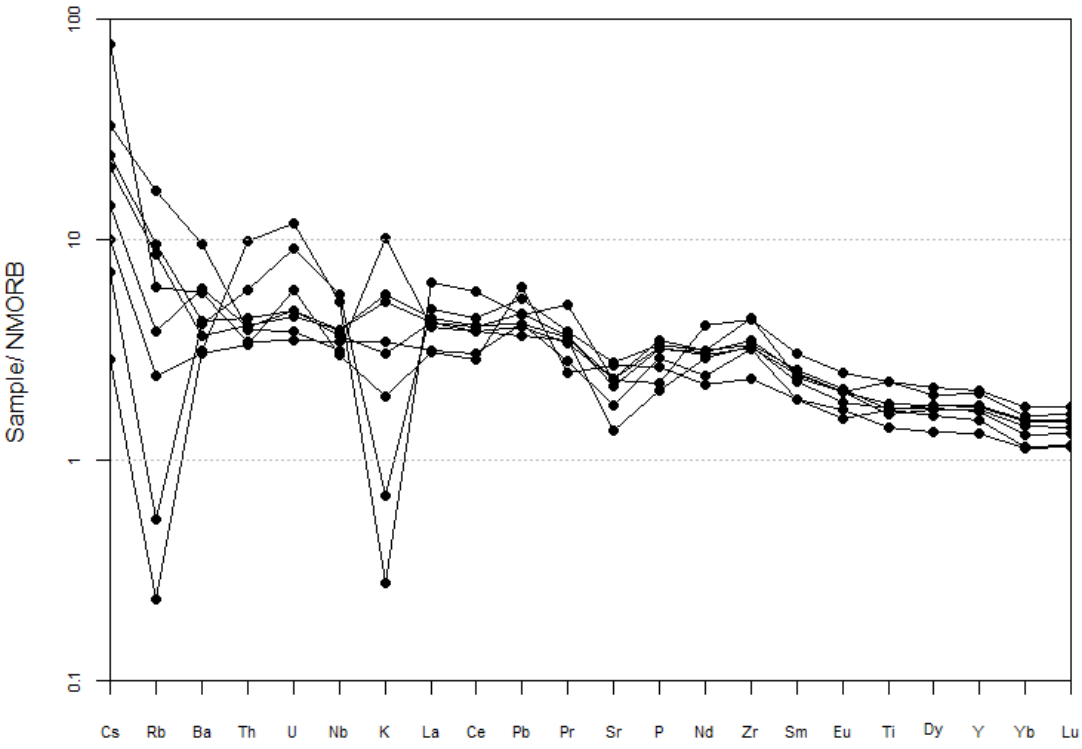

FIGURE 4.3: Trace element plot normalised to N-MORB (Sun and McDonough, 1989). Virtually all trace elements are enriched compared to N-MORB, a consequence of passive enrichment due to the loss of major elements. Data from Dale et al. (2007).

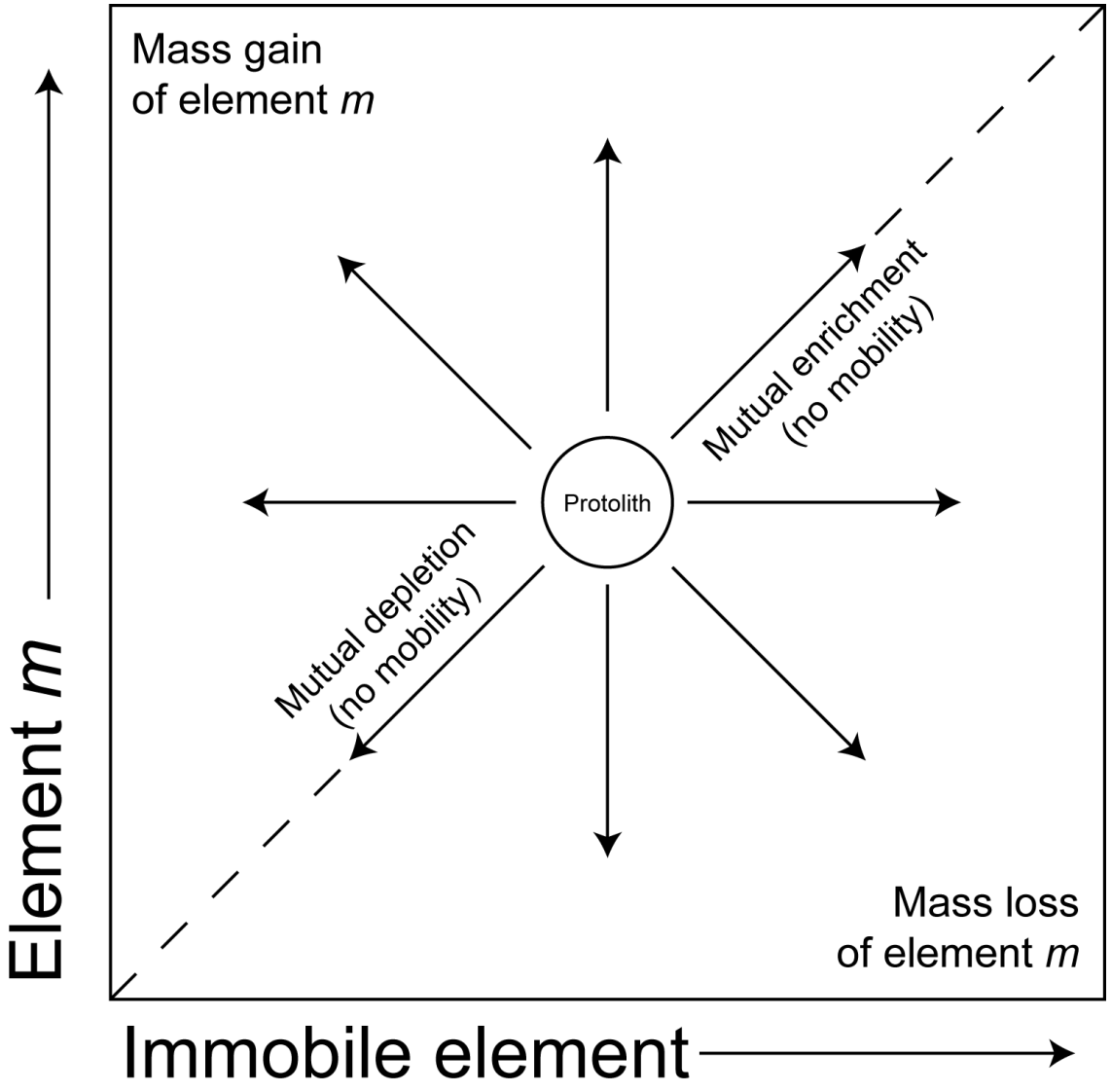

FIGURE 4.4: Graph of an immobile element, for example Zr, versus another element (m), with a hypothetical sample representing the protolith. During metamorphism the rock will experience relative loss of some elements and gain of others, whereas the immobile elements will move either left or right depending on whether the rock loses or gains mass overall. Diagonal trends (bottom left to top right) will result from the element m being equally as immobile as the immobile element chosen, where diagonal-up-right indicate the rock has lost mass overall and diagonal-down-left represent the rock has gained mass overall. Movement of the sample into the lower right half indicate the element m has been lost and is therefore mobile, whereas movement of the sample in to the upper left half indicate gain of element m from an external source, also indicating mobility. Vertical trends result from m being highly mobile, but are likely only if m has a comparable or lower concentration to the immobile element. For example, if m is a major oxide such as SiO_2, vertical trends are unlikely because loss or gain of that element will cause an overall mass loss or gain of the rock as a whole, which causes horizontal movement on the graph. With trace elements, vertical trends would indicate very high mobility compared to little overall mass gain in the rock. Diagonal (top left to bottom right) and horizontal trends are more likely.

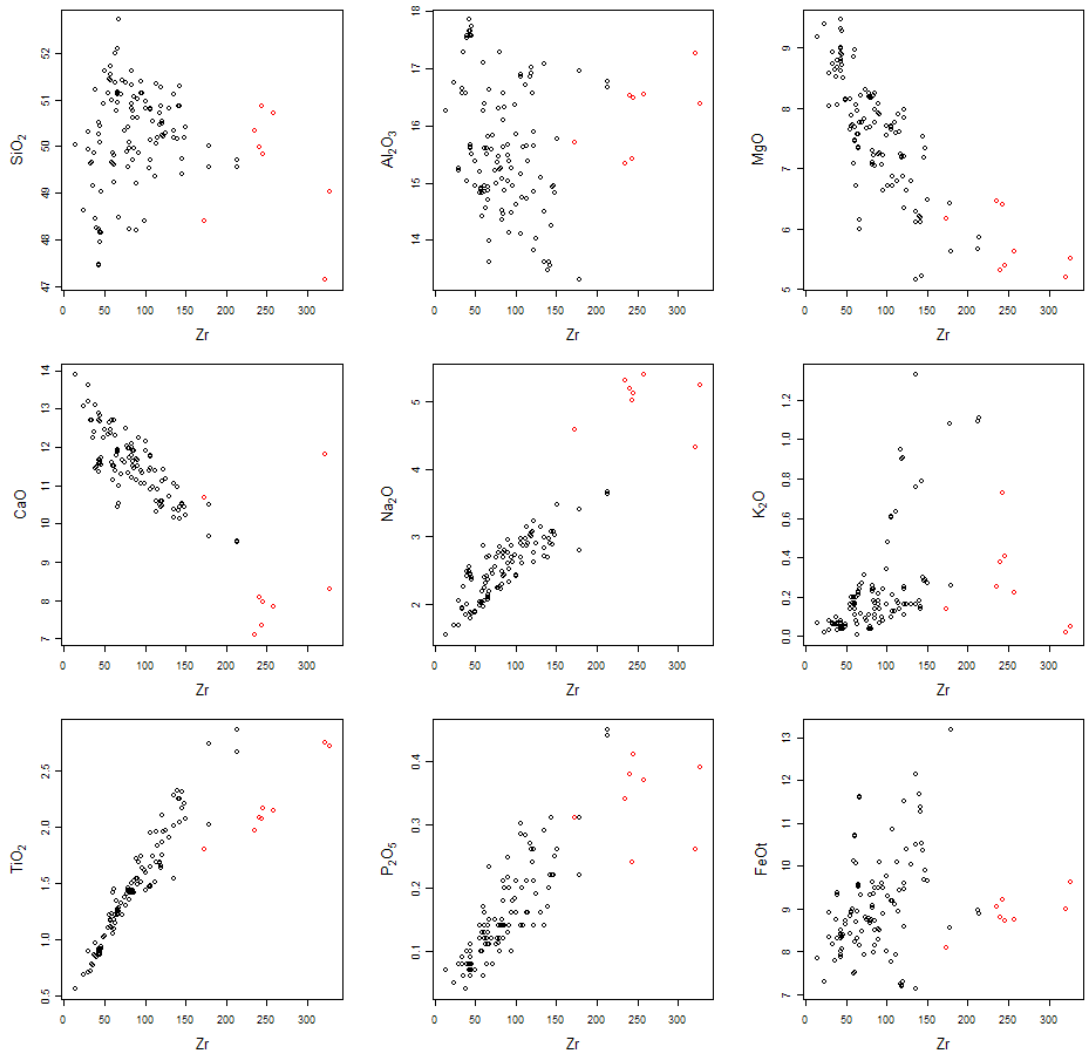

FIGURE 4.5: Major elements vs Zr. Since Zr is thought to be immobile, it can be used to gauge enrichments and depletion (and therefore mobility) of elements (Fig. 4.4). Some plots show evidence of loss (and therefore mobility). What is most apparent from these graphs is that the protolith composition of the basaltic eclogites was probably quite different to the MORB data displayed on these graphs. Zermatt basaltic eclogite data (Dale et al., 2007) in red and MORB data in (Jenner and O'Neill, 2012) in black. Major elements in wt% and Zr in ppm.

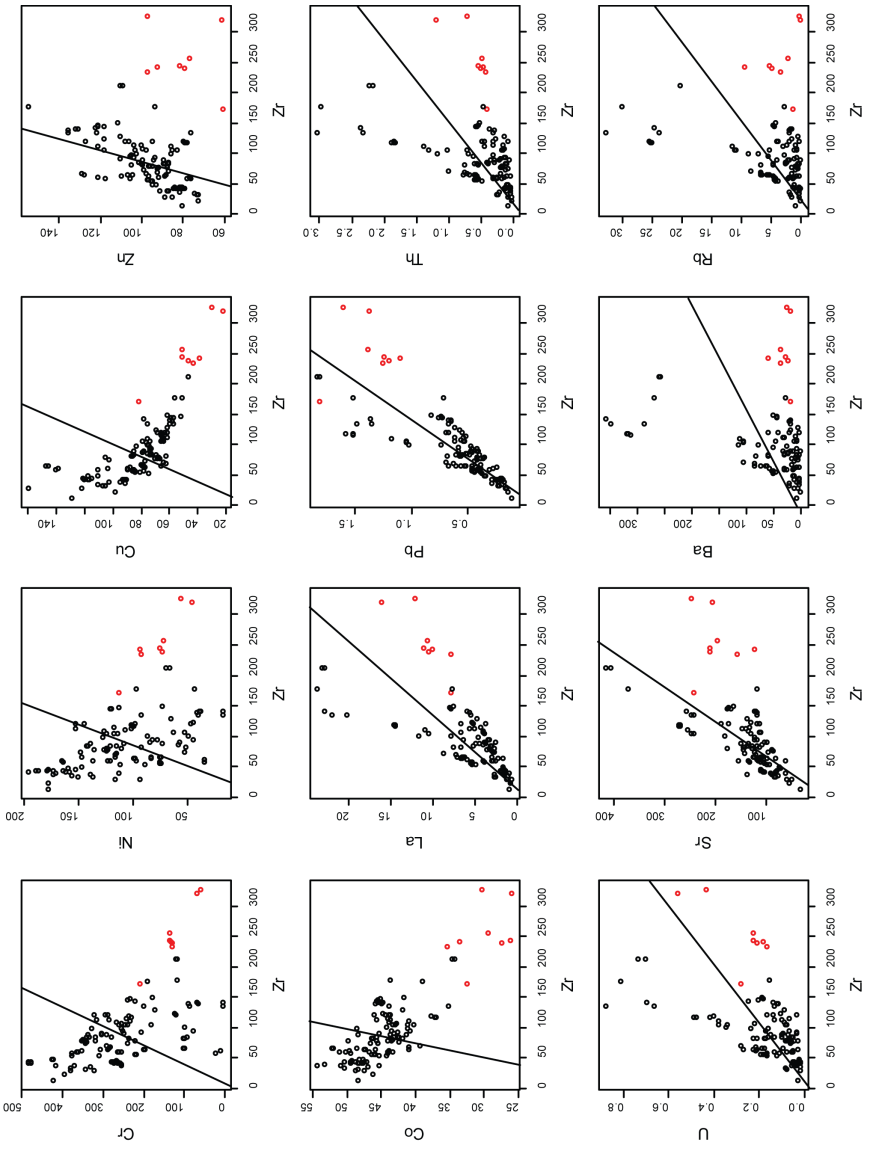

FIGURE 4.6: Selected trace elements vs Zr. Black lines represent the average ratio of element:Zr in the protolith. Many trace elements suggest mobility, including Cr, Ni, Cu, Zn, Co, Ba and Rb. Others show evidence of mutual enrichment to weak mobility, such as Pb, Th, U and Sr. Colours as Fig. 4.5, all elements shown in ppm.

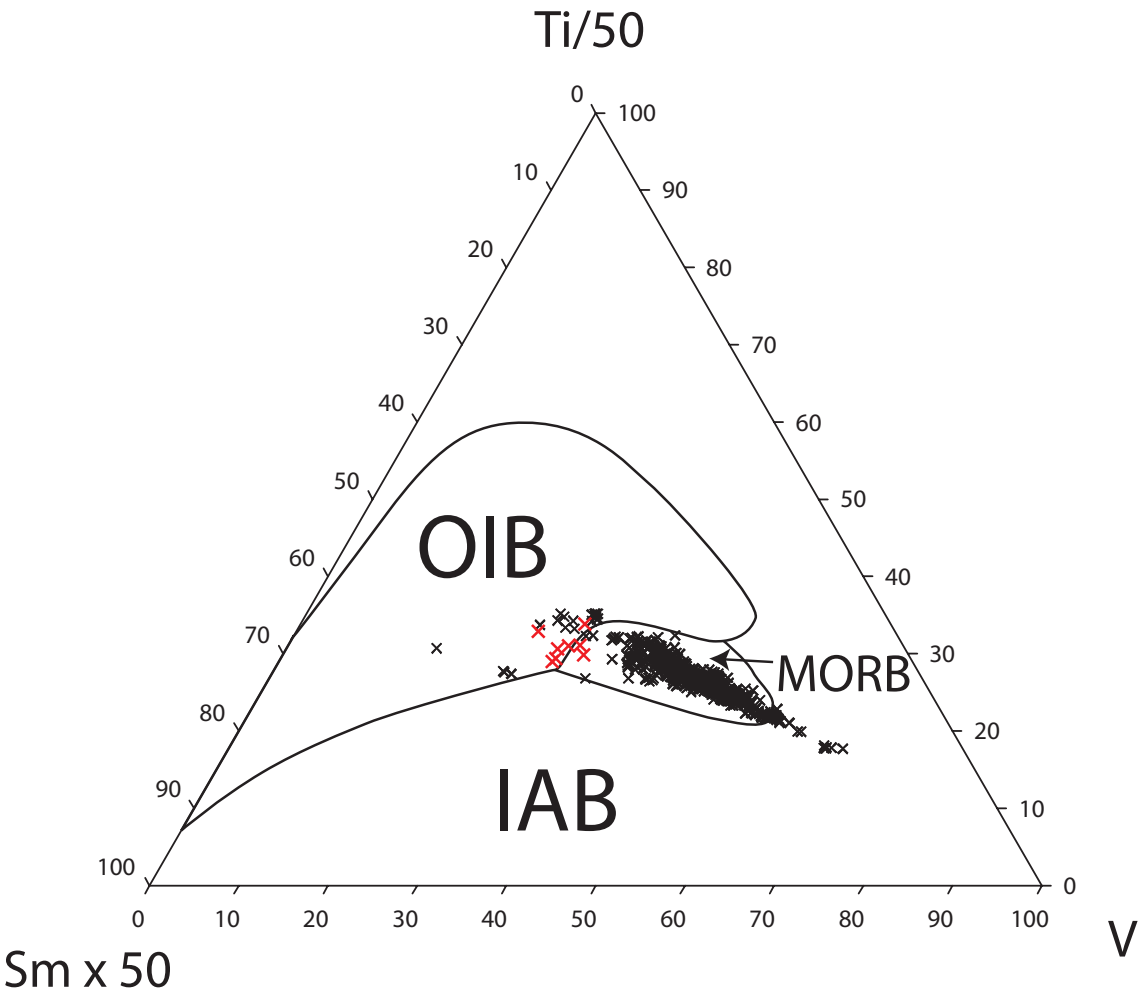

FIGURE 4.7: On an immobile element discrimination diagram, the Zermatt basaltic eclogites (red) plot on the edge of the MORB field and within the OIB field, whereas the vast majority of MORB data (Jenner and O'Neill, 2012) plot within the MORB field. A few plot in a similar, though not precisely the same, location as the Zermatt data, including basalts from the Bouvet Island median valley.

The isocon diagram is a way of representing the mobility of elements with respect to the composition of a protolith by assuming either one or more immobile elements, or a constant mass or constant volume of the rock (Grant, 1986). The concentration of all elements are plotted on a graph of C^O vs C^A, which are the concentration of an element in the protolith and the concentration of an element in the altered rock, respectively. A line, the isocon, is drawn through the origin which represents where an element would plot if it were immobile, and elements plotting above this line suggest element gain and below the line suggest element loss. The gradient of the isocon is dictated either by passing through an assumed immobile element or by the assumption of constant mass:

$$C^A = C^O \tag{4.1}$$

or constant volume:

$$C^A = (\rho^O/\rho^A)C^O \tag{4.2}$$

A suitable protolith should be chosen for C^O. The Zermatt-Saas basaltic eclogites have been recognised to be N- to E-MORB (Pfeifer et al., 1989). Lack of Nb, Ta and Zr anomalies has been demonstrated to support formation on a typical mid-ocean ridge rather than a supra-subduction environment (Dale et al., 2007). On immobile element discrimination diagrams plot (Vermeesch, 2006), the samples analysed here lie on the border between OIB and MORB or within the OIB field (Fig. 4.7). In comparison, this is a similar position occupied by basalts from Bouvet Island median valley, which is typified by E-MORB type basalt (Jenner and O'Neill, 2012). However, it's hard to assess the relevance of this similarity without knowing how immobile the elements used in these "immobile" element discrimination diagrams are under eclogite metamorphism, and thus whether the protolith would occupy a similar position on these plots. As well as a suitable protolith, an appropriate isocon should be selected. In previous studies Yb has been shown to be the least mobile element under eclogite metamorphism (Kessel et al., 2005) and has been used in assessing element mobility under eclogite metamorphism (Guo et al., 2009, 2012), and so an isocon drawn through Yb is used here. On isocon diagrams using basalts from a range of different tectonic settings including N- and E-MORB, similar mobility of elements is suggested and the type of basalt used as a protolith does not strongly affect which ones are shown to be mobile, only the degree to which they have been lost or gained (Fig. 4.8). The evidence of mobility is strongest for SiO_2, Al_2O_3, Fe_2O_3, MnO, MgO and CaO, with the graphs generally suggesting a depletion in those elements. TiO_2 appears to be relatively immobile or slightly mobile (lost), and Na_2O, K_2O and P_2O_5 showing inconclusive mobility. The mobilities are estimated using:

$$(\Delta C_i/C_i) = (C^O_{Yb}/C^A_{Yb})(C^A_i/C^O_i) - 1 \tag{4.3}$$

(Grant, 1986), where C^A_i and C^O_i are the concentration of an element i in the altered rock and protolith, respectively (Table 4.1).

Trace elements can be dealt with in a similar fashion (Fig. 4.9). In comparison to the Bouvet Island median valley basalts, the Zermatt basaltic eclogites show mobility of virtually all the selected trace elements. However, in comparison to a theoretical average

TABLE 4.1: Relative gains and losses of major elements with respect to 4 different protolith compositions (see Fig. 4.8).

Element Oxide	EPR NMORB	Mid-Cayman Rise	Bouvet Island	Mid-Atlantic E-MORB	Interpretation
SiO_2	-0.3	-0.31	-0.3	-0.32	Lost
TiO_2	0.09	-0.07	-0.37	-0.12	Immobile
Al_2O_3	-0.27	-0.29	-0.24	-0.25	Lost
Fe_2O_3	-0.26	-0.19	-0.33	-0.26	Lost
MnO	-0.24	-0.28	0.05	-0.24	Lost
MgO	-0.46	-0.44	-0.37	-0.45	Lost
CaO	-0.41	-0.41	-0.39	-0.42	Lost
Na_2O	0.29	0	0.19	0.16	Gained
K_2O	0.35	-0.27	-0.74	-0.67	Inconclusive
P_2O_5	0.87	0.1	-0.25	-0.07	Inconclusive

TABLE 4.2: Relative gains and losses of trace elements with respect to 2 different protolith compositions (see Fig. 4.9).

Element	Bouvet Island	Average MORB	Interpretation
Cr	-0.62	-0.75	Lost
Ni	-0.35	-0.73	Lost
Cu	-0.31	-0.56	Lost
Zn	-0.53	-0.27	Lost
Co	-0.48	-0.62	Lost
La	-0.54	1.04	Inconclusive
Pb	-0.28	0.48	Inconclusive
Th	-0.74	0.02	Inconclusive
Rb	-0.85	0.42	Inconclusive
Sr	-0.47	0.10	Inconclusive
Ba	-0.93	-0.68	Lost
U	-0.58	0.55	Inconclusive

MORB (Arevalo and McDonough, 2010), fewer of the elements demonstrate loss, with La, Pb, Rb and U showing significant enrichment over the protolith composition. Cr, Ni, Cu, Zn, Co and Ba show significant loss in both cases (Table 4.2).

Using the correct protolith composition is crucial to estimating mobility, however, as in the case of the Zermatt basaltic eclogites, this cannot be known for certain. To counter the need for exact compositional information, ratios of immobile elements, which restrict geochemical variations, are used, such as m/Yb vs Nb/Yb (Fig. 4.10). MORB usually forms a narrow array on such a plot with more enriched compositions (E-MORB) plotting to the right and more depleted compositions plotting to the left. Deviation from this track

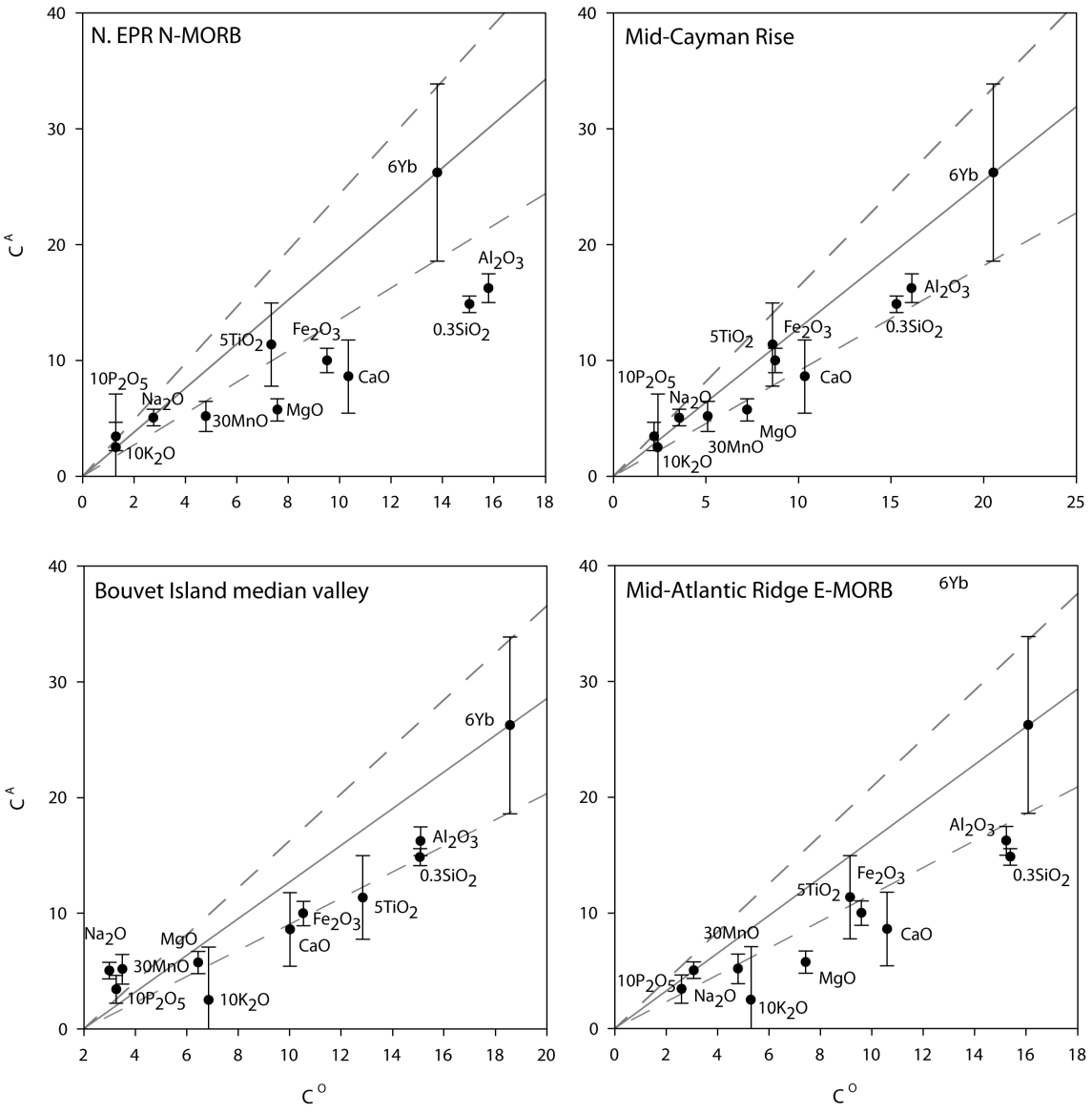

FIGURE 4.8: Isocon diagram for major elements, using 4 different protolith basalts. The Bouvet Island median valley basalts are the most chemically similar. C^A data is the mean average of Zermatt basaltic eclogite samples, with the error bars representing 2σ error. The isocon is drawn through the centre of the Yb range, with dashed lines representing the 2σ error on the Yb value. Yb is used since it has been shown to be the least mobile element under eclogite metamorphism. Units are wt% for major elements and ppm for Yb.

is then interpreted to indicate mobility. Such a plot should be interpreted with care since differences in the mobility of the element pairs will effect the position of data.

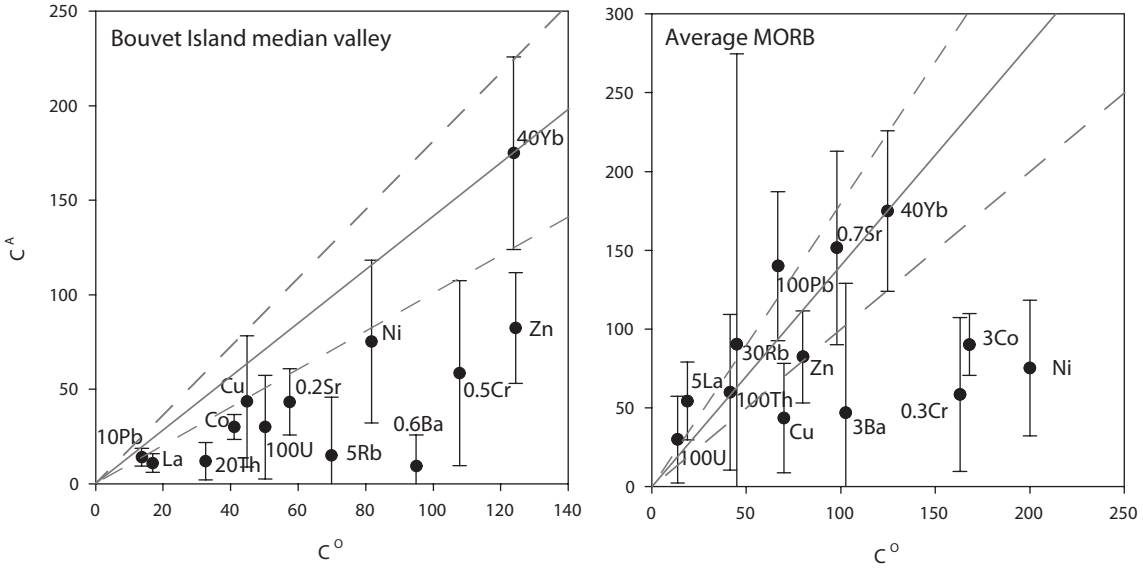

FIGURE 4.9: Isocon diagram for selected trace elements, using two different protolith materials. Bouvet Island median valley basalts are chemically similar. Average MORB data is from Arevalo and McDonough (2010). C^A data is the mean average of Zermatt basaltic eclogite samples, with the error bars representing 2σ error. The isocon is drawn through the centre of the Yb range, with dashed lines representing the 2σ error on the Yb value. Yb is used since it has been shown to be the least mobile element under eclogite metamorphism. Units are ppm.

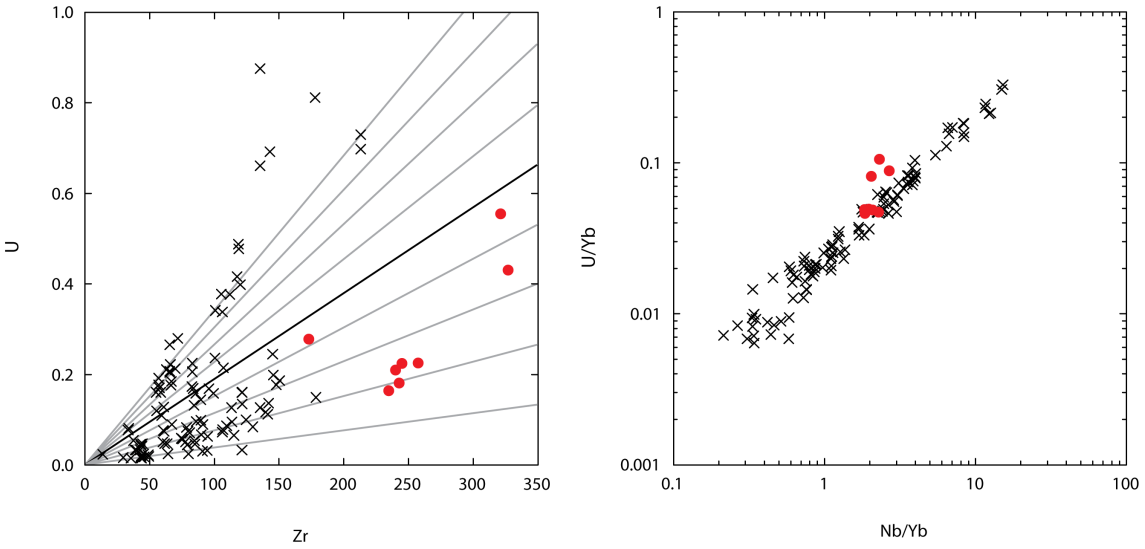

FIGURE 4.10: Left: U vs Zr. If Zr is immobile, deviation from movement along the protolith ratio line (black line) is interpreted to indicate mobile behaviour. However, the concentration of U in MORB is variable (black crosses) and so the gradient of the protolith ratio line is also variable (grey lines represent 20% increments around the mean average of U protolith concentration). Variation in Zr concentration complicates the issue even further. Right: To counter this problem, concentration of the element in question can be normalised to another supposedly immobile element, such as Yb and plotted against an immobile element ratio sensitive to parent melt composition, such as Nb/Yb. The MORB data then plot in a tight diagonal array and deviation from the array is interpreted to indicate mobility. Here, five U data lie within the MORB array indicating they are not mobile, whilst three data suggest gain of U. However, this could be due to imperfect immobility in Zr, Yb or Nb. Zermatt basaltic eclogite data (Dale et al., 2007) in red and MORB data in (Jenner and O'Neill, 2012) in black.

4.5 Au in oceanic crust

The Au composition of oceanic crust varies between 0.06 and 5.79 ppb, with a log-normal average of 0.95 ppb and standard deviation of 1.2 (Table 1.1). There exists 146 values for the concentration of Au in oceanic crust with accompanying Zr concentration. The ratio Au_{ppb}/Zr_{ppm} is highly skewed to the left and so a log-normal distribution is used to described it. The log-normal mean is 0.014 with a standard deviation σ_{log} of 0.49, equivalent to approximately an order of magnitude variation in the un-logged data (Fig. 4.11). Comparison is also made with platinum group elements (PGEs), especially Re, Pt and Pd, as they have been shown to be mobile in these samples (Dale et al., 2009).

4.6 Method

4.6.1 Samples

Sample location and collection methodology is described in Dale et al. (2007), and supporting data is presented in Dale et al. (2007, 2009). Basaltic eclogite samples were collected from the Pfulwe area of the Zermatt-Saas ophiolite (Fig. 4.1). They are composed of a metamorphic assemblage of garnet, omphacite, zoisite, glaucophane, phengite ± paragonite (Fig. 4.12)

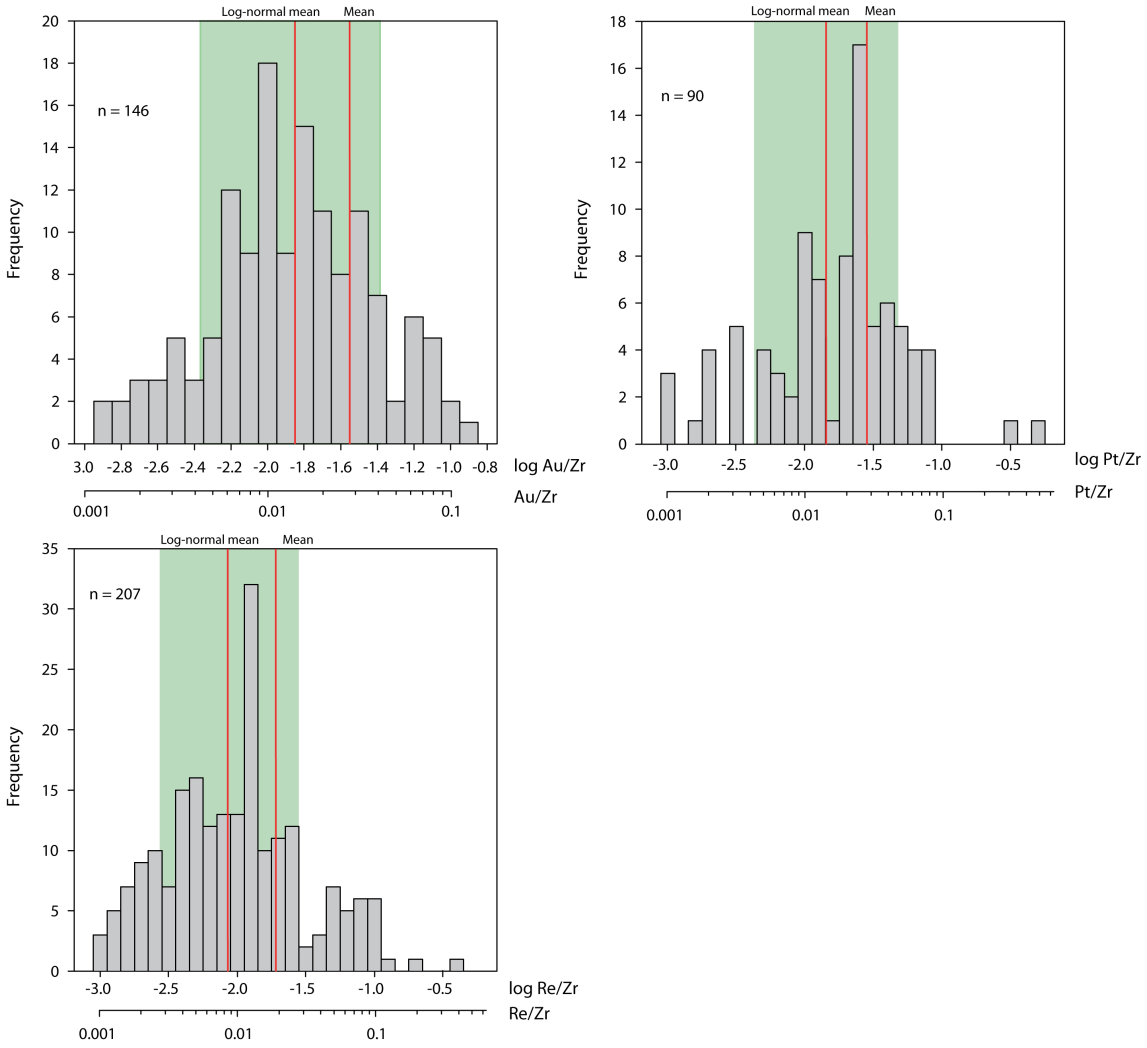

FIGURE 4.11: Histograms show the variation and distribution of log Au/Zr, log Re/Zr and log Pt/Zr. Log-normal means describe the data better than the arithmetic mean, whilst the standard deviation of logged data (shaded area) describe a variation of approximately 1 order of magnitude in the un-logged data. Data for Au from Tatsumi et al. (1999); Miller and C. (2002); Jenner and O'Neill (2012), Re data is from Keller et al. (2008); Jenner and O'Neill (2012) and Pt data from Jenner and O'Neill (2012).

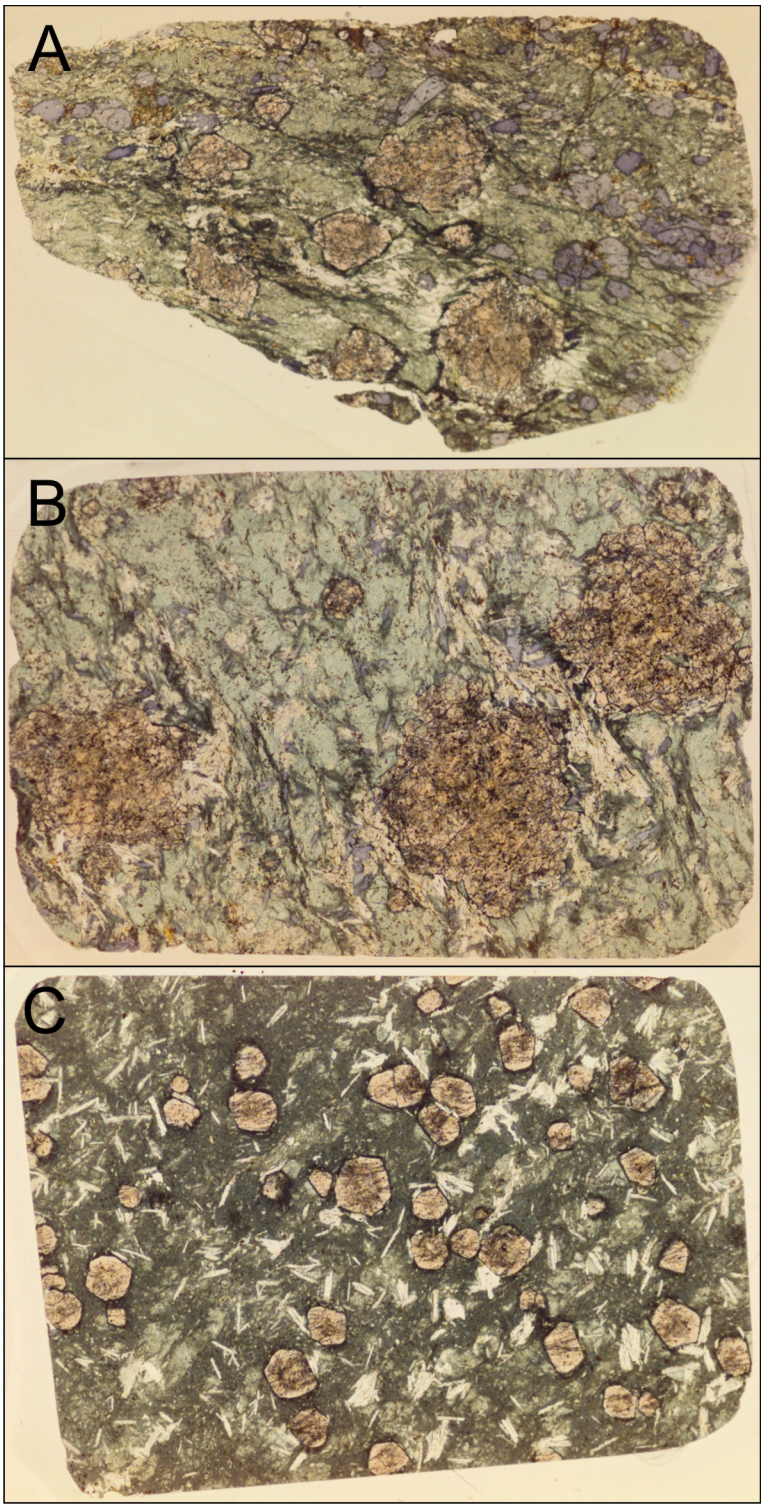

FIGURE 4.12: Zermatt basaltic eclogite thin sections. A: Sample S02 41v, B: Sample S02 41ii, Sample S02 75iiC.

TABLE 4.3: Results of Au analysis of Zermatt-Saas basaltic eclogites

Sample	Au ppb	%RSD	±
Blank	0.009	0.00	
S02/41ii	0.94	0.02	0.05
S02/41v	0.64	0.01	0.03
S02/74ii	0.78	0.01	0.04
S02/75iC	0.71	0.01	0.04
S02/75iiR	0.78	0.03	0.04
S02/75iiiC	0.65	0.02	0.03
S02/75iiiR	0.62	0.01	0.03
S02/75ivC	0.43	0.01	0.02

4.6.2 Analysis

Au analyses were carried out at the National Oceanography Centre, University of Southampton, UK. 4g of homogenised rock powder was digested in 60mL Teflon pots using a HF-HCLO4 mix as described by Yokoyama et al. (1999) to prevent insoluble fluoride formation. The samples were then dissolved in conc. HCl, dried down and re-dissolved in aqua-regia, ready for Au separation. This process uses solid-phase extraction columns and is detailed in Pitcairn et al. (2006b). Samples were run on a Thermo X-Series ICP-MS using external standards calibration. Repeated analysis of a basaltic amphibolite yielded a reproducibility of 20%, whilst comparison with synthetic standards produced an accuracy of ± 3%. It is likely that natural variation within the sample (the nugget affect) is responsible for a large part of the error, although this is mitigated as much as possible by homogenization of the powder.

4.7 Results

Results (Table 4.3) are between 0.43 ± 0.04 and 0.94 ± 0.09 ppb Au, mean average 0.68 ppb. On an immobile element plot, Au sits towards the low edge of the MORB array, perhaps indicating some mobility may have occurred, though the result is far from definitive (Fig. 4.13). However, the data form a sub-horizontal trend on Au vs Zr indicating immobility and loss of Au has occurred (Fig. 4.14). This is confirmed by positive correlation of Au/Zr vs Re/Zr, which indicate samples which show higher Re mobility also show higher Au mobility. In comparison to the PGEs, Au appears to be slightly less mobile than Re whereas Pt and Pd are both more mobile (Fig. 4.15). Comparison with Cu is useful due to the association between Cu and Au in arc mineralisation; Cu is shown to behave very similarly to Au.

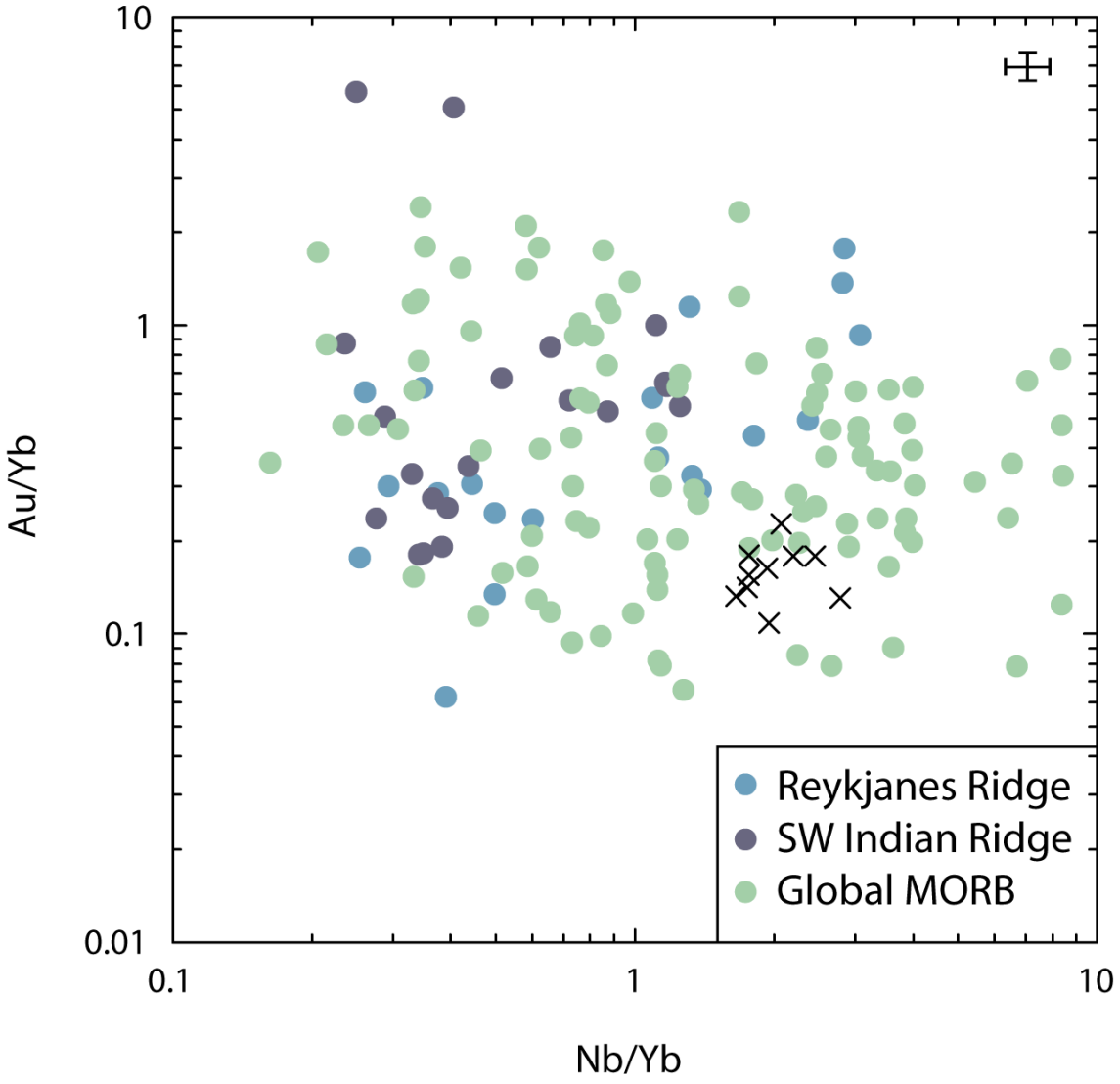

FIGURE 4.13: Au/Yb vs Nb/Yb. Zermatt-Saas eclogites (crosses) sit towards the lower edge of the main MORB array. Reykjanes Ridge data from Chapter 3, SW Indian Ridge data from Miller and Kelley (2004), global MORB data from Jenner et al. (2010). A representative error bar is shown in the top right.

4.7.1 Mass balance

The amount of Au depletion in the samples can be estimated using mass balance equations such as:

$$\tau_i^j = \left[\frac{FinalMass_j - InitialMass_j}{InitialMass_j}\right] = \left[\left(\frac{C_i^0}{C_i'}\right)\left(\frac{C_j^0}{C_j'}\right) - 1\right] \tag{4.4}$$

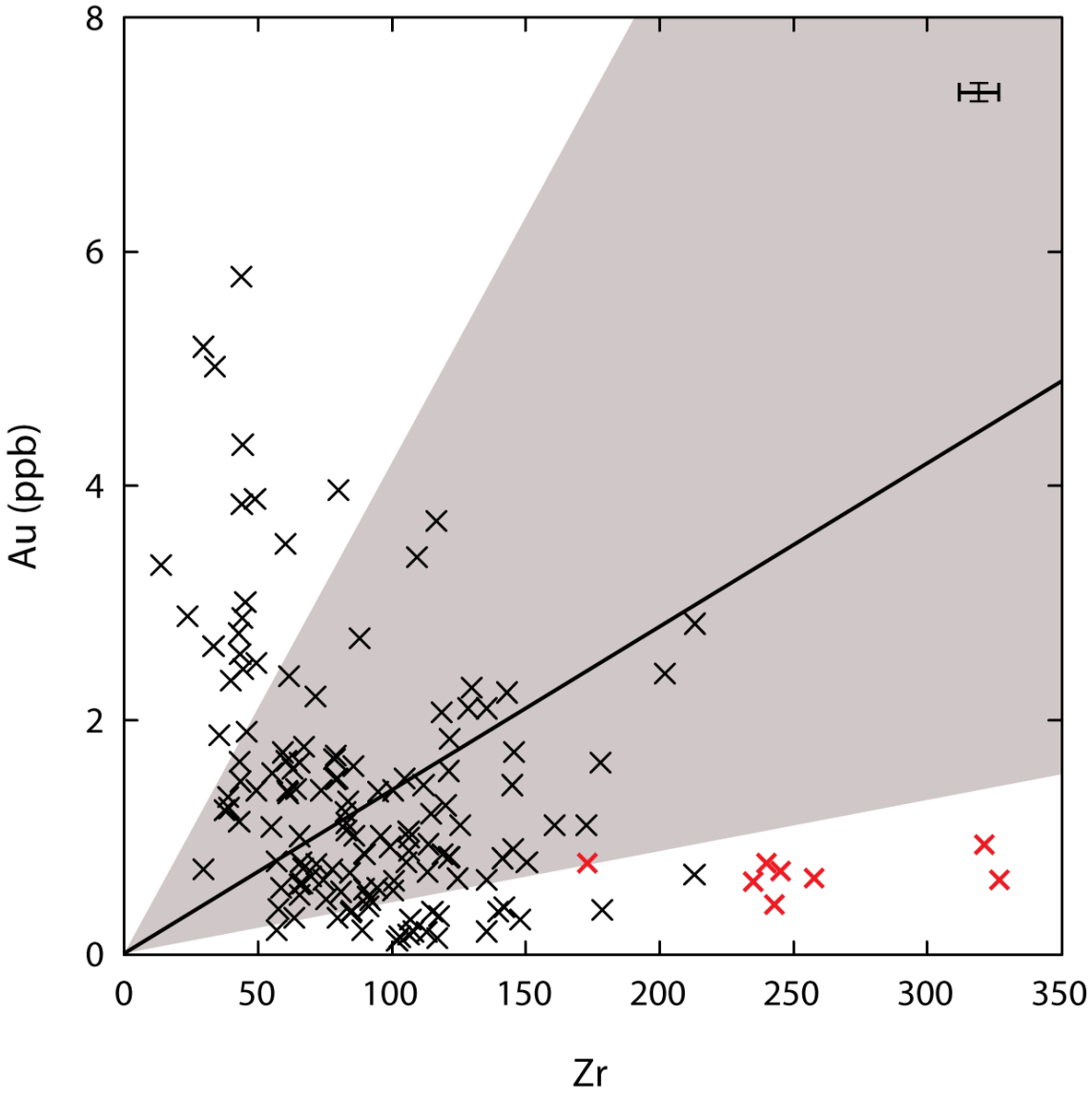

FIGURE 4.14: Au vs Zr. Black crosses are MORB, red crosses are Zermatt-Saas basaltic eclogites, the black line represents the average protolith ratio Au:Zr drawn through the log-normal mean average Zr/Au and the red envelope represents 1 standard deviation of the log-normal mean of Au data. Data follow a mobile element trend to the right. The trend is sub-horizontal, meaning it is unlikely to be caused by protolith composition. A representative error bar is shown in the top right. Data for MORB from Jenner and O'Neill (2012); Miller and Kelley (2004); Tatsumi et al. (1999), Zr data from Dale et al. (2007).

where τ_i^j is the proportional change of j using the reference species i, C_i^0 and C_j^0 are the concentration of i and j in the protolith, respectively, and C_i' and C_j' are the concentration of i and j in the altered rock, respectively (Ague, 1994). Negative and positive values of τ_i^j correspond to loss and lass gain, respectively. In ultra-high pressure facies, Yb is thought to be the most immobile element (Guo et al., 2012) and so it is the preferred element used in calculations. Using the average MORB Au and Yb concentration and the

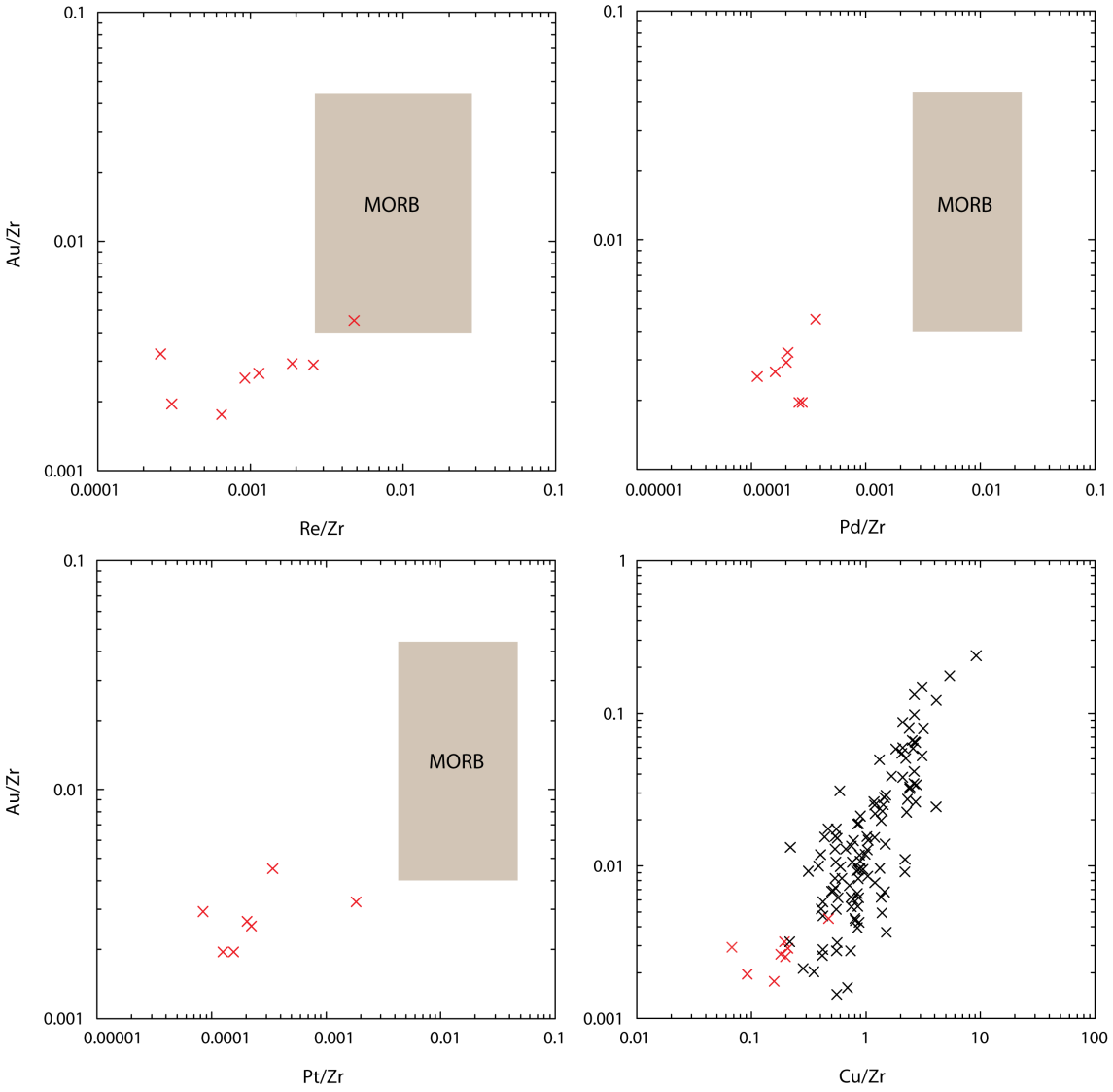

FIGURE 4.15: Au/Zr vs Re/Zr, Pt/Zr, Pd/Zr and Cu/Zr. All but one sample sits below the MORB array when normalised to Zr, which should be immobile. In comparison to mobile PGEs Re, Pt and Pd, Au behaves most similarly to Re whereas Pt and Pd are more mobile. Cu is more mobile than Au. Au/Zr, Pt/Zr and Re/Zr MORB arrays are defined by published data, see Fig. 4.11. Pd/Zr, Re/Zr and Pt/Zr arrays are formed by taking the published average Pd, Pt, Re and Zr concentrations of MORB (Arevalo and McDonough, 2010) and assuming 50% error on both values. Error bars on these plots would be within the size of the symbols.

average Zermatt basaltic eclogite Au and Yb yields a τ_i^j of -50.9, corresponding to a 51% loss of Au. In comparison, Cu has a τ_i^j of -58.9, showing it may be slightly more mobile than Au under the same conditions (see Table 4.4 for values used). The mass-balance equations also predict high mobility of the PGEs (Table 4.4), with the order of mobility being Pd>Ir>Pt>Re>Ru. Os shows significant gain of 78%. The total mass transfer of the rock as a whole can be calculated using:

TABLE 4.4: Values used and results of mass balance calculation, using three different "immobile" elements. Average Zr, Yb, Nb, Cu and PGEs from Arevalo and McDonough (2010), altered Cu, Zr, Yb, Nb and PGE values are mean averages from Dale et al. (2007) and Au protolith average from Chapter 1.

	Zr	Yb	Nb	Au	Cu	Ir	Ru	Pt	Pd	Re	Os
C_i^0	90	3	3.4	0.95	70	0.041	0.041	0.45	0.69	0.83	0.003
C_i'	260	4.37	9.43	0.68	41.90	0.01	0.03	0.09	0.05	0.32	0.01
τ_i^j Zr				-75.2	-79.3	-93.9	-77.9	-92.9	-97.3	-86.8	-10.4
τ_i^j Yb				-50.9	-58.9	-87.9	-56.1	-86.0	-94.6	-73.7	77.7
τ_i^j Nb				-74.2	-78.4	-93.6	-76.9	-92.7	-97.2	-86.2	-6.6
T_i	-65.38	-31.36	-63.93								

$$T_i = \left[\frac{FinalMass - InitialMass}{InitialMass}\right] = \left[\left(\frac{C_i^0}{C_i'}\right) - 1\right] \tag{4.5}$$

where T_i gives proportional change in total rock mass, negative and positive values indicating mass loss and gain, respectively (e.g. Ague 1994). Zr and Nb both indicate approximately 65% mass loss and Yb gives a more conservative 31% mass loss. The fact that Zr and Nb indicate higher mobility of both the total mass loss and trace elements suggest they have seen an overall mass gain.

The weakness in these calculations is assuming the protolith concentrations is comparable to average MORB. Table 4.5 gives values for τ_i^j assuming 50% error in the protolith concentrations of Yb, Cu and Au. For both Cu and Au, gain is only achieved when both the Yb concentration is 50% higher than expected and the Au and Cu concentrations are 50% lower than expected.

4.8 Discussion

These results show that basaltic eclogites subducted to 75 km depth contain ~50% less Au than their protolith basalts would have contained. Stable isotope data conducted on samples from the same area suggest these basalts were not significantly altered by seafloor hydrothermal circulation (Barnicoat and Cartwright, 1995), and so it is likely that Au depletion occurred during subduction metamorphism. The impact that such a Au-carrying fluid would have on the arc system depends on the depth at which the fluid was released and the fluid pathway post-release. The depth at which the Zermatt-Saas ophiolite is thought to have reached during subduction, 75km, is significant because it is thought to be approximately the shallowest depth to the slab beneath modern arcs (England and

TABLE 4.5: Values of τ_i^j assuming 50% error in the protolith Au, Cu and Yb concentrations. Only when Yb is 50% higher than expected and Cu and Au are 50% lower than expected do τ_i^j show mass gains.

		Au		
		-50%	Average	50%
	-50%	-50.9	-75.4	-83.6
Yb	Average	-1.7	-50.9	-67.2
	50%	47.4	-26.3	-50.9

		Cu		
		-50%	Average	50%
	-50%	-58.9	-79.5	-86.3
Yb	Average	-17.8	-58.9	-72.6
	50%	23.2	-38.4	-58.9

Katz, 2010). Consequently, the Zermatt-Saas ophiolite may be an analogue for a modern slab which is currently producing fluid, melting the mantle wedge and producing a volcanic arc. It is therefore possible that metal-bearing fluids released from a similar slab could go on to partially melt the mantle wedge and therefore supply metals including Au and other well-known fluid-mobile elements to the arc system. Earlier release of the fluid, perhaps during blueschist facies metamorphism is unlikely since blueschists generally have a higher water content than the precursor hydrated basalts (Peacock, 1993). The transition from blueschist to eclogite facies has been shown to release a large proportion of water, especially when crossing the low-T eclogite facies boundary (Peacock, 1990, 1993) as is the case for the Zermatt-Saas ophiolite (Barnicoat and Cartwright, 1995; Angiboust et al., 2009) which is thought to have released 0.25-2.5 wt% water. Additionally, dehydration of the associated serpentinites at the maximum subduction depth (return point) by the breakdown of antigorite may have been the mechanism for slab fragment detachment and exhumation (Bucher et al., 2005). The flushing of such a fluid through the slab could be responsible for metal loss.

An inherent limitation of such ultra-high pressure rocks is that they only enable us to see a specific depth into the system. Had the slab been allowed to continue to subduct, it is likely that further stages of fluid release would have occurred. The release of highly oxidising fluids at pressures and temperatures greater than that displayed by the Zermatt-Saas ophiolite is invoked as an important means of releasing Au from the mantle wedge (e.g. Mungall 2002). Such a fluid may also carry metals itself, further reducing the metal content of the slab. In this way, our estimate of Au depletion may be low if the entire depth of the subduction system is considered.

TABLE 4.6: Parameters used in modelling subduction and the flux of Au from the slab, the concentration of Au in slab fluids and the addition of Au to partial melts.

Parameter	Value
Angle of subduction	30°
Basalt thickness	2000 m
Subduction velocity	0.05 m/yr
Gold conc. of slab	0.95 and 4 ppb
Density of basalt	3000 kg/m^3
Loss into the wedge	50%
Depth of subduction	75 km
Density of mantle	3300 kg/m^3
Initial Au concentration of mantle wedge	1 ppb
Water loss from the slab	0.5 to 2.5 wt%
Water content of partial melt	3 to 5 wt%

4.9 Modelling Au loss over time

These new data indicate that Au could be added to the arc system by fluids released from the subducting slab. This indicates that over geological time scales, the concentration of Au in the subducted material may affect the bulk concentration of Au in the mantle wedge and therefore the arc system. A simple model has been constructed whereby this effect can be assessed. We use typical subduction zone parameters of 30° subduction, 5 cm/yr convergence, 2 km of basaltic material, and typical densities of the materials involved (Fig. 4.16 and Table 4.6 for parameters, further details in Appendix A). The mantle wedge is thus defined as a right-angled triangle with depth of 75 km and an angle of 30°. However, the mantle wedge does not occupy all of this volume, and so we assume 50% is occupied by the over-riding plate crust based on current subduction and mantle wedge corner flow models (e.g. Grove et al. 2006, Fig. 4.16). The loss of Au to the mantle wedge from the slab is estimated at 50%, as shown above. We find that if the oceanic crust contains 0.95 ppb Au then 1425 kg of Au is added to the mantle wedge for every metre of the arc every 10 Myr. However, if the subducted material has a Au concentration of 4 ppb, for example during subduction of plume-enriched crust (see Chapter 3), then 6000 kg of Au is added.

To put this into perspective, the average mantle wedge Au concentration would increase from 1 ppb to 1.5 ppb in the case of 1 ppb Au subducted slab, and from 1 ppb to 3.2 ppb Au in the case of a 4 ppb subducted slab. However, this process clearly does not operate indefinitely because the wedge experiences corner flow and recycling back into the mantle, and whilst this happens a proportion of melt is removed from it. Estimates of the proportion of the melt removed from the wedge are 2.5-15 wt% (e.g. Grove et al. 2006). If detailed parameters about the rate of flow of the wedge, oxygen fugacity and S content

of the wedge were known, it might be possible to estimate the Au concentration of the melts based on the amount of Au that has been lost from the slab. However, it is simpler to examine the Au concentration of the fluids which cause the flux-melting of the mantle. The Zermatt-Saas eclogites have lost 0.5-2.5 wt% water (Barnicoat and Cartwright, 1995). If this is taken as the amount of water lost to the mantle wedge in the same event that mobilises the Au, those fluids would contain 38-190 ppb Au based on 50% Au-loss from the downgoing slab. Mantle wedge partial melts contain 3-5 wt% H_2O (Grove et al., 2006). At these rates, the melts could contain between 1.14 to 9.5 ppb Au contribution from a subducted slab with a 0.95 ppb Au concentration. However, if the slab contains 4 ppb Au, these values increase to 4.8 to 40 ppb Au contribution.

As the melt migrates through the wedge, these values will be modified by the presence of an immiscible sulfide melt if one forms, a proportion of which could remain in the mantle (Mungall, 2002), and by crustal melt evolution processes such as magnetite crystallisation (Chapter 5) and sulfide saturation (Wyborn and Sun, 1994). Consequently, the concentration of Au in melts erupted at the surface represent an integrated result of all these different processes. Since $D_{Au}^{sulphide-melt/silicate-melt}$ is 10,000-13,000 (Peach et al., 1990), dissolving the sulphide melt into the silicate melt is thought to be a crucial control on the Au concentration of the resulting melt (Mungall, 2002). But such a view ignores the fact that the primary melt Au concentration could be variable, as shown here. Modelling of a sulfide-saturated melt in the upper mantle (see Chapter 3) shows that increasing the Au concentration of the mantle in turn increases the Au concentration of the melt across all feasible partial melt proportions, even when the proportion of sulphides is high. The above subduction model is simplistic, however the numbers serve to illustrate that the concentration of Au in the subducted slab potentially represents a very important contribution to the Au budget of arc melts and may explain the higher Au concentrations seen in arc magmas on average compared to MORB (see Chapter 1). Since the flux of Au from the subducted slab to the mantle wedge may significantly affect the concentration of Au in arc magmas, the concentration of Au in the subducted slab may in turn impart a significant control on the occurrence of Au mineralisation in the over-riding plate.

The model could be explored further using more advanced statistical and computational techniques such as Monte Carlo simulation, where uncertainty in variables is explored with random changes and repeated simulation. There are several parameters in the model which are not known with much certainty. By estimating how well the variables are known, a Monte-Carlo simulation could identify which variables are the most important and which need to be better understood to constrain the model.

4.10 Conclusions

The data presented here suggest that the Zermatt-Saas basaltic eclogites have likely lost some proportion of their original Au content, together with a similar or slightly larger proportion of their copper content. If it can be assumed that this Au is lost to the mantle wedge by metasomitic fluids, causing flux-melting of the wedge and the generation of basaltic arc magmas, these fluids will contribute a potentially significant proportion of Au to arc magmas.

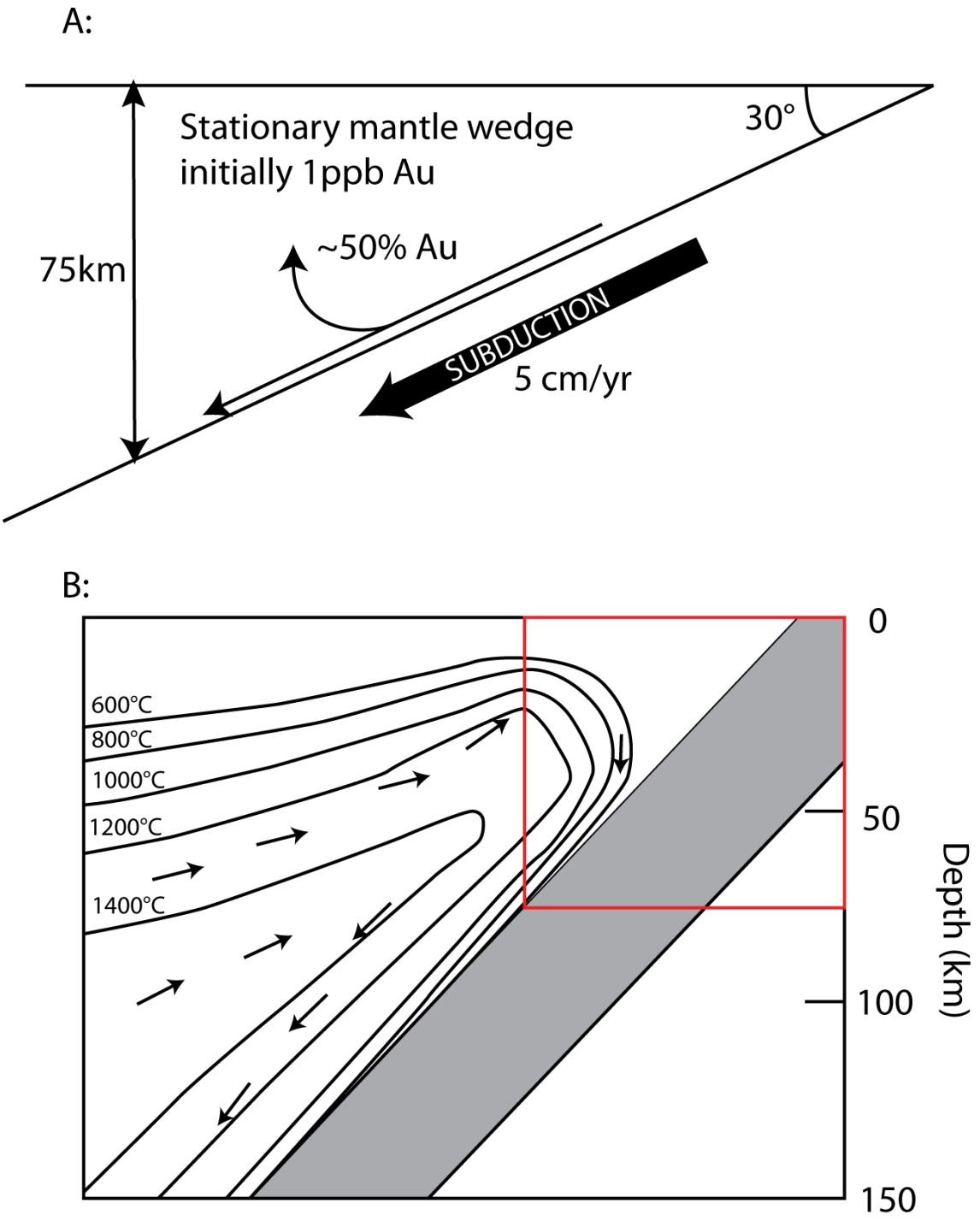

FIGURE 4.16: A: Model parameters used in constraining flux of Au from the slab. B: Diagram of mantle wedge corner flow demonstrating how the wedge only occupies ~50% of the region covered in (A). Figure adapted from Grove et al. (2006)

Chapter 5

The behaviour of Au in the Konya volcanic complex

5.1 Introduction

Arc-related epithermal Au and porphyry Cu-Au deposits account for 17% of the world's historic Au production and 23% in the last 26 years (Frimmel, 2008). In understanding these deposit types, emphasis has been placed on the exsolution of a sulphurous, high temperature (T>200°C), focussed, saline fluid from a magma which is able to transport Au, commonly in the complexes (from low to high pH) AuHS(aq), $Au(HS)^-$, AuOH(aq) and $AuCl_2^-$ (Stefansson and Seward, 2004), by reactions such as

$$Au(s) + H_2S(aq) = AuHS(aq) + 0.5H_2(g) \tag{5.1}$$

and

$$Au(s) + H_2S(aq) + HS^- = Au(HS)_2^- + 0.5H_2(g) \tag{5.2}$$

Clearly these reactions cannot occur unless Au is readily available to the scavenging hydrothermal fluid. Various studies have shown that there are sufficient metals in normal parent magmas or host rocks to create economic deposits (e.g. Cline and Bodnar 1991), and in these cases the lack of associated mineral deposits can be attributed to low efficiency in other parameters of the hydrothermal system such as ligand availability, water content of the parent magma, focussing of the hydrothermal fluid and precipitation of

metals in a confined zone of mineralisation. However, studies on the behaviour of Au in parent magmas have shown that the concentration of Au might be reduced by magnetite precipitation and settling (Togashi and Terashima, 1997; Bird et al., 1991) and as such the concentration of Au in a parent magma cannot be ignored as an important parameter of the mineralising system.

This work shows that magnetite crystallisation in the Konya Volcanic Complex (KVC) reduces the concentration of Au in lavas and lava domes by ~90%. Despite this severe reduction in magmatic Au content, the KVC hosts the economically viable 164,000 oz Inlice epithermal Au deposit, implying that volcanic complexes which show sequestering of Au by magnetite crystallisation may still be prospective.

5.2 Geological Setting

The KVC (also known as the Erenler Dağ Volcanic Centre) make up part of the Neogene volcanic belt on the northern margin of the Taurus mountains, Anatolia (Fig. 5.1). The belt is composed almost exclusively of calc-alkaline lava domes, flows and pyroclastic units related to subduction of the Afro-Arabian plate beneath the Eurasiatic plate in mid to late Miocene (Innocenti et al., 1975). At Konya, the volcanic units are composed of basaltic-andesite to dacite calc-alkaline lava domes and flow-banded andesitic flows, with agglomerates and pyroclastic units deposited radially around the complex (Fig. 5.2). The margins of the complex are interbedded with lacustrine sediments, which have been used to corroborate dating of the KVC.

The KVC has been divided into three domains based on K/Ar dating, the oldest being the Sille Volcanics to the north of Konya city (Besang et al., 1977), which have been dated at 11.45 ± 0.2 to 11.95 ± 0.2 Ma. The main complex was dated at 8.8-10.9 Ma for the northern half and 9.4-8 Ma for the SE of the complex near Hatunsary. Finally there are few eruptive centres on the western edge of the complex which appear to sit apart from the main complex. A single lava was dated at 3.72 ± 0.02 Ma, although this is at contrast to a lava dated to 6.9 Ma by Platzman et al. (1998).

Geochemically, the lavas are similar to those of Santorini, Milos, Aegean and Cappadocian volcanics (Temel et al., 1998). The lavas of the KVC have SiO_2 concentrations ranging from 54 to 70% (Fig. 5.3), and therefore span the compositions basaltic andesite to high SiO_2 dacite (Keller et al., 1977; Temel et al., 1998). Inverse correlation between SiO_2 and MgO, CaO, Fe_2O_3 and TiO_2 indicate closed system fractional crystallization, as do compatible-incompatible trace element variation diagrams (Temel et al., 1998). High field-strength elements (HFSE), which are retained in the subducting slab (e.g. Pearce and

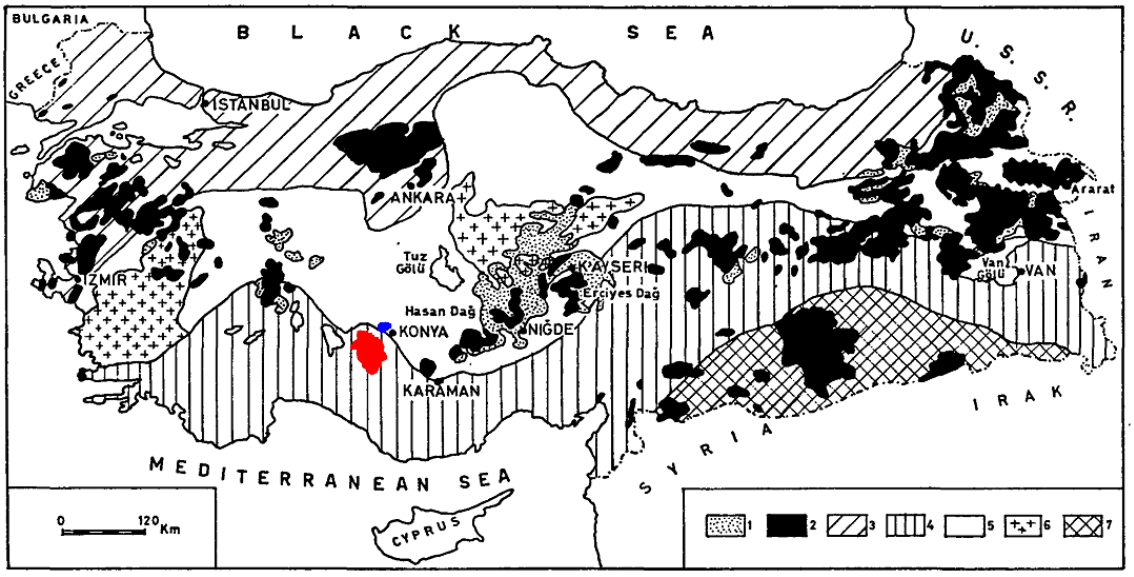

FIGURE 5.1: Map of the geology of turkey and the position of the Konya Volcanic Complex (red) and the Sille volcanics (blue). Both are part of a belt of volcanic centres running from east to west across Turkey, along the northern margin of the Tauric orogenic belt. Map from Innocenti et al. (1975). Key: 1 = Ignimbrite covers with subordinate lava flows, domes and tuffs. 2 = Lava domes and tuffs including volcanic agglomeration and tuffs, strato-volcanoes, shield volcanoes of eastern Anatolia, fissural basalts of Arabian platform and north-eastern Anatolia. 4 = Tauric orogenic belt. 5 = Anatolian median mass. 6 = crystalline massifs. 7 = Arabian Platform.

Peate 1995), are depleted in the KVC lavas, support their genesis as subduction related. The lavas have $^{87}Sr/^{86}Sr$ of 0.70484 to 0.70734, $^{143}Nd/^{144}Nd$ of 0.51239 to 0.51262, and reverse correlation between the two suggest a small degree of crustal contamination (Temel et al., 1998). The KVC rocks display geochemical characteristics typical to those of active continental margin calc-alkaline series, being high-K calc-alkaline in composition. Trace element ratios such as high Ba/Nb and low Nb/Y support this assertion (Temel et al., 1998). Since the lavas contain high concentrations of K, Rb, Sr, Ba, Zr, Ce, La, U and Th compared to ocean island arcs, geochemical input from sources such as thick sediments or even continental fragments should be considered (Keller et al., 1977).

The genesis of the arc is uncertain. Age dating suggests the volcanism is related to a former subduction zone which became active more than 12 m.yr ago. Geometrically, the Neogene volcanism as a whole lies parallel to the current Anatolian-African plate boundary along the Cyprian Arc (Fig. 5.4). For these reasons, the volcanism is attributed to paleo-subduction along the current plate boundary.

Hydrothermal alteration in the KVC has been well documented, although mineralisation was not identified until recently (Celik, 1999; Karakaya et al., 2001; Karakaya, 2009). Multiple phases of alteration to kaolinite, illite and smectite, together with intense zones of

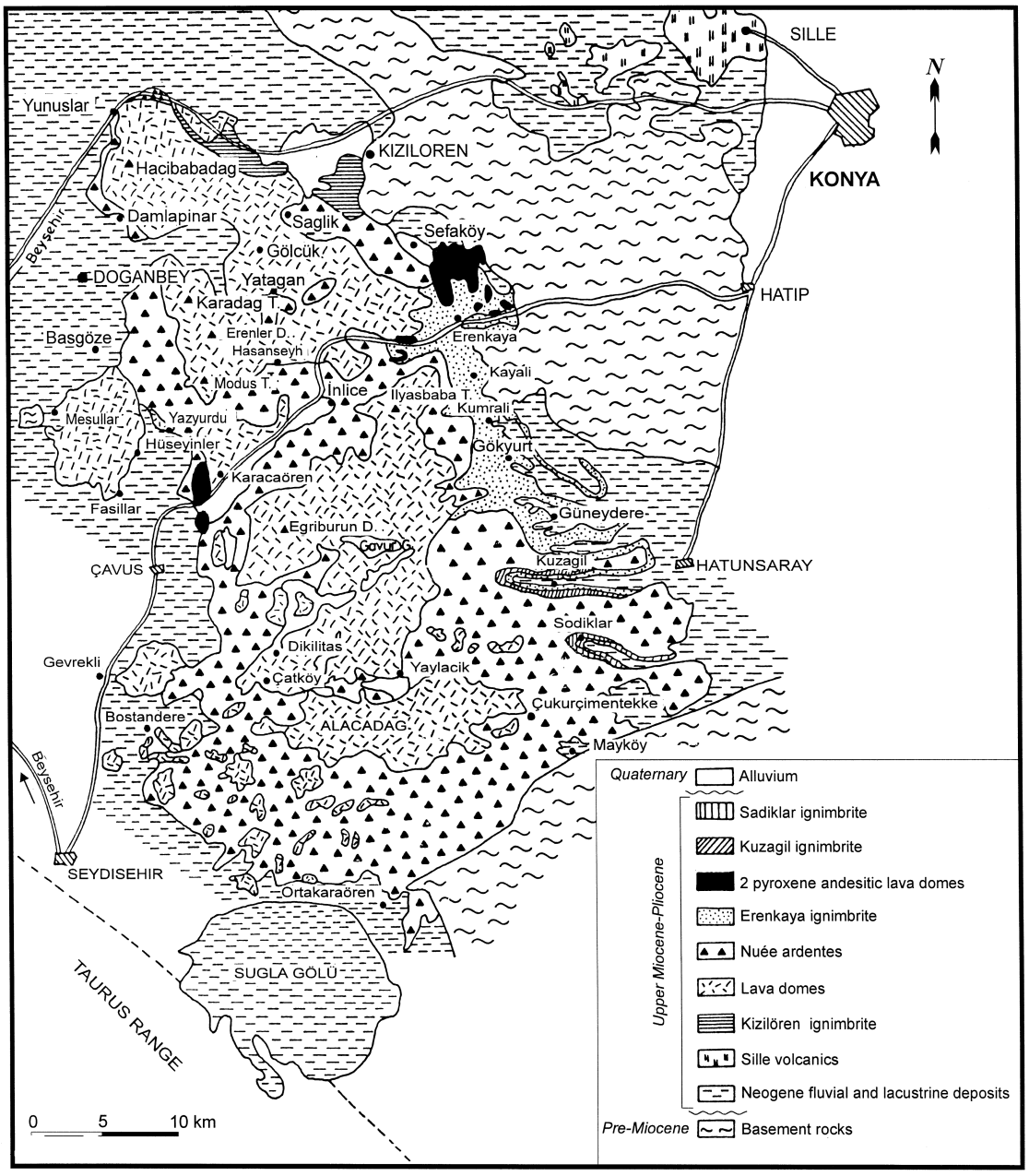

FIGURE 5.2: Geological map of the KVC (Temel et al., 1998).

silicification and quartz-alunite alteration have been identified (Karakaya et al., 2001). The association between kaolinite, cristobalite and quartz, suggests that most of the alteration took place at approximately 100°C. The source of silicification may be alunitisation via the oxidation of H_2S:

$$H_2S + 2O_{2(g)} \Rightarrow H_2SO4^- + H^+ \tag{5.3}$$

$$3KAlSi_3O_8 + 3H_2SO_4 \Leftrightarrow KAl_3(OH)_6(SO_4)_2 + 9SiO_2 + K^+ + SO_4^- \quad (5.4)$$

Alteration in the KVC is often well-zoned in nature, from (middle to edge) Silica → alunite zone → "Clayey zone" (kaolinite, halloysite, dickite, smectite and illite) → protoliths (Karakaya et al., 2001). Extensive mobility of major and trace elements has been identified (Karakaya, 2009), especially Na_2O, CaO, Fe_2O_3 and MgO. Al_2O_3 and K_2O were less easily leached, associated with preferential decomposition of plagioclase feldspar over k-feldspar and muscovite. Most of the REEs were probably mobilised, with the LREEs being easier to leach than the HREEs. La, Ce, Yb and Lu were precipitated with hydrothermal minerals and alteration. LILE elements were enriched, along with the transition metals such as Co, Cr, Cu, Ni, V, Sc and Zn. Karakaya et al. (2001) note the similarity of this alteration style to acid-sulphate type alteration associated with epithermal and silica deposits around the world

A paleomagnetic investigation of the KVC identified ferromagnetic phases of the KVC rocks as almost exclusively titanomagnetites to pure magnetite (Tatar et al., 2002). In a few samples, two separate titanomagnetite phases are evident, and another contains pure hematite. The paleomagnetic interpretation suggests the earliest KVC volcanics record anticlockwise rotation of 36±9° since *c.* 12 Ma and no significant rotation since *c.* 8 Ma. This is consistent with general anticlockwise rotation of the Anatolian block as the Afro-Arabian plate continues to impinge more heavily upon the eastern end of the Anatolian plate.

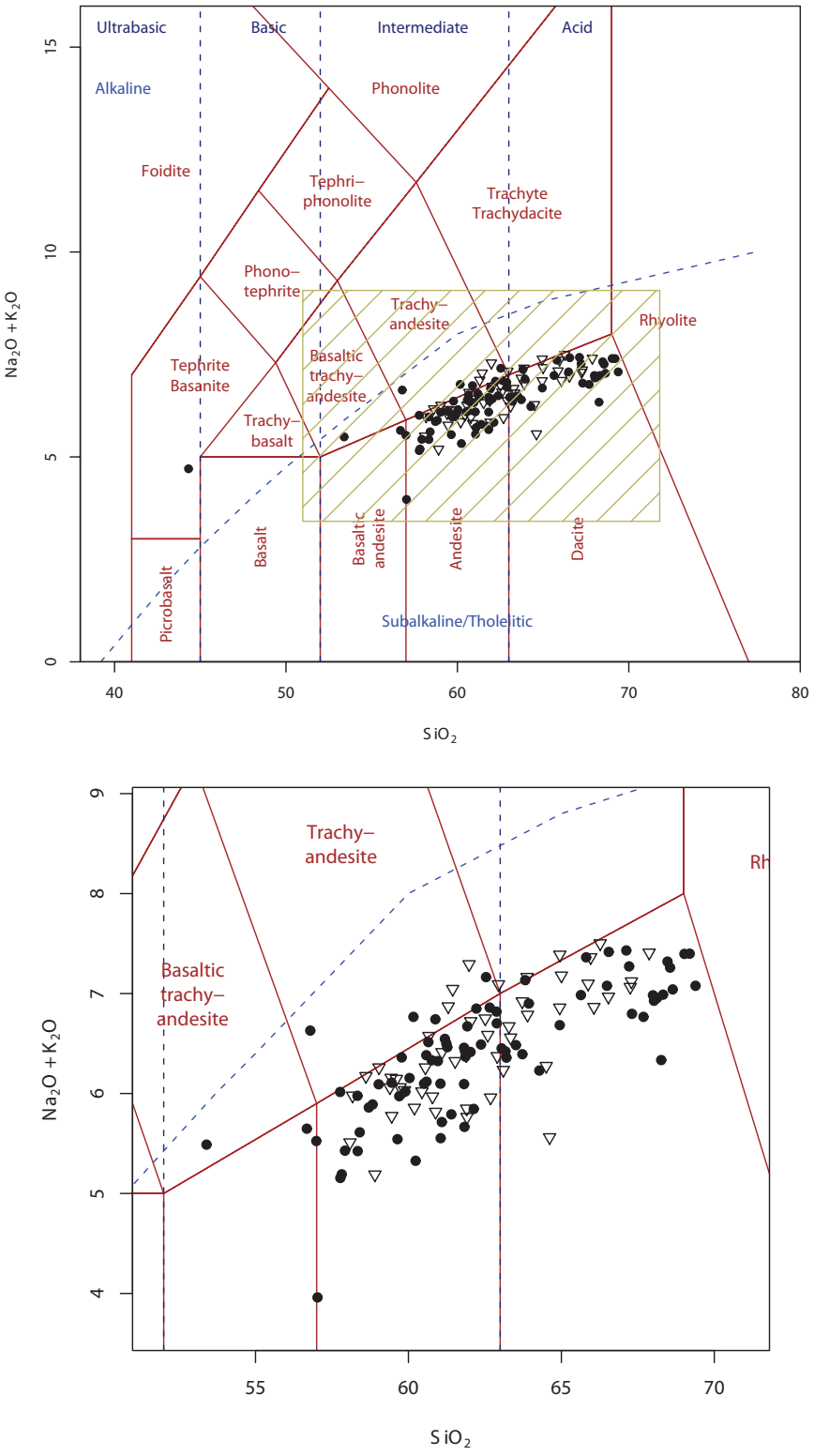

FIGURE 5.3: TAS diagram after Lebas et al. (1986) of existing data from the KVC. Circles are from Temel et al. (1998) and open triangles from Keller et al. (1977). Lower pane is resized view of top pane (hashed rectangle)

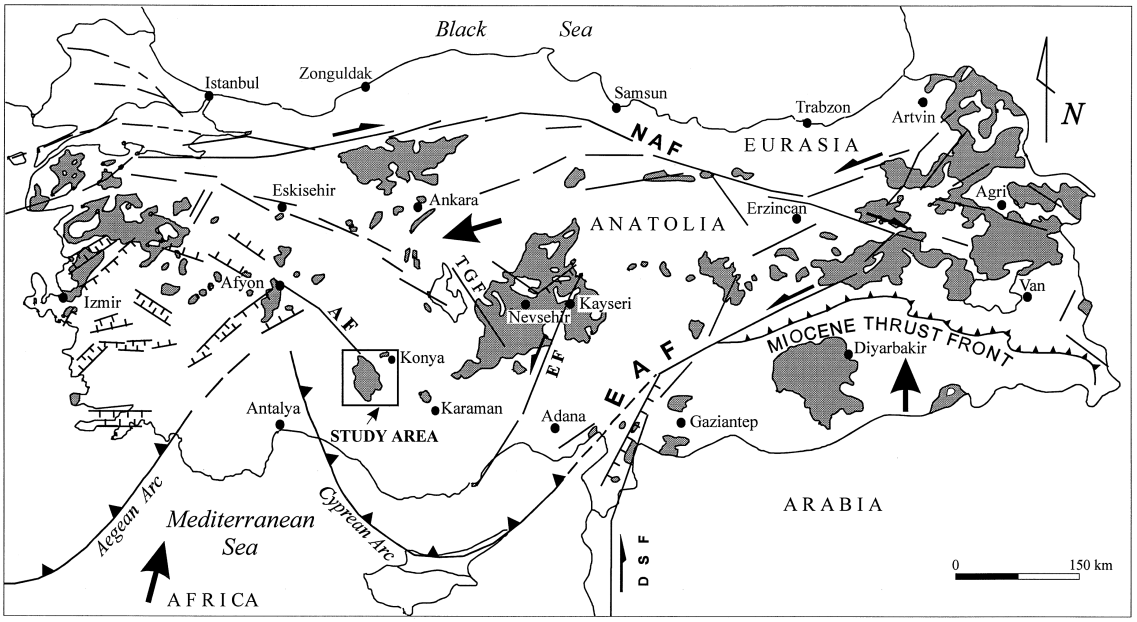

FIGURE 5.4: Map showing the tectonic setting of the KVC and how the geometry of the volcanic belt mirrors that of the current Cyprian subduction trace (Temel et al., 1998).

5.3 The behaviour of Au in magmatic systems

The concentration Au in igneous rock is known to be loosely associated with magmatic evolution - basalts tend to be higher in Au than more silicic varieties (e.g. Tilling et al. 1973). Whilst this may be true for a particular tectonic setting or suite of rocks, Pitcairn (2011) showed that there is a large variation of Au content between different types of rock of the same classification on the basis of silica and alkali content. For example, mid-ocean ridge basalt has an average Au content of 0.95 ppb, whereas arc-related basalts tend to be higher at ∼1.6 ppb (see section 1.1.4). Clearly Au content must be fundamentally linked to tectonic setting, much like many of the more familiar trace elements, such as Pb, Nb, Sr or the REEs.

The behaviour of Au in magmatic systems, especially arc-related magmas, is not well understood. There is some argument that Au may be present as a solid solution in some silicate phases (e.g. Shcherbakov and Perezhogin 1964; Weber and Stephenson 1973; Gijbels et al. 1974), however the overwhelming evidence suggests Au exists in close association with accessory oxide and sulphide phases (e.g. Keays and Scott 1976; Bird et al. 1991; Peach et al. 1990), or where these phases are not available, as native grains enclosed by silicate phases (Sisson, 2003; Zhang et al., 2006). The behaviour of Au in a magmatic system is thus controlled by the behaviour of its host phase or the physical dynamics of a native grain of gold in a magma. Accessory phases such as magnetite and sulphides are known for their irregular distribution in igneous bodies, sometimes forming rich horizons or cumulates, and in those cases Au has been found to be enriched in those particular areas of the magma body (e.g. Bird et al. 1991).

Several authors have placed importance on the timing of crystallisation and fractionation of magnetite. Togashi and Terashima (1997) observe a high Au concentration in titanomagnetite cumulates and increasing Au in suites that have seen titanomagnetite crystallisation at a later stage. They argue that titanomagnetite-free fractionation results in increasing Au in the residual melt (since no Au is being removed by titanomagnetite fractionation) and so a delay in titanomagnetite crystallisation produces higher Au contents in the more evolved melts. In contrast, Sun et al. (2004) argue that the crystallisation of magnetite affects the Au (and Cu) concentration of the residual melt in a different way, with magnetite crystallisation causing the exsolution of a S rich fluid (where S content of the magma is substantial) by driving the reduction of sulphate to SO^{2-}. This S-rich fluid would then scavenge Au and Cu, leading to a reduction in Au concentration post magnetite crystallisation. It is worth noting that the basic observation - lower Au content in magmas following magnetite crystallisation - is not incompatible with the theory proposed by Togashi and Terashima (1997).

The partition coefficient between the silicate melt and magnetite ($D_{Au}^{Mt/melt}$) for a crystallising system which produces a rhyolite melt has been experimentally determined to be approximately 4 (Simon et al., 2003). Using this value, magnetite might sequester 14-54% of the Au from a basaltic melt that evolves to a rhyolite. Simon et al. (2003) thus agree that magnetite crystallisation is detrimental toward producing a Au-rich ore fluid from a parent magma. However, Togashi and Terashima (1997) suggest a partition coefficient of between 13 and 127 can best explain their data. A detailed study into the distribution of Au within magnetite precipitating from a hydrothermal solution (450°C, 1kbar) revealed that Au is primarily held within a 330nm thick "non-autonomous phase" (NP) on the surface of the magnetite crystal (Tauson et al., 2012). The nature of the NP is not well understood, but it is probably a complex interwoven goethite-wuestite layer with vacant Fe sites in the goethite and nanometre-sized domains on the crystal surface of wuestite, which accommodate Au(III). The Au is thus primarily held in this thin surface layer, demonstrated by the near perfect (>0.9 correlation coefficient) correlation between surface area of the magnetite crystal and Au concentration (Tauson et al., 2012). The authors note that Au can therefore be considered a compatible element in magnetite, although since this experiment involved precipitation of magnetite from a hydrothermal fluid it is not clear if the NP would exist on the surface of a magmatic magnetite crystal.

5.4 Sample collection and methodology

Two sets of samples were collected: fresh, unaltered igneous rock and altered rock from the vicinity of the Inlice mineral deposit (Fig. 5.5). In the former case, the aim was to collect samples from all parts of the complex with as wide a range of chemical composition as possible. To that end, effort was taken to sample particularly interesting coloured or textured rock. Pale, silicic rocks were in abundance so darker units were sampled at every opportunity. In the vicinity of the Inlice mineral deposit, samples were taken of progressively altered rock of the same volcanic unit, although even the least altered appeared to exhibit some silicification. Large samples were taken of at least 2kg to mitigate sampling bias due to the "nugget" effect of gold within geological materials. In many cases the quantity was much larger, at 3 to 5kg. Samples were double-bagged in thick plastic sample bags to prevent contamination. Sample locations were recorded with GPS.

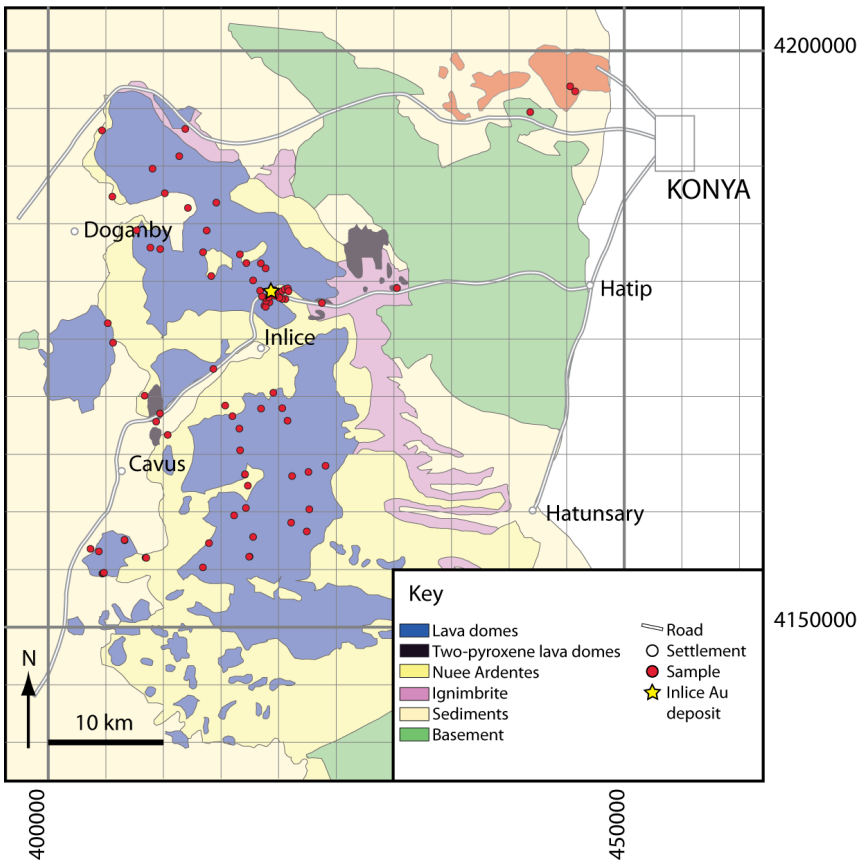

FIGURE 5.5: Map showing the locations of samples collected in the KVC, overlain on the geology from Keller et al. (1977); Temel et al. (1998). UTM WGS84.

5.5 Sample descriptions

All rocks collected are porphyritic, displaying phenocryst phases in a glassy to cryptocrystalline groundmass (Table 5.5, Fig. 5.6). Rocks generally fall into three categories: Dark, fine grained rocks emplaced into the shallow crust, with phenocrysts <1mm; flow banded extrusive lavas, often with alternating bands of glassy and cryptocrystalline material; pale, porous rocks with phenocrysts >3mm and massive texture. The latter are the most common, followed by the flow banded lava flows. The darker rocks are less conspicuous but are sometimes found as shallow dykes or sills within the more common units.

Phenocryst phases invariably include plagioclase, the most dominant feldspar, accompanied by clino- and ortho-pyroxene in basaltic rocks with rare olivine, and amphibole (hornblende) and biotite in the more evolved rocks. An opaque phase is present in all rocks, identified in polished section and as a mineral separate to be magnetite. Three

samples (K050, K062 and K093) exhibit oxidation of iron-bearing phases, interpreted to be weathering.

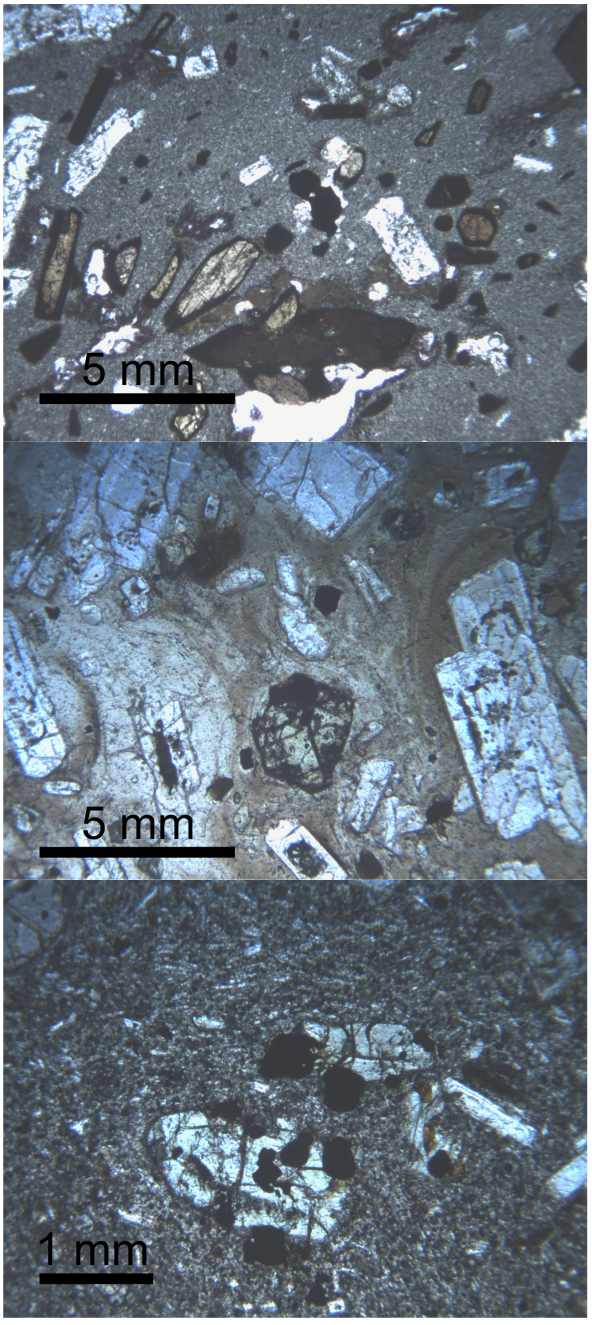

FIGURE 5.6: Slide photos (transmitted light) of selected samples showing igneous texture and relationship between phases, groundmass and magnetite.

5.5.1 Altered samples

Observed alteration is weak, with the most altered samples showing very slight clay-alteration to the margins of feldspars, destruction and oxidation of iron-bearing minerals, magnetite precipitation and a heavily silicified groundmass. Most of these samples are found in proximity to the Inlice mineral deposit, although this alteration type is not thought to be directly related to the high sulphidation alteration exhibited by the Inlice deposit, which would normally destroy magnetite rather than precipitate it (Irvine and Smith, 1990; Feebrey et al., 1998).

5.6 Sample preparation, selection and analysis

Samples were sawn to remove any trace of a weathered margin before being crushed in a fly press, using paper and sheets of plastic to prevent the rock contacting metal. Roughly half the sample was then powdered in agate, leaving half as pea-sized fragments which could later be used for mineral separation. All samples except the most highly altered were then analysed using XRF on pressed-pellets to obtain approximate major and accurate trace elements (Cu, Zn, Pb, Ba, Rb, Sr, Y, Zr, Nb, Th, U, La, Ga). Using this data, a sub-set of 40 samples were chosen on the following basis:

- An extensive sample set adjacent to the Inlice mineral deposit
- Full range of compositions as displayed on a total alkali - silica (TAS) diagram,
- Full range of compositions as displayed on a plot of SiO_2 vs FeOt, since crystallization of iron-rich magnetite is a likely control on Au content,
- Full range of compositions as displayed on a plot of TiO_2 vs Zr, which is a common proxy for evolution of silicic melts.

The samples were divided into the following groups - The Sille volcanics (the oldest and set apart from the main KVC, 1 sample), the main KVC samples, samples adjacent to the Inlice mineral deposit and samples from the KVC which show lower FeOt than the main array of samples. These samples were then analysed for Au, rare earth elements and trace elements (ICP-MS).

5.6.1 Au analysis

The rocks are all fine grained, with microcrystalline ground-mass and phenocrysts up to ~2 cm in size. Consequently, at least 4g of rock was digested for each sample, except K022 which was proximal to the Inlice mineral deposit and so could have had a much higher Au content than the rest of the samples.

The formation of insoluble fluorides during HF-HNO_3 acid digestion was a problem. These fluorides form when digesting larger quantities of rock with a high concentration of Al, Mg and Ca, although the relationship between quantity of powder, acid used and geochemical composition with respect to fluoride formation is poorly understood. The fluorides have been found to strongly sequester trace elements and can be avoided by using HClO4 attack (Yokoyama et al., 1999). However this technique is extremely time consuming because of the high boiling point of HClO4 and the low melting point of teflon. Instead, fluoride formation was suppressed using a larger ratio of HNO_3:HF in the initial attack, addition of extra HNO_3 during the first dry-down and additional attacks of aqua-regia to ensure all the Au is in solution. Using this method with the reference material EMC-1, an amphibolite, yielded good results. Au concentrations in reference materials were determined to within 5% (see Chapter 2).

5.6.2 Magnetite analysis

Quantification of the modal proportion of magnetite was undertaken by analysing images of polished thin sections under reflected light. These images were analysed using the ImageJ software, giving results for % area of the slide and particle analysis data such as grainsize and circularity (Fig. 5.7). The analysis was made by converting the images to greyscale and setting thresholds for the amount of light reflected. Magnetite, by far the most reflected phase in these rocks, stands out well. Each pixel containing magnetite is then counted as a proportion of the slide area. This method is effectively point-counting, using each pixel of the image as a point. At over 500,000 pixels per image, it is a much more comprehensive technique than manual point-counting. Since magnetite is distributed unevenly in the rock, the largest possible area should be used to gain a true value. In this case, the area of the polished thin section was used, which is on the order of 300-500 mm^2. The reliability of such a sample area can be explored by repeating the measurement on successively larger areas of the same slide photo (Fig. 5.8). Three samples analysed in this way suggest the sample size area used is fairly appropriate (Fig. 5.9). Sample K009, which has a small grainsize and relatively even distribution of magnetite, shows good agreement across all scales. Sample K039, which has a fairly even distribution of magnetite but wide

variation in grainsize, shows slightly worse agreement than K009. Sample K068 which has even distribution and size of magnetite grains apart from a few much larger grains, shows a high variation at low scales but appears to settle down to an average.

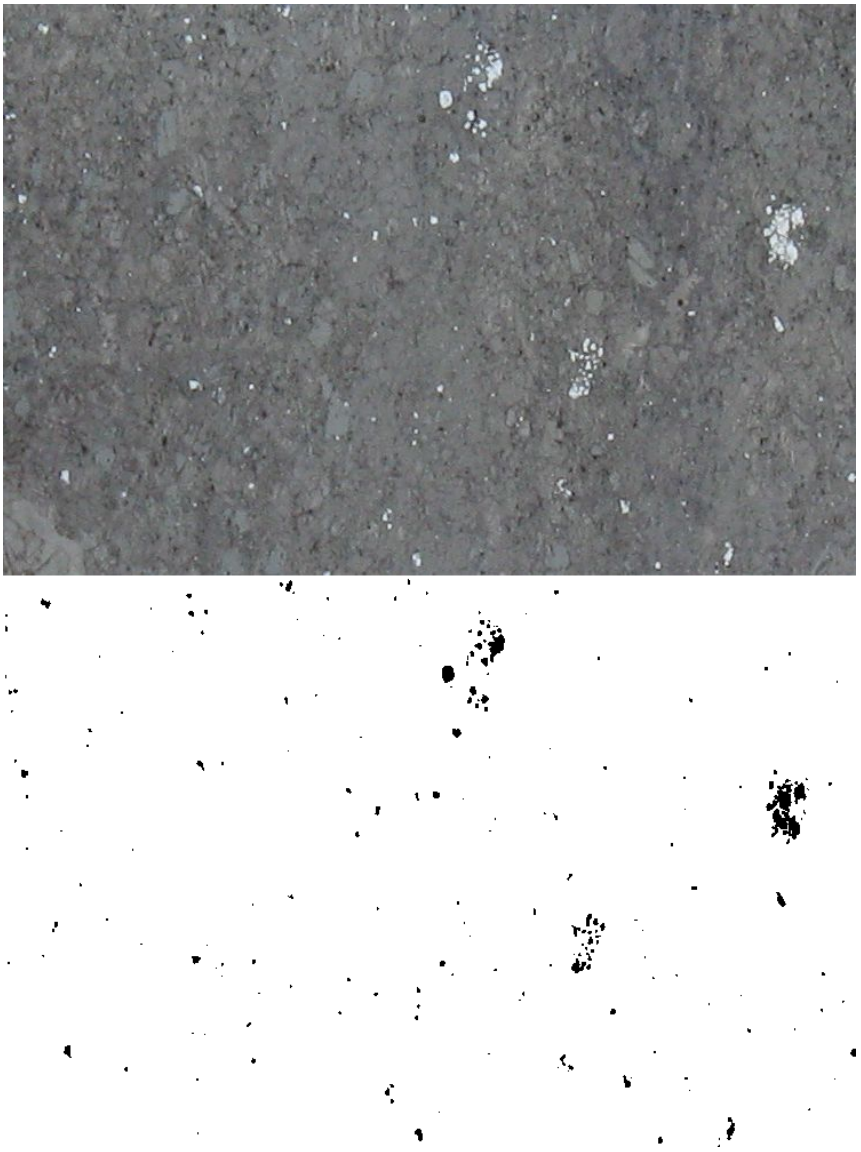

FIGURE 5.7: Top pane is a photo of a polished thin section of sample K020, under reflected light. The bright areas are magnetite. This image is analysed in ImageJ, which isolates the magnetite (lower pane). The total area of magnetite and information on individual grains can then be calculated.

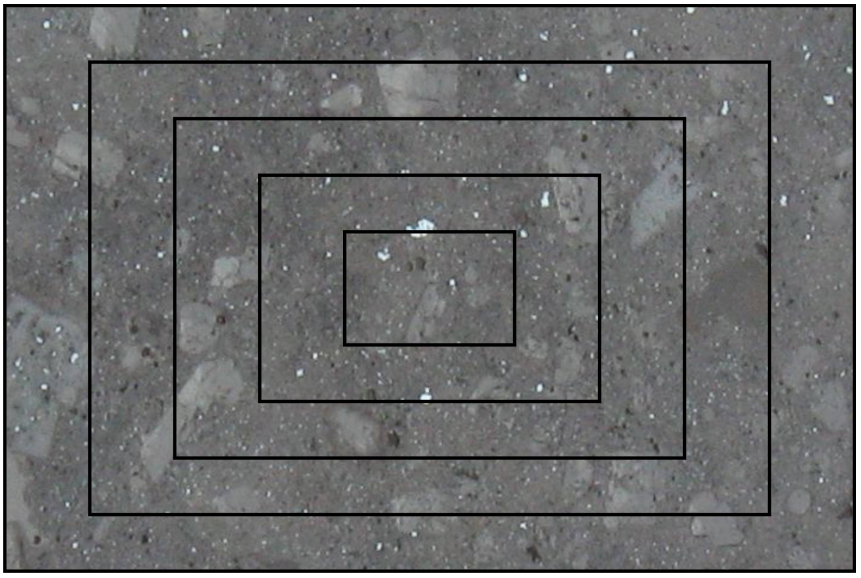

FIGURE 5.8: The reliability of the magnetite percentage data can be explored by repeating analysis on successively larger areas of the slide. The boxes represent areas 20%, 40%, 60% and 80% of the full slide.

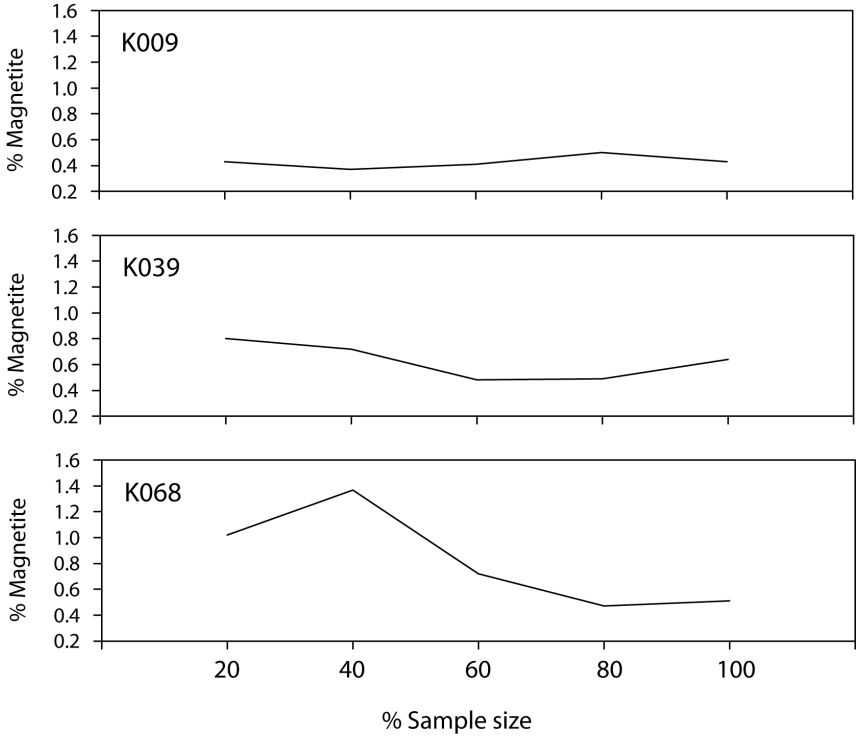

FIGURE 5.9: Repeated analysis of samples K009, K039 and K068 at different scales.

5.7 Results

Examination of polished thin sections under reflected light reveals that magnetite present within all thin sections but is found in three distinct settings. It can be found in the groundmass, strongly associated with mafic minerals (on the grain boundary or included within pyroxenes and amphiboles) or as apparently later replacement of iron-bearing phases like biotite. It is also found as rare, small inclusions in plagioclase. Where a rock contains mafic minerals such as pyroxene and amphibole, they invariably contain magnetite inclusions. Sometimes clusters of mafic minerals are seen which often include a high proportion of magnetite (Fig. 5.10). The rocks can be divided into 4 groups:

magnetite is contained within;

- groundmass only
- groundmass and late replacement
- groundmass and mafic minerals
- groundmass, mafic minerals and late replacement

The late replacement of iron-bearing phases by magnetite is only present in rocks that show other types of alteration such as a silicified groundmass and/or destruction of phenocryst phases. Most of them are proximal to the Inlice mineral deposit and they also form an array on the alteration boxplot along a hydrothermal alteration trend (AI vs CCPI, Large et al. 2001, Fig. 5.11). Sulphurous epithermal alteration, such as displayed by the Inlice deposit, is almost always magnetite destructive (Irvine and Smith, 1990; Feebrey et al., 1998), so it seems likely that this late magnetite could be the result of a porphyry related K-silicic alteration, which often includes magnetite precipitation (Gammons and Williams-Jones, 1997; Sillitoe, 2000; Cooke et al., 2004; Seedorff et al., 2005).

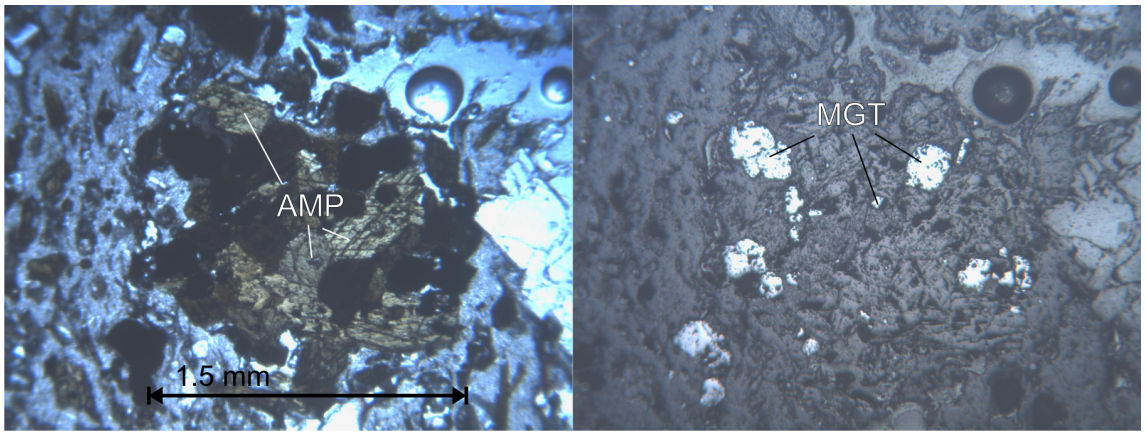

FIGURE 5.10: Possible amphibole-magnetite cumulate cluster incorporated into a flow-banded andesite. The cluster is approximately 1.5 mm wide. MGT = magnetite, AMP = amphibole

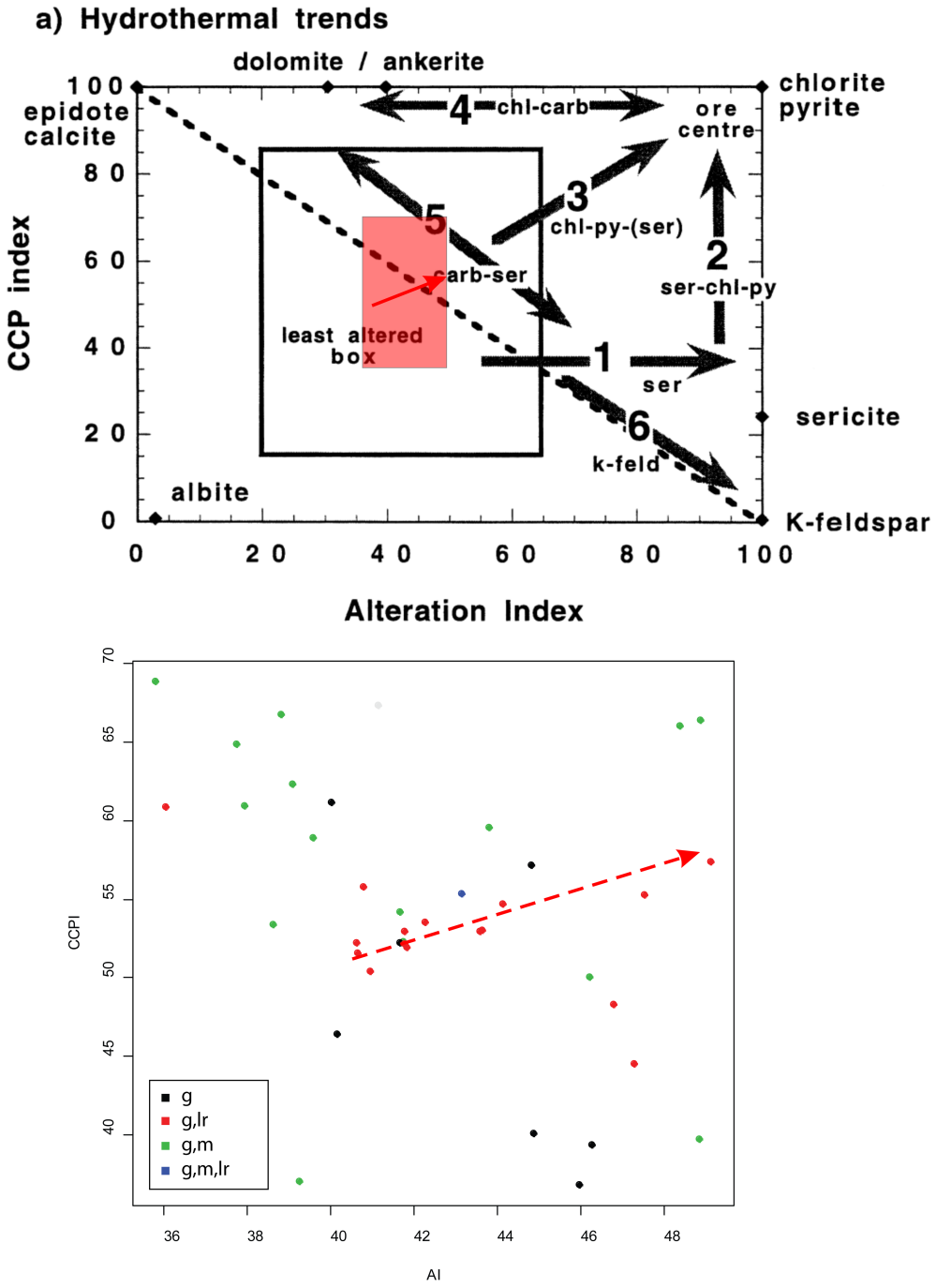

FIGURE 5.11: Alteration index (AI) vs chlorite-carbonate-pyrite index (CCPI). Colours defined by how the magnetite is sited in the rock. g = sited in the groundmass; g,lr = groundmass and late replacement; g,m = groundmass and within mafic minerals; g,m,lr = groundmass, mafic minerals and late replacement. The boxplot uses two different indexes of alteration to determine what sort of alteration has taken place. Trends into the top-right half indicate hydrothermal alteration, divided into different types based on the vector (top pane). Samples with magnetite as a late replacement form an array on the plot equivalent to a hydrothermal alteration trend (Large et al., 2001). Red area encompasses data shown on the lower pane.

5.7.1 Unaltered rocks

The primary geochemistry and the behaviour of Au in the KVC can be described by examining the rocks which do not show evidence of any alteration. Major elements behave as expected and as demonstrated in other studies (Fig. 5.12) (Keller et al., 1977; Temel et al., 1998). Trace elements are typical of continental arc magmas, with pronounced negative Nb, P and Ti anomalies and positive Cs and Pb anomalies with respect to N-MORB (Fig. 5.13). The profiles are very consistent with little variation, consistent with crystal fractionation being the primary control on magma evolution (Temel et al., 1998). REE profiles are LREE enriched with an occasional slight Eu anomaly (Fig. 5.14). Au concentration varies between 0.78 and 0.05 ppb, with a mean average of 0.27 ppb. Good (statistically significant) negative correlations between Au and SiO_2, and positive correlations between Au and TiO_2, FeOt, MnO, MgO and P_2O_5 are observed (Table 5.1, Fig. 5.15). Statistically significant positive correlations are observed between Au and compatible trace elements such as Co and V and the middle-REEs (Sm, Eu, Gd, Tb, Dy, Ho, Er, Tm), whilst the only significant negative correlation is observed with Li. Magnetite percentage is positively correlated with FeOt and TiO_2, as might be expected (Fig. 5.16). Au is not significantly correlated with magnetite percentage. However, it is interesting to note that only high Au and high magnetite contents are found in the more mafic compositions.

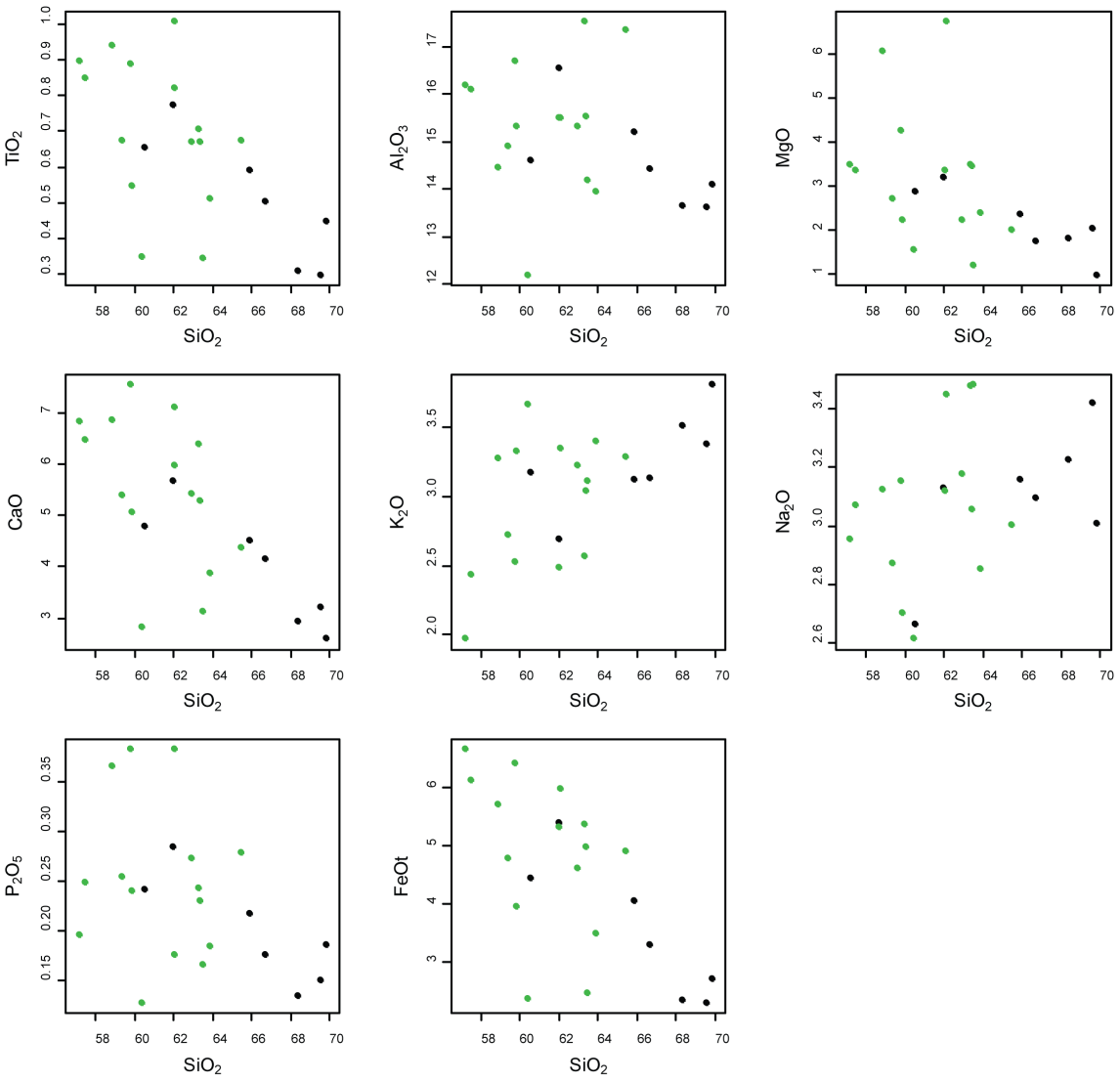

FIGURE 5.12: Major element variations in unaltered rocks. Green = magnetite present in the groundmass and the mafic minerals, black = magnetite present in just the groundmass. Units are wt%.

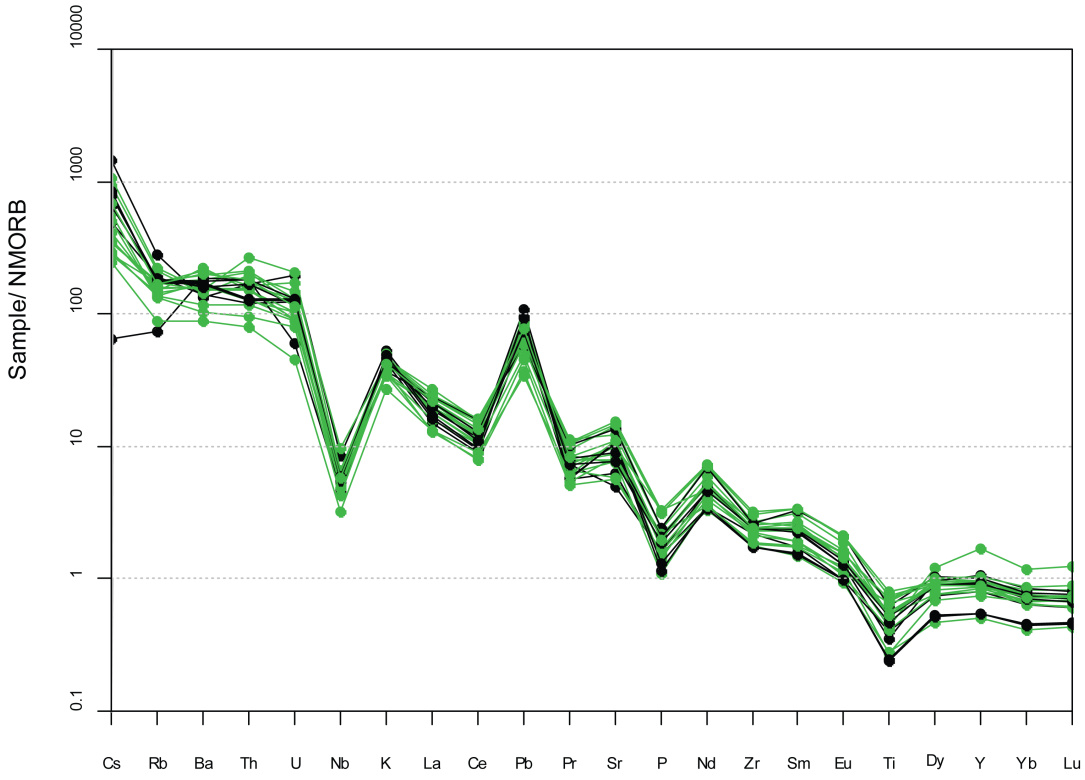

FIGURE 5.13: Trace element profiles normalised to N-MORB (Sun and McDonough, 1989) for the Konya volcanics. Profiles show typical arc patterns and are remarkably consistent. Colours as fig. 5.12

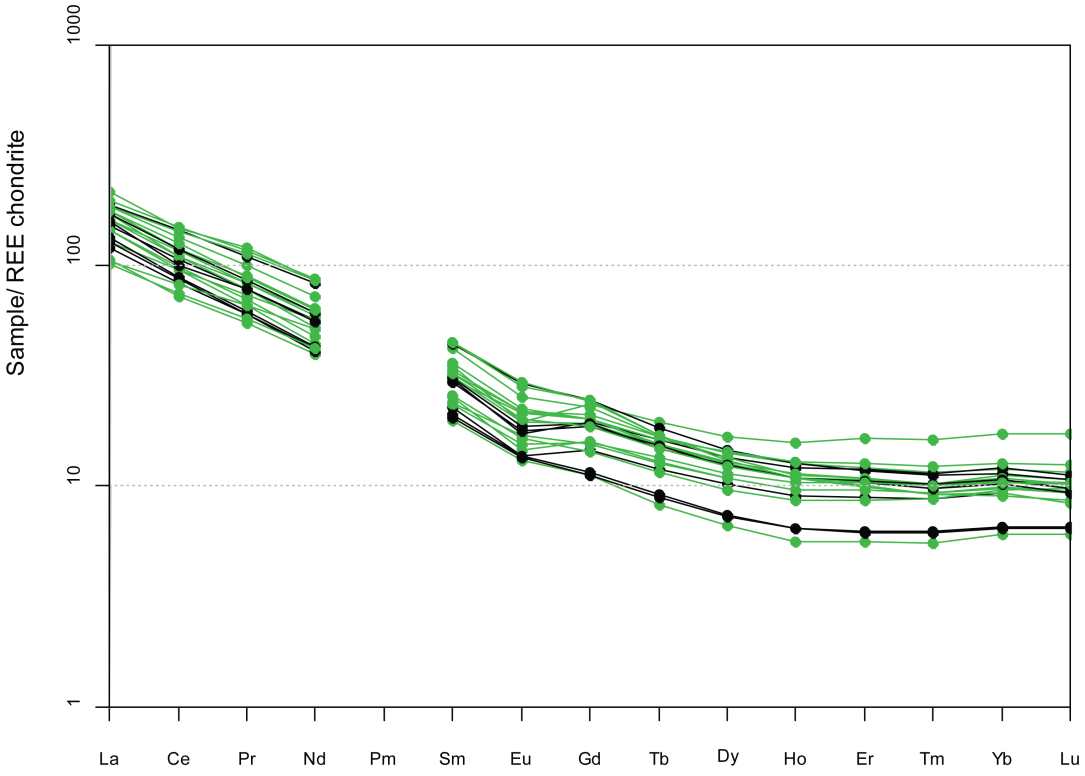

FIGURE 5.14: REE profiles relative to chondrite (Boynton, 1984). LREE-enriched with a slight Eu anomaly. The Eu anomaly is more pronounced in the samples adjacent to the Inlice mineral deposit, indicating mobilisation of Eu as it was altered. Colours as fig. 5.12

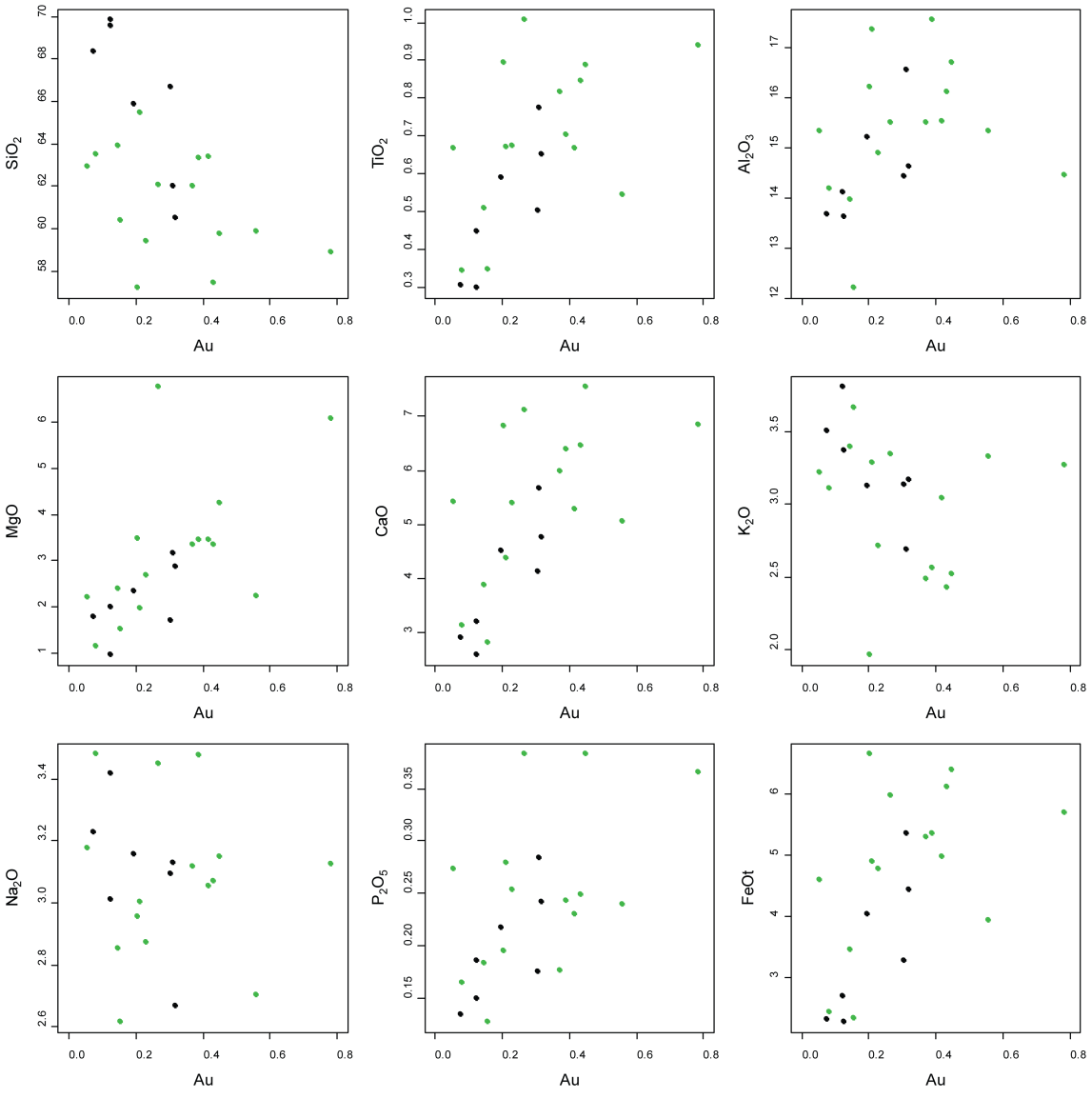

FIGURE 5.15: Au vs major elements. Au shows decreasing concentration with magma evolution, for example correlation with MgO and inverse correlation with SiO_2. Au in ppb, major oxides in wt%.

Element/Oxide	Correlation Coefficient
CaO	0.63
MgO	0.62
Co	0.59
TiO_2	0.58
Sc	0.58
V	0.57
P_2O_5	0.56
Zn	0.56
Fe_2O_3	0.56
Gd	0.56
Tb	0.54
Dy	0.52
Ho	0.50
Zr	0.48
Cu	0.47
Cr	0.47
Sm	0.47
Er	0.47
Y	0.47
Eu	0.46
Tm	0.43
MnO	0.42
Li	-0.44
SiO_2	-0.53

TABLE 5.1: Significant correlation coefficients between Au and the indicated element or oxide. Correlation measured using Pearson's correlation coefficient at 5% significance, two-tailed test.

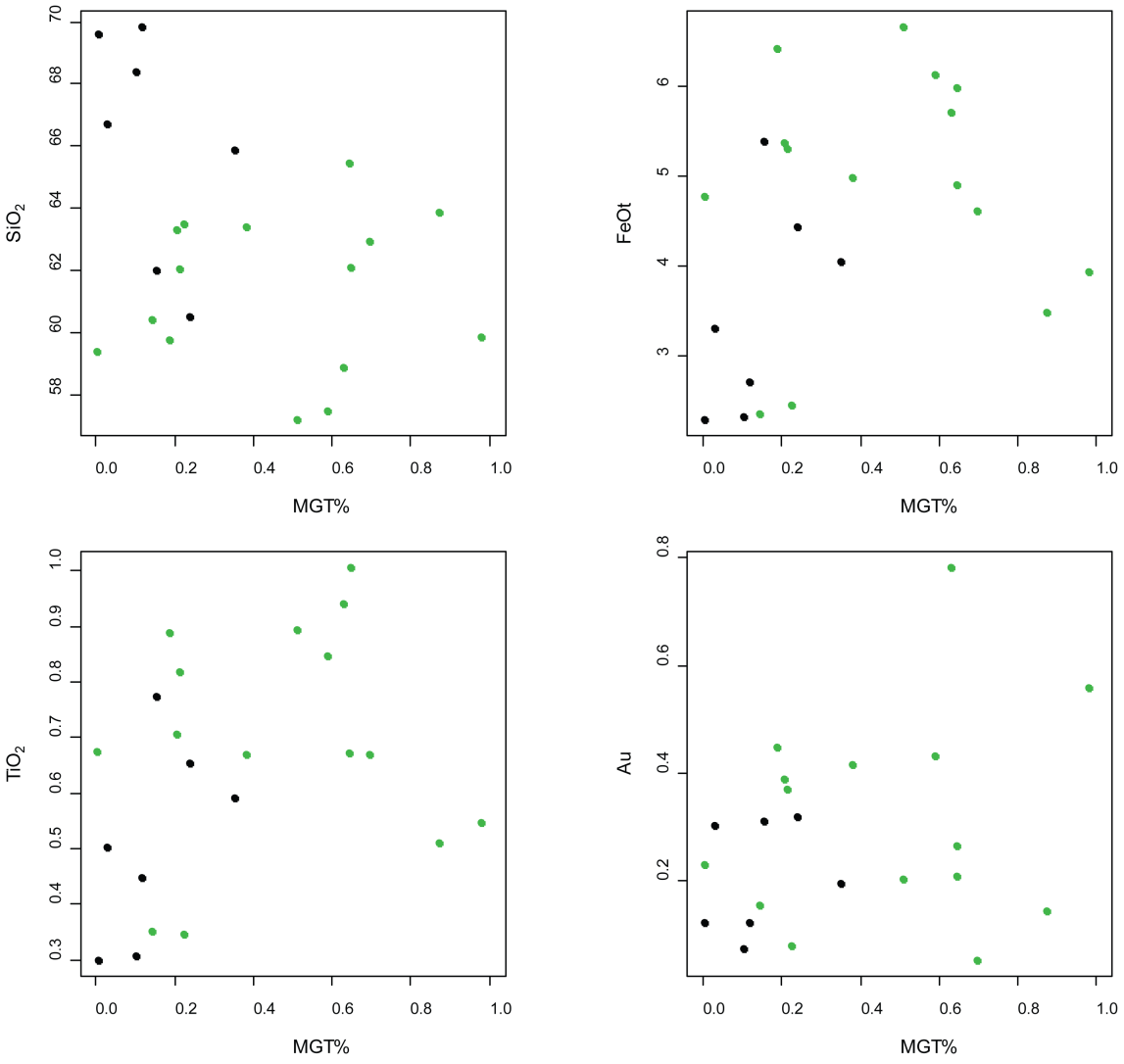

FIGURE 5.16: Magnetite percentage by volume verses SiO_2, TiO_2, FeOt and Au. Major elements behave as expected for magmatic fractionation of magnetite. Colours indicate magnetite is sited in the groundmass and within mafic minerals (green) or just the groundmass (black). The relationship for Au is less clear but overall, more evolved rocks contain less magnetite and less Au. Major oxides in wt%.

5.7.2 Altered rocks

Au concentration in these samples ranges from 0.43 to 0.07 ppb Au, with a mean average of 0.17 ppb. This is 0.1 ppb lower than the average for the unaltered rocks, although this could just be due to sampling bias since most altered samples come from the same rock unit. There is no relationship between Au concentration and distance from the deposit, alteration index (AI) or percentage magnetite (Fig. 5.17). There is some suggestion that other metals such as Ni, Co, Cu and Cr may be depleted with increasing degree of alteration, as they show relationships with AI (Fig. 5.18).

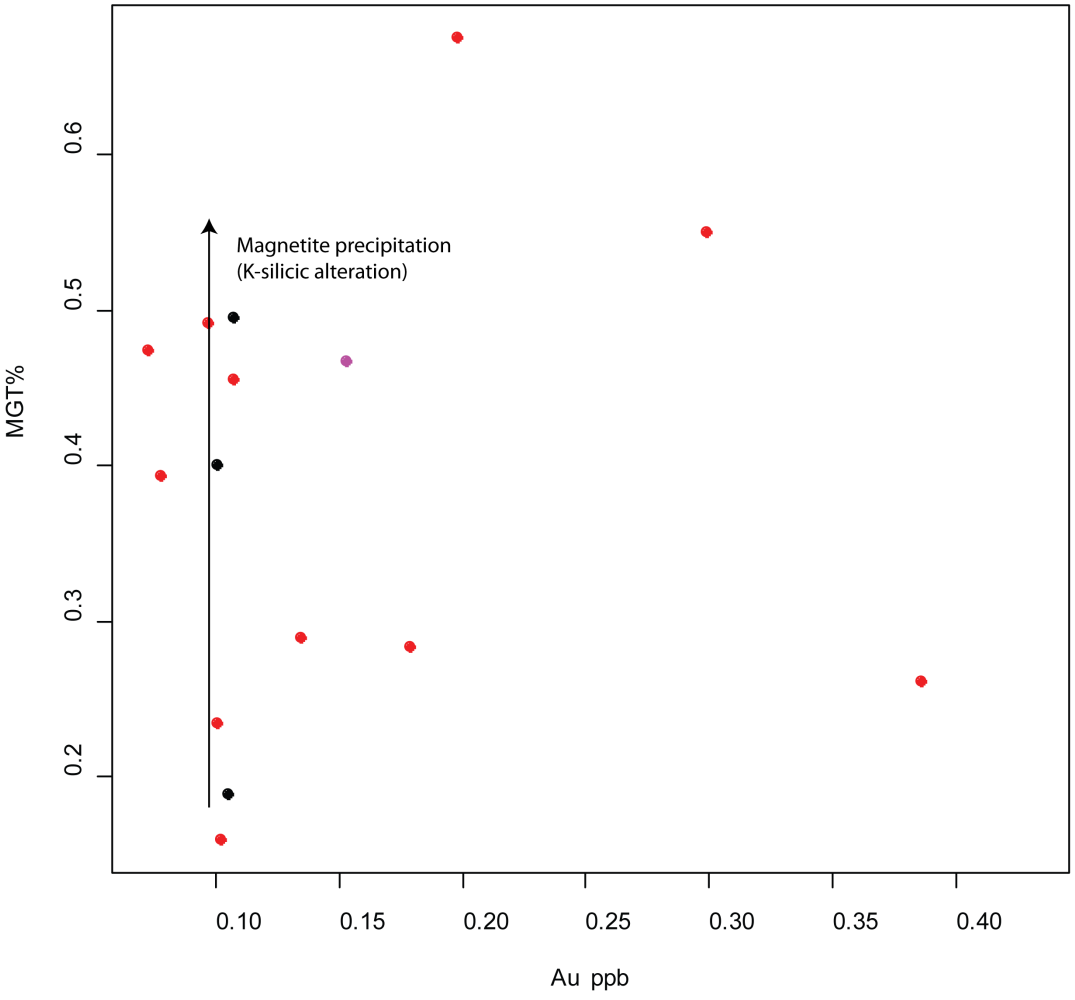

FIGURE 5.17: Au vs Magnetite % for altered samples. No relationship is observed due to late replacement of iron-bearing phases with magnetite during K-silicic alteration. Red symbols are adjacent to the Inlice deposit, black are background Konya rocks (but were later found to be slightly altered in thin section), pink are normal but low-Fe.

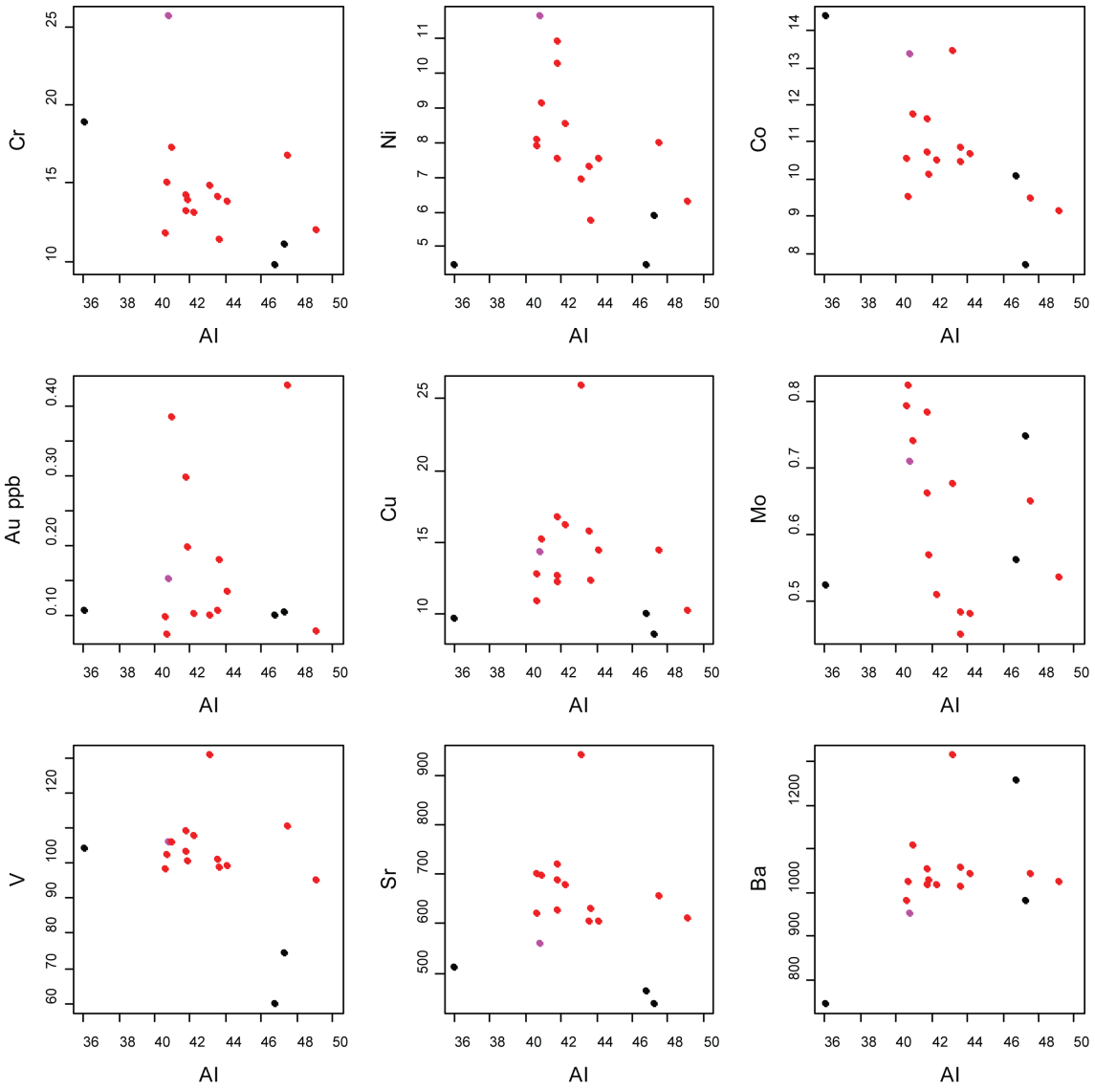

FIGURE 5.18: Trace element variation with alteration index (AI) of altered rocks found in the KVC. Alteration is weak, however there is some suggestion that Co, Ni, Cr and perhaps Cu have been mobilised, however the variation in AI is not great enough to properly assess the mobility and variations may just be due to magmatic evolution. Au shows no convincing relationship, apart from having generally a very low concentration. Au in ppb, all other elements in ppm. Colours as Fig. 5.17.

5.8 Discussion

The data presented here indicate Au concentrations in the KVC volcanic rocks are highly variable. The concentration ranges from 0.07 to 0.8 pp, a factor of over 11, which is the highest variation of any of the measured elements. This variation can be the result of two things, either variation in the initial magma at depth or variation due to magmatic differentiation. Statistically significant correlation is observed between Au and indicators of magmatic evolution, such as SiO_2, CaO, MgO. This would seem to support the idea that Au concentration has varied as a result of magmatic differentiation. Some scatter in the trends could be explained by variations in initial magmatic composition or the nugget effect of Au in natural materials.

Correlation between Au and magnetite is not statistically significant. It can be seen that only the more mafic compositions have both high Au and high magnetite, whilst the more felsic compositions all contain less than 0.4% magnetite and 0.35 ppb Au. Such an association does not prove that the Au is present within the magnetite phase. However, it is interesting to note that the trace elements which Au correlates best with; Co, Sc, V and Zn, all partition strongly into magnetite (Table 5.2). Similarly to Au, these elements do not correlate well with magnetite content (Fig. 5.19). The lack of a single trend might be explained by the ways in which the different magmas have evolved. It's clear that magnetite occurs with a wide range of grain sizes and morphologies, indicating that it crystallises and settles in different ways depending on the conditions in each individual magma. For example, if a particular magma was not oxidised enough to produce a great amount of magnetite, it could have a low magnetite but a high Au content, producing scatter on a graph of Au vs magnetite. Likewise, a highly oxidised magma could produce lots of magnetite and remove Au effectively, producing a rock with low Au but high magnetite content. Further to this, the grainsize of the magnetite produced would control how effectively the magnetite settles from the magma. Therefore it might be simplistic to expect a simple correlation between magnetite content and Au concentration. Poor accuracy from the magnetite content data could also account for some scatter. What we do see, for Au and other trace elements like Zn, Co, V and Sc is a broad trend towards more evolved compositions with a lower magnetite content and lower concentrations of those elements. From this data, it can not be said for certain whether magnetite crystallisation and settling is the primary cause of Au reduction in these lavas, however it is significant to consider that Au is widely known to be controlled by accessory phases like magnetite and no other phase in the Konya lavas is known to strongly partition Au.

Statistically significant trends between Au vs MgO, SiO_2, CaO, FeOt and TiO_2 indicate that Au concentration reduces during magmatic differentiation (Fig. 5.20). The amount of

Element	Correlation Coefficient	Average Kd Magnetite	n
Co	0.59	28.9	9
Sc	0.58	5.4	8
V	0.57	78	2
Zn	0.56	19.8	7

TABLE 5.2: The partition coefficients of some trace elements between melt and magnetite. Partition coefficients are the average of n experimentally derived or natural values. Correlation coefficients are between Au and the element, for reference. Data from: Bacon and Druitt (1988); Esperanca et al. (1997); Ewart and Griffin (1994); Latourrette et al. (1991); Lemarchand et al. (1987); Luhr et al. (1984); Mahood and Stimac (1990); Okamoto (1979)

	High (Au ppb)	Low (Au ppb)	Factor	Percentage (%)
CaO	0.48	0.12	4	75
MgO	0.7	0.13	5.4	81
TiO_2	0.48	0.12	4	75
SiO_2	0.41	0.12	3.4	71

TABLE 5.3: Estimated reduction in Au concentration due to magmatic differentiation. These figures are estimated from the trends displayed in Fig. 5.20.

reduction depends upon what is taken as the starting composition, and this varies widely from 0.8 to 0.2 ppb Au. Best fit lines through the data trends suggest rough fractionation trends, which can be used to estimate the degree of reduction in Au content (Table. 5.3). This is estimated at 70-80%.

The KVC hosts the economically viable Inlice Au deposit. The deposit is a high sulphidation epithermal type, exhibiting multiple stages of fluid flow and a narrow vuggy quartz ore body situated within a fairly confined zone of alteration. Au grades average 2.36 g/t. Whilst the KVC hosts many barren hydrothermal systems, the Inlice deposit demonstrates that this complex was able to produce a Au deposit despite substantial removal of Au from the melt. This paradox might be resolved in several ways.

1. Fluid exsolved from a melt which had not undergone removal of metals
2. Magnetite crystallisation occurred but the magnetite did not settle out of the melt
3. The parent magma saw removal of metals by magnetite crystallisation but produced this (relatively small) mineral deposit anyway. In other words, efficiency in other parameters of the hydrothermal system, such as metal dissolution or precipitation in a focussed ore body, compensated for the lack of Au in the parent magma
4. The Au, or some proportion of the Au, in the Inlice deposit did not originate from the same magma as exsolved the hydrothermal fluid, and instead the fluid scavenged

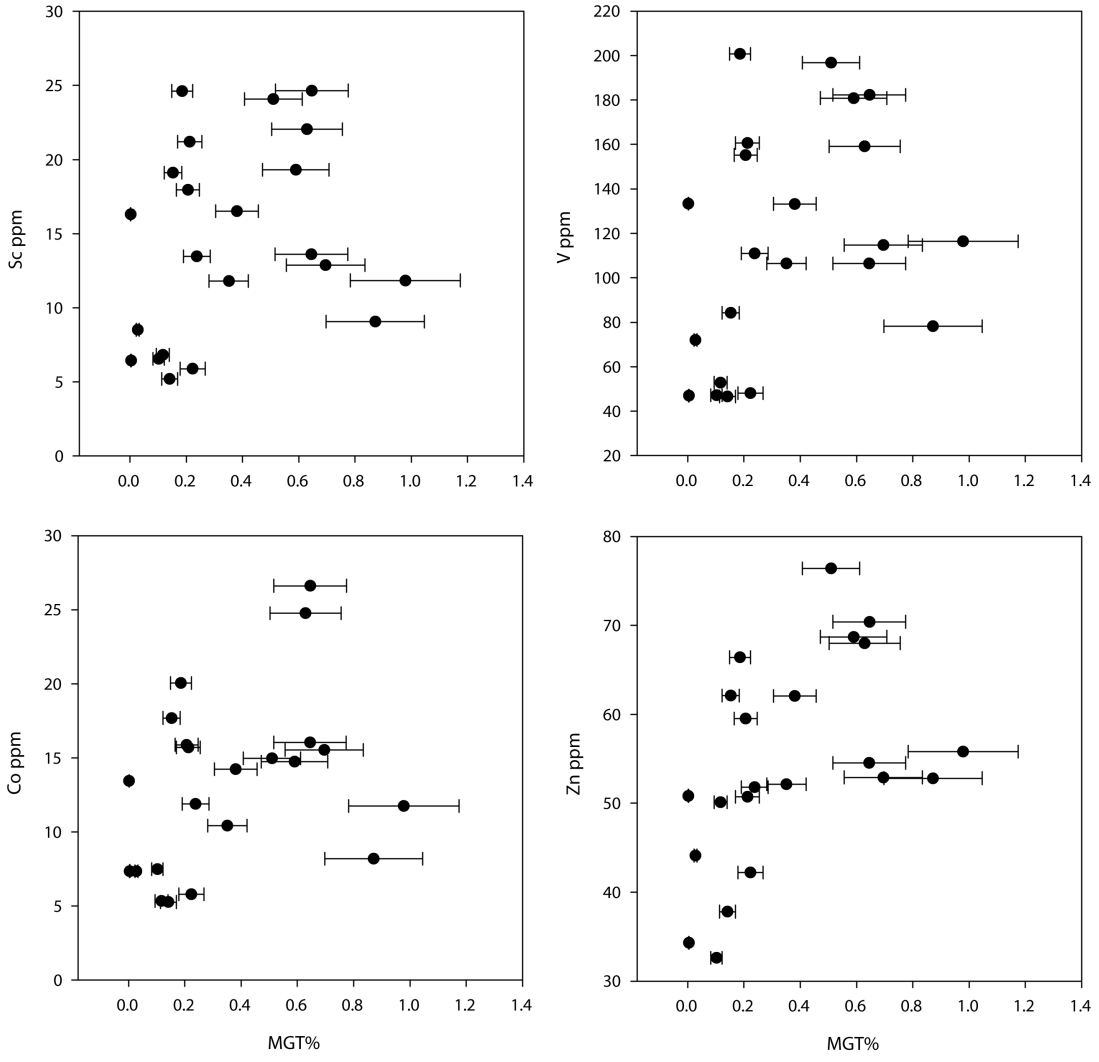

FIGURE 5.19: Selected trace elements vs magnetite content. Co, V, Sc and Zn are all strongly partitioned into magnetite and so a correlation might be expected. Strong correlations are not observed. Horizontal error bars represent an estimated 20% error on magnetite content.

metals from the surrounding host rocks which might include high level mafic melts or cumulates that have retained Au content.

The likelihood of these scenarios is discussed below:

(1) Given the remarkable similarity in mineral composition and geochemical evolution of the KVC samples, it seems unlikely that a melt would behave differently to the samples collected. The only samples that stand out are the low-Fe group, which contain less Fe for their SiO_2 content than the other rocks in the suite. However, these rocks do not contain particularly low magnetite proportions - in fact one contains the most magnetite out of all

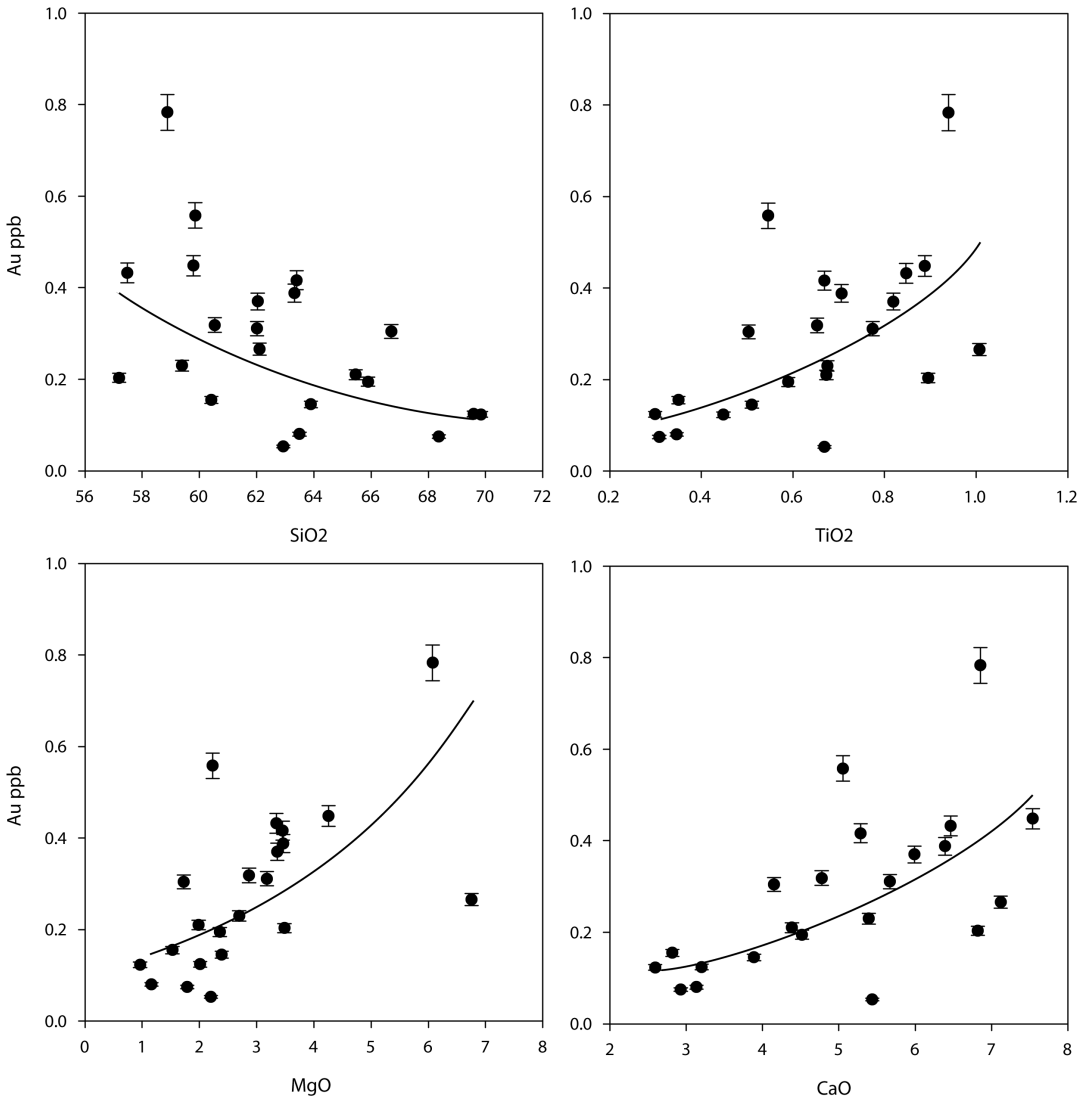

FIGURE 5.20: Trends in Au vs SiO_2, MgO, TiO_2 and CaO. Curves describe the logarithmic best fit lines. Major oxides in wt%.

the rocks at 0.98% by volume. In a similar way, (2) requires a reason that magnetite within a particular melt physically behaved differently to magnetite within the other melts of the KVC. (3) and (4) seem more likely, and the two can work together as long as free ligands exist to scavenge metals from the surrounding host rock. One particularly viable source rock could be magnetite-rich cumulates, suggested to exist since magnetite proportions decrease with melt evolution. Amphibole and pyroxene-rich clusters observed in some thin sections may give some idea as to what these cumulates may look like (Fig. 5.10). They generally contain at least 10% magnetite, often as large (0.3 mm) anhedral grains between sub to euhedral grains of amphibole or pyroxene. If such a cumulate contains

magnetite derived from a rock like K060, which contains 0.6% magnetite and 0.8 ppb Au, assuming the magnetite grains contain the majority of the Au, the cumulate could contain 13 ppb Au at 10% magnetite and 26 ppb Au at 20% magnetite. This represents a significant enrichment over the primary magma and a particular fertile source of Au for any scavenging fluid. Other authors have noted that a delay in magnetite crystallisation could be beneficial to the metal content of an exsolving fluid, but these data suggest that the early crystallisation of magnetite could create a Au-rich cumulate in a form that is readily available to a scavenging hydrothermal fluid (Fig. 5.21). Magnetite is easily soluble by fluids capable of mobilising Au (e.g. Gammons and Williams-Jones 1997). Alternatively, the cumulate could be assimilated into a subsequent magma which would then increase the Au concentration of that magma, although we see no direct evidence of this in the KVC. If 90% of the Au is present within the cumulate, this would almost double the concentration of Au in similar sized magma if all the cumulate is assimilated.

5.8.1 The partitioning of Au between magnetite and melt

Assuming magnetite crystallisation is the primary cause of the removal of Au with differentiation in these lavas, we can examine the process of partitioning using a Rayleigh fractionation model. The partition coefficient $D_{Au}^{Mt/melt}$ has been experimentally determined to be ~4 (Simon et al., 2003), and using this value magnetite crystallisation in a basaltic melt could account for 14-54% reduction in Au concentration for 1-5% modal abundance of magnetite, if fractionation is allowed to proceed to 90%. In contrast, magmatic differentiation in the KVC can be seen to remove at least 70-80% of the Au from the melt at modal abundances of no more than 0.8% magnetite. This may be an underestimate since we do not know the Au concentration of the parent melt. The Rayleigh fractionation equation is used:

$$m_{Au}^{melt} = m_{Au}^{melt,initial} \times F^{\bar{D}} \tag{5.5}$$

where m is the mass of Au in the melt, F is the fraction of melt remaining and $\bar{D}$ is the bulk partition coefficient. The model makes several assumptions: only magnetite is sequestering Au; there is no exsolution of a fluid which could potentially remove Au from the melt; a rhyolitic composition is reached by 90% crystallisation of an olivine tholeiite parent magma; crystallisation of magnetite is ongoing and removed from the melt, as per the conditions of the Rayleigh fractionation model. This model, with a $\bar{D}$ of 0.054, incorporating 0.8% modal abundance of magnetite and $D_{Au}^{Mt/melt}$ of 4, can only account for 12% loss of Au by magnetite crystallisation (Fig. 5.22). Gold loss of 70% is only achieved when $D_{Au}^{Mt/melt}$ is

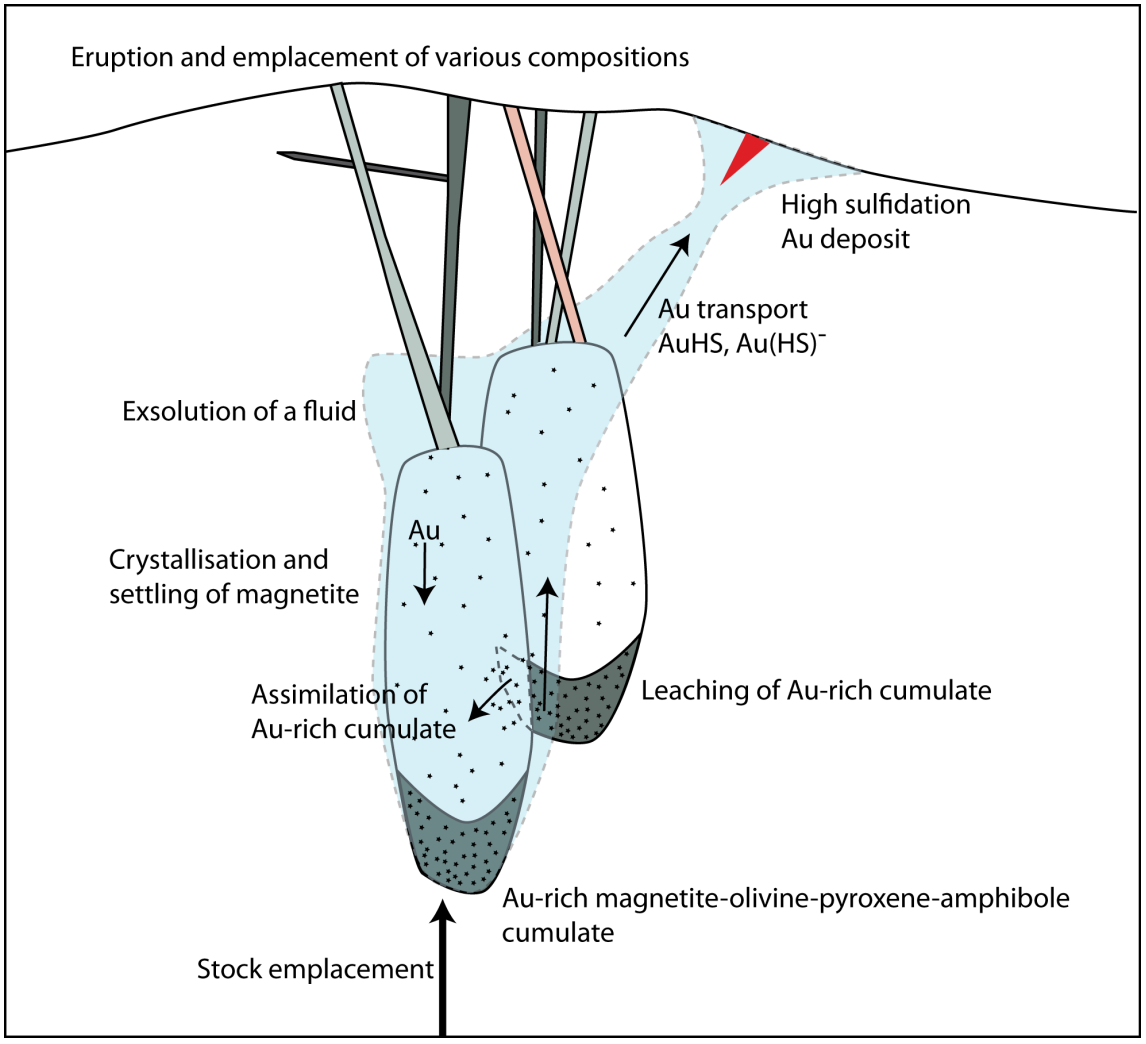

FIGURE 5.21: The above model depicts the emplacement of a porphyry stock beneath the KVC which then produces a Au-rich magnetite-bearing cumulate by early magnetite crystallisation and fractionation. Such a process may provide a source of Au for any scavenging S-rich fluid or increase the concentration of gold in a subsequent magma by assimilation.

raised to 38.4. In addition, the fractionation at the KVC is unlikely to have progressed to 90% crystal fraction since only melts up to dacite composition (70% SiO_2, Temel et al. 1998) have been recorded. A $D_{Au}^{Mt/melt}$ of approximately 97 is required to cause an 70% reduction in Au concentration at F = 0.4, which might result in a dacitic melt. These values are similar to the values of 13 to 127 suggested by magnetite crystallisation in lavas of the Izu-Oshima and Osoreyama volcanics (Togashi and Terashima, 1997).

There is a significant discrepancy between the $D_{Au}^{Mt/melt}$ of ~4 determined by Simon et al. (2003) and the data measured at the KVC. The experimental $D_{Au}^{Mt/melt}$ was determined by equilibrating a magnetite-bearing, Au-saturated rhyolitic melt in a gold capsule at 800°C, 140 MPa and over a time period of 2 hours. However, results were quite variable with

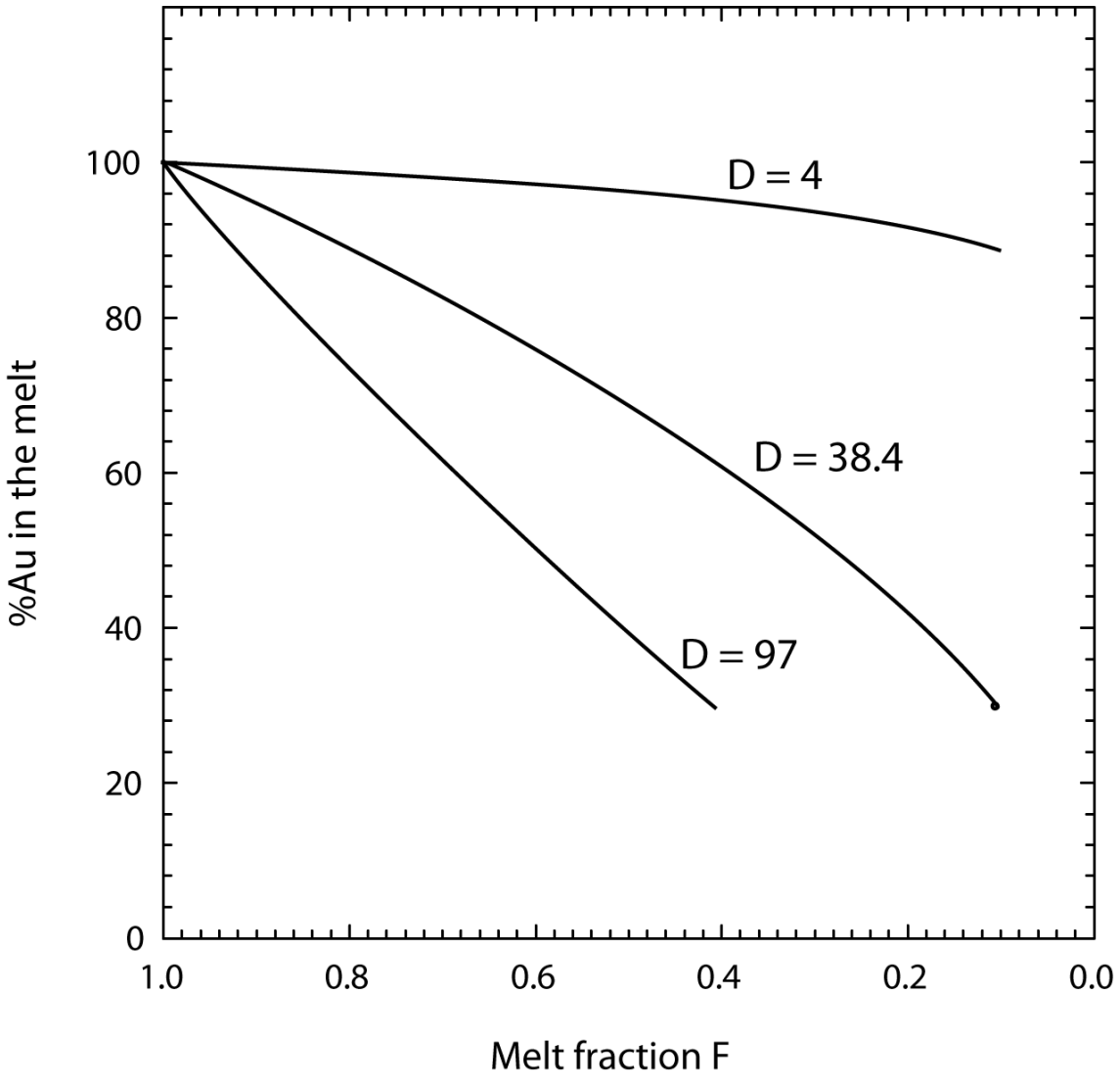

FIGURE 5.22: Melt fraction vs Au in the melt for modelling closed system Rayleigh fractionation of magnetite crystallisation. The published $D_{Au}^{Mt/melt}$ of 4 can only account for 12% loss of Au from the melt portion. A $D_{Au}^{Mt/melt}$ of 38.4 can produce a 70% reduction. However, these models require 90% crystallisation of the melt. A dacitic melt is more likely at around 60% crystallisation, in which case $D_{Au}^{Mt/melt} = 97$ is required to produce the observed loss of Au.

one magnetite recording a $D_{Au}^{Mt/melt}$ of 27. The magnetite which crystallised reached sizes of 4 to 12 μm. It has also been shown that magnetite precipitating from a hydrothermal fluid primarily holds Au within a 330 nm thick nonautonomous phase (NP) on the surface of the crystal, where Au is probably held within Fe-free sites in goethite and nanometre sized domains in wuestite (Tauson et al., 2012). This NP was shown to contain around 2000 ppm Au and consequently the bulk partition coefficient is significantly increased by its presence. Since surface area is inversely proportional to volume, the presence of an NP in the experimentally grown 4 to 12 μm magnetite would have greatly increased the Au

concentration of the magnetite. For example, an 8 μm spherical magnetite crystal with a 330 nm thick NP containing 2000 ppm Au would contain 271 μg/g Au, resulting in a bulk $D_{Au}^{Mt/melt}$ of 542. In comparison, under the same conditions, a 500μm magnetite, typical of a natural magmatic grain, would have a $D_{Au}^{Mt/melt}$ of 12. Therefore the presence of an NP has a strong potential to effect the bulk partitioning of Au between a magnetite crystal and a silicate melt. The discrepancy between the natural and experimentally derived data could be explained by either the naturally occurring magnetite having an NP whilst the experimentally grown magnetite does not, or that the NP of the experimentally grown magnetite does not have time to equilibrate during the 2 hours growth time.

Alternatively, the discrepancy could be explained by a weakness in the analysis shown here. A phase other than magnetite might be responsible for Au loss. No silicate phases have been implicated in strongly partitioning Au from the melt, but sulphide phases have. Only one, small (<0.1mm) grain of sulphide was observed in polished sections, implying sulphides do not play a major role in this system. Fluid exsolution has not been accounted for here and it may be that some of the reduction could be attributed to this process.

5.9 Conclusions

- Lavas of the Konya volcanic complex show a large range in Au content, with the most Au-rich lavas having 11 times more Au than the most Au-poor. This suggests that Au content of the leached rocks in a hydrothermal system could play a role in the Au content of hydrothermal fluids and thus the size of any Au deposit which may form.
- Au content also correlates well with indices of magma evolution such as SiO_2, MgO, CaO and K_2O. This indicates Au is removed from the melts whilst fractional crystallisation is ongoing.
- Fractionation trends suggest as much of 70-80% of the Au may be removed over the range of SiO_2 contents observed.
- In rocks surrounding the Inlice mineral deposit, magnetite is a replacement phase during alteration and this may mask any relationship between Au and magnetite content. Care should be taken when examining the relationship between Au and magnetite to only use primary magmatic magnetite.
- The notion that magnetite removes Au from the melt leads to the possibility of Au-bearing cumulates at depth. Such cumulates could contain many more times the amount of Au than the primary magma. Pre-enrichment of Au in this way would provide the ideal source rock for any Au-scavenging hydrothermal fluid in which magnetite is soluble, or for enriching a melt being emplaced in the crust.
- Despite removal of Au from the primary melt, the KVC hosts a mineral deposit and so the process of Au sequestering by magnetite may not be detrimental to developing a mineral deposit, and may even be beneficial if Au-rich cumulates form.
- It is hard to explain the extent of Au removal observed using published $D_{Au}^{Mt/melt}$. It might be that the bulk $D_{Au}^{Mt/melt}$ is enhanced by a nonautonomous phase on the surface of the magnetite crystal with a much higher partition coefficient for Au.

5.10 Data table

TABLE 5.4: Table of data for KVC samples. Major oxides in wt%, trace elements in ppm except Au in ppb.

	K002	K005	K008	K009	K012	K013	K015	K020	K022	K023
MGT citing	g		glr	gm	glr	glr	g	gm	glr	glr
Au ppb	0.3	0.39	0.2	0.43	0.1	0.11	0.12	0.15	0.43	0.14
SiO_2	66.71	60.3	67.35	57.49	69.03	70.41	69.84	63.9	65.34	65.89
TiO_2	0.5	0.84	0.59	0.85	0.63	0.46	0.45	0.51	0.62	0.55
Al_2O_3	14.43	16.23	15.58	16.11	16.19	14.21	14.11	13.95	15.55	15.12
Fe_2O_3	3.66	6.49	4.84	6.8	4.75	3.61	3	3.86	4.73	4.55
MnO	0.07	0.11	0.06	0.12	0.1	0.1	0.03	0.09	0.08	0.09
MgO	1.73	4.5	2.25	3.35	1.04	1.72	0.96	2.39	3.05	2.85
CaO	4.15	7.27	4.33	6.46	2.62	3.17	2.59	3.89	3.88	4.64
K_2O	3.14	2.54	3.25	2.44	3.58	3.73	3.81	3.4	3.23	3.17
Na_2O	3.1	2.79	3.32	3.07	2.62	2.9	3.01	2.85	3.06	2.97
P_2O_5	0.18	0.19	0.22	0.25	0.18	0.16	0.19	0.18	0.23	0.21
sum	97.64	101.26	101.78	96.92	100.73	100.47	98	95.02	99.78	100.02
Li	18.11	17.12	26.53	12.42	20.08	35.81	40.75	24.84	21.33	29.13
Sc	8.52	21.6	11.7	19.31	11.43	9.12	6.82	9.06	11.55	10.98
V	71.93	166.96	100.79	180.8	59.92	74.16	52.69	78.19	110.75	99.27
Cr	6.23	67.16	13.9	7.32	9.77	11.07	8.12	9.85	16.76	13.82
Co	7.34	19.95	10.11	14.73	10.09	7.69	5.33	8.19	9.48	10.68
Ni	3.31	23.79	10.26	4.49	4.47	5.87	4.26	4.22	8	7.53
Cu	5.42	47.98	12.21	12.14	10.04	8.57	5.31	5.39	14.38	14.42
Sr	554.12	556.57	625.42	704.3	462.3	438.08	448.27	519.72	655.92	604.04
Y	22.31	30.7	26.29	26.82	20.13	31.49	29.57	23.28	28.69	23.79
Nb	14.14	13.11	14.55	13.37	15.27	15.39	19.74	14.51	14.12	14.09
Mo	0.43	1.74	0.57	1.61	0.56	0.75	0.47	2.21	0.65	0.48
Sn	1.92	2.16	1.6	1.77	1.7	2.29	2.6	1.98	1.78	1.76
Cs	3.45	5.4	4.74	4.02	5.47	6.7	10.2	6.57	4.47	4.96
La	37.31	34.48	47.89	49.96	49.82	49.38	47.54	45.17	50.57	47.05
Ce	67.37	65.3	83.57	94.41	90.4	84.72	85.93	80.22	84.77	83.76
Pr	7.39	7.64	9.34	10.26	9.5	9.12	9.61	8.58	10.01	9.06
Nd	25.49	27.97	32.05	36.74	32.22	30.97	33.84	28.95	34.93	31.28
Sm	4.48	5.51	5.52	6.55	5.35	5.38	5.95	5	6.15	5.38
Eu	1	1.3	1.21	1.6	1.24	1.05	1.28	1.07	1.36	1.17
Gd	3.8	5.12	4.62	5.44	4.08	4.7	5.08	4.14	5.28	4.54
Tb	0.57	0.8	0.69	0.8	0.6	0.73	0.77	0.62	0.79	0.66
Dy	3.31	4.66	3.84	4.56	3.38	4.18	4.36	3.48	4.4	3.7
Ho	0.65	0.92	0.76	0.9	0.67	0.87	0.87	0.69	0.86	0.72
Er	1.88	2.68	2.14	2.55	1.89	2.46	2.49	2.01	2.45	2
Tm	0.28	0.39	0.31	0.38	0.29	0.36	0.37	0.3	0.35	0.29
Yb	1.95	2.65	2.14	2.48	1.93	2.44	2.54	2.06	2.34	1.97
Lu	0.27	0.39	0.3	0.38	0.29	0.36	0.36	0.3	0.33	0.29
Ta	1.33	1.26	1.32	0.96	1.51	1.63	1.87	1.5	1.3	1.31
Zn	44.1	66.3	56.3	68.7	54.1	69.6	50.1	52.8	60	64.8
Pb	20.4	20.6	21.9	21	25.5	28	32.6	25.7	23.5	26.4
Ba	879.3	635.5	1027.5	1096.7	1259.3	979.7	849.9	917.7	1043.4	1043.7
Rb	107.7	80.5	108.4	75.7	123	134	157	118.1	108.9	107.4
Zr	160.5	149.7	181.8	199.1	179.8	162.3	179.3	163.7	176.7	173.8
Th	14.6	16	19.8	15.4	24.6	22.9	20	23.3	20.4	19.2
U	5.8	5.3	5.5	4.3	7.1	5.7	9.1	6.9	5.8	5.1
Ga	17.3	18.1	17.9	19.2	18.2	17	17.7	17.1	18.6	17.6
MGT%	0.028		0.676	0.59	0.401	0.189	0.117	0.872		0.29

table 5.4 continued...

	K024	K026	K030	K033	K038	K039	K043	K048	K050	K053
MGT citing	glr	gm	gm	glr	gm	gm	gm	g	gm	gm
Au ppb	0.11	0.08	0.16	0.15	0.21	0.05	0.56	0.31	0.37	0.45
SiO_2	65.76	63.5	60.42	59.83	65.46	62.93	59.85	62.01	62.04	59.79
TiO_2	0.54	0.35	0.35	0.63	0.67	0.67	0.55	0.77	0.82	0.89
Al_2O_3	15.01	14.19	12.2	14.83	17.35	15.34	15.32	16.56	15.51	16.71
Fe_2O_3	4.57	2.72	2.61	4.93	5.44	5.11	4.37	5.97	5.9	7.13
MnO	0.08	0.09	0.06	0.09	0.11	0.1	0.09	0.11	0.09	0.11
MgO	2.48	1.16	1.53	2.44	1.99	2.2	2.23	3.18	3.36	4.26
CaO	4.41	3.14	2.82	5.05	4.38	5.44	5.06	5.67	5.99	7.54
K_2O	3.25	3.11	3.66	3	3.29	3.22	3.33	2.69	2.49	2.53
Na_2O	3.01	3.48	2.62	2.85	3	3.18	2.71	3.13	3.12	3.15
P_2O_5	0.21	0.17	0.13	0.3	0.28	0.27	0.24	0.28	0.18	0.38
sum	99.32	91.89	86.39	93.94	101.97	98.46	93.75	100.38	99.49	102.49
Li	28.18	21.43	18	22.89	17.14	14.51	19.96	14.93	10.36	12.74
Sc	11.4	5.89	5.18	15.56	13.61	12.87	11.84	19.11	21.21	24.63
V	101.13	48.04	46.6	106.2	106.43	114.7	116.41	84.14	160.62	200.7
Cr	14.12	3.33	5.86	25.69	20.43	16.73	8.87	44.1	65.76	48.36
Co	10.84	5.79	5.27	13.35	16.04	15.53	11.74	17.68	15.7	20.04
Ni	7.3	4.36	5.93	11.65	31.17	25.24	7.69	14.55	11.44	12.51
Cu	15.76	7.97	6.01	14.32	35.92	34.84	30.52	31.92	18.42	40.41
Sr	604.28	918.3	692.44	560.8	1095.67	1291.1	664.03	1228	504.66	894.7
Y	23.2	20.84	13.84	30.41	26.35	26.42	47.13	28.15	24.16	25.28
Nb	14.25	22.41	10.14	14.5	14.2	13.42	15.42	10.86	12.04	11.34
Mo	0.48	0.99	1.12	0.71	0.62	0.81	3.92	0.27	1	0.83
Sn	1.61	1.58	1.41	1.89	1.56	1.69	1.55	1.75	1.36	1.67
Cs	5.68	4.86	2.89	4.22	2.45	2.41	7.59	0.46	2.08	1.96
La	47.84	53.16	45.26	55.75	67.72	58.16	55.39	59.04	33.02	39.77
Ce	86.29	89.73	78.13	83.97	118.6	108.73	95.82	117.2	58.86	77.28
Pr	9.21	9.55	8.13	10.44	14.74	12.31	11.06	13.5	6.67	9.05
Nd	31.6	31.74	26.63	35.97	51.48	43.35	38.84	50.06	23.76	34.31
Sm	5.37	5.06	3.88	6.13	8.2	7.08	6.87	8.66	4.56	6.38
Eu	1.2	1.21	0.96	1.41	1.88	1.65	1.45	2.13	1.14	1.6
Gd	4.37	3.73	2.92	5.11	5.95	5.26	6.1	6.4	4.11	5.21
Tb	0.65	0.55	0.39	0.76	0.8	0.72	0.93	0.88	0.64	0.74
Dy	3.6	3.12	2.13	4.38	4.34	4.07	5.43	4.72	3.69	4.15
Ho	0.7	0.62	0.4	0.89	0.81	0.78	1.14	0.91	0.75	0.82
Er	1.97	1.81	1.17	2.53	2.28	2.23	3.47	2.49	2.17	2.28
Tm	0.28	0.28	0.18	0.38	0.33	0.33	0.52	0.36	0.31	0.33
Yb	1.88	2	1.26	2.51	2.28	2.34	3.6	2.39	2.2	2.21
Lu	0.28	0.31	0.19	0.39	0.33	0.34	0.55	0.35	0.31	0.33
Ta	1.31	1.61	0.79	1.43	1.29	1.26	1.63	0.99	1.05	0.93
Zn	61.4	42.2	37.8	46.8	54.5	52.9	55.8	62.1	50.7	66.4
Pb	24.2	28.5	24.9	27	18.9	18.2	24	17.3	11.1	14.7
Ba	1057.3	1334	1396.1	950.1	1246	1144.1	961.2	1159.6	736.5	1043
Rb	112.4	97.6	82	108.6	98.1	95.9	126.2	41.7	76.8	81.3
Zr	177.1	158.5	130.5	164.1	196.2	187.3	180	194.2	135.3	173
Th	20.7	19.9	18.3	23.3	25.5	24.6	31.7	21.9	13.9	15.2
U	5.2	8	4.8	6.8	6.1	5.5	9.8	2.8	4.1	4.9
Ga	16.9	18.5	16.3	17.1	20.3	20	17.5	19.6	18.3	19.3
MGT%	0.456	0.223	0.141	0.467	0.645	0.696	0.979	0.153	0.213	0.186

table 5.4 continued...

	K055	K060	K062	K064	K065	K066	K067	K068	K073	K074
MGT citing	gm	gm	gm	g	g	gm	gm	glr	g	glr
Au ppb	0.39	0.78	0.27	0.07	0.12	0.23	0.2	0.11	0.19	0.3
SiO_2	63.32	58.88	62.1	68.37	69.58	59.39	57.2	65.66	65.89	64.03
TiO_2	0.71	0.94	1.01	0.31	0.3	0.68	0.9	0.79	0.59	0.58
Al_2O_3	17.54	14.46	15.51	13.67	13.63	14.9	16.2	17.02	15.21	14.74
Fe_2O_3	5.97	6.35	6.65	2.58	2.53	5.31	7.4	6.63	4.5	4.48
MnO	0.1	0.1	0.1	0.06	0.06	0.1	0.12	0.11	0.07	0.07
MgO	3.47	6.08	6.76	1.79	2.01	2.7	3.49	1.89	2.36	2.25
CaO	6.39	6.85	7.12	2.93	3.2	5.39	6.82	4.8	4.52	4.49
K_2O	2.57	3.27	3.35	3.51	3.38	2.72	1.97	2.5	3.13	3.15
Na_2O	3.48	3.13	3.45	3.23	3.42	2.87	2.96	2.98	3.16	3.03
P_2O_5	0.24	0.37	0.38	0.13	0.15	0.25	0.2	0.16	0.22	0.22
sum	103.8	100.42	106.42	96.58	98.26	94.31	97.25	102.52	99.63	97.03
Li	12.28	11.43	12.32	24.26	25.22	15.1	11.85	9.22	28.07	29.65
Sc	17.95	22.04	24.65	6.55	6.44	16.31	24.08	22.2	11.8	11.75
V	155.21	159.08	182.2	47.17	46.9	133.34	196.7	104.37	106.48	103.2
Cr	10.29	152.94	174.3	11.65	11.06	12.29	16.97	18.92	16.9	14.23
Co	15.88	24.76	26.61	7.48	7.35	13.44	14.97	14.4	10.42	10.73
Ni	9.89	58.09	65.76	22.5	22.26	3.97	5.35	4.49	8.59	7.52
Cu	24.56	50.39	66.36	12.55	14.84	10.96	11.6	9.65	12.66	12.65
Sr	789.92	1297.39	1387	943.3	951.3	749.79	977	509.84	688.1	689
Y	26.4	25.21	23.92	15.27	15.13	22.54	28.81	27.29	25.9	23.12
Nb	14.13	12.09	12.23	13.03	12.73	9.84	7.5	10.15	13.75	13.7
Mo	1.21	1.3	0.77	1.01	1.02	1.31	1.31	0.53	0.81	0.66
Sn	1.51	1.69	1.58	1.3	1.25	1.32	1.21	1.49	1.87	1.59
Cs	2.56	2.53	1.98	5.88	5.72	3.57	1.72	1.31	4.57	5.18
La	50.12	57.55	61.01	42.06	40.15	31.88	32.53	36.68	49.39	47.25
Ce	88.98	115.64	121.4	71.81	70.97	60.85	66.81	60.82	81.55	83.52
Pr	10.12	13.84	14.24	7.63	7.34	7	8.09	7.82	9.54	9.06
Nd	35.91	51.78	52.76	25.83	24.74	25.53	31.06	28.42	33.33	31.25
Sm	6.18	8.76	8.77	4.09	3.97	4.69	5.96	5.37	5.79	5.38
Eu	1.45	2.1	2.18	1.01	0.99	1.26	1.57	1.34	1.3	1.27
Gd	4.99	6.38	6.28	3	2.9	4.01	5.22	4.62	4.87	4.39
Tb	0.72	0.81	0.81	0.43	0.42	0.6	0.77	0.74	0.72	0.64
Dy	4.07	4.24	4.22	2.38	2.35	3.48	4.59	4.2	3.99	3.67
Ho	0.78	0.78	0.78	0.46	0.46	0.69	0.93	0.84	0.78	0.73
Er	2.26	2.13	2.08	1.31	1.29	2.01	2.67	2.48	2.19	2
Tm	0.33	0.3	0.3	0.2	0.2	0.3	0.4	0.36	0.31	0.3
Yb	2.26	1.96	1.9	1.36	1.35	2.06	2.65	2.42	2.14	1.98
Lu	0.33	0.27	0.28	0.21	0.21	0.3	0.4	0.35	0.3	0.29
Ta	1.3	0.85	0.78	1.08	1.05	0.84	0.54	0.93	1.26	1.23
Zn	59.5	68	70.4	32.6	34.3	50.82	76.4	55.1	52.1	53.1
Pb	17.6	19.7	19.6	28.1	28.3	13.48	10.2	11.3	22.4	21.7
Ba	1011.4	982.6	949.1	1056.1	1085.9	654.24	556	744.3	1008.7	1017.6
Rb	86.3	88.9	96.5	97.7	98.6	74.08	49.4	72.7	104.3	106.1
Zr	174.5	226.2	234	128.4	128.3	139.1	169.4	143.7	177.8	176.3
Th	20.2	18.5	18.3	15.3	15.6	11.44	9.5	13.4	20	18.8
U	6	4.3	4.3	5.9	6.1	3.72	2.1	3.5	5.5	5.7
Ga	18.8	19	19	17.2	16.8	18.44	19.4	19.6	18.3	17.7
MGT%	0.206	0.629	0.646	0.102	0.004	0.002	0.51	0.495	0.351	0.55

table 5.4 continued...

	K076	K078	K079	K081	K084	K085	K087	K091	K092	K093
MGT citing	glr	glr	g	glr	glr	glr	glr	glr	gm	gmlr
Au ppb		0.07	0.32	0.39	0.1	0.1	0.18	0.08	0.42	0.1
SiO_2	66.45	68.2	60.54	64.29	65.27	65.69	65.3	65.4	63.39	65.68
TiO_2	0.6	0.6	0.65	0.58	0.59	0.59	0.54	0.56	0.67	0.67
Al_2O_3	15.22	15.55	14.62	14.55	14.89	15.06	14.99	15.07	15.54	15.39
Fe_2O_3	4.87	4.99	4.93	4.57	4.99	4.73	4.46	4.29	5.53	5.56
MnO	0.1	0.06	0.1	0.1	0.09	0.07	0.08	0.06	0.1	0.09
MgO	2.36	1.92	2.87	1.78	2.32	2.27	2.69	4.04	3.45	2.22
CaO	4.52	4.31	4.77	4.36	4.48	4.66	4.48	4.79	5.28	4.49
K_2O	3.2	3.26	3.18	3.3	3.23	3.15	3.2	3.34	3.05	3.39
Na_2O	3.23	3.24	2.67	2.96	3.11	3.25	3.12	2.86	3.06	2.9
P_2O_5	0.21	0.21	0.24	0.21	0.22	0.21	0.21	0.2	0.23	0.23
sum	100.77	102.34	94.57	96.7	99.19	99.68	99.08	100.62	100.31	100.61
Li	27.19	28.32	21.24	22.02	24.22	23.67	29.68	30.71	23.54	19.24
Sc	12.57	12.05	13.46	13	11.89	11.57	11.72	10.95	16.51	16.39
V	109.3	102.34	110.95	106.1	107.73	98.25	98.75	95.33	133.2	131
Cr	13.18	15.06	12.3	17.31	13.14	11.83	11.36	11.98	20.24	14.83
Co	11.6	9.54	11.88	11.73	10.52	10.55	10.46	9.15	14.22	13.45
Ni	10.9	7.91	6.23	9.13	8.52	8.09	5.73	6.32	7.57	6.94
Cu	16.75	12.72	10.07	15.17	16.19	10.9	12.28	10.26	29.29	25.93
Sr	720	619.23	796.32	698.7	679.77	700.54	631.22	611.72	1000	942.1
Y	23.55	25.13	25.66	24.65	24.98	24.15	23.69	21.1	24.84	22.81
Nb	14	14.46	13.55	14.52	13.73	13.53	13.97	13.72	13.51	13.59
Mo	0.78	0.83	1.81	0.74	0.51	0.79	0.45	0.54	1.33	0.68
Sn	1.59	1.83	1.99	1.76	1.73	1.8	1.59	1.65	1.71	1.75
Cs	5.39	5.03	5.52	5.22	4.64	5.04	5.07	5.17	4.87	4.63
La	46.99	47.31	53.12	49.2	46.75	45.98	47.66	47.36	55.27	54.33
Ce	85.06	82.31	96.2	88.61	83.13	82.04	85.84	85	102.4	98.96
Pr	9.11	9.27	10.55	9.45	9.19	9.02	9.19	9.02	10.91	10.68
Nd	31.87	32.18	36.7	32.67	31.94	31.22	31.38	30.6	37.87	37.08
Sm	5.59	5.61	6.09	5.62	5.54	5.49	5.42	5.16	6.32	6.13
Eu	1.3	1.22	1.38	1.31	1.23	1.26	1.23	1.19	1.48	1.44
Gd	4.53	4.59	4.98	4.62	4.61	4.57	4.37	4.12	4.85	4.72
Tb	0.66	0.68	0.7	0.67	0.68	0.66	0.65	0.6	0.7	0.68
Dy	3.74	3.8	4	3.83	3.85	3.69	3.68	3.39	3.97	3.82
Ho	0.72	0.74	0.78	0.77	0.74	0.72	0.72	0.65	0.78	0.74
Er	2.05	2.1	2.22	2.14	2.12	2.05	2.03	1.83	2.19	2.05
Tm	0.3	0.32	0.33	0.31	0.31	0.3	0.29	0.28	0.33	0.3
Yb	1.97	2.04	2.23	2.08	2.09	2.04	1.98	1.8	2.18	2.01
Lu	0.29	0.3	0.31	0.31	0.3	0.28	0.29	0.26	0.33	0.29
Ta	1.25	1.37	1.27	1.3	1.28	1.26	1.29	1.26	1.19	1.19
Zn	52	57.6	51.8	51	53.1	56.2	58.9	47.4	62.05	54.8
Pb	19.4	19.5	23	21.5	19.8	21.5	23.4	23.2	23.2	21.6
Ba	1053.5	1025.9	1105.4	1107	1015.65	979.7	1014	1023.6	1262.65	1316.5
Rb	107.2	107.4	101.1	114.7	106.1	103.7	108.4	114.2	93.75	108
Zr	181.8	186.8	176.7	175.2	173.2	175.9	178.3	172.5	177.4	179.5
Th	19.4	21	21.6	20	19.35	19.6	19.7	20	21.8	21.4
U	5.9	5.6	6.1	5.9	5.7	5.5	6.1	5.9	5.3	5.9
Ga	17.7	17.9	18.2	18.8	18.5	18.1	18.1	17.4	18.5	18.7
MGT%	0.252	0.474	0.238	0.262	0.159	0.492	0.284	0.394	0.38	0.234

TABLE 5.5: Thin section descriptions. Ol = olivine, Opx = orthopyroxene, Cpx = clinopyroxene, Hbl = hornblende, Bi = biotite, Plag = plagioclase, Qtz = quartz, Mgt = magnetite, py = pyrite.

Sample	Ol %	mm	Opx %	mm	Cpx %	mm	Hbl %	mm	Bi %	mm	Plag %	mm	Qtz %	mm	Minor phases
K002									5	1			10	2	mgt
K008							5	3	20	3	40	4			mgt
K009							20		5		20				mgt
K012									10	3	40	5	10	2	mgt
K013			5	2					10	3	30	5			mgt
K015							10		10	3	30	6	10	1	mgt
K020					2	2	5	2	10	3	30	4			mgt
K022							5	2	10	3	40	5			mgt
K023									5	3	35	5			mgt
K024											30	5			mgt
K026							10	2	10	2	20	4			mgt
K030							10	4	10	3	15	4	20	2	mgt
K033					3	1	5	2	5	2	20	5			mgt
K038	3	1	3	2	3	2			2	2	30	4			mgt
K039			10	2	5	1	2	2	5	3	20	3			mgt
K043			5	2	15	1			3	3	50	5			mgt
K048									5	2	20	4			mgt
K050			3	3	3	2	5	3	5	2	20	5			mgt, Feoxide
K053	2	1	5	2							10	5			mgt
K055			5	2	5	2	3	4			20	5			mgt
K060			10	3			20	4	5	1	5	4			mgt,py
K062			5	2	5	1	30	3	10	2					mgt. Feoxide
K064							20	3	5	3	5	4			mgt
K065							20	2	5	3	5	5			mgt
K066			5	2	5	3	5	3	3	3	50	6			mgt
K067			5	2	5	2	10	2			60	5			mgt
K068							10	4	5	2	30	6	5	2	mgt
K073							5	3	10	2	30	4			mgt
K074							5	2	5	3	40	3			mgt
K076									10	3	30	3			mgt
K078									5	3	40	3			mgt
K079							20	2	5	2	35	4			mgt,py
K081									5	2	40	5			mgt
K084									5	2	35	5			mgt
K085									10	3	35	4			mgt
K087									10	2	45	4			mgt
K091									10	3	45	5			mgt
K092							30	3	10	4	30	3			mgt
K093					2		20	3	5	2	20	4			mgt.Feoxide

table 5.5 continued...

Sample	Hbl %	Plag %	Micro-crystalline %	Glass %	Texture
K002			85		microcrystalline to amorphous silica groundmass
K008			35		Porphyritic with microcrystalline (silica) groundmass
K009			55		Porphyritic, vuggy
K012			40		Porphyritic, microcrystalline
K013			55		Porphyritic
K015			40		Porphyritic
K020			23	30	Porphyritic, flow banded. Botryoidal cryptocrystalline groundmass juxtaposed with glassy flow bands
K022			45		Porphyritic
K023			60		Porphyritic
K024			70		Porphyritic
K026		2	58		Porphyritic, flow banded.
K030			45		Porphyritic, fibrous flow texture
K033		10	57		Porphyritic
K038			59		Porphyritic
K039		20	38		Porphyritic with needles of plag(?) groundmass
K043				27	Porphyritic with glassy groundmass, flow banding
K048			75		Porphyritic with amphibole needles groundmass
K050		50	14		Porphyritic, plag groundmass
K053		70	13		Porphyritic, plag groundmass
K055		50	17		Porphyritic, plag groundmass
K060		40	20		Porphyritic, plag groundmass
K062		30	20		Porphyritic
K064		20	50		Porphyritic glassy groundmass (put % in microcrystalline but it's extremely fine)
K065		20	50		Porphyritic glassy groundmass (put % in microcrystalline but it's extremely fine)
K066		20	12		Porphyritic, plag groundmass
K067		15	5		Porphyritic, plag groundmass
K068			50		Porphyritic
K073			55		Porphyritic
K074			50		Porphyritic
K076			60		Porphyritic
K078			55		Porphyritic
K079			40		Porphyritic, vuggy and flow texture
K081			55		Porphyritic
K084			60		Porphyritic
K085			55		Porphyritic
K087			45		Porphyritic
K091			45		Porphyritic
K092	5	5	20		Porphyritic
K093	10	5	38		Porphyritic

table 5.5 continued...

Sample	Dis-equilibrium texture	Alteration	Mgt siting
K002		none	g
K008		Vuggy, decomposed amphibole and biotite, feldspar slightly decomposed, silicified groundmass	g,lr
K009		minor oxidation on vug rims	g,m
K012		Feldspars show altering of core to clay minerals	g,lr
K013		Silicification of groundmass	g,lr
K015		Silicified groundmass and clay-alteration of amphibole, biotite and some feldspar	g
K020		none	g,m
K022		Silicified groundmass, some clay alteration of feldspars, some vugs	g,lr
K023		Heavily silicified groundmass, replacement of a mafic phase, clay alteration of feldspars	g,lr
K024		Heavily silicified, virtually just plagioclase left.	g,lr
K026	Botryoidal cryptocrystalline overgrowths on all minerals	none	g,m
K030		none	g,m
K033	Feldspar rims on cryptocrystalline interior	oxidation of biotite, amphibole	g,lr
K038	overgrowth of opx and amphibole	perhaps some weathering	g,m
K039		slight clay alteration to margins of plagioclase	g,m
K043		none	g,m
K048		none	g
K050		none	g,m
K053		none	g,m
K055		none	g,m
K060		none	g,m
K062		none	g,m
K064		none	g
K065		none	g
K066		none	g,m
K067		none	g,m
K068		chloritisation of amphibole and biotite	g,lr
K073		weak silicification, clay alteration and oxidation mafic phases	g
K074		weak silicification, clay alteration and oxidation mafic phases	g,lr
K076		Amphibole destroyed, silicification and some clay alteration of feldspars	g,lr
K078		Amphibole destroyed, silicification and some clay alteration of feldspars	g,lr
K079		none	g
K081		Amphibole destroyed, silicification and some clay alteration of feldspars	g,lr
K084		Amphibole destroyed, silicification and some clay alteration of feldspars	g,lr
K085		Amphibole destroyed, silicification and some clay alteration of feldspars	g,lr
K087		Amphibole destroyed, biotite almost completely destroyed and heavy silicification	g,lr
K091		Amphibole destroyed, biotite almost completely destroyed and heavy silicification	g.lr
K092		none	g,m
K093		Oxidation of amphiboles	g,m,lr

Chapter 6

Fluid mixing and thermal regimes beneath the PACMANUS hydrothermal field, Papua New Guinea: helium and oxygen isotope data

6.1 Prologue

This chapter is based on a manuscript published in Earth and Planetary Science Letters (Webber et al. 2011).

6.2 Introduction

Ocean Drilling Program (ODP) leg 193 drilling of the PACMANUS hydrothermal field in the Manus Basin, Papua New Guinea, provided a unique insight into the sub-seafloor geology of an active felsic-hosted hydrothermal system (Barriga et al., 2007). Fluid inclusion and geochemical investigations of anhydrite veins, which persist to the deepest units recovered during drilling (386.7 mbsf), has yielded further information on temperature profiles and the geochemical characteristics of the hydrothermal fluids within the system. These data show that contrasting fluid chemistries and fluid mixing regimes were evident from sites of hydrothermal activity less than 1000 m apart. In particular, the chemistry

of hydrothermal fluids emanating on the seafloor at PACMANUS appear to be variably influenced by seawater-volcanic basement interaction, mixing with ambient and heated seawater, boiling and a local contribution of magmatic volatiles (e.g. Bach et al. 2003; Kim et al. 2004; Roberts et al. 2003; Vanko et al. 2004; Reeves et al. 2010).

Previous studies on seafloor vent sites have established that the $^{3}He/^{4}He$ isotope ratios of hydrothermal fluids are preserved when trapped as fluid inclusions by mineral phases such as pyrite and anhydrite and can therefore be used to trace fluid-rock interaction (e.g. Jean-Baptiste and Fouquet 1996; Stuart et al. 1994; Turner and Stuart 1992). Consequently, to establish a more robust understanding of the PACMANUS hydrothermal system, we completed helium isotope analyses of fluid inclusions within anhydrite and pyrite precipitates. These data were augmented by measuring the oxygen isotope ratios of the anhydrites. These new data allow us to test initial hypotheses on the nature of the hydrothermal regime at PACMANUS and further develop our understanding of sub-seafloor hydrothermal systems.

6.2.1 Geological Setting

The PACMANUS hydrothermal field is located along the crest of Pual Ridge in the East Manus Volcanic Zone (EMVZ) within the eastern part of the Manus back-arc basin, north of the New Britain subduction zone (Fig. 6.1) (Binns et al., 2007). Several minor and three major hydrothermal fields are recognized in the EMVZ: PACMANUS on Pual Ridge; DESMOS, about 23 km to the east and Susu Knolls, about 40 km east of PACMANUS (Barriga et al., 2000). Back arc spreading in the central Manus basin 160 km to the west of PACMANUS is characterized by mid-ocean ridge style spreading and produces melt of essentially MORB composition (Sinton et al., 2003). At the EMVZ the volcanic basement is more siliceous and of Eocene-Oligocene age, which formed when active subduction was directed southwestward along the now extinct Manus subduction zone. Extension in the EMVZ is currently occurring in a pull-apart fashion between the Djaul and Weitin sinistral transform faults. This extension has resulted in several recent volcanic edifices, including Pual Ridge, which show a progressive evolution from basaltic and basaltic andesite through to rhyodacitic composition, with geochemical traits which may either reflect crustal assimilation or a genetic relationship with the New Britain arc volcanic rocks (Sinton et al., 2003).

The PACMANUS field contains several discrete vent sites with active chimneys, iron-oxide mounds, and areas of diffuse venting (Binns and Scott, 1993). Fluid temperatures measured at the orifice of black or gray smokers and clear fluid sulphide chimneys range from 220 up to ~360°C. The end-member vent fluids exhibit variable salinities, low in-situ

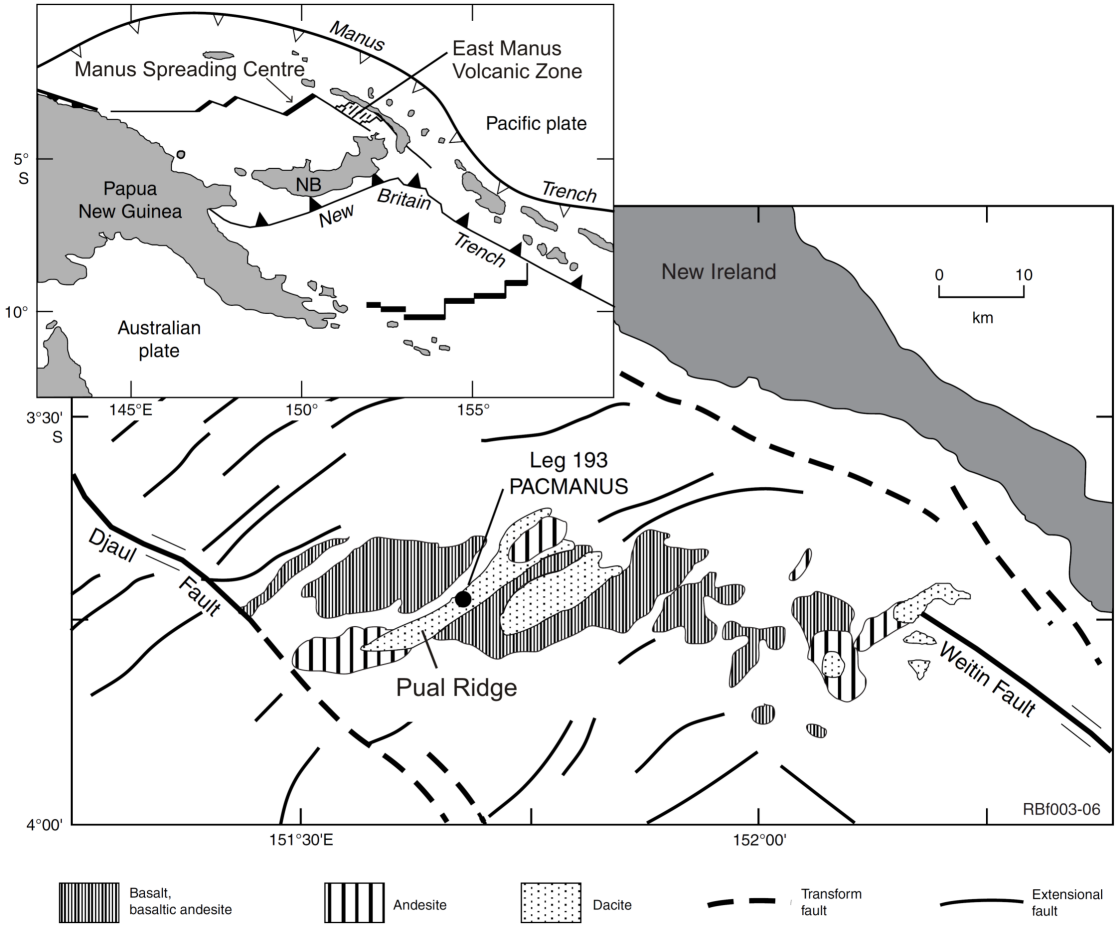

FIGURE 6.1: Map of the region surrounding PACMANUS, showing the tectonic setting (inset) and geology. PACMANUS is located on the rhyodacite-dacite Pual Ridge in the East Manus Volcanic Zone (EMVZ). NB = New Britain. Figure adapted from Binns (2004)

pH (∼3.5), variable and typically high concentrations of H_2S, CO_2 and CH_4, and elevated base metal concentrations (Douville et al., 1999; Ishibashi et al., 1998; Shitashima et al., 1997). A more complete review of vent fluid chemistry is presented in Reeves et al. (2010). Geochemical analyses of dredged chimney materials show elevated trace metals including Cu, Zn, Pb, Ba, Au, and Ag (Moss and Scott, 2001; Parr et al., 1996; Scott and Binns, 1995). The PACMANUS field has several separate vent sites which show contrasting venting characteristics, with the most significant sites at Snowcap, Roman Ruins, Satanic Mills and Fenway. The latter three are high temperature sites, with hydrothermal fluid temperatures commonly at 250°C but ranging up to 356-358°C at the Fenway vent site (Tivey et al., 2006; Seewald et al., 2006; Craddock and Bach, 2010). Snowcap is a low temperature venting site characterized by shimmering (∼6°C) venting and Mn-Fe crusts, although higher temperatures of 150-182°C emanate from discrete orifices (Tivey et al.,

2007; Craddock and Bach, 2010).

6.2.2 Prior Research

Coring during ODP Leg 193 showed that the active vent sites at Snowcap and Roman Ruins are capped by unaltered dacite and rhyodacite, ranging from 10 to 40 m thick, with a sharp underlying transition to pervasively altered rocks. Pyrite is a conspicuous disseminated mineral at the 1% to 5% level, except in the lower, somewhat less altered succession at Roman Ruins. Pyrite is also present in thin veins and vein networks and is especially prominent in a stockwork zone underlying the high temperature chimney site at Roman Ruins, where it forms centimeter-scale pods and veins of massive pyritic sulphide. Hydrothermal alteration varies with depth and between the two sites. At Snowcap, the most pervasive alteration comprises silica polymorphs, varying with increasing depth below the seafloor from opaline silica, through cristobalite, to quartz accompanied by clays (Lackschewitz et al., 2004). The clays are mostly illite, but there is also a significant amount of pyrophyllite (especially at higher levels) and chlorite (at depth); anhydrite and magnetite are abundant secondary phases. The consistent appearance of pyrophyllite within the Snowcap core suggests the passage of hydrothermal fluids of moderate temperatures and low pH (Reyes, 1990). At Roman Ruins the pervasive alteration involves quartz with illite, chlorite-smectite, K-feldspar, and sodic plagioclase. Little pyrophyllite and secondary magnetite is observed, and anhydrite is less abundant and mainly confined to veins. The quartz-, chlorite-, and feldspar-bearing alteration assemblages indicate higher fluid pH than at Snowcap. At both sites, quartz and chlorite become more abundant with depth.

Fluid flow is thought to be mainly fracture-controlled, as core-scale dacite permeability is low compared to vent fluid flux (Christiansen and Iturrino, 2007). Fractures within the system are primarily sub-vertical and show a preferred strike to the NNE, suggesting a tectonic control on fluid flow (Bartetzko et al., 2006; Iturrino et al., 2002). There are also numerous highly permeable volcaniclastic horizons within the volcanic pile, which are also suggested to exert a control on fluid flow (Paulick et al., 2004).

Temperature profiles have been calculated from oxygen isotope ratios of alteration minerals. The profiles show higher temperatures towards the top of the profile, explained by a strong advective heat transfer system and a lack of seawater infiltration due to the fresh dacite cap. Temperature profiles have also been calculated from fluid inclusion studies of vein anhydrites (Vanko et al., 2004). These show that the Snowcap site experiences a greater range of temperatures as the fluid approaches the surface, from 330-400°C at the base (∼400mbsf) to <100-300°C at the top of the profile, whereas temperatures at Roman

Ruins appear to be more restricted; 220-360°C throughout the section. Overall the fluid inclusion profile shows a general cooling trend towards the surface at Snowcap, in contrast to the mineral alteration temperature profile which shows higher temperatures at the top of the profile than at the base or mid-section (Lackschewitz et al., 2004).

Analysis of the $^{87}Sr/^{86}Sr$ ratios and $\delta^{34}S$ of anhydrite from within PACMANUS suggest that fluid mixing contrasts between the high temperature (Roman Ruins) and low temperature (Snowcap) sites. The $^{87}Sr/^{86}Sr$ (0.70487-0.708606) ratios predict mixing between a hydrothermal end-member and seawater, showing 0 to 89% seawater at Snowcap and 7 to 74% seawater at Roman Ruins during anhydrite precipitation. Overall the data suggest an increase in seawater content as the hydrothermal fluid approaches the surface, however the high variability of $^{87}Sr/^{86}Sr$ ratios at a given depth indicates a very heterogeneous mixing system (Bach et al., 2005; Roberts et al., 2003). Data from Snowcap indicate higher sulphate concentrations, which can be linked to a magmatic contribution by SO_2 dissociation (Roberts et al., 2003). Furthermore, Bach et al. (2003) and Craddock and Bach (2010) propose that the variation in REE content of anhydrite within the PACMANUS system reflects a waxing and waning input of magmatic volatiles (HF, SO_2) with associated variable complexation of REEs in the fluids. This is consistent with contrasting alteration assemblages at the two sites, with pyrophyllite at Snowcap indicative of low pH, and secondary feldspar at Roman Ruins suggesting higher pH. Contributions of substantial magmatic components into the EMVZ hydrothermal systems has also been suggested by the $^{87}Sr/^{86}Sr$, $\delta^{34}S$ and Pb isotope systematics of sulphide chimneys from both PACMANUS and Susu Knolls (Kim et al., 2004).

In 2006 an expedition to the EMVZ extensively sampled PACMANUS vent fluid (Reeves et al., 2010; Seewald et al., 2006; Tivey et al., 2006). Among many observations made, of interest here are constrained temperatures (272-341°C and 152-180°C for Roman Ruins and Snowcap, respectively), vent fluid $\delta^{18}O$ (1.1 to 1.6 and 1.2 to 1.8 for Roman Ruins and Snowcap, respectively) and an end-member $^{87}Sr/^{86}Sr$ for Roman Ruins of 0.70425. The study made several major advancements in the understanding of the PACMANUS system, including the interpretation from δD_{H_2O} isotope ratios that up to 20% of the venting fluid may be magmatic, advancing earlier interpretations by Roberts et al. (2003), Kim et al. (2004), Bach et al. (2003) and Craddock and Bach (2010).

Samples of basaltic glasses from the Manus Spreading Centre (MSC) indicate the mantle underlying the Manus Basin has a $^{3}He/^{4}He$ ratio above the MORB value of 8.75±2.14 R_A (Graham, 2002), with a mean of 12.6 ($1\sigma = 0.95$) if radiogenic values are excluded (<0.1 R_A). The presence of a plume beneath the Manus basin has been invoked to explain these relatively high ratios with respect to normal MORB (Macpherson et al., 1998, 2000).

However, the EMVZ basement shows lower $^3He/^4He$ ratios, more akin to arc crust, in the range between 0.61 and 6.44R_A, mean average 4.26 (Macpherson et al., 1998, 2000; Marty et al., 2001).

The Manusflux and Manaute cruises in 1995 and 2000, respectively, measured vent fluid He concentrations and ratios at the PACMANUS vent field (Fourre et al., 2006). The measured vent fluid ratios of 5.95 to 7.77 R_A, and concentrations from 1.7×10^{-7} to 2×10^{-6} cm^3 STP/g. These data describe a mixing line between hydrothermal fluid and seawater (see 6.5.1).

6.3 Methods

6.3.1 Drilling

Samples for this study were obtained by rotary coring of altered dacite and rhyodacite during ODP Leg 193 (Fig. 6.2, Binns et al. 2007). Total core recovery was 13.9% at Snowcap and 7.4% at Roman Ruins. Specimen depths are given as the depth to the top of the 10 m core that contained each specimen. Because of the recovery limitations, it is not known whether a given sample is from the top, middle, or bottom of the section, so depths are approximate. Samples are taken from sites 1188 (Snowcap) and 1189 (Roman Ruins), and in both cases two separate holes are combined to obtain the full sample depth; holes 1188A, 1188F for Snowcap and holes 1189A, 1189B for Roman Ruins. Of the two sites, Snowcap was the more successful, reaching a maximum depth of 386.7 m. The Roman Ruins hole achieved a depth of 206 m.

Samples analysed in this study cover the depth interval 49 to 363 m at Snowcap and 11 to 158 m at Roman Ruins and were selected to provide a good depth interval and using the best examples of anhydrite and pyrite veins.

6.3.2 Noble Gases

Anhydrite and pyrite mineral grains were hand picked under a binocular microscope before being transferred to a pneumatic crushing device. 0.5-1g of sample was crushed under vacuum to a fine powder ($\pm$ 100µm) to liberate gases trapped in the fluid inclusions. The crushing apparatus was cleaned with acetone to prevent contamination. The gas purification and analysis process is detailed in Stuart et al. (2000). Several blank measurements were taken to derive corrections, and pipettes of known concentrations of noble gases were used to derive abundances.

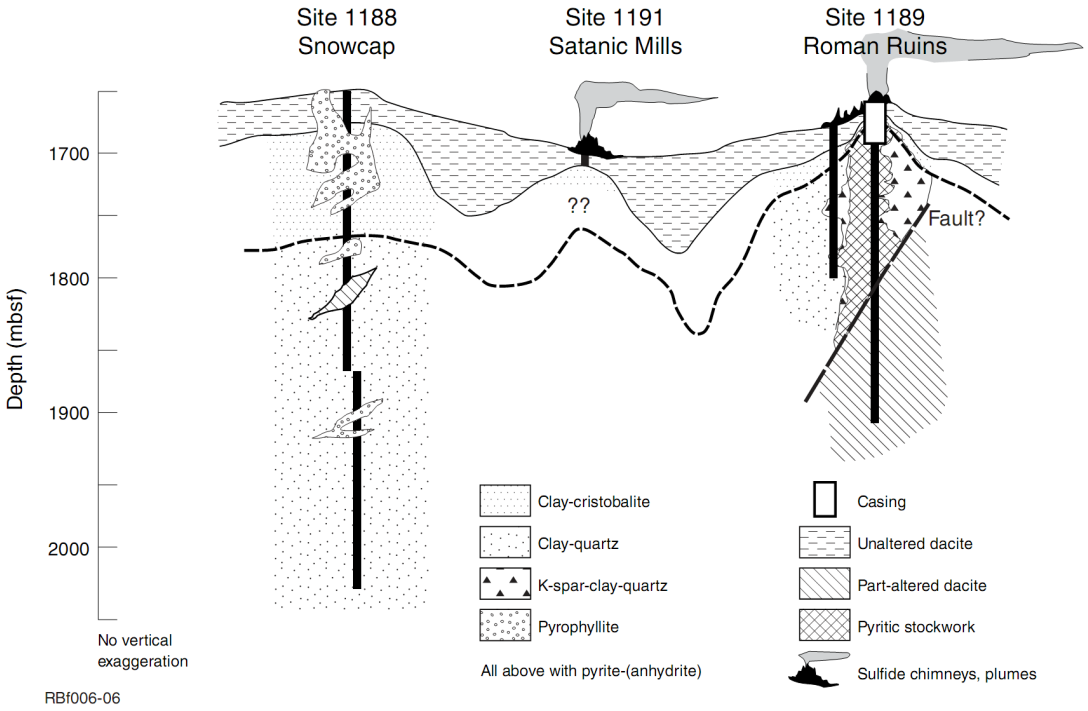

FIGURE 6.2: Schematic section of drilling at the PACMANUS vent field. Figure from Barriga et al. (2007).

Helium isotopes are recorded as R/R_A, that is, the ratio of $^3He/^4He$ in the sample (R) to $^3He/^4He$ in the atmosphere (R_A), which is 1.384×10^{-6}. ^4He is produced by the radioactive decay of uranium and thorium, whereas ^3He is essentially primordial. This has resulted in the development of several distinct reservoirs of helium within the Earth. Mid-ocean ridge basalt (MORB) averages 8.75 ± 2.14 R_A (Graham, 2002) whereas ocean island basalt displays a much greater range of 4 to 32 R_A, and is often characterized as being higher than MORB (Farley and Neroda, 1998). Continental rocks are generally $<<1R_A$ due to the high abundance of uranium and thorium in the crust (Craig and Lupton, 1976).

The He abundances (7.86×10^{-9} to 1.39×10^{-7}) are reported as cm^3 STP/gram of the total sample, and require correction to establish the concentration of helium in the hydrothermal fluid. Due to the degassing of the mantle, the abundance of ^{36}Ar is exceptionally high in the atmosphere compared to that in typical mantle-derived igneous rocks. We can therefore assume that all of the ^{36}Ar in the sample is derived from seawater. The concentration of ^{36}Ar in seawater of 1.2×10^{-6} cm^3 STP/g (Bieri and Koide, 1972) can therefore be used to determine the concentration of ^4He in the fluid;

$$^4He_{fluid} = (^{36}Ar_{seawater}/^{36}Ar_{sample}) \times^4 He_{sample}$$

This method assumes 100% of the fluid is derived from seawater with no magmatically degassed component. Such a component is estimated to compose as much as 20% of some vent fluids (Reeves et al., 2010), which could represent a significant quantity of He which is not accounted for by ^{36}Ar. Our corrected He concentrations may therefore be over-estimated (see 6.5.1).

6.3.3 Oxygen Isotopes

The sulphate-oxygen analysis procedure is detailed in Hall et al. (1991). Picked anhydrite samples were mixed with graphite and placed in a clean Pt crucible and evacuated. The crucible was then induction heated to 700°C until the vacuum had recovered, indicating complete devolatisation. The temperature was then raised to 1000°C, when most of the oxygen was released as carbon oxides, then slowly raised to 1200°C to ensure complete release. CO was converted to CO_2 and C in a Pt-electrode, high voltage (2 kV) discharge vessel at liquid nitrogen temperature. CO_2 gases were analysed on a VG Isogas SIRA 10 mass spectrometer. Results are reported versus V-SMOW, and the error of reproducibility, based on repeat analyses of the NBS 127 standard (with lab value of +8.7‰) was ±0.3‰. Natural variation within the samples exceeds this range of reproducibility.

6.4 Results

6.4.1 Noble Gases

^{3}He/^{4}He ratios of the fluids released from the precipitate inclusions vary from 0.29±0.00 R_A to 6.91±0.77 R_A (Table 6.1), with Snowcap and Roman Ruins showing comparable ratios at a given depth (Fig. 6.3A). There are no systematic differences in either ^{3}He/^{4}He or He concentrations between the anhydrite and pyrite samples. Since pyrite is believed to retain trapped ^{3}He/^{4}He for 100 Ma (Jean-Baptiste and Fouquet, 1996), this suggests the ^{3}He/^{4}He ratio remained fixed in both minerals since initial mineral precipitation and fluid inclusion entrapment. The highest ratios are recorded at Snowcap (^{3}He/^{4}He = 6.9 R_A at 288 mbsf), whereas the lowest ratio is recorded at Roman Ruins (0.29 R_A at 107.25 mbsf). ^{3}He/^{4}He values at Snowcap show a weak relationship with depth below the seafloor (Fig. 6.3A). Roman Ruins shows no such trend, possibly due to the more restricted sampling depth. The corrected helium concentrations (see 6.3.2) give values in the range 0.17-5.52 $\times 10^{-5}$ cm^3 STP/g.

TABLE 6.1: Analyses of helium and argon fluid inclusions in precipitates from the subsurface of PACMANUS.

Sample	Depth (mbsf)	Mineral	R/R_A	^4He cm^3 STP/gram	$^4He_{fluid}$	$^{40}Ar/^{36}Ar$
1188A-7R-1,61-64	48.81	Anhydrite	4.83 ±0.36	2.37×10^{-8}	3.33×10^{-6}	299.3 ±9.5
1188A-7R-1-14,87-89	49.07	Anhydrite	3.56 ±0.15	8.03×10^{-8}	8.72×10^{-6}	297.9 ±9.7
1188A-15R-1-1,0-2	125.7	Anhydrite	3.50 ±0.42	2.21×10^{-8}	2.67×10^{-6}	299.7 ±9.7
1188F-1Z-1-1,0-2	218	Pyrite	4.49 ±0.36	3.45×10^{-8}	3.16×10^{-6}	301.4 ±9.6
1188F-23Z-2-3B,30-33	288.4	Anhydrite	6.91 ±0.77	7.87×10^{-9}	4.97×10^{-6}	310.7 ±10.3
1188F-23Z-2-3C,34-36	288.44	Anhydrite	6.58 ±0.63	7.16×10^{-9}	1.7×10^{-6}	299.8 ±9.6
1188F-37Z-2-9,145-147	347.27	Anhydrite	5.66 ±0.45	3.38×10^{-8}	7.44×10^{-6}	297.2 ±9.7
1189B-1R-1,10-12	31.1	Pyrite	4.72±0.02	1.23×10^{-8}	1.45×10^{-6}	298.8 ±9.6
1189B-2R-1,29-30	40.39	Pyrite	2.19±0.00	1.51×10^{-8}	3.17×10^{-6}	299.1 ±9.6
1189A-7R-1-6,43-46	58.73	Anhydrite	3.45±0.18	3.26×10^{-8}	4.17×10^{-6}	298.2 ±9.5
1189A-8R-1,61-64	68.61	Anhydrite	5.30±0.36	3.64×10^{-8}	5.33×10^{-6}	297.0 ±9.6
1189A-12R-1,125-127	107.25	Pyrite	0.29±0.00	1.38×10^{-7}	5.52×10^{-5}	302.7 ±9.7
1189B-10R-1-5,42-44	118.32	Anhydrite	4.34±0.31	3.66×10^{-8}	9.2×10^{-6}	295.2 ±9.7

$^{40}Ar/^{36}Ar$ ratios are all slightly elevated above the accepted value for seawater of 295.5 (Farley and Neroda, 1998); in the range 297-310 for Snowcap and 295-302 for Roman Ruins (Fig. 6.3B, Table 6.1). However, given the $^{40}Ar/^{36}Ar$ of the mantle is up to ~40,000 (Farley and Neroda, 1998) these ratios indicate that Ar is dominated by the seawater end-member. Similar to the helium data, no difference is observed between the pyrite and anhydrite samples for either Ar abundance or $^{40}Ar/^{36}Ar$.

6.4.2 Oxygen Isotope Data

The $\delta^{18}O$ signature of anhydrite precipitates from Snowcap range between 7.5 - 11‰ SMOW (Table 6.2), whereas the data from Roman Ruins lie between 8.5 and 11.9‰(Fig. 6.4). For Snowcap the majority of data are lower than the $\delta^{18}O$ of seawater sulphate at 9.5‰(Lloyd, 1967) whereas at Roman Ruins the majority of data show $\delta^{18}O$ above the seawater value. This may be a consequence of the different sampling depths of the two sites; where the sampling depths overlap, $\delta^{18}O$ compares well between the two sites. However, overall there appears to be no trend with depth below the sea floor, nor with $^{3}He/^{4}He$ or published $\delta^{34}S$ (Bach et al., 2005). The anhydrite $\delta^{18}O$ values are comparable to data from the TAG mound which varied between 6.5‰to 9.5‰, and where most values were lower than $\delta^{18}O$ of seawater sulphate, showing no obvious trend of $\delta^{18}O$ with depth below seafloor (Chiba et al., 1998).

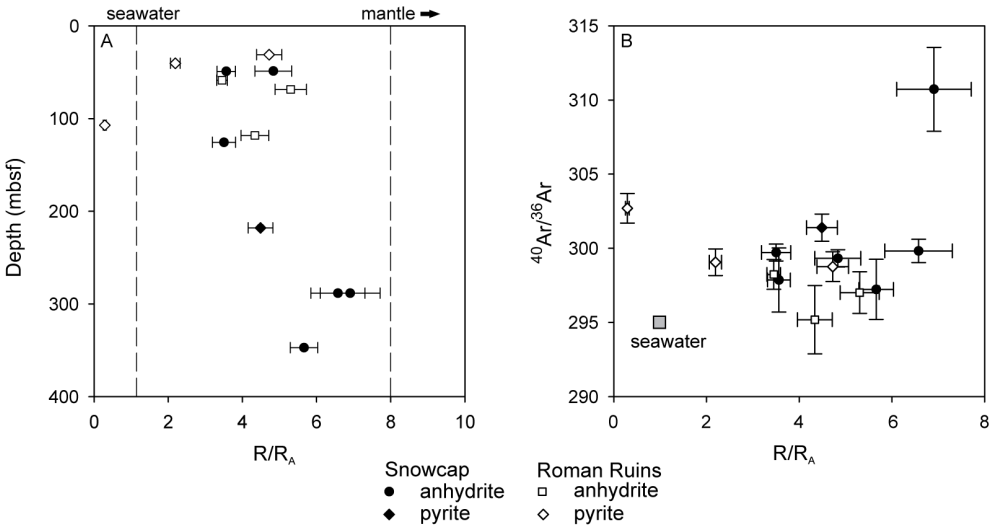

FIGURE 6.3: Results of $^{3}He/^{4}He$ and $^{40}Ar/^{36}Ar$ precipitate fluid inclusion analysis. A: R/R_A vs depth. Data are generally dispersed between the value of seawater and mantle values. B: No correlation is observed between $^{3}He/^{4}He$ and $^{40}Ar/^{36}Ar$.

TABLE 6.2: Oxygen isotope analysis of bulk anhydrite from the subsurface of PACMANUS.

Sample	Depth (mbsf)	$^{87}Sr/^{86}Sr$	$\delta^{18}O$	$\delta^{34}S$	R/R_A
1188A-7R-1,87-89	50	0.708606	10.5	21.6	3.56
1188A-15R-1,0-2	125	0.705725	7.5	21.1	3.5
1188A-15R-1,29-31	125	0.705726	9.2	20.6	-
1188A-17R-1,133-136	146	0.706281	11	20.6	-
1188F-1Z-1,0-2	218	0.70671	7.9	20.3	4.49
1188F-1Z-3,48-50	220	0.705679	10.3	20.7	-
1188F-23Z-2,30-33	286	0.706116	8	19.8	-
1188F-23Z-2,34-36	288	0.706089	8	20	6.91,6.58
1188F-35Z-1,94-99	340	0.705753	9.6	20	-
1188F-37Z-2,145-147	347	0.706296	8.3	20.5	5.66
1188F-41Z-1,137-138	363	0.705832	10.1	19.8	-
1189A-2R1,128-129	11	0.707642	10.5	21.88	-
1189A-5R-1,0-3	39	0.706565	9.7	18.8	-
1189A-7R-1,43-46	59	0.706579	10.2	21.97	3.45
1189B-10R-1,42-44	118	0.70721	10	21.39	4.34
1189B-12R-3,7-10	130	0.706373	8.5	21.09	-
1189B-14R-1,112-115	157	0.705451	10.5	22.15	-
1189B-14R-2,23-28	158	0.707029	11.9	22.12	-

6.5 Discussion

6.5.1 Noble Gases

Hydrothermal fluids measured at many vent sites show a well-defined mixing line between the hydrothermal end-member and seawater when $^3He/^4He$ is plotted against helium concentration (Fig. 6.5A). This observation holds for PACMANUS vent fluid data, suggesting that helium within PACMANUS behaves similarly to other vent sites (Fourre et al., 2006). However, in fluid inclusions from the sub-surface we see a significant departure in $^3He/^4He$ from the predicted mixing line between hydrothermal end-member and seawater, potentially revealing the presence of at least one further He component (Fig. 6.5B). In comparison with PACMANUS vent fluid, subsurface PACMANUS data show lower $^3He/^4He$ than expected for a given helium concentration for simple seawater-mantle mixing. Consideration of the $^{87}Sr/^{86}Sr$ ratios of the anhydrites (0.70487-0.708606) reinforces this departure (Bach et al., 2005; Roberts et al., 2003); mixing of hydrothermal fluid with seawater to the predicted degree (0-89% seawater, based on $^{87}Sr/^{86}Sr$ ratios) would cause only a minor decrease of $^3He/^4He$ due to the high concentration of ^4He in hydrothermal fluid (10^{-6} to 10^{-5} cm^3 STP/g observed) compared to that in seawater ($\sim 3.8 \times 10^{-8}$ cm^3 STP/g) (Fourre et al., 2006), whereas we observe a larger variation in $^3He/^4He$. The Fourre et al. (2006) dataset samples only a small proportion of the fluid chemistries available at PACMANUS, and this may account for some of the variation observed, however due to the magnitude of the variation we believe another process is at work. Similar departures from a simple mixing line have been observed in other vent site data (Fig. 6.5B). At the Snakepit and TAG hydrothermal sites, vent helium data show a similar scattering to PACMANUS

subsurface data (Rudnicki and Elderfield, 1992). Fluids in sulphide inclusions from EPR 13°N are more varied but are within the range encompassed by the rest of the available data (Stuart et al., 1995). Departures from the simple mixing line can be achieved by in-situ radiogenic production of ^{4}He. The amount this affects the ^{3}He/^{4}He ratio can be estimated using:

$$f_{3/4} = 1 - \left\{ t \left[1.207 + 0.278 \left({}^{232}Th/{}^{238}U \right) \right] \times 10^{-13} \times \left({}^{238}U/{}^{4}He \right) \right\}$$

(Stuart et al., 1995) where t is the age in years, U and Th are measured in ppm and ^{4}He is measured in cm^3 STP/gram. $F_{3/4}$ is the factor by which the ^{3}He/^{4}He ratio is altered

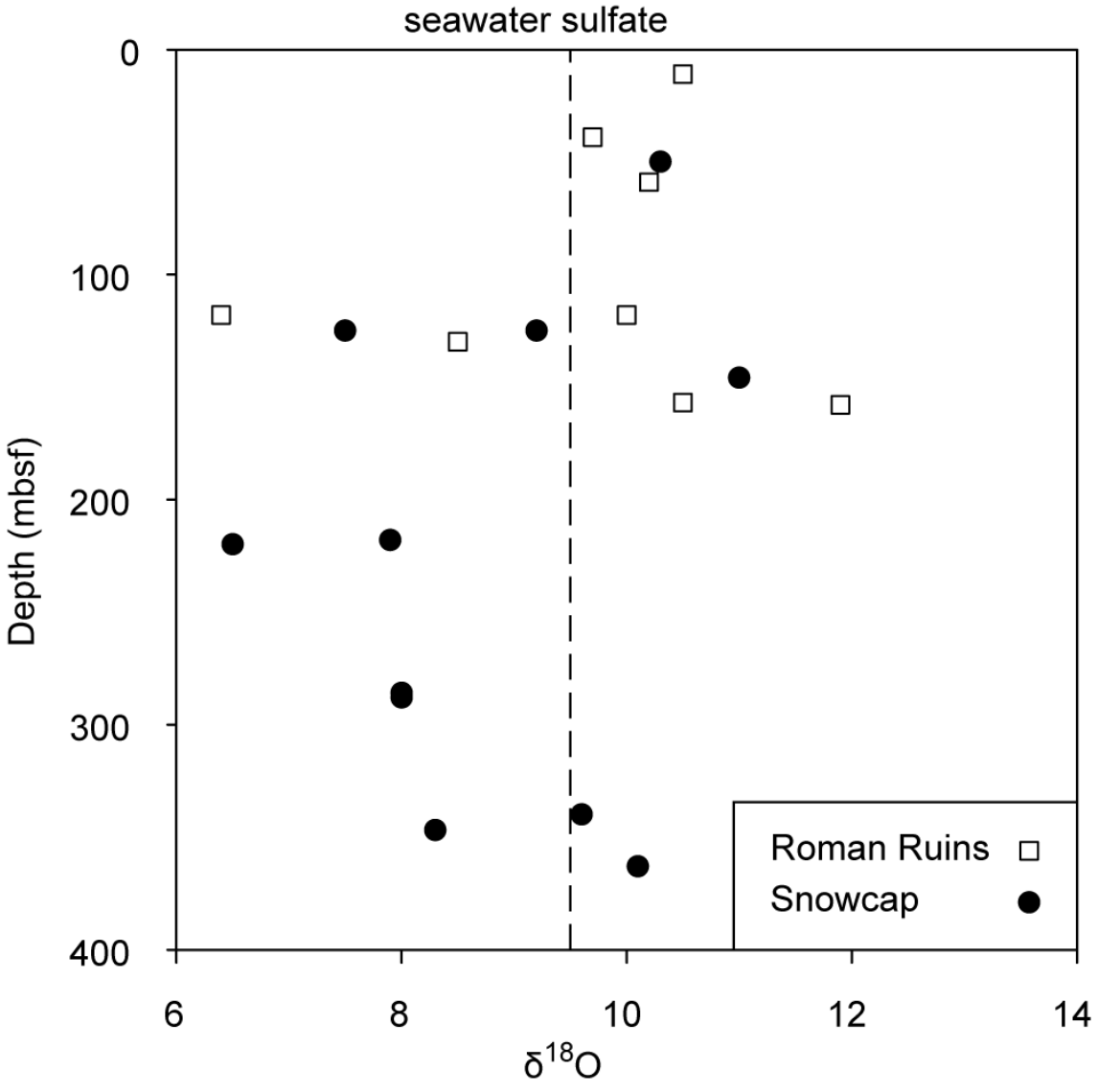

FIGURE 6.4: Results of δ^{18}O analyses of bulk anhydrite precipitates vs depth

by the introduction of radiogenic ^{4}He. The maximum U concentration measured in vein precipitates at PACMANUS is 0.044 ppm (Paulick et al., 2005) and 3.5 ppb in borehole fluids (Binns, 2004). A value of 10.15 ppm is recorded in an anhydrite/pyrite sample from Roman Ruins (Paulick et al., 2005), however the average U concentration of the published data for altered rocks at PACMANUS is only 1.6 ppm (n = 77, 1σ = 1.8). Gamma ray wire-line logging to determine K_2O, U and Th contents of Snowcap and Roman Ruins was problematic. By comparison with geochemistry data, peak values of 15-20 ppm and 6-8 ppm U for Snowcap and Roman ruins, respectively, are estimated (Bartetzko, 2008). This is higher than values from core geochemistry indicate; Bartetzko (2008) speculate this could be due to a sampling bias. Softer, more heavily altered rocks, presumably with the higher U contents, may not have been recovered. It was noted that gamma ray activity is particularly high at intervals with no or extremely poor core recovery (1-2%). The highest predicted uranium concentration of 20 ppm at Snowcap would reduce an R/R_A of 7 to ~6 after 250,000 years, given a reasonable initial ^{4}He concentration of $5\times\ 10^{-6}$ cm^3 STP/g. Thorium makes a negligible difference at realistic concentrations. An alternative mechanism to explain our data is the potential over-estimation of He concentration in the fluid inclusions given by the correction technique (see 6.3.2), caused by the presence of a magmatic component to the fluid. This fluid would provide He which is not accounted for by ^{36}Ar, since the concentration of ^{36}Ar in rocks is very low. Given a 20% component of magmatic fluid, the maximum estimated by Reeves et al. (2010), the He concentration of the magmatic fluid would need to be in excess of 1×10^{-4} cm^3 STP/g to account for the extra He we calculate. This seems fairly realistic given that similar concentrations have been recorded in vent fluid at other hydrothermal sites (Fig. 6.5). Consequently, the addition of a large proportion of a magmatically degassed component is seen as a potential cause of the discrepancy between the vent fluid and fluid inclusion helium concentrations observed. However, this mechanism cannot explain the depressed ^{3}He/^{4}He ratios we observe in comparison to vent fluid (Fourre et al., 2006). One mechanism which could explain both increased He concentrations and depressed ^{3}He/^{4}He is diffusive exhange between the crystal lattice and air upon exposure to the atmosphere. The atmosphere contains a very high concentration of He (5.2 ppm, Oliver et al. 1984) compared to the amount in the samples and so the observed deviation from the mixing line can be explained by 0.001 to 0.01% He exchange with the atmosphere. Normally the ^{4}He/^{20}Ne ratio is used to correct for atmospheric contamination (Sano and Wakita, 1985) but in this case it does not provide the magnitude of correction needed. We suggest that He-Ne fractionation occurs during the diffusive exchange since Ne has a greater ionic radius. This may represent a fundamental limitation with measuring He concentration in fine grained drillcore alteration minerals, and steps must be taken to reduce the contamination risk. Air contamination can be corrected simply by extrapolating values back to the ventfluid-seawater mixing line along

the air-exchange mixing line (Fig. 6.5B and C), and doing this yields a remarkably narrow range of $^3He/^4He$ ratios of 7.4 to 7.8R_A for Roman Ruins and 7.6 to 7.8R_A for Snowcap. However the validity of this method is questionable given the number of variables involved and the natural variation of end-member fluid chemistry. We suspect the deviation from the mixing line seen in TAG and Snakepit vent fluids (Rudnicki and Elderfield, 1992) could be a similar issue to that observed here as their data may not have been corrected for air contamination. We note that an earlier dataset for Snakepit vent fluid shows a very tight, predictable trend which conforms to the expected mixing line (Jean-Baptiste et al., 1991), in contrast to the later dataset of Rudnicki and Elderfield (1992) (Fig. 6.5A).

6.5.2 Oxygen isotope data - temperature equilibrium and fractionation

Temperature profiles for Snowcap and Roman Ruins have previously been calculated from fluid inclusion studies in anhydrite (Vanko et al., 2004) and yield temperatures in the range ~100°C to ~400°C for Snowcap, with a profile of ~350 to ~400°C at the base of the hole and ~100°C to ~350°C towards the top. Roman Ruins shows a much more restricted profile, with temperatures in the range ~250 to ~375°C, and with no trend to cooler temperatures towards the top (Fig. 6.6). The $\delta^{18}O$ value for the anhydrite can be used to estimate precipitation temperatures, assuming isotopic equilibrium between the anhydrite and water, using the geothermometer:

$$10^3 ln\alpha_{anhydrite-water} = (3.21 \times 10^3/T^2) - 4.72$$

(Chiba et al., 1981). Averaged end-member fluid $\delta^{18}O$ compositions are 1.38‰ and 1.5‰ for Roman Ruins and Snowcap, respectively (Reeves et al., 2010). Using the above geothermometer, we calculate anhydrite precipitation temperatures which fall within a narrow band throughout the profiles at both Snowcap and Roman Ruins. At Snowcap, these temperatures are significantly cooler than the fluid inclusion trapping temperature profile at depth, and at Roman Ruins we calculate temperatures consistently cooler than the fluid inclusion trapping temperatures (Fig. 6.6). Accounting for a variable $\delta^{18}O$ value of the fluid due to mixing with seawater, using $^{87}Sr/^{86}Sr$ as a proxy for seawater proportion, does not significantly affect the profile. This discrepancy between temperature profiles is a similar observation to that made at the TAG system where Chiba et al. (1998) speculate that anhydrite precipitated so rapidly that oxygen isotope equilibrium was not attained. Temperature profiles can also be constructed based on simple adiabatic mixing between a 360°C hydrothermal end-member and 2°C seawater, at proportions indicated by $^{87}Sr/^{86}Sr$ ratios (e.g. Chiba et al., 1998; Teagle et al., 1998). Using this method utilizing published

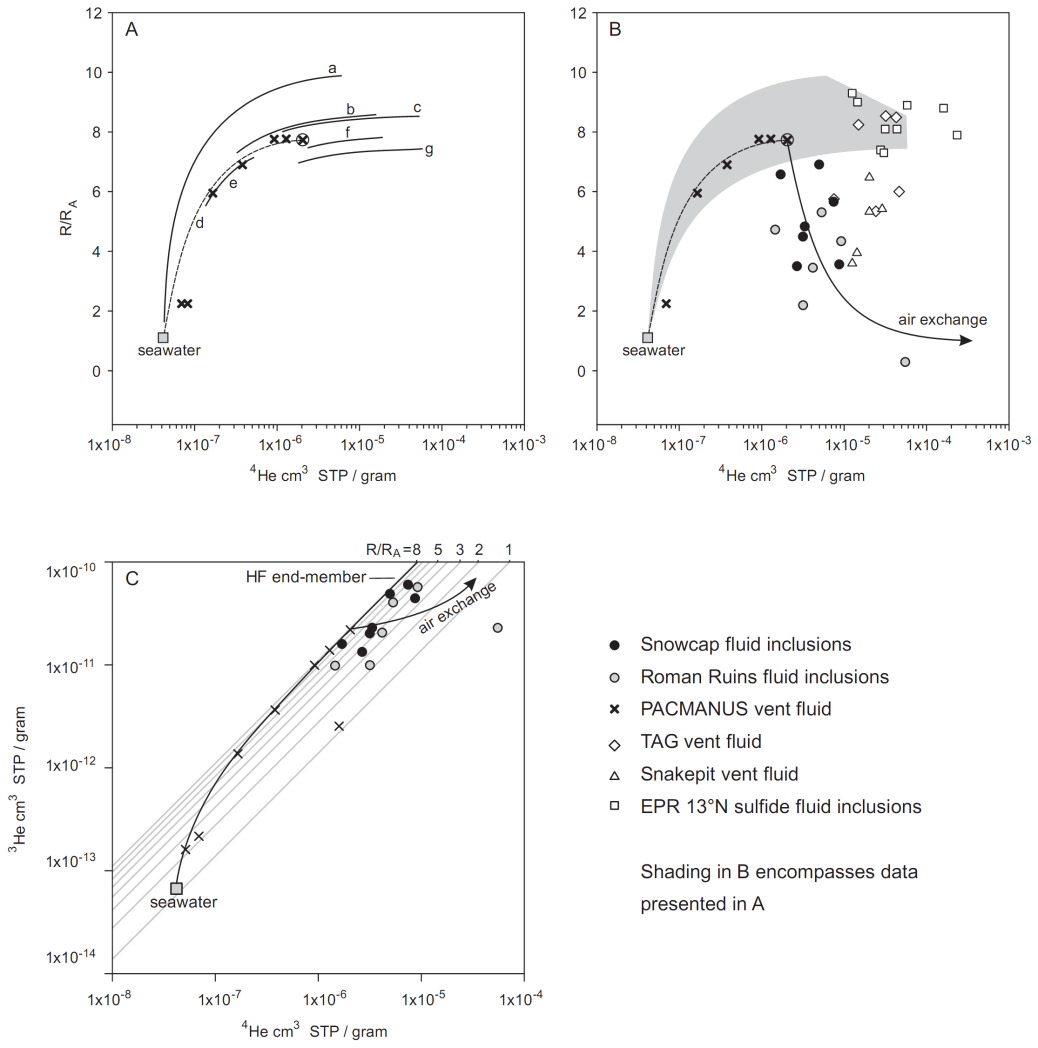

FIGURE 6.5: A: Vent fluid data from various hydrothermal sites, approximated by solid arcs, lie on well-defined mixing lines between a hydrothermal end-member and seawater; a = Grimsby-Kolbeinsey field vent fluid (Botz et al., 1999); b = East Pacific Rise (EPR) 17°and 19°S vent fluid (Jean-Baptiste et al., 1997); c = Snakepit vent fluid (Jean-Baptiste et al., 1991); e = TAG hydrothermal plume (Rudnicki and Elderfield, 1992); f = EPR 21°N sulphide fluid inclusions (Turner and Stuart, 1992); g = Rainbow vent fluid (Jean-Baptiste et al., 2004). Dashed arc d is a computed two-end member mixing model between the circled data point and seawater, showing PACMANUS vent fluid (Fourre et al., 2006) behaves in the expected manner. B: However, fluid from precipitate inclusions in the subsurface at PACMANUS do not lie on these lines, showing more radiogenic values. Such departures are also observed for TAG and Snakepit vent fluid (Rudnicki and Elderfield, 1992), despite an earlier Snakepit vent fluid dataset behaving normally (plate A, arc c) (Jean-Baptiste et al., 1991). Data from EPR 13°N sulphide inclusions are similarly scattered but lie within the range of other predictable systems (Stuart et al., 1995). The solid arrow is a modelled mixing line between the circled vent fluid sample and air, demonstrating that air contamination can explain the depressed ^{3}He/^{4}He ratios. C: ^{3}He vs ^{4}He measured in precipitate fluid inclusions, compared to the computated mixing line (solid arc) between seawater and PACMANUS vent fluid. Mixing with air is demonstrated by the arrow.

anhydrite $^{87}Sr/^{86}Sr$ ratios (Bach et al., 2003; Roberts et al., 2003) provides temperature estimates with much cooler profiles than fluid inclusion trapping temperatures at both Snowcap and Roman Ruins. This suggests that the seawater was at a higher temperature than 2°C prior to mixing, and so conductive heating of the seawater must have occurred. This is also observed at TAG, where it is considered that seawater must be conductively heated to 100-180°C prior to mixing (Chiba et al., 1998; Teagle et al., 1998). The conductive heating of seawater can be estimated based on calculating the expected $\delta^{18}O$ of anhydrites precipitated from seawater that has been conductively heated to varying degrees before mixing with hydrothermal fluid (Teagle et al., 1998)(Fig. 6.7). The PACMANUS anhydrites appear to have been precipitated extremely rapidly as many points lie well out of the range of expected compositions, based on end member composition of Roman Ruins vent fluid (Reeves et al., 2010). However, we observe segregation between Roman Ruins and Snowcap anhydrite chemistry in $\delta^{18}O$ - $^{87}Sr/^{86}Sr$ space, with the Roman Ruins data indicating a greater degree of conductive heating of seawater prior to anhydrite precipitation, and/or precipitation at a lower temperature upon mixing with hydrothermal fluid. In particular, five Snowcap anhydrites appear to have precipitated from a fluid which underwent very little conductive heating prior to mixing with hydrothermal fluid, whilst all but two precipitated from a mixed fluid which was at a much higher temperature during anhydrite precipitation, in comparison to Roman Ruins. The discrimination of the two sites is not total, however, as both sites have one sample lying well within range of the other. Overall the PACMANUS data reveals a more varied system than TAG, with cooler fluids penetrating deep within the system, perhaps facilitated by the volcaniclastic horizons present within the volcanic pile (Paulick et al., 2004).

Previously, a model describing a build up of hot fluid beneath the relatively impermeable dacite cap has been proposed to explain higher temperatures from geothermometry of alteration clays and quartz at the top of the system (Lackschewitz et al., 2004). It is based mainly on very high temperatures given from the $\delta^{18}O_{silica-water}$ system of Knauth and Epstein (1976), which is a geothermometer designed for very low temperature (0 to 65°C) chert nodule formation within soft sediment, and so its relevance to a high temperature hydrothermal system is highly questionable. This led Lackschewitz et al. (2004) to underestimate the fluid $\delta^{18}O$ value, whereas the real value would have given unrealistically high temperatures. Using other, more suitable geothermometers yields temperatures even higher for these quartz samples, suggesting they are not in equilibrium. We would instead reinforce the general cooling trend seen uphole at Snowcap and a more constant high temperature regime at Roman Ruins given by fluid inclusion trapping temperatures (Vanko et al., 2004).

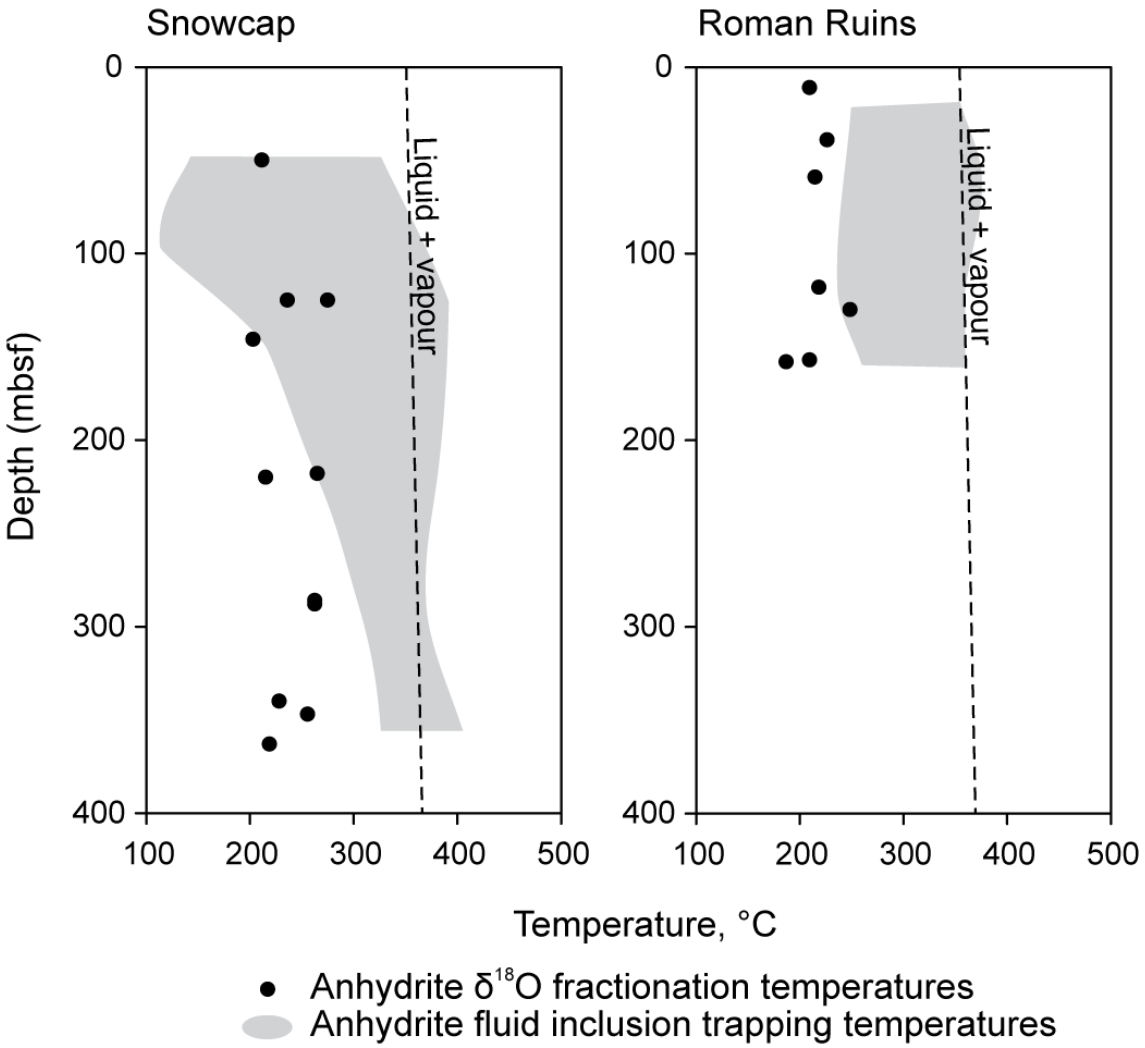

FIGURE 6.6: Calculated anhydrite δ^{18}O precipitation temperatures verses depth. In comparison with fluid inclusion trapping temperatures (shaded area, Vanko et al. 2004), we see cooler temperatures at depth at Snowcap and a generally cooler profile at Roman Ruins.

6.5.3 A revised PACMANUS fluid mixing model

6.5.3.1 Snowcap

Venting at Snowcap is characterized by lower temperature 'shimmering water' venting, but with higher temperature (150-182°C) focused venting. Temperatures provided by fluid inclusion studies in anhydrites (Vanko et al., 2004) provide minimum and maximum isotherms for the system and show an increased minimum temperature gradient above 150 mbsf, whilst hot ~360-400°C fluid persists at least to this level. $^{87}Sr/^{86}Sr$ seawater content percentages support this profile (Bach et al., 2005; Roberts et al., 2003). Anhydrite δ^{18}O

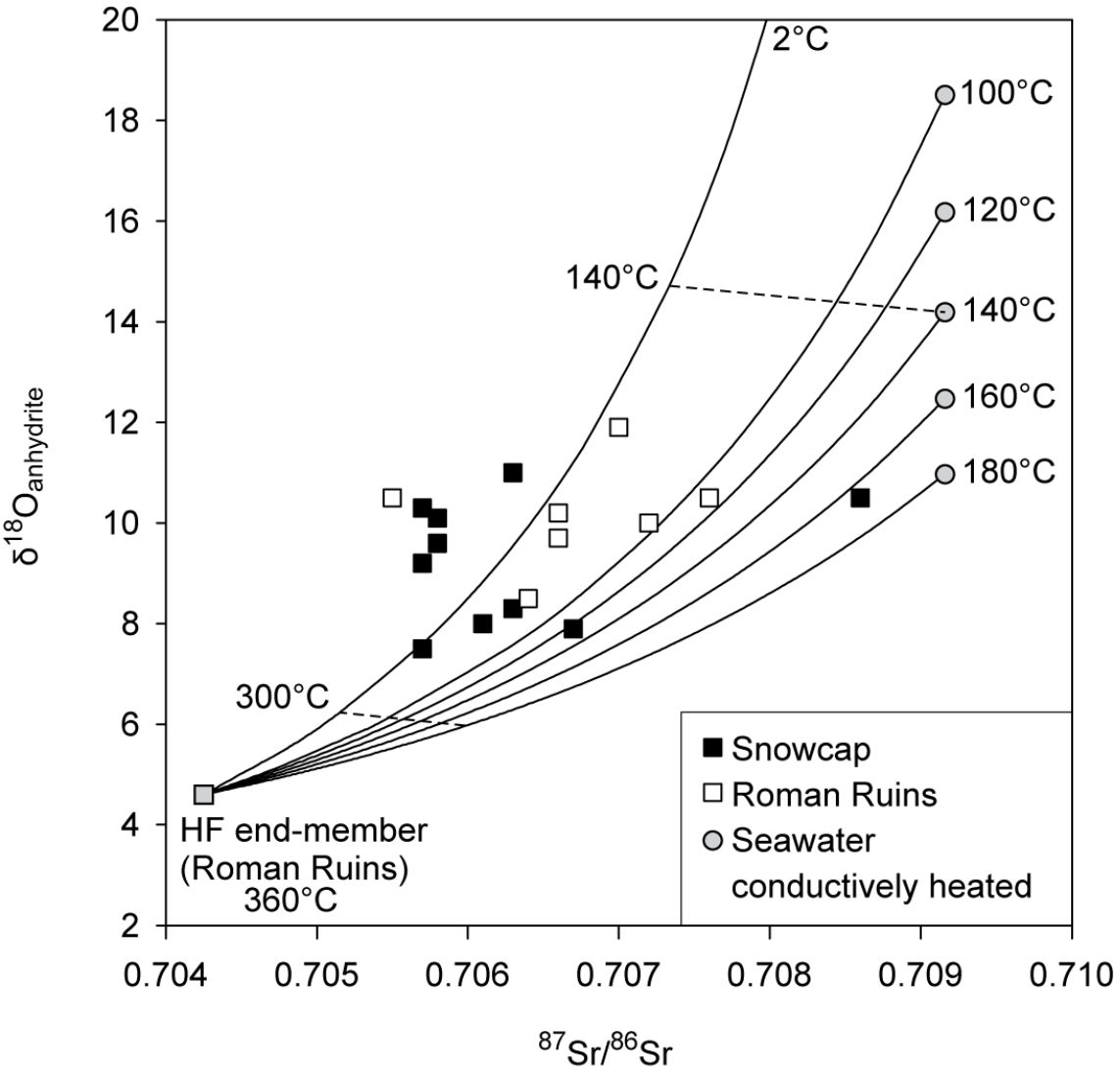

FIGURE 6.7: $^{87}Sr/^{86}Sr$ vs $\delta^{18}O$ of anhydrite samples within PACMANUS. The trajectories show expected anhydrite compositions precipitated from seawater conductively heated to the indicated temperature before mixing with hydrothermal fluid (HF). Dashed isotherms indicate the temperature of the mixed fluid. Diagram adapted from Teagle et al. (1998). End-member compositions are $^{87}Sr/^{86}Sr = 0.7042$, $\delta^{18}O = 1.38$ (HF) and $^{87}Sr/^{86}Sr = 0.70916$, $\delta^{18}O = 0$ (seawater) (Reeves et al., 2010). Snowcap $^{87}Sr/^{86}Sr$ end-member is not reliably known.

compositions indicate very cool seawater penetrates deep into the system, and that mixing and anhydrite precipitation occurs very rapidly.

Hot fluid at ~400°C rises from the base of the system, including a component of directly degassed magmatic volatiles (Roberts et al., 2003; Kim et al., 2004; Reeves et al., 2010; Bach et al., 2003; Craddock and Bach, 2010). As the fluid rises, it interacts with fresh seawater, causing rapid anhydrite precipitation, varying fluid temperatures, and isotopic signatures

($^{87}Sr/^{86}Sr$, $\delta^{34}S$) which move towards seawater values. Hydrothermal end-member (360-400°C) fluid is somewhat ephemeral, sometimes being overwhelmed by cooler fluids which have mixed with seawater. At ~150 mbsf, mixing either increases in intensity, consistent with increased permeability and porosity at shallower levels (Christiansen and Iturrino, 2007), or the temperature of the fresh seawater is lower, causing increased temperature gradients. 360-400°C fluids cease to exist above this level and the cooling towards Snowcap venting temperatures continues (Fig. 6.8).

6.5.3.2 Roman Ruins

Fluids approaching 400°C persist to ~50 mbsf, with small amounts of mixing causing a variation in temperature of up to 150°C, as opposed to ~300°C at Snowcap. Seawater penetrating the system experiences a greater degree of conductive heating prior to mixing, reflecting the steep geotherm. This is a simple system whereby hot fluid from depth has enough energy and volume to reach the surface, maintaining a low seawater:hydrothermal fluid ratio and so little change in bulk temperature (Fig. 6.8).

6.5.3.3 Venting Styles

The above data and supporting model explains how Snowcap shows lower temperature venting than Roman Ruins, but not why. In speculation, it could be that the basal supply of 370-400°C fluid at Snowcap is less than at Roman Ruins, allowing the seawater:hydrothermal fluid ratio to be greater, causing lower temperature fluid and less vigorous venting. This requires less energy in the Snowcap system, either conductively (cooler or deeper heat source at Snowcap) or advectively (a greater supply of hydrothermal end-member at Roman Ruins). The former seems unlikely due to the proximity of the two sites. Furthermore, less hydrothermal input at the base of the system at Snowcap would explain the greater proportion of directly degassed component seen in the fluid at that site (Roberts et al., 2003; Reeves et al., 2010), if the overall volume of directly degassed component is the same at both sites. An alternative way to increase the seawater:hydrothermal fluid ratio is to increase seawater input at the top of the system, which in itself could be facilitated by less hydrothermal input from the base. There is some evidence for this at Snowcap, including rapid cooling of the minimum isotherm above ~130 mbsf, as indicated by fluid inclusion trapping temperatures (Vanko et al., 2004), and cool seawater penetrating deep within Snowcap, indicated by combining $^{87}Sr/^{86}Sr$ and $\delta^{18}O$ of anhydrites. Snowcap is also located close to a steep slope in the Pual Ridge (Reeves et al., 2010) which could well allow easy access for seawater to enter the top of the system.

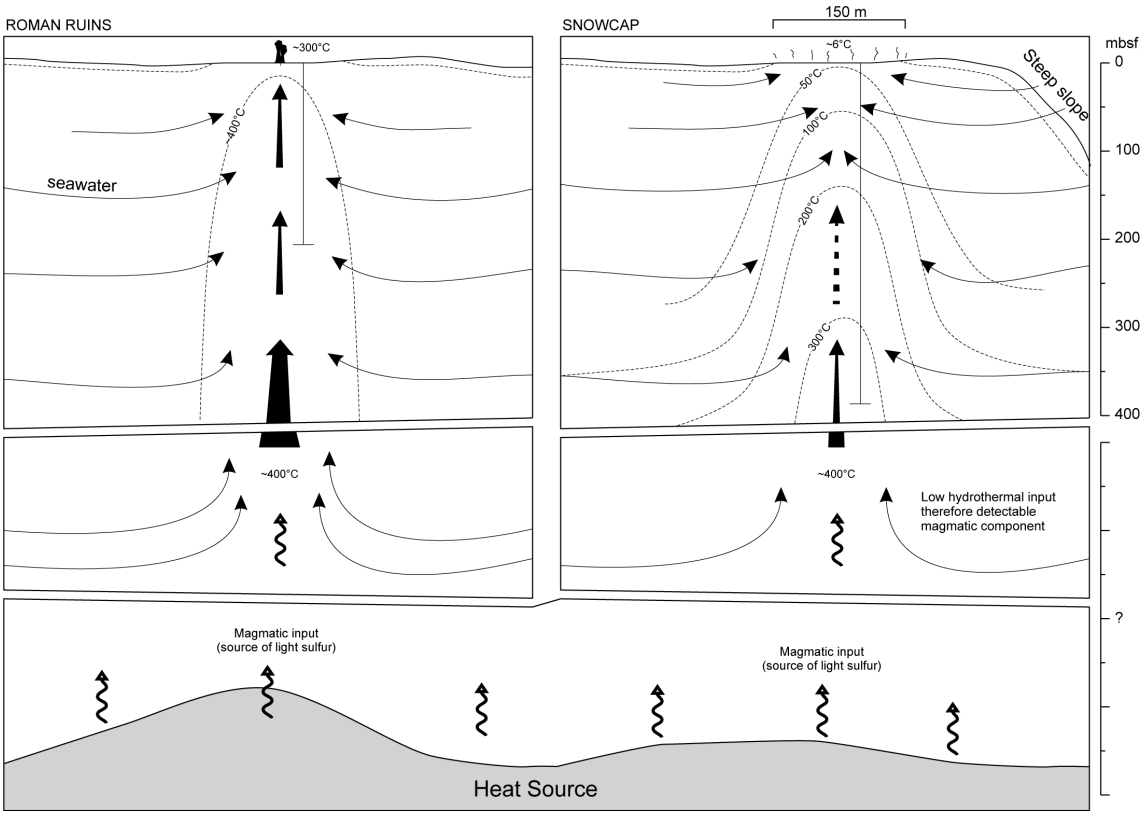

FIGURE 6.8: Revised fluid mixing and thermal model for Snowcap and Roman Ruins. In this model, Snowcap receives less hydrothermal fluid at the base of the system, allowing greater proportions of seawater in mixing events, cooler temperatures, less vigorous venting and a detectable magmatic sulphur component (Roberts et al., 2003; Kim et al., 2004). Isotherms shown are the lower limit supplied from anhydrite trapping temperatures (Vanko et al., 2004), whilst the solid and broken arrow represents the influx and overwhelming of ~400°C hydrothermal end-member. Roman Ruins receives a greater amount of hydrothermal end-member, supplying enough energy to rise up through the column with little temperature change. The directly degassed component is harder to detect because it is a smaller proportion of the fluid. The ~400°C isotherm is variable but rises on occasion at least to the depth shown. The dacitic cap is also taken to be somewhat permeable (Christiansen and Iturrino, 2007), allowing further cooling to venting temperatures at Snowcap.

6.6 Conclusions

$^{3}He/^{4}He$ ratios from fluid inclusions in vein precipitates reflect the natural variation in $^{3}He/^{4}He$ of the host rocks, as well as significant atmospheric diffusive exchange prior to sample analysis. Furthermore, this diffusive exchange appears to fractionate He-Ne concentrations, which precludes the possibility of correction using ^{20}Ne. Correction by extrapolating back to the vent fluid mixing line along the air exchange mixing line yields a very narrow range of $^{3}He/^{4}He$ ratios.

$^{40}Ar/^{36}Ar$ ratios indicate the genesis of the majority of the fluid as seawater but suggest a small magmatic contribution, either through interaction with the host rock or through directly degassing fluid. This magmatic input may contribute a major portion of He to the fluid, so that the ^{36}Ar method of He concentration correction may over-estimate the He concentration of the precipitating fluid.

Temperature profiles have been constructed from the $\delta^{18}O_{anhydrite-water}$ system. These profiles are generally cooler than previously determined fluid inclusion trapping temperatures (Vanko et al., 2004). This suggests anhydrite precipitation occurs too rapidly for $\delta^{18}O$ equilibration to occur. This is similar to observations made at the TAG system, however, PACMANUS shows a much greater range in conductive heating of the incoming seawater than TAG, indicating a more dynamic system, with low temperature seawater penetrating deep within the system at Snowcap.

Collectively, the above data and previously published results allow fluid mixing at PACMANUS to be simply described. At Snowcap, rising hot hydrothermal fluid becomes progressively mixed with seawater, causing a cooling trend uphole, although higher temperature fluid can persist to ∼100 mbsf at times. This process may be facilitated by less hydrothermal end-member input at the base of the system, allowing the system to be cooled more easily. At Roman Ruins less mixing with seawater occurs allowing a more restricted temperature range and higher temperature venting.

Chapter 7

Conclusions

7.1 The behaviour of Au within the Earth

This thesis addresses three different aspects of the behaviour of Au within the Earth. First, it examines the addition of Au to oceanic crust by ridge-plume interaction. It looks at the behaviour of Au in the subduction setting and the flux of Au from the subducting slab, and it assesses the behaviour of Au in a continental arc magma system which hosts an economical mineral deposit. To summarise the major findings:

- Mantle plumes are capable of producing Au-rich oceanic crust. This material can be richer in Au by around an order of magnitude compared to melt extracted from normal "depleted" upper mantle, the source of most primary crustal magmas.
- Eclogites from the Zermatt-Saas ophiolite exhibit strong evidence for depletion of Au with respect to N-MORB. Loss of Au to the mantle wedge may represent one source of Au for arc magmas and mineral deposits.
- Au in high level, oxidised arc magmas is strongly controlled by the crystallisation of magnetite, to the extent that 70-80% of the Au can be lost during the evolution of a magma. However, volcanic complexes which demonstrate Au sequestration by magnetite are still prospective and the generation of Au-rich cumulates could play an important pre-enrichment role in the generation of an epithermal Au deposit.

Together, these points describe a path by which Au moves throughout the Earth, from the lower mantle and potentially the core, into oceanic crust, into a subduction zone and then finally into the mineralising system in the upper crust (Fig. 7.1).

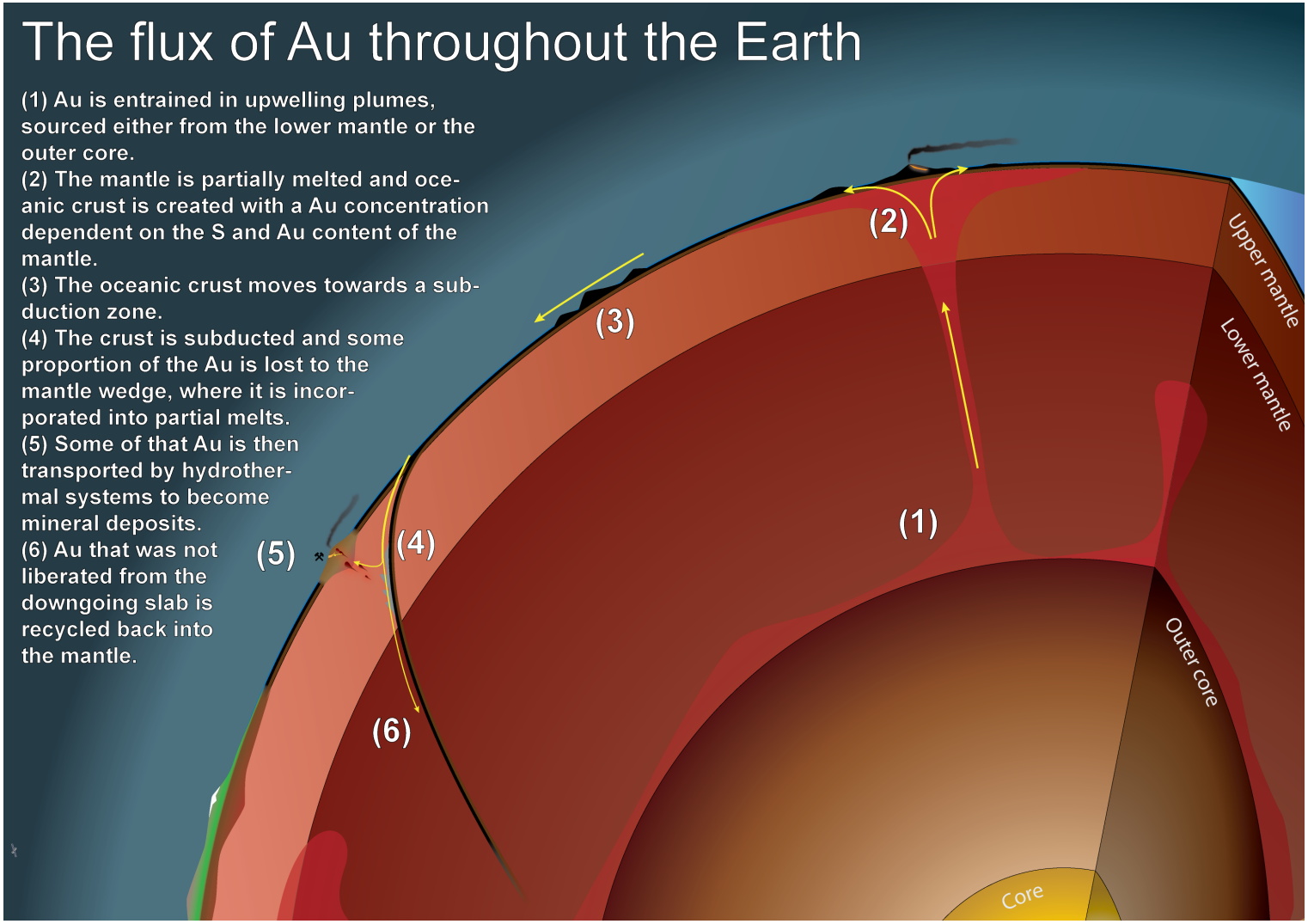

FIGURE 7.1: Summary diagram of the flux of Au within the Earth that is explored in this thesis. Chapter 3 discusses (2), Chapter 4 discusses (4) and chapter 5 discusses (5).

7.2 Hydrothermal systems and PACMANUS

The work presented here on the PACMANUS system included two important findings.

- The diffusion of atmospheric helium into anhydrite contaminated samples in such a way that cannot be corrected using ^{20}Ne, presumably due to the larger ionic radius of the latter isotope.
- Re-examination of evidence for fluid mixing and flow paths leads to a simple explanation for differing venting styles at the two sites, where venting style is controlled by fluid pathways and permeability at depth.

The first conclusion is logistical in nature. It shows that steps must be taken to prevent atmospheric contamination of samples during storage if analysis of elements like helium, which is small and highly concentrated in the atmosphere compared to rock, is likely in the future. The diffusion of helium in geological samples has been recognised before but has not been recognised as a problem, even to the extent that one published data set apparently contains atmospherically-contaminated ^{3}He/^{4}He ratios (Rudnicki and Elderfield, 1992).

The second conclusion is important when you consider that the two venting styles are associated with completely different mineralisation. Roman Ruins, the high-temperature vent site, comprises sulphide chimneys rich in base and precious metals. This site, in a back-arc setting with a high preservation potential, is presumably a good analogue for ancient volcanogenic massive sulphide deposits. Just ∼1 km away is Snowcap, the low temperature, metal-poor vent site comprised of Mn-Fe crusts. In this case the control of fluid flow at depth seems to control the occurrence of mineralisation.

7.3 Further Work

Further work is needed to fully understand the behaviour of Au within the Earth and how this behaviour influences the generation of mineral deposits.

7.3.1 Au, mantle plumes and oceanic crust.

In this work it is shown that the Reykjanes Ridge is anomalously rich in Au compared to average oceanic crust due to the influence of the Iceland Mantle Plume. However, it is still not certain whether this is due to an innate Au-enrichment in the plume itself or

whether the mechanics of the sulphide-chalcophile elements system is responsible. Detailed modelling of the system together with direct observation of S and sulphides within the Reykjanes MORB could lead to a definitive answer. In addition, the idea of mantle-core interaction is often cited as a way to generate mantle rich in siderophile elements, but there is conflicting evidence as to whether this actually takes place (Brandon and Walker, 2005). If core-mantle interaction does not take place then an alternative explanation for siderophile-rich plumes may be required. There is also the question of Iceland and its apparent lack of any mineralisation, despite having extensive geothermal systems. On the Reykjanes Peninsula, the geothermal waters are rich in Au and other metals, and they circulate through rocks with an unusually high Au concentration (chapter 3 and Hardardottir et al. 2010; Momme et al. 2003). This seems like the perfect environment for a low-sulphidation epithermal mineral deposit and yet none seems to exist.

Few data exist for the concentration of Au in oceanic gabbros and as a result its behaviour during oceanic crust formation is not understood. Additional Au analyses of gabbro at different depths in the crust are required together with data for S and Au analysis of accessory minerals.

7.3.1.1 Au fluxes during subduction

Further work is needed to confidently assess the mobility of Au in the subducting slab and the importance of its addition to the mantle wedge. Osmium isotope analysis of Au ores from typical arc-related epithermal and porphyry Cu-Au could help constrain the origin of metals. The budget of the subducting slab and mantle wedge system needs to be assessed in order to constrain how much Au the slab would need to contribute to make a significant difference to the system. The flux of Au from eclogite needs to be better assessed by studying the distribution of Au between less altered eclogite and eclogite adjacent to veins, interpreted to be the main fluid pathways through the slab. Flux from the gabbro and serpentinite layers also needs to be assessed. The flux of Au during the entire prograde metamorphic path during subduction needs to be understood in order to confirm Au-loss occurs during eclogite facies metamorphism.

7.3.2 Au in arc magmas

The behaviour of Au in primitive arc magmas in the mantle wedge and lower-to-mid crust needs to be considered. Once the melt reaches the upper crust, the exact timing of fluid exsolution, sulfide saturation and accessory mineral crystallisation needs to be understood,

particularly in relation to Sun et al. (2004)'s model of magnetite crystallisation causing fluid exsolution.

Appendix A

A model to describe the addition of Au to the mantle wedge from a subducting slab

This model describes in simple terms how much Au is added to the mantle wedge given a certain Au flux from the subducting slab, as used in Chapter 4. Some equations are given below, symbols are listed in table A.1. All Au concentrations given in ppb.

To describe the mass of basalt subducted per year:

$$M_b = t \times v \times \rho_{basalt} \tag{A.1}$$

TABLE A.1: Parameters used in modelling subduction and the flux of Au from the slab, the concentration of Au in slab fluids and the addition of Au to partial melts.

Parameter	Value	Symbol
Angle of subduction	30°	α
Basalt thickness	2000 m	t
Subduction velocity	0.05 m/yr	v
Gold conc. Of slab	0.95 and 4 ppb	C_{Au}
Density of basalt	3000 kg/m^3	ρ_b
Loss into the wedge	51%	F
Depth of subduction	75 km	D
Density of mantle	3300 kg/m^3	ρ_m
Initial Au concentration of mantle wedge	1 ppb	G
Water loss from the slab	0.5 to 2.5 wt%	F_w
Water content of partial melt	3 to 5 wt%	W_m

Table A.2: Additional symbols

Parameter	Symbol
Mass of basalt subducted per year	M_b
Mass of Au subducted per year	M_{Au}
Mass of Au added to the wedge per year	M_{Au}^{wedge}
Initial mass of Au in the mantle wedge	M_{Au-i}^{wedge}
Mass of the mantle wedge	M_{wedge}
Volume of the mantle wedge	V_w
Final Au concentration in the wedge	C_{final}^{Au}

The mass of Au subducted per year:

$$M_{Au} = M_b \times \left(\frac{C_{Au}}{10^9}\right) \tag{A.2}$$

The mass of Au lost to the mantle wedge:

$$M_{Au}^{wedge} = M_{Au} \times F \tag{A.3}$$

The volume of the mantle wedge, assuming the wedge is 50% of a right angled triangle with an angle of α and opposite side length of D:

$$V_w = \frac{D^2 \times tan(\alpha)}{4} \tag{A.4}$$

Mass of the mantle wedge:

$$M_{wedge} = V_w \times \rho_m \tag{A.5}$$

Initial mass of Au in the mantle wedge:

$$M_{Au-i}^{wedge} = M_{wedge} \times \left(\frac{C_i^w}{10^9}\right) \tag{A.6}$$

Total Au in the mantle wedge after time t:

$$M_{Au-T}^{wedge} = (t \times M_{Au}^{wedge}) + M_{Au-i}^{wedge} \tag{A.7}$$

Final Au concentration of the wedge

$$C_{final}^{Au} = \left(\frac{M_{Au-T}^{wedge}}{M_{wedge}} \right) \times 10^9 \tag{A.8}$$

Bibliography

Ague, J.J., 1994. Mass-Transfer during Barrovian Metamorphism of Pelites, South-Central Connecticut .2. Channelized Fluid-Flow and the Growth of Staurolite and Kyanite. American Journal of Science 294, 1061–1134.

Amato, J.M., Johnson, C.M., Baumgartner, L.P., Beard, B.L., 1999. Rapid exhumation of the Zermatt-Saas ophiolite deduced from high-precision Sm-Nd and Rb-Sr geochronology. Earth and Planetary Science Letters 171, 425–438.

Angiboust, S., Agard, P., Jolivet, L., Beyssac, O., 2009. The Zermatt-Saas Ophiolite; the largest (60-km wide) and deepest (c. 70-80 km) continuous slice of oceanic lithosphere detached from a subduction zone? Terra Nova 21, 171–180.

Arevalo, Ricardo, J., McDonough, W.F., 2010. Chemical variations and regional diversity observed in MORB. Chemical Geology 271, 70–85.

Arevalo, R., McDonough, W.F., Luong, M., 2009. The K/U ratio of the silicate Earth: Insights into mantle composition, structure and thermal evolution. Earth and Planetary Science Letters 278, 361–369.

Bach, W., Roberts, S., Binns, R.A., 2005. Data report: Chemical and isotopic (S, Sr) composition of anhydrite from ODP Leg 193, PACMANUS hydrothermal system, Manus Basin, Papua New Guinea, in: Barriga, F., Binns, R., Miller, D., Herzig, P. (Eds.), Proceedings of the Ocean Drilling Program, Scientific Results. volume 193, p. 23.

Bach, W., Roberts, S., Vanko, D.A., Binns, R.A., Yeats, C.J., Craddock, P.R., Humphris, S.E., Bau, M., Lueders, V., 2003. Controls of fluid chemistry and complexation on rare-earth element contents of anhydrite from the Pacmanus subseafloor hydrothermal system, Manus Basin, Papua New Guinea. Mineralium Deposita 38, 916–935.

Bacon, C.R., Druitt, T.H., 1988. Compositional Evolution of the Zoned Calcalkaline Magma Chamber of Mount-Mazama, Crater Lake, Oregon. Contributions to Mineralogy and Petrology 98, 224–256.

Barnicoat, A.C., Cartwright, I., 1995. Focused fluid flow during subduction; oxygen isotope data from high-pressure ophiolites of the Western Alps. Earth and Planetary Science Letters 132, 53–61.

Barnicoat, A.C., Cartwright, I., 1997. The gabbro-eclogite transformation; an oxygen isotope and petrographic study of West Alpine ophiolites. Journal of Metamorphic Geology 15, 93–104.

Barriga, F., Binns, R., Miller, D., Herzig, P., 2007. Proceedings of the Ocean Drilling Programme, Scientific Results. volume 193. Ocean Drilling Programme, College Station, TX.

Barriga, F., Binns, R.A., Baldauf, J., Miller, D.J., 2000. Ocean Drilling Program; Leg 193 scientific prospectus; anatomy of an active, felsic-hosted hydrothermal system, eastern Manus Basin. Scientific Prospectus 193.

Bartetzko, A., 2008. Gamma ray spectrometric analysis of hydrothermally altered dacite samples from the PACMANUS hydrothermal field; implications for the interpretation of gamma ray wireline measurements. Journal of Volcanology and Geothermal Research 175, 269–277.

Bartetzko, A., Klitzsch, N., Iturrino, G.J., Kaufhold, S., Arnold, J., 2006. Electrical properties of hydrothermally altered dacite from the PACMANUS hydrothermal field (ODP Leg 193). Journal of Volcanology and Geothermal Research 152, 109–120.

Bearth, P., 1967. Die Ophiolithe der Zone von Zermatt-Saas Fee. The ophiolites of the Zermatt-Saas Fee zone. Beitraege zur Geologischen Karte der Schweiz = Materiaux pour la Carte Geologique de la Suisse = Materiali per la Carta Geologica della Svizzera 132, 130.

Bearth, P., Schwander, H., 1981. The post-Triassic sediments of the ophiolite zone Zermatt-Saas Fee and the associated manganese mineralizations. Eclogae Geologicae Helvetiae 74, 189–205.

Besang, C., Eckhardt, F., Harre, W., Kreuzer, H., Muller, P., 1977. Radiometricshe alternbestimmungen an Neogenen eruptivgesteinen der Turkei. Geologisches Jahrbuch B25, 3–36.

Bieri, R.H., Koide, M., 1972. Dissolved Noble Gases in the East Equatorial and Southeast Pacific. Journal of Geophysical Research 77, 1667–1676.

Bierlein, F.P., Groves, D.I., Goldfarb, R.J., Dube, B., 2006. Lithospheric controls on the formation of provinces hosting giant orogenic gold deposits. Mineralium Deposita 40, 874–886.

Bierlein, F.P., Pisarevsky, S., 2008. Plume-related oceanic plateaus as a potential source of gold mineralization. Economic Geology and the Bulletin of the Society of Economic Geologists 103, 425–430.

Binns, R., 2004. Eastern Manus Basin, Papua New Guinea: guides for volcanogenic massive sulphide exploration from a modern seafloor analogue, in: McConachy, T., McInnes, B. (Eds.), Copper-Zinc Massive Sulphide Deposits in Western Australia. CSIRO Explores. volume 2, pp. 59–80.

Binns, R., Barriga, F.A.S., Miller, D.J., 2007. Anatomy of an active hydrothermal system hosted by felsic volcanic rocks at a convergent plate margin; ODP Leg 193, in: Barriga, F., Binns, R., Miller, D., Herzig, P. (Eds.), Proceedings of the Ocean Drilling Pogramme, Scientific Results. Ocean Drilling Programme, College Station, TX. volume 193, pp. 1–17.

Binns, R.A., Scott, S.D., 1993. Actively forming polymetallic sulfide deposits associated with felsic volcanic rocks in the eastern Manus back-arc basin, Papua New Guinea. Economic Geology and the Bulletin of the Society of Economic Geologists 88, 2226–2236.

Bird, D.K., Brooks, C.K., Gannicott, R.A., Turner, P.A., 1991. A gold-bearing horizon in the Skaergaard Intrusion. Economic Geology and the Bulletin of the Society of Economic Geologists 86, 1083–1092.

Boer, R.H., Beukes, G.J., Meyer, F.M., Smith, C.B., 1993. Fluoride Precipitates in Silicate Wet-Chemistry - Implications on Ree Fractionation. Chemical Geology 104, 93–98.

de Boorder, H., Spakman, W., White, S.H., Wortel, M.J.R., 1998. Late Cenozoic mineralization, orogenic collapse and slab detachment in the European Alpine Belt. Earth and Planetary Science Letters 164, 569–575.

Borisov, A., Palme, H., 1997. Noble metal/silicate melt equilibria: experimental investigations and geochemical implications. European Journal of Mineralogy 9, 59.

Botz, R., Winckler, G., Bayer, R., Schmitt, M., Schmidt, M., Garbe-Schoenberg, D., Stoffers, P., Kristjansson, J.K., 1999. Origin of trace gases in submarine hydrothermal vents of the Kolbeinsey Ridge, North Iceland. Earth and Planetary Science Letters 171, 83–93.

Boyle, R.W., 1979. The geochemistry of gold and its deposits. Bulletin Geological Survey of Canada 280, 584.

Boynton, W., 1984. Geochemistry of the rare earth elements: meteorite studies, in: Henderson, P. (Ed.), Rare Earth Element Geochemistry. Elsevier, Amsterdam, pp. 63–114.

Brandon, A.D., Walker, R.J., 2005. The debate over core-mantle interaction. Earth and Planetary Science Letters 232, 211–225.

Brimhall, George H., J., 1987. Preliminary fractionation patterns of ore metals through Earth history. Chemical Geology 64, 1–16.

Bucher, K., Fazis, Y., de Capitani, C., Grapes, R., Sorensen, S.S., Carlson, W., 2005. Blueschists, eclogites, and decompression assemblages of the Zermatt-Saas Ophiolite; high-pressure metamorphism of subducted Tethys lithosphere. American Mineralogist 90, 821–835.

Burke, K., Steinberger, B., Torsvik, T.H., Smethurst, M.A., 2008. Plume generation zones at the margins of large low shear velocity provinces on the core-mantle boundary. Earth and Planetary Science Letters 265, 49–60.

Celik, M., 1999. Minamiite and Alunite Occurrences Formed From Volcanic Emanations, West-Southwest of Konya, Turkey. Geological Bulletin of Turkey 42, 89–97.

Chiba, H., Kusakabe, M., Hirano, S.i., Matsuo, S., Somiya, S., 1981. Oxygen isotope fractionation factors between anhydrite and water from 100 to 550 degrees C. Earth and Planetary Science Letters 53, 55–62.

Chiba, H., Uchiyama, N., Teagle, D.A.H., 1998. Stable isotope study of anhydrite and sulfide minerals at the TAG hydrothermal mound, Mid-Atlantic Ridge, 26 degrees N, in: Herzig, P.M., Humphris, S.E., Miller, D.J. (Eds.), Proceedings of the Ocean Drilling Program, Scientific Results. Ocean Drilling Programme, College Station, TX. volume 158, pp. 85–90.

Christiansen, L.B., Iturrino, G.J., 2007. Core-scale permeability of an actively venting, felsic-hosted hydrothermal system; the PACMANUS hydrothermal field, in: Barriga, F., Binns, R., Miller, D., Herzig, P. (Eds.), Proceedings of the Ocean Drilling Program, Scientific Results. Ocean Drilling Programme, College Station, TX. volume 193, pp. 1–19.

Cline, J.S., Bodnar, R.J., 1991. Can economic porphyry copper mineralization be generated by a typical calc-alkaline melt? Journal of Geophysical Research 96, 8113–8126.

Constantin, M., 2009. Trace Element Data for Gold, Iridium and Silver in Seventy Geochemical Reference Materials. Geostandards and Geoanalytical Research 33, 115–132.

Cooke, C., Wilson, A.J., Davies, A.G.S., 2004. Characteristics and genesis of porphyry copper-gold deposits, in: Cooke, R., D., Deyell, Cari, Pongratz, June (Eds.), Special Publication - Centre for Ore Deposit and Exploration Studies (CODES). University of Tasmania, Hobartm Tasmania. volume 5, pp. 17–34.

Cooke, D.R., Hollings, P., Walshe, J.L., 2006. Tectonic triggers for giant porphyry and epithermal deposits of the circum-Pacific region. Geochimica et Cosmochimica Acta 70, A110–A110.

Craddock, P.R., Bach, W., 2010. Insights to magmatic-hydrothermal processes in the Manus back-arc basin as recorded by anhydrite. Geochimica et Cosmochimica Acta 74, 5514–5536.

Craig, H., Lupton, J.E., 1976. Primordial neon, helium, and hydrogen in oceanic basalts. Earth and Planetary Science Letters 31, 369–385.

Croudace, I.W., 1980. A Possible Error Source in Silicate Wet-Chemistry Caused by Insoluble Fluorides. Chemical Geology 31, 153–155.

Dale, C.W., Burton, K.W., Pearson, D.G., Gannoun, A., Alard, O., Argles, T.W., Parkinson, I.J., 2009. Highly siderophile element behaviour accompanying subduction of oceanic crust; whole rock and mineral scale insights from a high-pressure terrain. Geochimica et Cosmochimica Acta 73, 1394–1416.

Dale, C.W., Gannoun, A., Burton, K.W., Argles, T.W., Parkinson, I.J., 2007. Rhenium-osmium isotope and elemental behaviour during subduction of oceanic crust and the implications for mantle recycling. Earth and Planetary Science Letters 253, 211–225.

Douville, E., Bienvenu, P., Charlou, J.L., Donval, J.P., Fouquet, Y., Appriou, P., Gamo, T., 1999. Yttrium and rare earth elements in fluids from various deep-sea hydrothermal systems. Geochimica et Cosmochimica Acta 63, 627–643.

Drake, M.J., 2000. Accretion and primary differentiation of the Earth: A personal journey. Geochimica et Cosmochimica Acta 64, 2363–2369.

England, P.C., Katz, R.F., 2010. Melting above the anhydrous solidus controls the location of volcanic arcs. Nature 467, 700–U84.

Esperanca, S., Carlson, R.W., Shirey, S.B., Smith, D., 1997. Dating crust-mantle separation: Re-Os isotopic study of mafic xenoliths from central Arizona. Geology 25, 651–654.

Ewart, A., Griffin, W.L., 1994. Application of Proton-Microprobe Data to Trace-Element Partitioning in Volcanic-Rocks. Chemical Geology 117, 251–284.

Falkner, K., 1989. An investigation of the Marine Geochemistry of Gold. Ph.D. thesis.

Farley, K.A., Neroda, E., 1998. Noble gases in the Earth's mantle. Annual Review of Earth and Planetary Sciences 26, 189–218.

Feebrey, C.A., Hishida, H., Yoshioka, K., Nakayama, K., 1998. Geophysical expression of low sulphidation epithermal Au-Ag deposits and exploration implications - Examples from the Hokusatsu region of SW Kyushu, Japan. Resource Geology 48, 75–86.

Finlowbates, T., Stumpfl, E.F., 1981. The Behavior of So-Called Immobile Elements in Hydrothermally Altered Rocks Associated with Volcanogenic Submarine-Exhalative Ore-Deposits. Mineralium Deposita 16, 319–328.

Fourre, E., Jean-Baptiste, P., Charlou, J.L., Donval, J.P., Ishibashi, J.I., 2006. Helium isotopic composition of hydrothermal fluids from the Manus back-arc basin, Papua New Guinea. Geochemical Journal 40, 245–252.

Frimmel, H.E., 2008. Earth's continental crustal gold endowment. Earth and Planetary Science Letters 267, 45–55.

Fryer, B.J., Greenough, J.D., 1992. Evidence for Mantle Heterogeneity from Platinum-Group-Element Abundances in Indian-Ocean Basalts. Canadian Journal of Earth Sciences 29, 2329–2340.

Gammons, C.H., Williams-Jones, A.E., 1997. Chemical mobility of gold in the porphyry-epithermal environment. Economic Geology and the Bulletin of the Society of Economic Geologists 92, 45–59.

Gazel, E., Carr, M.J., Hoernle, K., Feigenson, M.D., Szymanski, D., Hauff, F., van den Bogaard, P., 2009. Galapagos-OIB signature in southern Central America: Mantle refertilization by arc-hot spot interaction. Geochemistry Geophysics Geosystems 10.

Gijbels, R.H., Millard, H.T., Desborou.Ga, Bartel, A.J., 1974. Osmium, Ruthenium, Iridium and Uranium in Silicates and Chromite from Eastern Bushveld Complex, South-Africa. Geochimica et Cosmochimica Acta 38, 319–337.

Graham, D.W., 2002. Noble gas isotope geochemistry of mid-ocean ridge and ocean island basalts: Characterization of mantle source reservoirs. Noble Gases in Geochemistry and Cosmochemistry 47, 247–317.

Grant, J., 1986. The isocon diagram; a simple solution to Gresens' equation for metasomatic alteration. Economic Geology 81, 1976–1982.

Grove, T.L., Chatterjee, N., Parman, S.W., Medard, E., 2006. The influence of H2O on mantle wedge melting. Earth and Planetary Science Letters 249, 74–89.

Guo, S., Ye, K., Chen, Y., Liu, J.B., 2009. A Normalization Solution to Mass Transfer Illustration of Multiple Progressively Altered Samples Using the Isocon Diagram. Economic Geology 104, 881–886.

Guo, S., Ye, K., Chen, Y., Liu, J.B., Mao, Q., Ma, Y.G., 2012. Fluid-rock interaction and element mobilization in UHP metabasalt: Constraints from an omphacite-epidote vein and host eclogites in the Dabie orogen. Lithos 136, 145–167.

Hall, A.J., Boyce, A.J., Fallick, A.E., Hamilton, P.J., 1991. Isotopic evidence of the depositional environment of late Proterozoic stratiform barite mineralisation, Aberfeldy, Scotland. Chemical Geology; Isotope Geoscience Section 87, 99–114.

Hardardottir, V., Hannington, M., Hedenquist, J., Kjarsgaard, I., Hoal, K., 2010. Cu-Rich Scales in the Reyksjanes Geothermal System, Iceland. Economic Geology 105, 1143–1155.

Hawkesworth, C., Schersten, A., 2007. Mantle plumes and geochemistry. Chemical Geology 241, 319–331.

Henley, R.W., Ellis, A.J., 1983. Geothermal Systems Ancient and Modern - a Geochemical Review. Earth-Science Reviews 19, 1–50.

Hertogen, J., Janssens, M.J., Palme, H., 1980. Trace elements in ocean ridge basalt glasses; implications for fractionations during mantle evolution and petrogenesis. Geochimica et Cosmochimica Acta 44, 2125–2144.

Hilton, D.R., Thirlwall, M.F., Taylor, R.N., Murton, B.J., Nichols, A., 2000. Controls on magmatic degassing along the Reykjanes Ridge with implications for the helium paradox. Earth and Planetary Science Letters 183, 43–50.

Hoernes, S., Friedrichsen, H., Schock, H.H., 1979. Oxygen- and hydrogen-isotope and trace-element investigations on rocks of DSDP Hole 395A, Leg 45, in: Melson, W.G., Rabinowitz, P.D., Bougault, H., Fuji, T., Graham, A.L., Johnson, H.P., Natland, J.H., Prosser, E.C., Rhodes, J.M., Zolotarev, B.P. (Eds.), Initial reports of the Deep Sea Drilling Project Leg 45; San Juan, Puerto Rico to San Juan, Puerto Rico.

Hofmann, A., 1997. Mantle geochemistry: the message from oceanic volcanism. Nature 385, 219–229.

Holzheid, A., Sylvester, P., O'Neill, H.S.C., Rubie, D.C., Palme, H., 2000. Evidence for a late chondritic veneer in the Earth's mantle from high-pressure partitioning of palladium and platinum. Nature 406, 396–399.

Humphris, S.E., Thompson, G., 1978a. Hydrothermal Alteration of Oceanic Basalts by Seawater. Geochimica et Cosmochimica Acta 42, 107–125.

Humphris, S.E., Thompson, G., 1978b. Trace-Element Mobility during Hydrothermal Alteration of Oceanic Basalts. Geochimica et Cosmochimica Acta 42, 127–136.

Innocenti, F., Mazzuoli, R., Pasquare, G., Radicati di Brozolo, F., Villari, L., 1975. The Neogene calcalkaline volcanism of Central Anatolia: geochronological data on Kayseri?Nigde area. Geological Magazine 112, 349–360.

Irvine, R.J., Smith, M.J., 1990. Geophysical Exploration for Epithermal Gold Deposits. Journal of Geochemical Exploration 36, 375–412.

Ishibashi, J., Takahashi, H., Gamo, T., Okamura, K., Yamanaka, T., Chiba, H., Charlou, J.L., Shitashima, K., 1998. Fluid chemistry of seafloor magmatic hydrothermal system in the Manus Basin, PNG. Proceedings - International Symposium on Water-Rock Interaction 9, 735–737.

Iturrino, G.J., Bartetzko, A., Anonymous, 2002. Subsurface fracture patterns in the PACMANUS hydrothermal system identified from downhole measurements and their potential implications for fluid circulation. Eos, Transactions, American Geophysical Union 83, F1335.

Jagoutz, E., Palme, H., H., B., K., B., M., C., G., D., Spettel, B., V., L., H, W., 1979. The abundance of major, minor and trace elements in the earth's mantle as derived from primitive ultramafic rocks.

Jamais, M., Lassiter, J.C., Brugmann, G., 2008. PGE and Os-isotopic variations in lavas from Kohala Volcano, Hawaii: Constraints on PGE behavior and melt/crust interaction. Chemical Geology 250, 16–28.

Jean-Baptiste, P., Charlou, J.L., Stievenard, M., Donval, J.P., Bougault, H., Mevel, C., 1991. Helium and methane measurements in hydrothermal fluids from the Mid-Atlantic Ridge; the Snake Pit site at 23 degrees N. Earth and Planetary Science Letters 106, 17–28.

Jean-Baptiste, P., Dapoigny, A., Stievenard, M., Charlou, J.L., Fouquet, Y., Donval, J.P., Auzende, J.M., 1997. Helium and oxygen isotope analyses of hydrothermal fluids from the East Pacific Rise between 17 degrees S and 19 degrees S. Geo-Marine Letters 17, 213–219.

Jean-Baptiste, P., Fouquet, Y., 1996. Abundance and isotopic composition of helium in hydrothermal sulfides from the East Pacific Rise at 13 degrees N. Geochimica et Cosmochimica Acta 60, 87–93.

Jean-Baptiste, P., Fourre, E., Charlou, J.L., German, C.R., Radford-Knoery, J., 2004. Helium isotopes at the Rainbow hydrothermal site (Mid-Atlantic Ridge, 36 degrees 14'N). Earth and Planetary Science Letters 221, 325–335.

Jenner, F.E., O'Neill, H.S., 2012. Analysis of 60 elements in 616 ocean floor basaltic glasses. Geochemistry Geophysics Geosystems 13.

Jenner, F.E., O'Neill, H.S.C., Arculus, R.J., Mavrogenes, J.A., 2010. The Magnetite Crisis in the Evolution of Arc-related Magmas and the Initial Concentration of Au, Ag and Cu. Journal of Petrology 51, 2445–2464.

Karakaya, M.C., Karakaya, N., Temel, A., 2001. Kaolin occurrences in the Erenler Dagi volcanics, southwest Konya Province, Turkey. International Geology Review 43, 711–721.

Karakaya, N., 2009. REE and HFS element behaviour in the alteration facies of the Erenler Dagi Volcanics (Konya, Turkey) and kaolinite occurrence. Journal of Geochemical Exploration 101, 185–208.

Kay, S.M., Mpodozis, C., 2001. Central Andean ore deposits linked to evolving shallow subduction systems and thickening crust. GSA Today 11, 4–9.

Keays, R.R., 1983. Archaean gold deposits and their source rocks: the Upper Mantle connection, in: Foster, R.P. (Ed.), Gold '82?The Geology, Geochemistry and Genesis of Gold Deposits. Balkema, Amsterdam, pp. 17–51.

Keays, R.R., 1987. Principles of mobilization (dissolution) of metals in mafic and ultramafic rocks ? The role of immiscible magmatic sulphides in the generation of hydrothermal gold and volcanogenic massive sulphide deposits. Ore Geology Reviews 2, 47–63.

Keays, R.R., 1995. The Role of Komatiitic and Picritic Magmatism and S-Saturation in the Formation of Ore-Deposits. Lithos 34, 1–18.

Keays, R.R., Scott, R.B., 1976. Precious metals in ocean-ridge basalts; implications for basalts as source rocks for gold mineralization. Economic Geology and the Bulletin of the Society of Economic Geologists 71, 705–720.

Keller, J., Jung, D., Burgath, K., Wolff, F., 1977. Geologie und Petrologie des neogenen Kalkalkali-Vulkanismus von Konya (Erenler Dag-Alaca Dag-Massiv, Zentral-Anatolien). Geology and petrology of the Neogene calc-alkalic volcanism of Konya, Erenler Dag, Alaca Dag Massif, central Anatolia. Geologisches Jahrbuch. Reihe B: Regionale Geologie Ausland, no 25, 37–117.

Keller, N.S., Arculus, R.J., Hermann, J., Richards, S., 2008. Submarine back-arc lava with arc signature: Fonualei Spreading Center, northeast Lau Basin, Tonga. Journal of Geophysical Research-Solid Earth 113.

Kepezhinskas, P., Defant, M.J., Widom, E., 2002. Abundance and distribution of PGE and Au in the island-arc mantle: implications for sub-arc metasomatism. Lithos 60, 113–128.

Kerrich, R., Goldfarb, R.J., Groves, D.I., Garwin, S., 2000. The geodynamics of world-class gold deposits; characteristics, space-time distribution, and origins. Reviews in Economic Geology 13, 501–551.

Kessel, R., Schmidt, M.W., Ulmer, P., Pettke, T., 2005. Trace element signature of subduction-zone fluids, melts and supercritical liquids at 120-180 km depth. Nature 437, 724–727.

Kim, J., Lee, I., Lee, K.Y., 2004. S, Sr, and Pb isotopic systematics of hydrothermal chimney precipitates from the eastern Manus Basin, western Pacific; evaluation of magmatic contribution to hydrothermal system. Journal of Geophysical Research 109, no.B12, 13.

Kimura, K., Lewis, R.S., Anders, E., 1974. Distribution of Gold and Rhenium between Nickel-Iron and Silicate Melts - Implications for Abundance of Siderophile Elements on Earth and Moon. Geochimica et Cosmochimica Acta 38, 683–701.

Knauth, L.P., Epstein, S., 1976. Hydrogen and oxygen isotope ratios in nodular and bedded cherts. Geochimica et Cosmochimica Acta 40, 1095–1108.

Lackschewitz, K.S., Devey, C.W., Stoffers, P., Botz, R., Eisenhauer, A., Kummetz, M., Schmidt, M., Singer, A., 2004. Mineralogical, geochemical and isotopic characteristics of hydrothermal alteration processes in the active, submarine, felsic-hosted PACMANUS field, Manus Basin, Papua New Guinea. Geochimica et Cosmochimica Acta 68, 4405–4427.

Langmyhr, F., Kringstad, K., 1966. An investigation of the composition of the precipitates formed by the decomposition of silicate rocks in 39-48% hydrofluoric acid. Anal. Chim. Acta 35, 131–135.

Lapukhov, A.S., Simonov, V.A., Pavlova, L.K., 1999. Noble metals in the bedrocks from the Mid-Atlantic Ridge (15 degrees 20'N fracture zone). Oceanology 39, 719–727.

Large, R.R., Gemmell, J.B., Paulick, H., Huston, D.L., 2001. The alteration box plot: A simple approach to understanding the relationship between alteration mineralogy and lithogeochemistry associated with volcanic-hosted massive sulfide deposits. Economic Geology and the Bulletin of the Society of Economic Geologists 96, 957–971.

Lassiter, J.C., 2006. Constraints on the coupled thermal evolution of the Earth's core and mantle, the age of the inner core, and the origin of the (OS)-O-186/(OS)-O-188 "core signal" in plume-derived lavas. Earth and Planetary Science Letters 250, 306–317.

Latourrette, T.Z., Burnett, D.S., Bacon, C.R., 1991. Uranium and Minor-Element Partitioning in Fe-Ti Oxides and Zircon from Partially Melted Granodiorite, Crater Lake, Oregon. Geochimica et Cosmochimica Acta 55, 457–469.

Lebas, M.J., Lemaitre, R.W., Streckeisen, A., Zanettin, B., 1986. A CHEMICAL CLASSIFICATION OF VOLCANIC-ROCKS BASED ON THE TOTAL ALKALI SILICA DIAGRAM. Journal of Petrology 27, 745–750.

Lemarchand, F., Villemant, B., Calas, G., 1987. Trace-Element Distribution Coefficients in Alkaline Series. Geochimica et Cosmochimica Acta 51, 1071–1081.

Li, C.S., Ripley, E.M., 2005. Empirical equations to predict the sulfur content of mafic magmas at sulfide saturation and applications to magmatic sulfide deposits. Mineralium Deposita 40, 218–230.

Lloyd, R.M., 1967. Oxygen-18 composition of oceanic sulfate. Science 156, 1228–1231.

Luhr, J.F., Carmichael, I.S.E., Varekamp, J.C., 1984. The 1982 Eruptions of El-Chichon Volcano, Chiapas, Mexico - Mineralogy and Petrology of the Anhydrite-Bearing Pumices. Journal of Volcanology and Geothermal Research 23, 69–108.

Macpherson, C.G., Hilton, D.R., Day, J.M.D., Lowry, D., Gronvold, K., 2005. High-He-3/He-4, depleted mantle and low-delta O-18, recycled oceanic lithosphere in the source of central Iceland magmatism. Earth and Planetary Science Letters 233, 411–427.

Macpherson, C.G., Hilton, D.R., Mattey, D.P., Sinton, J.M., 2000. Evidence for an (super 18) O-depleted mantle plume from contrasting (super 18) O/ (super 16) O ratios of back-arc lavas from the Manus Basin and Mariana Trough. Earth and Planetary Science Letters 176, 171–183.

Macpherson, C.G., Hilton, D.R., Sinton, J.M., Poreda, R.J., Craig, H., 1998. High (super 3) He/ (super 4) He ratios in the Manus backarc basin; implications for mantle mixing and the origin of plumes in the Western Pacific Ocean. Geology 26, 1007–1010.

Mahood, G.A., Stimac, J.A., 1990. Trace-Element Partitioning in Pantellerites and Trachytes. Geochimica et Cosmochimica Acta 54, 2257–2276.

Marty, B., Sano, Y., France-Lanord, C., 2001. Water-saturated oceanic lavas from the Manus Basin: volatile behaviour during assimilation-fractional crystallisation-degassing (AFCD). Journal of Volcanology and Geothermal Research 108, 1–4.

McInnes, B.I.A., McBride, J.S., Evans, N.J., Lambert, D.D., Andrew, A.S., 1999. Osmium isotope constraints on ore metal recycling in subduction zones. Science 286, 512–516.

Miller, D.J., C., P., 2002. Sulfide mineral chemistry and petrography and platinum group element composition in gabbroic rocks from the southwest indian ridge, in: Natland, J.H., H.J.B, D., Miller, D.J., Von Herzen, R. (Eds.), Proceedings of the Ocean Drilling Programme, Scientific Results. volume 176.

Miller, D.J., Kelley, J., 2004. Low-Temperature Alteration of Basalt over Time: A Synthesis of Results from Ocean Drilling Program Leg 187, in: Pedersen, R., Christie, D., Miller, D. (Eds.), Proc. ODP, Sci. Results, 187.

Momme, P., Oskarsson, N., Keays, R.R., Horan, M.F., Brandon, A.D., Neal, C.R., 2003. Platinum-group elements in the Icelandic rift system; melting processes and mantle sources beneath Iceland. Chemical Geology 196, 209–234.

Morgan, J.W., Wandless, G.A., Petrie, R.K., Irving, A.J., 1981. Composition of the Earths Upper Mantle .1. Siderophile Trace-Elements in Ultramafic Nodules. Tectonophysics 75, 47–67.

Moss, R., Scott, S.D., 2001. Geochemistry and mineralogy of gold-rich hydrothermal precipitates from the eastern Manus Basin, Papua New Guinea. Canadian Mineralogist 39, 957–978.

Muller, D., Kaminski, K., Uhlig, S., Graupner, T., Herzig, P.M., Hunt, S., 2002. The transition from porphyry- to epithermal-style gold mineralization at Ladolam, Lihir Island, Papua New Guinea: a reconnaissance study. Mineralium Deposita 37, 61–74.

Mungall, J.E., 2002. Roasting the mantle; slab melting and the genesis of major Au and Au-rich Cu deposits. Geology 30, 915–918.

Murton, B.J., Taylor, R.N., Thirlwall, M.F., 2002. Plume-ridge interaction: A geochemical perspective from the Reykjanes Ridge. Journal of Petrology 43, 1987–2012.

Nehring, F., Jacob, D.E., Barth, M.G., Foley, S.F., 2008. Laser-ablation ICP-MS analysis of siliceous rock glasses fused on an iridium strip heater using MgO dilution. Microchimica Acta 160, 153–163.

Noll, P.D., Newsom, H.E., Leeman, W.P., Ryan, J.G., 1996. The role of hydrothermal fluids in the production of subduction zone magmas: Evidence from siderophile and chalcophile trace elements and boron. Geochimica et Cosmochimica Acta 60, 587–611.

Okamoto, K., 1979. Geochemical study on magmatic differentiation of Asama Volcano, central Japan. Journal of the Geological Society of Japan 85, 525–535.

Oliver, B., Bradley, J., Farrar, H., 1984. Helium concentration in the Earth's lower atmosphere. Geochimica et Cosmochimica Acta 48, 1759–1767.

Oppliger, G.L., Murphy, J.B., Brimhall, George H., J., 1997. Is the ancestral Yellowstone hotspot responsible for the Tertiary "carlin" mineralization in the Great Basin of Nevada? Geology 25, 627–630.

Parr, J.M., Binns, R.A., Gemmel, J., 1996. Sulfide chimneys from the Satanic Mills site in the PACMANUS hydrothermal field, eastern Manus Basin, Papua New Guinea. Eos, WPGM Supplement 77, W120.

Paulick, H., Herzig, P.M., Hoernes, S., 2005. Data report: a comprehensive geochemical, mineralogical, and isotopic data set of altered dacitic volcanic rocks from the subsurface of the PACMANUS hydrothermal field (ODP Leg 193), in: Barriga, F., Binns, R., Miller, D., Herzig, P. (Eds.), Proceedings of the Ocean Drilling Program, Scientific Results. Ocean Drilling Programme, College Station, TX. volume 193.

Paulick, H., Vanko, D.A., Yeats, C.J., 2004. Drill core-based facies reconstruction of a deep marine felsic volcano hosting an active hydrothermal system (Pual Ridge, Papua New Guinea, ODP Leg 193). Journal of Volcanology and Geothermal Research 130, 31–50.

Peach, C.L., Mathez, E.A., Keays, R.R., 1990. Sulfide melt-silicate melt distribution coefficients for noble metals and other chalcophile elements as deduced from MORB; implications for partial melting. Geochimica et Cosmochimica Acta 54, 3379–3389.

Peacock, S.M., 1990. Fluid processes in subduction zones. Science 248, 329–337.

Peacock, S.M., 1993. The importance of blueschist –¿ eclogite dehydration reactions in subducting oceanic crust. Geological Society of America Bulletin 105, 684–694.

Pearce, J.A., Peate, D.W., 1995. Tectonic Implications of the Composition of Volcanic Arc Magmas. Annual Review of Earth and Planetary Sciences 23, 251–285.

Pfeifer, H.R., Colombi, A., Ganguin, J., 1989. Zermatt-Saas and Antrona Zone; a petrographic and geochemical comparison of polyphase metamorphic ophiolites of the west-central Alps. Schweizerische Mineralogische und Petrographische Mitteilungen = Bulletin Suisse de Mineralogie et Petrographie 69, 217–236.

Pitcairn, I.K., 2011. Background concentrations of gold in different rock types. Applied Earth Science 120, 31–8.

Pitcairn, I.K., Teagle, D.A.H., Craw, D., Olivo, G.R., Kerrich, R., Brewer, T.S., 2006a. Sources of metals and fluids in orogenic gold deposits: Insights from the Otago and Alpine schists, New Zealand. Economic Geology 101, 1525–1546.

Pitcairn, I.K., Warwick, P.E., Milton, J.A., Teagle, D.A.H., 2006b. Method for ultra-low-level analysis of gold in rocks. Analytical chemistry 78, 1290–5.

Plank, T., Spiegelman, M., Langmuir, C.H., Forsyth, D.W., 1995. The Meaning of Mean-F - Clarifying the Mean Extent of Melting at Ocean Ridges. Journal of Geophysical Research-Solid Earth 100, 15045–15052.

Platzman, E.S., Tapirdamaz, C., Sanver, M., 1998. Neogene anticlockwise rotation of central Anatolia (Turkey): preliminary palaeomagnetic and geochronological results. Tectonophysics 299, 175–189.

Reeves, P.R., Seewald, J., Saccocia, P., Walsh, E., Bach, W., Craddock, P., Shanks, W.C., Sylva, S., Pichler, T., Rosner, M., 2010. Geochemistry of hydrothermal fluids from the PACMANUS, Northeast Pual and Vienna Woods vent fields, Manus Basin, Papua New Guinea. Geochimica et Cosmochimica Acta 75, 1088–1123.

Reimann, C., Siewers, U., Skarphagen, H., Banks, D., 1999. Does bottle type and acid-washing influence trace element analyses by ICP-MS on water samples? A test covering 62 elements and four bottle types: high density polyethene (HDPE), polypropene (PP), fluorinated ethene propene copolymer(FEP) and perfluoroalkoxy polymer(PFA). Science of the Total Environment 239, 111–130.

Reyes, A.G., 1990. Petrology of Philippine geothermal systems and the application of alteration mineralogy to their assessment. Journal of Volcanology and Geothermal Research 43, 279–309.

Robb, L.J., 2005. Introduction to ore-forming processes. Blackwell Pub., Malden, MA.

Roberts, S., Bach, W., Binns, R.A., Vanko, D.A., Yeats, C.J., Teagle, D.A.H., Blacklock, K., Blusztajn, J.S., Boyce, A.J., Cooper, M.J., Holland, N., McDonald, B., 2003. Contrasting evolution of hydrothermal fluids in the PACMANUS system, Manus Basin; the Sr and S isotope evidence. Geology 31, 805–808.

Rock, N.M.S., Groves, D.I., 1988. Can lamprophyres resolve the genetic controversy over mesothermal gold deposits? Geology 16, 538–541.

Rubatto, D., Gebauer, D., Fanning, M., 1998. Jurassic formation and Eocene subduction of the Zermatt-Saas-Fee ophiolites; implications for the geodynamic evolution of the Central and Western Alps. Contributions to Mineralogy and Petrology 132, 269–287.

Rubie, D.C., Frost, D.J., 2007. New constraints on conditions of core formation and the light element content of the Earth's core. Geochimica et Cosmochimica Acta 71, A857–A857.

Rudnicki, M.D., Elderfield, H., 1992. Helium, radon and manganese at the TAG and Snakepit hydrothermal vent fields, 26 degrees and 26 degrees N, Mid-Atlantic Ridge. Earth and Planetary Science Letters 113, 307–321.

Sano, Y., Terada, K., Fukuoka, T., 2002. High mass resolution ion microprobe analysis of rare earth elements in silicate glass, apatite and zircon: lack of matrix dependency. Chemical Geology 184, 217–230.

Sano, Y., Wakita, H., 1985. Geographical Distribution of 3He/4He Ratios in Japan: Implications for Arc Tectonics and Incipent Magmatism. Journal of Geophysical Research 90, 9729–8741.

Scott, S., Binns, R., 1995. Hydrothermal processes and contrasting styles of mineralization in the western Woodlark and eastern Manus Basins of the western Pacific. Geological Society, London, Special Publications 87, 191–205.

Seedorff, E., Dilles, J.H., Phoffett, J., J.M., Einaudi, M., 2005. Porphyry deposits: Characteristics and origin ofhypogene features. Economic Geology 100th Anniv.Vol., Soc. Econ. Geol., Littleton.

Seewald, J., Reeves, E., Saccocia, P., Rouxel, O., Walsh, E., Price, R., Tivey, M., Bach, W., 2006. Water-rock reaction, substrate composition, magmatic degassing, and mixing as major factors controlling vent fluid compositions in manus basin hydrothermal systems, in: American Geophysical Union, Fall Meeting.

Seward, T.M., 1973. Thio Complexes of Gold and Transport of Gold in Hydrothermal Ore Solutions. Geochimica et Cosmochimica Acta 37, 379–399.

Shcherbakov, Y.G., Perezhogin, G., 1964. Geochemistry of Gold. Geochemistry International 6, 489–496.

Shimizu, K., Chang, Q., Nakamura, K., 2010. Flux-free fusion of silicate rocks preceding acid digestion of ICP-MS bulk analysis. Geostandards and Geoanalytical Research 35, 45–55.

Shitashima, K., Gamo, T., Okamura, K., Ishibashi, J.I., 1997. Trace elements at the Manus Basin, Papua New Guinea. JAMSTEC J. Deep Sea Res. 13, 249–255.

Sillitoe, R.H., 1997. Characteristics and controls of the largest porphyry copper-gold and epithermal gold deposits in the circum-Pacific region. Australian Journal of Earth Sciences [AUST. J. EARTH SCI.]. 44, 373–388.

Sillitoe, R.H., 2000. Gold-rich porphyry deposits; descriptive and genetic models and their role in exploration and discovery. Reviews in Economic Geology 13, 315–345.

Simon, A.C., Pettke, T., Candela, P.A., Piccoli, P.M., Heinrich, C.A., 2003. Experimental determination of Au solubility in rhyolite melt and magnetite; constraints on magmatic Au budgets. American Mineralogist 88, 1644–1651.

Sinton, J.M., Ford, L.L., Chappell, B., McCulloch, M.T., 2003. Magma genesis and mantle heterogeneity in the Manus back-arc basin, Papua New Guinea. Journal of Petrology 44, 159–195.

Sisson, T.W., 2003. Native gold in a Hawaiian alkalic magma. Economic Geology and the Bulletin of the Society of Economic Geologists 98, 643–648.

Solomon, M., 1990. Subduction, Arc Reversal, and the Origin of Porphyry Copper-Gold Deposits in Island Arcs. Geology 18, 630–633.

Stefansson, A., Seward, T.M., 2004. Gold(I) complexing in aqueous sulphide solutions to 500 degrees C at 500 bar. Geochimica et Cosmochimica Acta 68, 4121–4143.

Stoll, B., Jochum, K.P., Herwig, K., Amini, M., Flanz, M., Kreuzburg, B., Kuzmin, D., Willbold, M., Enzweiler, J., 2008. An automated iridium-strip heater for LA-ICP-MS bulk analysis of geological samples. Geostandards and Geoanalytical Research 32, 5–26.

Stuart, F.M., Ellam, R.M., Harrop, P.J., Fitton, J.G., Bell, B.R., 2000. Constraints on mantle plumes from the helium isotopic composition of basalts from the British Tertiary Igneous Province. Earth and Planetary Science Letters 177, 273–285.

Stuart, F.M., Harrop, P., Knott, R., Fallick, A.E., Turner, G., Fouquet, Y., Rickard, D., 1995. Noble gas isotopes in 25000 years of hydrothermal fluids from 13N on the East Pacific Rise, in: Parson, L., Walker, C., Dixon, D.R. (Eds.), Hydrothermal Vents and Processes. Geological Society Special Publication. volume 87, pp. 133–143.

Stuart, F.M., Turner, G., Duckworth, R.C., Fallick, A.E., 1994. Helium isotopes as tracers of trapped hydrothermal fluids in ocean-floor sulfides. Geology 22, 823–826.

Sun, S.S., McDonough, W.F., 1989. Chemical and isotopic systematics of oceanic basalts; implications for mantle composition and processes. Geological Society Special Publications 42, 313–345.

Sun, S.S., Tatsumoto, M., Schilling, J.G., 1975. Mantle plume mixing along the Reykjanes Ridge axis; lead isotopic evidence. Science 190, 143–147.

Sun, W., Arculus, R.J., Kamenetsky, V.S., Binns, R.A., 2004. Release of gold-bearing fluids in convergent margin magmas prompted by magnetite crystallization. Nature 431, 975–978.

Tatar, O., Gursoy, H., Piper, J.D.A., 2002. Differential neotectonic rotations in Anatolia and the Tauride Arc; palaeomagnetic investigation of the Erenlerdag volcanic complex and Isparta volcanic district, south-central Turkey. Journal of the Geological Society of London 159, 281–294.

Tatsumi, Y., Oguri, K., Shimoda, G., 1999. The behaviour of platinum-group elements during magmatic differentiation in Hawaiian tholeiites. Geochemical Journal 33, 237–247.

Tatsumi, Y., Oguri, K., Shimoda, G., Kogiso, T., Barsczus, H.G., 2000. Contrasting behavior of noble-metal elements during magmatic differentiation in basalts from the Cook Islands, Polynesia. Geology 28, 131–134.

Tauson, V.L., Babkin, D.N., Pastushkova, T.M., Akimov, V.V., Krasnoshchekova, T.S., Lipko, S.V., Belozerova, O.Y., 2012. Dualistic distribution coefficients of elements in the system mineral-hydrothermal solution. II. Gold in magnetite. Geochemistry International 50, 227–245.

Taylor, R.N., Thirlwall, M.F., Murton, B.J., Hilton, D.R., Gee, M.A.M., 1997. Isotopic constraints on the influence of the Icelandic plume. Earth and Planetary Science Letters 148, E1–E8.

Teagle, D.A.H., Alt, J.C., Chiba, H., Humphris, S.E., Halliday, A.N., 1998. Strontium and oxygen isotopic constraints on fluid mixing, alteration and mineralization in the TAG hydrothermal deposit. Chemical Geology 149, 1–24.

Temel, A., Gundogdu, M.N., Gourgaud, A., 1998. Petrological and geochemical characteristics of Cenozoic high-K calc-alkaline volcanism in Konya, central Anatolia, Turkey. Journal of Volcanology and Geothermal Research 85, 327–354.

Thirlwall, M.F., Gee, M.A.M., Lowry, D., Mattey, D.P., Murton, B.J., Taylor, R.N., 2006. Low delta O-18 in the Icelandic mantle and its origins: Evidence from Reyjanes Ridge and Icelandic lavas. Geochimica et Cosmochimica Acta 70, 993–1019.

Thirlwall, M.F., Gee, M.A.M., Taylor, R.N., Murton, B.J., 2004. Mantle components in Iceland and adjacent ridges investigated using double-spike Pb isotope ratios. Geochimica et Cosmochimica Acta 68, 361–386.

Tilling, R.I., Gottfried, D., Rowe, J.J., 1973. Gold Abundance in Igneous Rocks; bearing on Gold Mineralization. Economic Geology and the Bulletin of the Society of Economic Geologists 68, 168–186.

Tivey, M., Bach, W., Seewald, J., Craddock, P., Rouxel, O., Yoerger, D., Yeats, C., McConachy, T., Quigley, M., Vanko, D., Mgln06Mv, a.S., 2006. Investigating the influence of magmatic volatile input and seawater entrainment on vent deposit morphology and composition in manus basin (back-arc) hydrothermal systems, in: Proceedings of the American Geophysical Union, Fall Meeting.

Tivey, M., Bach, W., Seewald, J., Tivey, M., Vanko, D., Teams, S.S., Technical, 2007. Cruise Report R/V Melville, MAGELLAN-06, in: Hydrothermal systems in the Eastern Manus Basin: Fluid chemistry and magnetic structures as guides to subseafloor processes. Woods Hole Oceanographic Institution, p. 67.

Togashi, S., Terashima, S., 1997. The behavior of gold in unaltered island arc tholeiitic rocks from Izu-Oshima, Fuji, and Osoreyama volcanic areas, Japan. Geochimica et Cosmochimica Acta 61, 543–554.

Turner, G., Stuart, F.M., 1992. Helium/heat ratios and deposition temperatures of sulphides from the ocean floor. Nature 357, 581–583.

Vanko, D., Bach, W., Roberts, S., Yeats, C., Scott, S., 2004. Fluid inclusion evidence for subsurface phase separation and variable fluid mixing regimes beneath the deep-sea PACMANUS hydrothermal field, Manus Basin back-arc rift, Papua New Guinea. Journal of Geophysical Research 109, 14.

Vermeesch, P., 2006. Tectonic discrimination diagrams revisited. Geochemistry Geophysics Geosystems 7.

Walker, R.J., Morgan, J.W., Horan, M.F., 1995. Os-187 Enrichment in Some Plumes - Evidence for Core-Mantle Interaction. Science 269, 819–822.

Walter, M.J., Tronnes, R.G., 2004. Early Earth differentiation. Earth and Planetary Science Letters 225, 253–269.

Webber, A.P., Roberts, S., Burgess, R., Boyce, A.J., 2011. Fluid mixing and thermal regimes beneath the PACMANUS hydrothermal field, Papua New Guinea: Helium and oxygen isotope data. Earth and Planetary Science Letters 304, 93–102.

Webber, A.P., Roberts, S., Taylor, R., Pitcairn, I.K., In Press. Golden Plumes: Substantial gold-enrichment of oceanic crust during ridge-plume interaction. Geology .

Weber, W., Stephenson, J., 1973. The content of mercury and gold in some Archean rocks of the Lake area. Economic Geology 68, 401–407.

Wortel, M.J.R., Spakman, W., 2000. Subduction and slab detachment in the Mediterranean-Carpathian region. Science 290, 1910–1917.

Wyborn, D., Sun, S.S., 1994. Sulphur-undersaturate magmatism - A key factor for generating magma-related copper-gold deposits. AGSO Research News-letter 21, 7–8.

Yokoyama, T., Makishima, A., Nakamura, E., 1999. Evaluation of the coprecipitation of incompatible trace elements with fluoride during silicate rock dissolution by acid digestion. Chemical Geology 157, 175–187.

Zhang, Z., Mao, J., Wang, F., Pirajno, F., 2006. Native gold and native copper grains enclosed by olivine phenocrysts in a picrite lava of the Emeishan large igneous province, SW China. American Mineralogist 91, 1178–1183.